BIOMIMETIC ENGINEERING OF COLLOIDAL NANOARCHITECTURES WITH *IN VITRO* AND *IN VIVO* FUNCTIONALITY

Inauguraldissertation
Zur

Erlangung der Würde eines Doktors der Philosophie
vorgelegt der
Philosophisch-Naturwissenschaftlichen Fakultät der Universität Basel

von
Tomaž Einfalt

aus Laško, Slowenien

Basel, 2017

Genehmigt von der Philosophisch-Naturwissenschaftlichen Fakultät

auf Antrag von

Prof. Dr. Cornelia G. Palivan (Universität Basel)

Prof Dr. Jörg Huwyler (Universität Basel)

und

Prof. Dr. Viola Vogel (ETH Zürich)

Basel, den 20.6.2017

Prof. Dr. Martin Spiess

(Dekan)

To my family and friends.

“Prijatli obrodile so trte vince nam sladko.”

“Freunde, die Rebe hat den süssen Wein beschert.”

TABLE OF CONTENTS

ACKNOWLEDGEMENTS

I would like to take this opportunity to express my deepest appreciation and gratefulness to prof. Dr. Cornelia Palivan and prof. dr. Jörg Huwyler who in early 2013 offered me the unique opportunity of pursuing my doctorate studies in the field of nanosciences at the departments of Physical Chemistry and Pharmaceutical sciences. Taking this path was by far one of the most important decisions in my life and has had a great impact on how I view the world. Thank you both for leaving me with the freedom to follow my own ideas and for your unconditional encouragement to do good science. Being a good scientist is not only about research, but also about passing on the acquired knowledge, which you two certainly did.

To you Cornelia, thank you, for you have always been there to guide me, not only when providing valuable scientific advice, but moreover also when teaching me very important life lessons through long afternoon conversations. You are a very tough supervisor, but together with your kind and patient nature it is that what makes you great. I hope, that in the future you do not change your ways.

To you Jörg, thank you, for having trust in me and always supporting me when I came with new ideas, despite the fact that I frequently missed the Pharmaceutical group meetings. Thank you for recruiting such an amazing team of scientists that form your group and for ensuring a great work atmosphere. Your constant enthusiasm for new discoveries is inspiring.

I would like to thank prof. Dr. Wolfgang Meier for integrating me in his department and giving me valuable scientific and professional advice. I thank prof. Dr. Viola Vogel for accepting to join as an external committee member and for sparking a great scientific collaboration and friendship with Dr. Jain Nikhil.

I would furthermore like to thank my postdocs and close friends Dr. Anja Car and Dr. Mariana Spulber for always being there for me, professionally and personally. Anja, hvala za vse – res. Mariana it was always great to discuss with you and I will certainly miss the early morning T. Pratchett talks. I thank Dr. Ioana Craciun, Dr. Jens Gaitzsch and Dr. Gesine Gunkel-Grabole for proof reading the thesis. During my doctorate studies, I was lucky enough to interact with many great people, that have over the past four years become a very important part of my life. Some had a great impact on my research and personal life. I thank Roland Goers, for many advice and for being great company in Lab 501 when we started out with our PhDs, Dr. Mihai

Lomora for all the discussions and great times we had together when traveling abroad. Mihai – I think we will always remember that time in Israel. To Dr. Dominik Witzigmann, Dr. Adrian Najer and soon to be Dr. Sandro Sieber - thank you for enjoying scientific work so much, it is your attitude that makes science so incredibly fulfilling. Sandro and Dominik - so long, and thanks for all the (zebra) fish. To my other collegues that have made the work possible: many thanks go to the Physical Chemistry and Pharmaceutical technology team. I am furthermore very thankful for the technical / buerocratical support by dr. Michael Devereux, Daniela Tischhauser, Maya Greuter, Sven Kasper.

A person that I would like to thank specially is Martina Garni. Thank you for the endless hours we spent together measuring, chatting and at some point even yelling at each other in the CLSM room. Thank you for keeping me company over the long weekends and for pushing things to the limits. I will never forget that moment when the GUV starting to glow bright red on that late Friday afternoon and the "oh, that's funny" moment that followed.

I dedicate this work to my family and friends. Mami, Ati in Matej, hvala vam za vašo podporo, vaš trud in ker ste bili vedno tu zame. Hvala Mami, ker si me naučila potrpežljivosti in vztrajnosti in ker si vedno skrbela da nisem lačen. Hvala Ati, ker si me naučil, da se je vedno treba znajdti. (Mother, Father and brother, thank you for your unconditional support and for always being there for me.) I also thank the Wildcats Swiss Triathlon Team for all the support and for keeping me on my toes ever since I arrived in Basel. Special thanks go to the Swim coaches Tobias Gross und Nathanael Adolf who were always there in the early morning hours, making the 6 AM trainings before work possible. I would also like to use this opportunity to thank the family Wolf and a special group of friends, who supported me during my studies: Tadej Razboršek, David Sakič, David Polak, Urban Horjak, Dejan Pinter, Nejc Zdovc, Jan Jagrič, Matevž Starič, Dr. Maria Foraster, Vincent Haenen, Federica Richina, Jana Kovač, Evelin Kranjc, Klemen Hrovat and finally Gurpreet Chabal Mond.

I am incredibly grateful to the Swiss Nanoscience Institute. Not only for funding my PhD, but also for providing an environment where new ideas and friendships are made. In this respect I thank Prof. Dr. Christian Schönenberger, Dr. Michel Calame, Dr. Kersin Beyer Hans and Dr. Christel Möller and Claudia Wirth.

Basel, in June 2017

ABSTRACT

Biomimetic engineering opens unprecedented possibilities of combining biomolecules (i.e. proteins, DNA, polysaccharides) with synthetic materials (i.e. synthetic polymers). This combination results in unique hybrid systems with functionalities that mimic processes in living organisms. While the translational value of functional biomimetically engineered structures is of exceptional importance in fields such as technology, engineering, chemistry, biology and medicine, due to the properties the structures inherit from both the synthetic and bio-materials, the understanding of how biomimetically engineered systems self-assemble and function is equally important, as it gives insight in how non-living systems progressed to living organisms. Some of the most prominent examples of functional biomimics include polymersome based catalytic nanocompartments, multicompartment systems that mimic cellular organization and artificial organelles. In this thesis, the focus lies on understanding and applying the fundamental principles of biomimetic engineering by equipping colloidal nanoarchitectures (soft polymer nanoparticles and hollow sphere polymersomes) with functional biomolecules (transmembrane proteins and enzymes).

First, the most important questions are addressed – why do polymer nanoarchitectures present ideal building blocks for creating novel biomimics, how do biomimics self-assemble in solution, which methods are most frequently used for their characterization, and where the applications of biomimics are in technology and medicine. Both colloidal and 2D supported/free standing polymeric nanoarchitectures structures are discussed in order to familiarize the reader with the wide range of nanoarchitectures that can be formed by polymers, however the focus primarily rests on biomimetic design of colloidal nanoarchitectures, as their colloidal nature favours them as therapeutic agents that can act on the cellular level.

To develop a pH responsive protein delivery agent, a biomimetic approach is applied in equipping self-assembled poly(ethylene glycol)-*b*-poly(methylcaprolactone)-*b*-poly(2-(N,Ndiethylamino)ethyl methacrylate) (PEG-*b*-PMCL-*b*-PDMAEMA) polymer nanoparticles with a therapeutic enzyme, acid sphingomyelinase. Due to the electrostatic interactions between the negatively charged enzyme and the positively charged PDMAEMA groups present in the nanoparticle corona, the biomimetically engineered nanoparticles display a distinct protein localization on their corona and a pH dependent release behavior of the attached protein. The application of the self-assembled system as a very efficient delivery agent for catalytically active biomolecules is demonstrated in human epithelial HeLa cells.

Next, a more complex nanoscale biomimic - a pH triggered catalytic nanocompartment - is built by biomimetically engineering the nanoarchitecture of poly(2-methyl-2-oxazoline)-block-polydimethylsiloxane-block-poly(2-methyl-2-oxazoline) (PMOXA-*b*-PDMS-*b*-PMOXA) polymersomes. Aqueous cavities of polymersomes are loaded with horseradish peroxidase while a chemically modified Outer membrane protein F (OmpF) is reconstituted in polymersome membranes. The chemical modification of OmpF transforms the otherwise unspecific pore into a selective and pH responsive pore, through which molecules can only diffuse once the attached molecular cap blocking the pore is cleaved. Hence, once the modified OmpF is functionally reconstituted in polymersome membranes it allows the developed biomimic to present an on demand catalytic activity. As a first proof of concept of a pH responsive catalytic nanocompartment the system demonstrates that a spatial control of a reaction inside a nanocompartment can be achieved and supports the further development of complex reaction spaces that can act in an analogous manner to cellular compartments, where *in situ* reactions are modulated by a plethora of responsive proteins.

Finally, biomimetically engineered polymersomes are designed for an *in vitro* and *in vivo* application as artificial organelles. In order to mimic processes taking place in lipid membranes of cellular organelles, polymersome membranes are equipped with a genetically and chemically modified OmpF. The structural modifications done at the rim of the OmpF pore, limit the OmpF permeability to small molecular weight molecules, but make it capable of responding to the presence of small signaling molecules. When the modified OmpF is reconstituted in membranes of enzyme loaded polymersomes it prevents the enzyme to access enzymatic substrates. However, the presence of of glutathione, which for example is found in abundant concentrations in the cytoplasm, readily cleaves the chemical modification of OmpF and opens the pore, thereby allowing the encapsulated enzyme to catalyze a reaction. The responsiveness of the self-assembled system to glutathione, abundantly present in the cytoplasm, makes the developed biomimic a suitable candidate for intracellular functionality as an artificial organelle. To demonstrate this, we not only show that the system is functional in the cellular microenvironment of human epithelial HeLa cells but also that it is robust enough to function *in vivo* in Zebrafish embryos.

Chapter 1.

FUNCTIONAL BIOMIMETIC DESIGN OF POLYMER NANOARCHITECTURES[⊥]

The first chapter serves to introduce the fundamental principles of biomimetical engineering of polymer nanoarchitectures and their applications. The reader is familiarized to amphiphilic block-copolymers - central building blocks of supramolecular polymer nanoarchitectures. Next, the thermodynamically driven self-assembly and characterization of both colloidal polymer nanoarchitectures (micelles, soft nanoparticles and polymersomes) and 2D polymer nanoarchitectures (films and membranes) is discussed. Both colloidal and 2D polymer nanoarchitectures equally serve as suitable platforms to which biomimetic engineering can be applied, however the focus here is primarily on the biomimetic engineering and application of colloids, due to their high translational value in biomedicine. Together the size, colloidal nature and fundamental architecture of colloid based biomimics support a wide range of applications, such as that of drug delivery agents, defined catalytic compartments, nanoscale systems that can imitate functions of cellular organelles or even micro scale cell mimics in the form of polymer based multicompartments.

[⊥⊥] This chapter is partially reprinted and has been published: T. Einfalt, G. Gunkel-Grabole, A. Najer, M. Spulber, C.G. Palivan, Supramolecular Architectures: Supramolecular Architectures from Self-Assembled Copolymers, *CRC Conciese Encyclopedia of Nanotechnology*, 2015, 1055-1072

1.1 INTRODUCTION

Inspired by nature, biomimetical engineering represents a scientific approach where fundamental principles acquired in engineering, chemistry and biology are applied to combine synthetic and bio- materials for the design of hybrid systems with functions that mimic biological processes. Motivated by structures and processes present in nature, such as the cellular plasma membrane, nanoscale biomimics represent hybrid materials that function with a high degree of precision and efficiency, for example when in the role of artificial organelles. The concept is especially important in the field of nanotechnology, as the unique combination of synthetic supramolecular nanoarchitectures and biomolecules gives rise to novel materials that inherit both the robust nature of the synthetic nanoarchitecture and the well-defined and efficient function of biomolecules. In order to favor an interaction with biomolecules the synthetic backbone of nanoscale biomimics needs to possess highly defined structural properties (i.e a well-defined membrane fluidity and thickness), which makes only a few synthetic systems eligible for this role[1]. The role of biomimetically engineered systems ranges from that of versatile agents in drug delivery to catalytic nanocompartments and functional cell mimics[1,2].

Thermodynamically driven self-assembly of molecules in solution represents a key process in nature and serves as inspiration to build a variety of biomimetical supramolecular nanoarchitectures, by starting with the corresponding building blocks. In nature, the result of self-assembly appears in examples like the tertiary structure of proteins, the helical structure of DNA, or the bilayer morphology of cellular membranes[1,2]. Driving forces behind molecular self-assembly involve various molecular interactions such as van der Walls interactions, hydrogen bonds and hydrophobic/hydrophilic balance. Biomimetic engineering of novel hybrid materials relies on the functional incorporation of biomacromolecules (DNA, proteins, polyssacharides) into the synthetic supramolecular nanoarchitectures, either during the self-assembly or after the synthetic backbone of the nanoarchitectures has already been formed. When combined, robust synthetic materials and highly functional biomacromolecules complement each other in stability and functionality. The synergistic effect between them gives rise to a high mechanical and chemical stability along with a highly defined, modulated and efficient functionality. When designing biomimetic nanoarchitectures the high degree of stability of the synthetic material along with the preservation of biomolecule functionality has to be taken into account. In this respect polymers and copolymers are synthetic macromolecules that represent prominent materials for biomimetic systems, as they can be chemically engineered to possess a specifically tailored composition in addition to possessing a very robust structure that allows complex interplay with a variety of biomolecules[3]. Depending on their chemical nature, and conditions in which the self-assembly process takes place, synthetic polymers alone or in combination with biomolecules generate a plethora of different supramolecular architectures, which range in size from a few nanometers in diameter up to several micrometers. This versatility has been explored extensively in the past, giving access to wide range of hybrid structures including biomimetically engineered micelles, soft nanoparticles, worms, or vesicles in solution, as well as planar membranes and polymer films[1,4] (Scheme 1.).

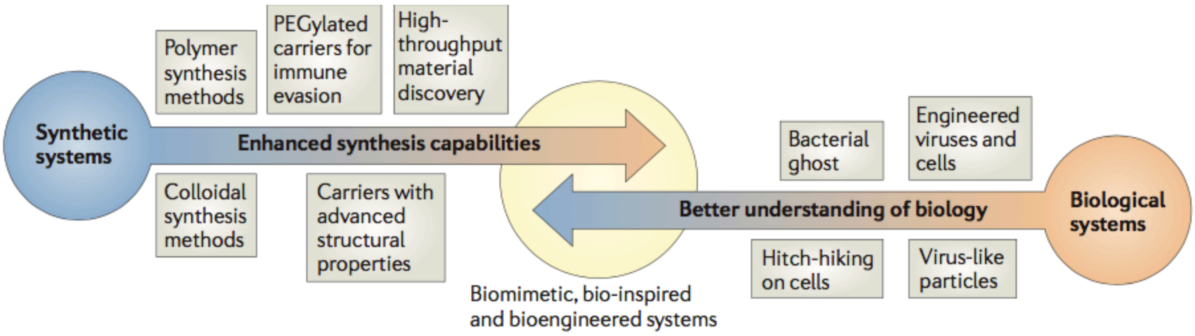

Scheme 1. Biomimetically engineered artificial nanoarchitectures. Principles of biomimetic engineering are applied to merge the gap between synthetic and biological systems, leading to the design of new hybrid systems that inherit the properties of both synthetic and biological systems. Adapted from *Ref*[2] with permission.

1.2 AIM OF THE THESIS

The aim of this thesis is to advance the state of the art in development of biomimetically engineered polymer nanoarchitectures, with the focus on designing novel hybrid colloidal structures with enhanced functionalities. The colloidal nature, shape and size makes polymersomes, micelles and soft nanoparticles some of the most prominent materials in modern day drug delivery applications. However, in order to design systems that go beyond established drug delivery methods, very important properties like the ability of molecular recognition, an enhanced catalytic activity or triggered functionality all have to be taken into account. Biomimetic engineering offers a way to introduce these properties to the otherwise inert nature of synthetic nanoarchitectures in a way where they are combined with biomolecules that present some kind of intrinsic functionality. Previously this methodology has been applied to colloidal nanoarchitectures for the development of systems like the first artificial peroxisome[5], organelle like polymersome DNA clusters[6], targeted antigen functionalised polymersomes[7] and heparin decorated polymersome[8] based nanomimics. Here we begin by designing a protein carrier based on PEG-*b*-PMCL-*b*-PDMAEMA polymer nanoparticles[9], that can attach and release therapeutic proteins on demand. This mimics a fundamental phenomena of carrier nanostructures found in nature, where for example nano sized globular proteins and lipoproteins, such as high density lipoproteins, low density lipoproteins [10], transferrin and ferritin[11] have their architectures specifically tailored to carry molecules, such as cholesterol and iron, from one organ to the other in the human body. Further, we investigate how the hollow-sphere nature of PMOXA-*b*-PDMS-*b*-PMOXA polymerosmes can be engineered to design a synthetic compartment system with on demand catalytic functionality[12]. Such as spatial control of compartmentalised reactions is vital for the advance of novel therapeutics, as it mimics the natural function of cellular organelles and provides a mean to design artificial organelles. Finally, the aim of the thesis is to advance the state of the art design of polymersome based artificial organelles, by testing the functionality and stability of responsive catalytic nanocompartments *in vitro* and *in vivo*.

1.3 SYNTHETIC POLYMER NANOARCHITECTURES AND THEIR SELF-ASSEMBLY

Synthetic polymers represent essential building units for the self-assembly of colloidal and 2D (supported or free standing) nanoarchitectures, such as micelles, soft nanoparticles, disks, worm like structures, polymeric vesicles, polymer films, polymer membranes[1,13].

The diversity of assemblies generated by polymers is a consequence of the wide variety of compositions, functionalities and shapes in which polymers occur. Synthetic polymers - classified in homopolymers, copolymers- are obtained by a variety of synthetic polymerization procedures [1,14]. Homopolymers consist of identical repeating units of monomers connected by covalent bonds, whereas block-copolymers are polymers made of two or three or more different blocks of covalently linked homopolymers. In most frequent methods of synthetizing block-copolymers, monomers are first polymerized to longer homopolymeric blocks. Once these are complete, two, three or more homopolymeric blocks are linked together in a final step that yields the desired block-copolymer. However alternative means of synthesis, such as one pot reactions where all the monomers are reacted together, also exist and should be considered[15]. In this way, amphiphilic properties of the final product are the result of different hydrophyilic and hydrophobic properties of induvidual homopolymer blocks. The amphiphilic properties of the along with the respective lengths of polymer chains and the method used in preparation of nanoarchitectures predominantly determine shape of the self-assembled nanoarchitectures[13]. An exception are polyelectrolytes, which represent a special group of polymers that display characteristic charged functional groups along the polymer chains, which lead to the assembly of nanoarchitectures based on the opposite charges of the polyelectrolyte multilayers[16].

To synthetize the desired product, the polymerization reaction is selected depending on the nature of the monomers and the desired products. During synthesis, key parameters (i.e solvent, temperature and time) have to be controlled in order to obtain a molecular weight and narrow dispersity of the polymer[17]. Several methods of synthesis exist to synthetize polymers, each with advantages, such as a narrow polydispersity of the product, and disadvantages, such as the need of organic solvents or toxic catalysts. Some of the most prominent synthesis routes are: (a) living anionic and cationic polymerization[18,19], (b) controlled ring-opening polymerization[20], and (c) controlled radical polymerization (CRP), which includes: (i) atom transfer radical polymerization (ATRP)[21], (ii) reversible addition-fragmentation chain transfer polymerization (RAFT)[22] and (iii) nitroxide mediated radical polymerization (NMP)[23].

The poly(2-methyl-2-oxazoline)-block-polydimethylsiloxane-block-poly(2-methyl-2-oxazoline) PMOXA-*b*-PDMS-*b*-PMOXA and PEG-*b*-PMCL-*b*-PDMAEMA copolymers, discussed later on in Chapter two, three and four are obtained by controlled ring opening polymerization. The PEG-b-PMCL-b-PDMAEMA copolymers require an additional step of ATRP polymerization. Ring opening polymerization techniques (ROPT) are widely used for the synthesis of well-defined polymers, since by controlling the catalyst, monomer type and nature of the initiator tailor made polymers can be synthetised[18,20,21].

1.4 COLLOIDAL NANOARCHITECTURES

Micelles, soft nanoparticles and polymersomes are colloidal assemblies generated by the self-assembly of amphiphilic block-copolymers in aqueous or organic media. They are the most frequently mentioned colloidal nanostructures, due to their popularity in a large variety of medicinal applications as biosensors, drug/contrast agent carriers, mimics of biomembranes, catalytic nanocompartments, and very recently, as model nanocompartment spaces for the design of artificial cell organelles (Figure 1.)[17,24,25].

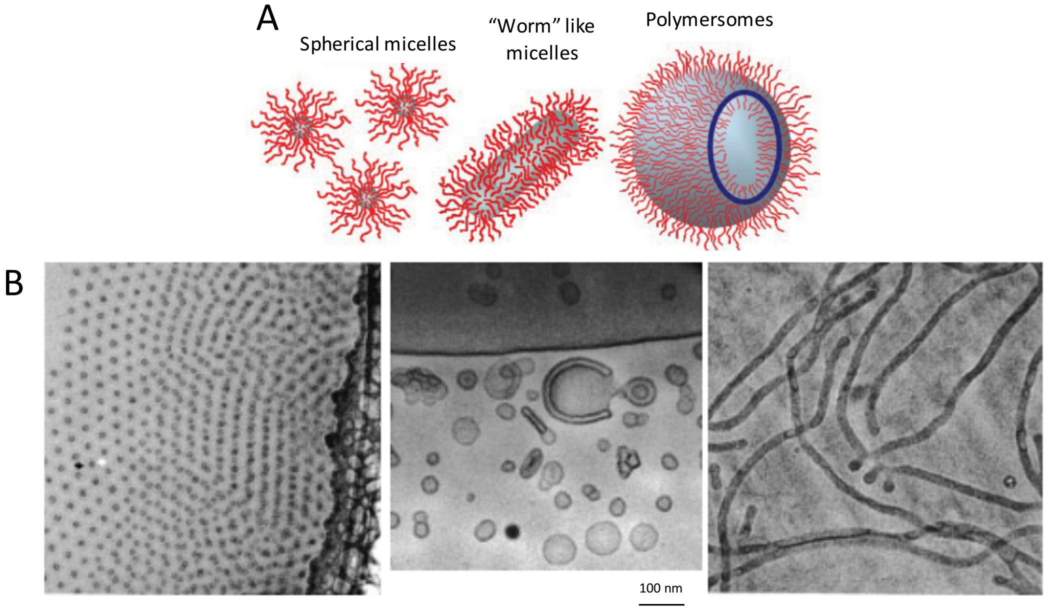

Figure 1. Schematic representations and respective cryo-TEM images of colloidal nanoarchitectures. Panel A. Schematic drawing of colloidal nano-scaled self assemblies, micelles, cylindrical micelles – „worm like“ structures, and polymersomes. Adapted from *Ref*[17] with permission. Panel B. Cryo-TEM pictures of micelles, vesicles, and worm-like micelles. Adapted from *Ref*[26] with permission.

1.4.1 MICELLES

Micelles are colloidal nanoarchitectures generated, and thermodynamically stabilized, when the polymer concentration in a given solvent is higher than the critical micellar concentration (CMC), and disassemble upon dilution of the polymer concentration below the CMC. Primarily the process is governed by the reduction of Gibbs free energy. The rate of the assembly and disassembly is dependent on the structure of the amphiphilic polymers, such as the chain length, hydrophobicity, hydrophylicity. These properties determine the interactions between the polymer chains in solution, such as hydrogen bonds and van der Walls interactions[27]. The critical micellization temperature (CMT) represents the temperature above which amphiphilic molecules can be found as aggregates. Below the CMT they remain as unimers[28]. The critical micellar temperature is a point of phase change below which the surfactant remains in crystalline form, even in aqueous solution. Micelles have a broad size distribution. Their architecture consists of an inner core, generated by the hydrophobic domain, and hydrophilic corona, which shields the core[29].

Micelles are generated by a variety of amphiphilic copolymers: diblocks, triblocks, or grafted copolymers[30,31]. Depending on the copolymer chemical composition, solvent, and preparation method micelles have different shapes, ranging from spheres to cylinders and lamellar bilayers[32]. For example, coil-coil block copolymers can lead to either spherical star-like micelles or "crew-cut" micelles, depending on the length of the corona chains (Figure 2.)[33,34]. Rod-coil block copolymers can form either disk-like micelles or rod structures depending on the lengths of the corona chains[35,36].

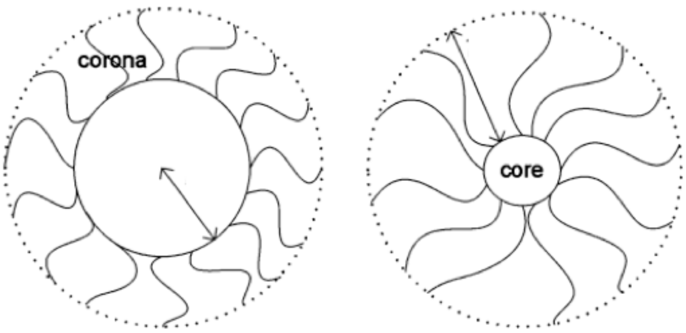

Figure 2. **Schematic illustration of micellar nanoarchitecture.** A crew-cut micelle (left) and a starlike micelle (right). Adapted from *Ref* [34] with permission.

The terms "nano-rods", "nanotubes", "worm like" "disk" micelles refers to cylindrical structures with a tubular core diameters ranging from a few 5 nm to 100 nm[37]. Their length, however, can exceed 1μm, as the thermodynamic favored state of longer structures is favored over short ones. ”Worm-like” micelles have two distinct architectures: linear and branched. The predominant topological effect determines the morphology: linear morphology in the case of end-caps, and branched in the case of Y-junctions (Figure 3). There are situations where both types of architectures can coexist in different proportions[38].

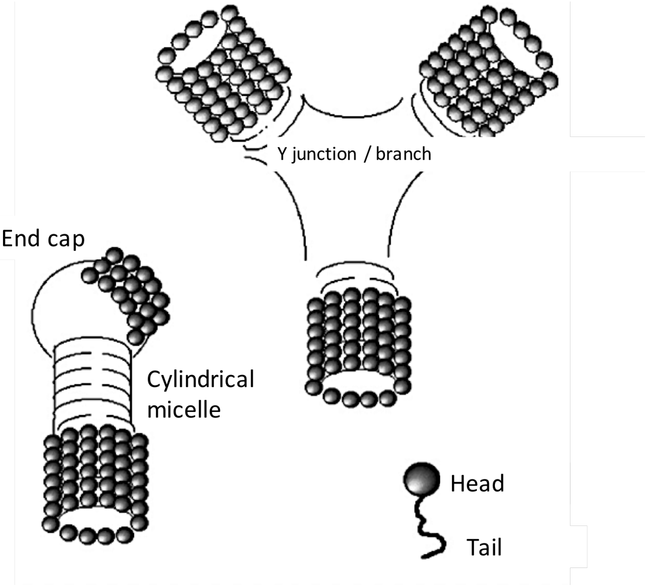

Figure 3. Cylindrical micelles. Topological defects in cylindrical micelles: end caps and y-branch junctions adapted from *Ref*[38] with permission.

Spherical micelles are the most frequently used micellar structures, with sizes ranging from 10-100 nm[39]. Their popularity is a consequence of their size, spherical shape and the hydrophobic core that can serve to entrap hydrophobic molecules. The latter is beneficial for various applications - the most prominent being as drug delivery systems or solubilization agents. One of the most frequently used hydrophilic domains is poly(ethyleneglycol) (PEG) due its biocompatibility, and low toxicity[39]. As hydrophobic blocks, polyamino acids, polyethers, and polyesters, such as poly(propylene oxide) (PPO), poly(D,L-lactic acid) (PDLLA), poly(ε-capro- lactone) (PCL), poly(L-aspartate) and poloxamers are typically employed[30,31].

Commonly applied methods for micelle formation and entrapment of molecules in micelle cores are: i. direct dissolution, ii. solvent exchange, and iii. film rehydration. More elaborate techniques, in terms of equipment, are evaporative spin coating and corona cross-linking strategies or the combination of direct dissolution / solvent exchange with microfluidics[40]. An amphiphilic block copolymer in aqueous medium around the CMC of the copolymer represents the most straight forward approach of generating micelles. The dissolution is followed by heating and the addition of hydrophobic molecules in order to promote encapsulation. Once the temperature drops below the CMT the hydrophobic molecules are encapsulated in the inner core of micelles. The solvent exchange method is based on dissolution of copolymers and molecules to be entrapped in an organic solvent, and subsequent addition of water, which will favor micelle formation. The inverse method is used as well, depending on the copolymer solubility: the addition of an organic solution to an aqueous solution of copolymers and hydrophobic molecules intended to be entrapped. Lack of miscibility of the organic solvent in the aqueous medium can lead to oil in water (O/W) emulsion, which requires subsequent removal of the organic phase. The rate by which the organic solvent is removed not only determines the number of micelles, but also their size and the possible creation of aggregates. Film rehydration method is based on dissolution of the block-copolymer in a suitable organic solvent, which is then evaporated under reduced pressure resulting in a thin polymer film[41]. The film is then rehydrated by addition of aqueous solution under stirring, and 3D assemblies are formed. Spin coating method is based on a deposition of copolymers as uniform thin films on flat surfaces, which favors the formation of micelles due to preferential interactions between one of the copolymer blocks and the solid surface. Corona cross-linking strategies employ chemical cross-linking of the polymer chains, which form the micellar corona of preformed micelles[42,43].

1.4.2 SOFT NANOPARTICLES

Amphiphilic block copolymers can form spherical colloidal structures named soft-nanoparticles. Despite the similarity of soft nanoparticles to micelles in size and composition, the equilibrium dynamics of soft-nanoparticles are different and are not driven by the self-assembly of block-copolymer around the CMC. Soft-nanoparticle self-assembly relies highly on the hydrophobic interactions and molecular entanglement of polymer chains within the nanoparticle core and is in general irreversible. In this respect the hydrophobic unit of the polymer chains should be long enough to assure a consequent "frozen" state of molecular entanglement (Figure 4.)[44]. Interestingly, soft nanoparticles can be formed by folding a single chain of polymer, if the chain is sufficiently long[45]. This demonstrates that the self-assembly is driven by the same forces as the self-assembly of protein molecules, which are folded from a single chain of amino acids. Typically, the size of soft-nanoparticles ranges between 50 to 200nm. Once self-assembled, the colloidal stability of the nanoparticles is assured by steric or electrostatic repulsions between individual nanoparticles, which prevents fusion from Brownian collision [44]. Preparation techniques for nanoparticles include direct dissolution and nanoprecipitation followed by solvent removal, which influence the size or aggregation number of particles depending on the rate and magnitude of the solvent dilution or removal[46,47].

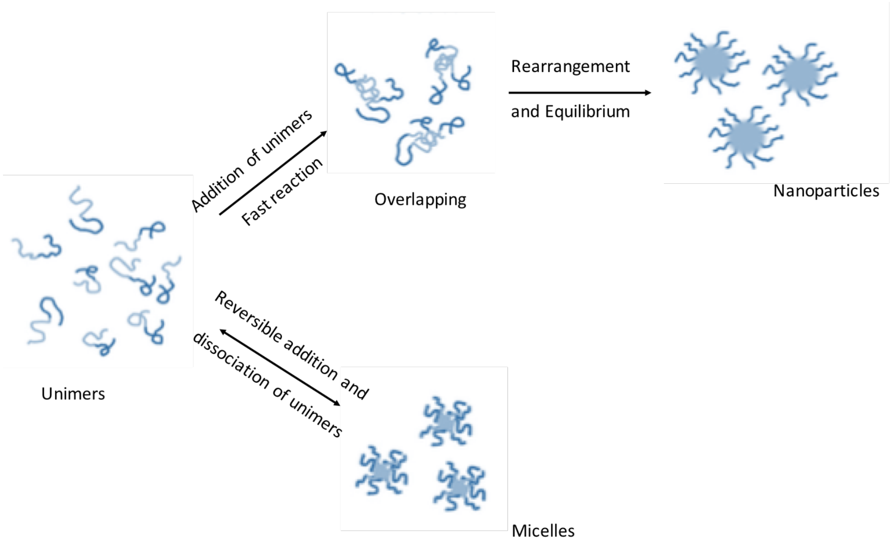

Figure 4. Soft-nanoparticle formation via self-assembly. Pathways of polymer chain self-assembly and the products. Micelles are formed by the CMC driven self-assembly of amphiphilic block copolymers. Nanparticles are formed by the rapid and non-equilibrium self assembly of amphiphilic block-copolymers. Adapted from *Ref*[44] with permission.

1.4.3 POLYMERSOMES

Polymer vesicles, named polymersomes[48] ,are structural analogues to lipid vesicles (liposomes) built from amphiphilic block copolymers instead of lipids (Figure 5). During self assembly of polymersomes either spherical mono- (ABA-type polymer) or bilayer membranes (AB-type) enclosing a watery core are formed. The hydrophilic to total mass ratio (*f*-value), the packing parameter ($p = v/a_0l_c$), and the polydispersity index are key parameters, which govern the self-assembly process (v = volume of hydrophobic part, a_0 = contact area of head group, l_c = length of hydrophobic part) [3,49]. *f*-ratios in a range of 25 - 45% and p parameters between 0.5 and 1 and a polydispersity index around 1 favour formation of polymersomes. The polymerization routes used to obtain well-defined amphiphilic copolymers have been described above[18-21,50,51].

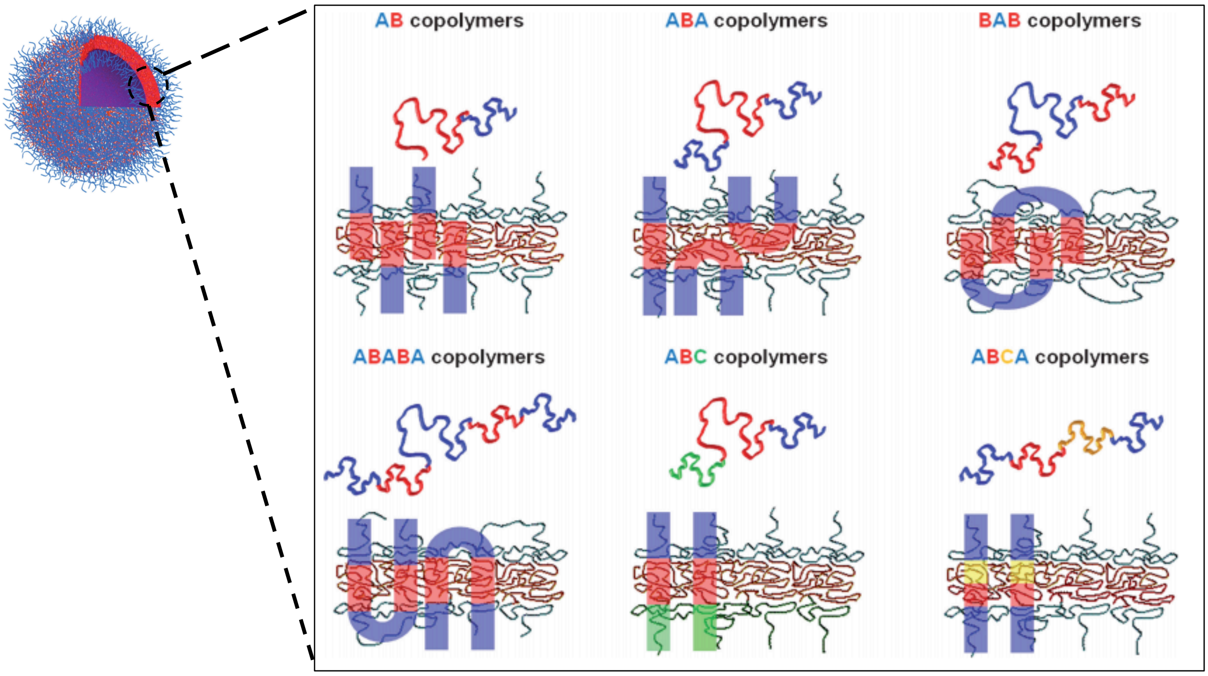

Figure 5. Membrane composition of polymersomes. The polymeric membrane is formed by either diblock (AB), triblock (ABA or BAB), or multiblock polymers (ABABA, ABC or ABCA), where A, B and C are chemically different polymer blocks. Adapted from *Ref*[52].

While lipid membranes are typically 3 – 5 nm thick; the membrane thickness of polymersomes can be fine-tuned in the range of about 5 to 30 nm, depending on the length of the blocks[53]. In contrast to micelles and soft nanoparticles, polymersomes can also be found in sizes from 1μm-

20μm. The larger giant unilamellar vesicles (GUVs) are especially appealing due to their potential as cell mimics. Polymersomes offer a wide variety of advantages compared to liposomes, especially higher mechanic stability, and greater chemical versatility[48,54,55]. The driving force for polymersome formation is mostly the hydrophobic effect. A special group are polymersomes with a polyion complex membrane (PICsomes), formed by ionic interactions of oppositely charged polymers (Polyelectrolytes) [16]. The composition of the amphiphilic block-copolymer used for polymersome formation can be either purely synthetic [3], biohybrid[16,56], or purely biological [57,58]. Specific functions, such as targeting properties, can be implemented by including biological entities directly into the block copolymer before vesicle formation[56] or by functionalizing of preformed vesicles with targeting ligands[59,60].

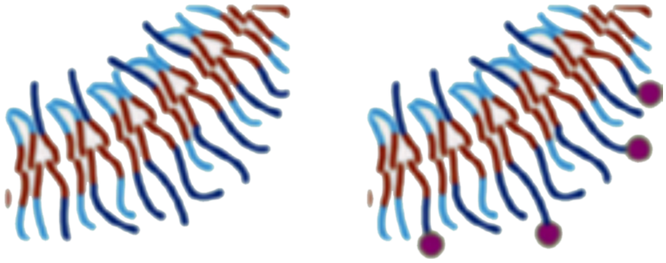

Figure 6. Membrane functionalisation of vesicles. Left: Unmodified polymersome membranes, Right: Polymersome membranes modified with targeting ligands. Adapted from *Ref*[61] with permission.

Another critical step is to choose the appropriate polymersome formation technique. The latter is usually specific for each polymer - a technique that works for one polymer cannot necessarily be applied to other polymers. The most suitable technique might even change depending on the nature of the desired molecules to be encapsulated. Currently used polymersome formation methods are similar to those used for micelle formation: direct dissolution of dry polymer powder, film rehydration, solvent exchange method in addition to double emulsion technique, electroformation and microfluidics[60,62,63]. Polymersome size is highly dependent on the preparation method. For example, film rehydration yields small multilamellar vesicles, whereas electroformation was specifically developed to produce micrometer-sized polymersomes[60]. After formation of the polymersomes, extrusion – separating a polymersome solution through a filter with defined pore sizes – is often applied to obtain smaller polymersomes with a narrower size distribution. Interestingly polymersomes made from diblock, but not triblock, copolymers can be transformed from unilamellar to bilamelar "double" polymersomes under hypertonic shock, demonstrating the close relation, and the intrinsic differences of polymersomes and liposomes (Figure 7)[64].

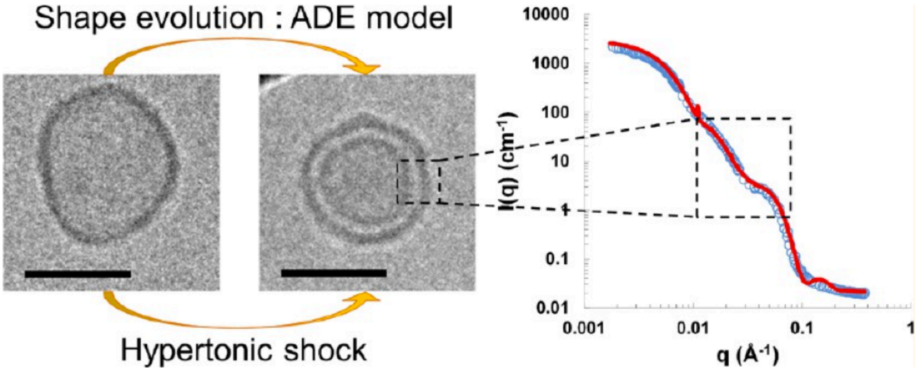

Figure 7. Osmotic transformation of polymersome vesicles. Cryo-TEM images of shape transformation from unilamellar vesicles to bilamellar vesicles due to hypertonic shock. Small-angle neutron scattering performed on polymersomes. Adapted from *Ref*[64], with permission.

1.5 SUPPORTED AND FREE STANDING 2D POLYMER NANOARCHITECTURES

Polymer-films, self-assembled monolayers, polymer membranes, polymer brushes and polymer layers represent supported and/or free standing 2D polymer nanoarchitectures that can equally serve as platforms for the design of nano-scale biomimics. However, as biomimetic engineering of 2D polymer structures is beyond the scope of this thesis, the following paragraphs serve to briefly introduce the reader to the variety of 2D nanoarchitectures formed by synthetic polymers.

1.5.1 POLYMER FILMS

Polymer films are thin layers of polymers that are typically attached to a solid substrate, but they can be also found as entirely free-standing between air-water interfaces. They represent one of the simplest models of biological self-assemblies and are important as they provide information about the fundamental thermodynamics behind self-assembly [1].Their size ranges from a few nm up to several micrometers in thickness, and largely depends on the type of film and the preparation method. Owing to the wide range of polymer synthesis techniques and polymer film types available, the characteristics and film properties can be effectively tuned to specific needs. Their permeability, wettability, mechanical, optical or adhesive properties can be controlled [65] making them ideal candidates for a plethora of different applications in biomedical coatings, sensors, photovoltaics, lubrication, and filtration.

1.5.2 SELF-ASSEMBLED MONOLAYERS

Self-assembled monolayers (SAMs) are the thinnest polymer films on solid support, having a thickness up to a few nanometers (Figure 7.)[66]. The monolayers are formed spontaneously through chemisorption of functional molecules at the interface of solid surfaces with liquids or gases[67,68]. The most commonly used systems include thiol-functionalized molecules on gold surfaces (Figure 9) and alkylsilanes on silicon or glass[69]. The resulting polymer films are thermodynamically stable, highly ordered, and nearly defect-free surface coatings[66,68]. A range of solid substrates is available for functionalization through this method, particularly hydroxylated surface of different materials can for example react with alkylsilanes[68]. This method of surface modification is not limited to attachment of polymers. In fact, small molecules are frequently immobilized *via* this method.

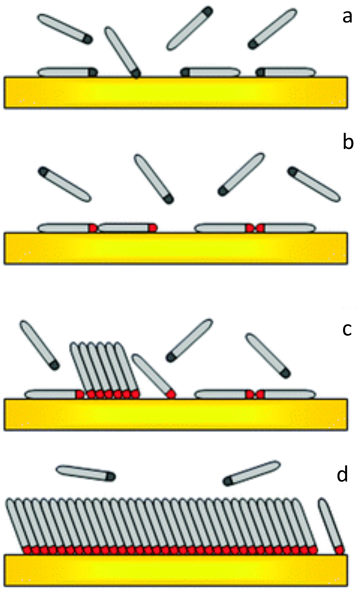

Figure 8. Self-assembled polymer monolayer. Different steps take place during the self-assembly of self-assembled moolayer on a gold surface. In order to allow chemical binding of the polymer molecules (red) to the gold surface (yellow) thiol groups are presented at the end of polymer chains (black). The different phases are presented: a.) physiosorption, b.) lying phase formation for molecules, c.) nucleation of the standing up phase and finally the completion of the standing up hase of the self-assembled monolayer. Adapted from *Ref*[67] with permission.

1.5.3 POLYMER MEMBRANES

A polymeric membrane can be formed from amphiphilic di- or triblock copolymers, thereby resembling the structure of naturally occurring lipid-based cellular membranes [70,71] These membranes are very soft and flexible and do not require covalent attachment to an underlying substrate. The membranes can be formed directly on the surface through synthesis of block copolymer brushes from surface-immobilized initiator moieties or through grafting of polymer chains to the surface. Alternatively, the membrane can be pre-formed and subsequently deposited on a solid support using the Langmuir-Blodgett method[72,73]. A third synthetic route is to first assemble polymeric vesicles (as discussed above), which are then ruptured on the solid support to yield a planar membrane (Figure 9.)[74].

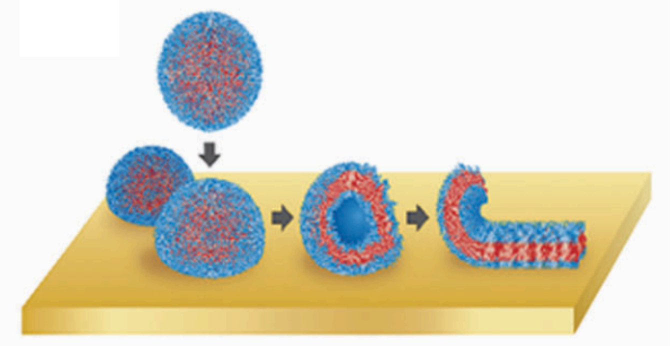

Figure 9. From polymersomes to planar membranes. Preformed polymersomes are ruptured on solid support to yield planar membranes. Adapted from *Ref*[4] with permission.

1.5.4 POLYMER BRUSHES

Polymer brushes are another well-studied class of polymers on solid support. However, unlike polymer membranes they are not directly self-assembled in solution but require covalent attachment on a surface. They obtained their name "brushes" because the polymer chains are stretched away from the substrate, resembling a brush (Figure 10.)[75]. Depending on external stimuli (i.e pH), the polymer chains forming the brush can be extended or coiled. Polymer brushes can be synthesized in solution and subsequently grafted to a surface, or they can be grown directly on the surface from previously immobilized initiator molecules[76]. The different types of living/controlled radical polymerization techniques[77,78] are established to synthesize polymer brushes;, however, metathesis polymerization[79] and supramolecular polymerization[80] methods have also been employed successfully. The accessible thickness, which relates to the degree of polymerization in free polymers[81], depends on the parameters of the polymerization reactions such as time, catalytic system, or solvent, but typically thicknesses around or exceeding 100 nm are generated. Different nanomorphologies of the polymer film can be generated depending on the lengths of the polymer blocks and the exposed solvent[77].

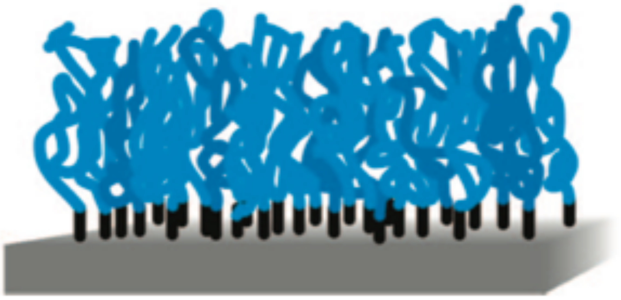

Figure 10. Polymer brushes and polymer film formation. Schematic illustration of a polymer brush, where the polymer chains are stretched away from the surface giving a dense polymer film . Adapted from *Ref*[78] with permission.

1.5.5 POLYMER CARPETS

More recently, polymer brushes have also been synthesized on soft and thin initiator layers to yield entirely free standing polymer films termed "polymer carpets"[82,83]. Other free-standing films are pore-spanning membranes,[74] or polyelectrolyte layers bridging pores as large as 100 µm[2,84]. Polymer sheets of only a few nanometers in thickness have been obtained by using specifically designed monomers [85] and by cross-linking of aromatic self-assembled monolayers [86]. These different types of free-standing polymeric films have their general synthetic route in common; typically, the film is first generated on a solid support and subsequently lifted off [82,83,86] (Figure 11).

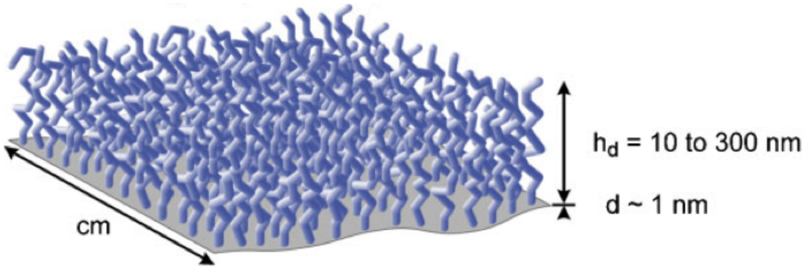

Figure 11. Freestanding Polymer carpet. Dimensions of an exemplary polymer carpet composed of a crosslinked substrate and a polymer brush. Adapted from *Ref*[82] with permission.

1.5.6 POLYMER LAYERS

Thicker and thus more robust polymer layers can be obtained by deposition of polymers on solid support. Typical methods include spin-coating[87] and layer-by-layer (LbL) assembly of polyelectrolytes (Figure 12.)[88]. In both techniques, the thickness of the polymer film can be easily controlled by the preparation parameters, and thicknesses in the micrometer range are accessible. The ease of film formation using the LbL method and the solubility of polyelectrolytes in aqueous systems set important prerequisites for biomedical applicatons[89], but the method is also used to deposit polymerization initiators[83,90]. A more laborious method of preparation presents spin coating spin-coating, on the other hand, that can be used for the formation of polymer layers used in various applications[91].

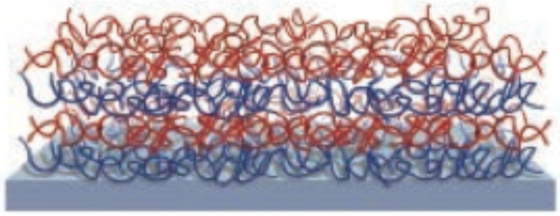

Figure 12. Polymer films formed with layer-by-layer method. Model of a polymer film formed with the layer-by-layer method, in blue a charged polymer and in red an oppositely charged polymer, adapted from *Ref*[89] with permission.

1.6 CHARACTERIZATION OF POLYMER NANOARCHITECTURES

1.6.1 CHARACTERIZATION METHODS FOR COLLOIDAL NANOACHITECTURES

For proper characterization of the assembled colloidal nanoarchitectures various properties, such as assembly size, homogeneity, shape, and surface charge must be analyzed. The characterization techniques are roughly divided in:

i. scattering methods (light and neutrons scattering)
ii. microscopy techniques

SCATTERING METHODS

Light scattering methods such as static and dynamic light scattering (SLS and DLS respectively) and flow cytometry are commonly used as non-destructive methods that assess various colloidal nanoarchitecture parameters such as the size, concentration, architecture (solid sphere, vesicular structure, cylindrical micelles, etc), and presence of various populations of assemblies (for example micelles and vesicles). In addition, the vesicular zeta potential can be determined by measuring the electrophoretic mobility of assemblies in a capillary cell, where they are exposed to an alternating current[92,93,94] (Figure 14).

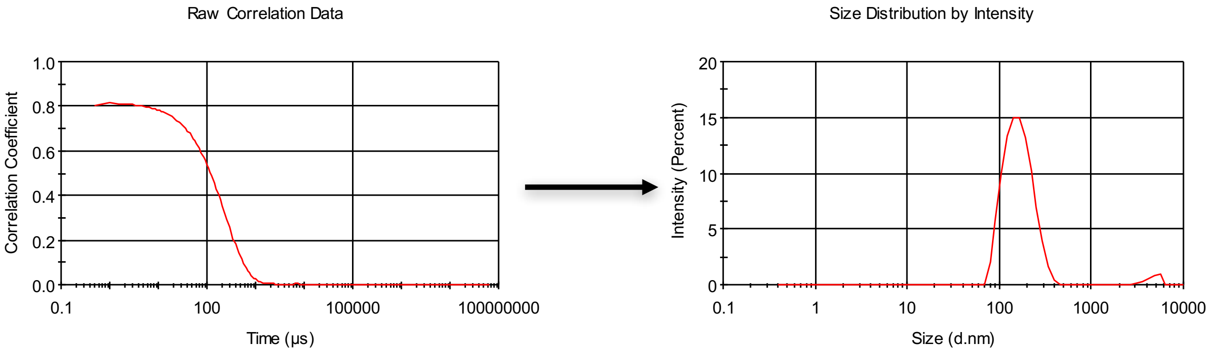

Figure 13. Prinicples of light scattering analysis. The intensity correlation function is correlated to a size distribution by intensity.

Small angle neutron scattering (SANS) is a technique in which a neutron beam passes through a sample and the resulting scattered neutrons are counted as a function of angle and wavelength providing information about the morphology, size, and interactions of 3D assemblies present in the sample[95].

MICROSCOPY TECHNIQUES

Electron microscopy techniques such as scanning electron microscopy (SEM), transmission electron microscopy (TEM), and cryogenic TEM (Cryo –TEM) are frequently used when high resolution is required, for example when examining the architecture and membranes of colloidal nanoarchitectures (Figure 14.). These techniques are based on focusing a beam of electrons on the specimen: the acquired images are the result of the interactions of electrons through the sample[26,53].

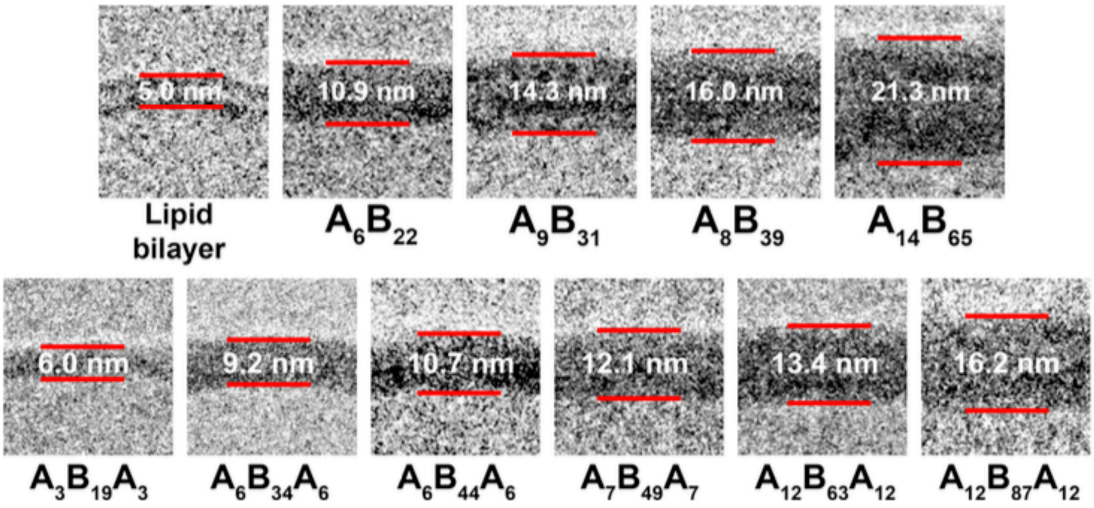

Figure 14. Cryo-TEM of PMOXA-*b*-PDMS-*b*-PMOXA. Application of cryo-TEM for the determination of the thickness of PMOXA-*b*-PDMS-*b*-PMOXA polymersome membranes. Adapted from *Ref*[53] with permission.

Conventional microscopy is normally used in the case of colloidal structures that present a relatively big size (>1μm) or when investigating the intracellular localization and function of colloidal nanostructures. It is of exceptional value, when it is necessary to obtain information on the behavior of specific structural domains. The latter can be labelled with fluorophores, which serve to distinguish the labelled domain from the rest of the nano/micro architecture (Figure 15) [96,53]. In this respect, fluorescence microscopy is most frequently applied as confocal laser scanning microscopy (CLSM). CLSM is an optical imaging technique, which leverages on a spatial pinhole placed at the confocal plane of the lens. This eliminates out of focus light and enables reconstruction of 3D structures from images that are acquired with optical sectioning. Until recently the intrinsic resolution of CLSM was limited by the diffraction limit of light, meaning that objects smaller than 200-300nm could not be distinguished. However recent advances in techniques such as the stimulated emission and depletion allow a lateral resolution of down to 60nm[97].

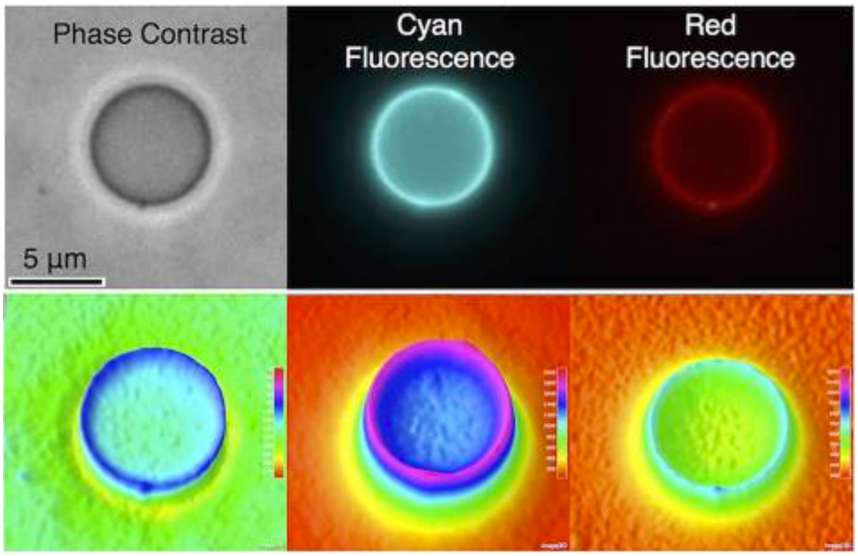

Figure 15. Fluorescence microscopy images of polymeric giants. Fluorescence images of giant unilamellar polymersomes, acquired by CLSM. Red fluorescence: m-Cherry, Cyan fluorescence coumarin fluorophore. Adapted from *Ref*[96] with permission.

.

Data collected by fluorescence microscopy or computer-enhanced video microscopy can be applied to single particle tracking (SPT). By using SPT the relative position of an object is directly monitored in time and recorded. This provides information about the movement of the observed objects and their paths, which can be analyzed independent of theoretical fitting models. The typical size resolutions of this technique are in the range between 20 – 100 nm, while time resolutions range from 25μs to 100ms and heavily depend on the type of camera that is used in the measuring device. The camera can for example, capture a video file of the particles moving under Brownian motion. By using nanoparticle tracking analysis (NTA) many individual particles can be followed simultaneously individually and their hydrodynamic diameters determined using the Stokes Einstein equation (Figure 16.)[98].

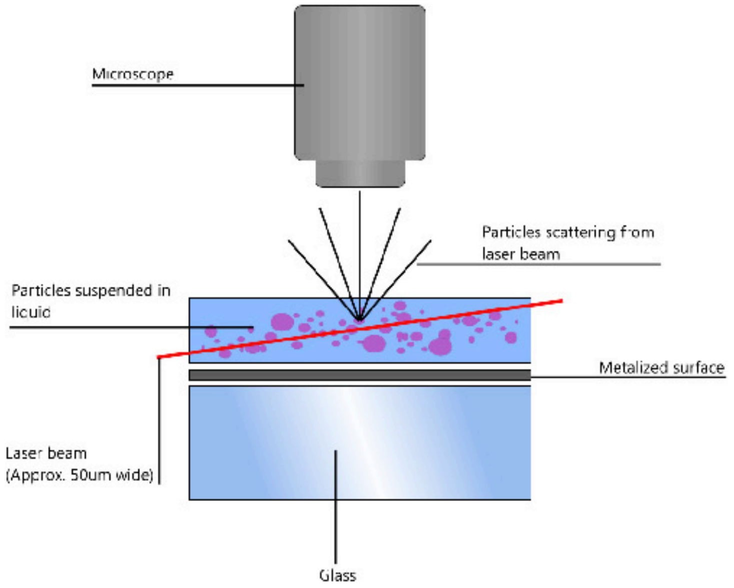

Figure 16. Nanoparticle tracking analysis. Principle of using microscopy for single particle analysis. Adapted from Malvern.com.

A particular useful technique to study both the sizes of nanoarchitectures and their interactions with specific molecules is fluorescence correlation spectroscopy (FCS). FCS makes use of a very small observation volume (~ 1 fl), named confocal volume, and follows the diffusion of fluorescent molecules through it. Much information relevant to analyzing the behavior of nanoarchitectures can be extracted from the autocorrelation curve of the signal, which is related to the diffusion of fluorophores in and out of the focal volume. The half-value decay time gives an estimate of the mean diffusion time. Information about particle concentration can also be determined, as the inverse amplitude of the correlation curve equals the average particle number within the focal volume. In the case when there are multiple molecules in the confocal volume, there is a higher average fluorescence but a smaller relative fluctuation from each molecule. Hence, the effect of a single molecule is diminished, giving smaller fluctuations and a lower correlation amplitude[55,99] (Figure 17.). The significant advantage of FCS is that it is capable of detecting single molecules at high spatial and temporal resolutions, while the concentrations can be kept in the nanomolar range. A drawback however is, that the observed molecules have to be fluorescent and that the appropriate dye has to be selected for each purpose. It is a technique that is of tremendous importance in biomimetic engineering of nanoarchitectures as it allows to determine diffusion coefficients, correlated to possible interactions of fluorescent molecules with supramolecular assemblies, such as polymersomes, liposomes and nanoparticles in the pico- to nanomolar concentration region [8,100-103].

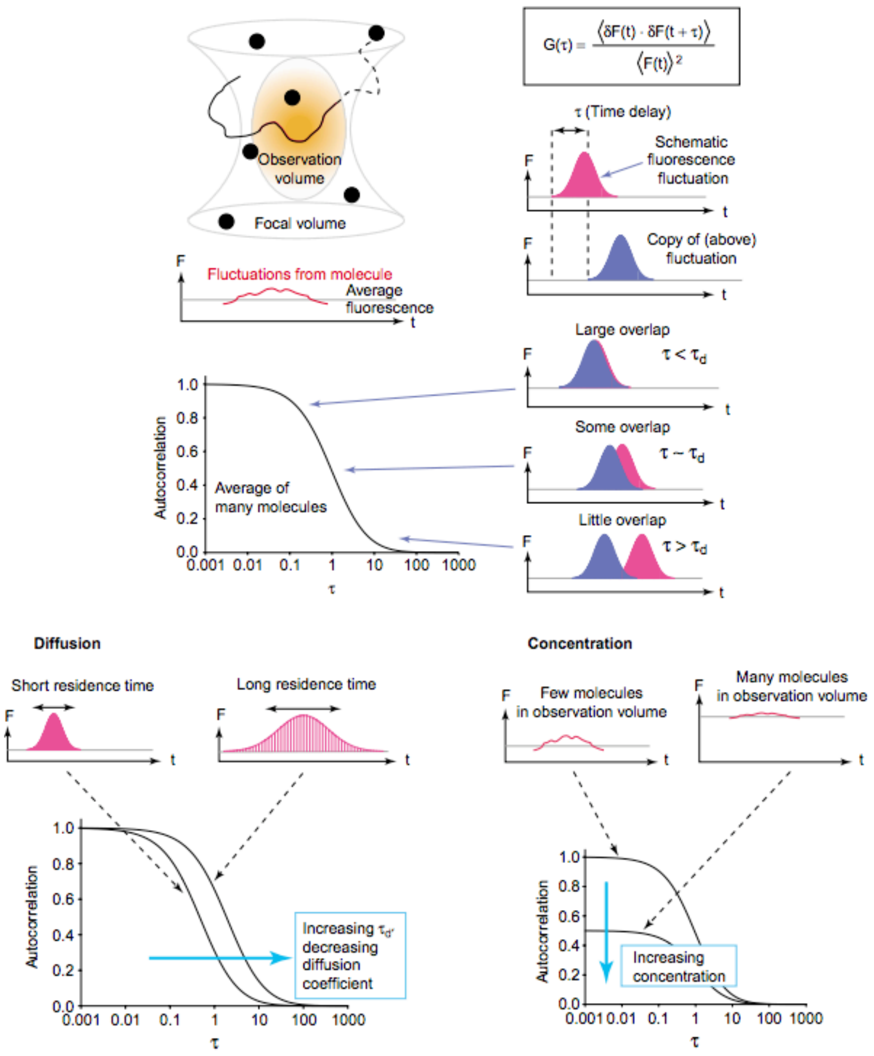

Figure 17. General principles of fluorescence correlation spectroscopy. Application of a focused laser beam, FCS can be used to determine fluctuations of fluorophores diffusing either freely in solution or when they are bound to larger objects. This is done by observing their diffusion through a very small, optically defined volume, referred to as the confocal volume, that is illuminated by a focused laser beam. The autocorrelation function of the recorded signals

describes the normalized variance of the fluorescence fluctuations and tells how self-similar the recorded signal is after a certain time delay. The shape of the autocorrelation curve G(t) provides the characteristic times for molecular residence in the focal volume (τ_d). In the case of a short time delay relative to the τ_d, the normalized integral of the overlapping region is close to 1, and the autocorrelation function has a maximal amplitude. However, with longer time delays, the overlapping region gradually decreases until the autocorrelation function has fallen to zero. Conversely, a few molecules in the observation volume result in a low average fluorescence with larger fluorescence fluctuations detected from a single molecule and a higher correlation amplitude. Adapted from *Ref*[104] with permission.

1.6.2 CHARACTERIZATION METHODS FOR 2D POLYMER NANOARCHITECTURES

CHARACTERIZATION METHODS FOR POLYMER FILMS AND MEMBRANES

The formation of polymer films on solid support, or as free-standing films, requires specialized characterization methods[78]. The central parameters of interest are the polymer film and membrane thickness, the homogeneity, and the morphology. Different methods are available to determine these parameters; for example, the thickness can be determined by spectroscopic ellipsometry or by atomic force microscopy, which also images the morphology and the homogeneity. Insights into the mass of immobilized polymer on a surface as well as interactions of the polymer film (e.g. with biomolecules) can be studied in detail by quartz crystal microbalance [105] and surface plasmon resonance [106]. The composition of polymer films can be probed by infrared spectroscopy, x-ray photoelectron spectroscopy, and mass spectrometry[107], while surface characteristics such as the wettability are accessible through contact angle measurements. Particular applications of polymer films require more specialized techniques like the determination of adhesion phenomena,[108] charges in the polymer film,[109] or the insertion of proteins into the film[71].

1.7 BIOMIMETIC ENGINEERING OF COLLOIDAL POLYMER NANOARCHITECTURES

Mimicking biological processes, by engineering biomimetic nanostructures, named biomimics, is an elegant strategy that is relevant to various scientific fields such as materials science, chemistry, electronics and medicine[1,110,111]. The biomimetic design is realized by applying a bottom-up approach – arranging of synthetic and biological molecules at the nanoscale via self-assembly. In this way it is possible to combine individual biological units, known for their sophisticated structure and activity (e.g. proteins, lipids, DNA), with robust synthetic materials (e.g. polymers, porous silica surfaces, nanoparticles) [2,8,112-115]. The combination results in new hybrid materials that present emergent properties and functionalities. Biomimics contribute to the basic understanding of engineered materials at the nanoscale and are already being used in a wide range of applications, such as sensitive diagnostic surfaces[116], efficient systems for precise local therapy,[117,118] patient orientated tailored medicine [8,102,119,120], and highly efficient detoxification of environmental pollutants[121]. In addition to their translational potential, biomimics contribute to our present understanding of synthetic biology and evolution, and provide a deep insight in the progression from non-living materials to living systems by imitating the molecular organisation found in prokaryotic and eukaryotic cells[103,121-125].

Nanoscale biomimics must cope with a complex scenario of requirements to preserve the structure and functionality of the biomolecules that are included in the hybrid assembly and finally serve the desired applications. For example, extreme temperatures, organic solvents and denaturizing reactants, normally used in catalysis or for the preparation of colloidal assemblies, need to be avoided because they lead to loss of biomolecule functionality[126]. Here the most common methods of biometical engineering of colloidal nanostructures (micelles, soft nanoparticles and polymersomes) will be presented. 2D supported and free standing polymer architectures can eaqually serve as platforms for biomimetic engineering, however that topic is beyond the scope of this thesis.

1.7.1 BIOMIMETIC ENGINEERING OF MICELLES AND SOFT NANOPARTICLES

Micelles and soft nanoparticles offer possibilities of modifying their synthetic nanoarchitecture in a biomimetic fashion by either encapsulation of biomolecules inside their hydrophobic core, entrapment of biomolecules between the polymeric chains of the corona or by anchoring of biomolecules on the surface of their corona.

ENTRAPMENT OF BIOMOLECULES

Entrapment has previously been used to carry therapeutic biomolecules[127] or catalytically active biomolecules [128]. The nature of micellar / soft particle self-assembly offers a straight forward approach to entrap molecules, readily protecting the encapsulated biomolecules from degradation. Once buried between the hydrophobic polymer chains biomacromolecules preserve their structure and functionality but cease to be active as the crowded molecular environment prevents them to access binding sites or substrates. Hence, the entrapped biomolecules remain protected, but inactive until the nanoarchitetures are disassembled[127].

ANCHORING OF BIOMOLECULES

In this respect to entrapment of biomolecules in micelles / soft nanoparticles, anchoring of biomolecules (proteins, sugars, DNA) on the micellar / soft nanoparticle corona by either covalent bonds or ionic interactions provides the possibility of using micelles and nanoparticles as carriers, that allow the attached biomacromolecules to interact with their environment, especially important when molecular recognition when used as a targeted delivery approach[31]. An example of biomimetic decoration of soft polymer based nanoparticles with therapeutic enzymes is presented in this thesis and will be discussed in Chapter 2.

1.7.2 BIOMIMETIC ENGINEERING OF POLYMERSOMES

Unlike micelles and soft-nanoparticles, that temporary inactivate entrapped biomolecules, by steric effects of polymer chains, polymersomes can preserve the functionality of biomolecules, while keeping the polymersome nanoarchitecture intact. The robust membrane of polymersomes serves as a border for a confined inner aqueous compartment where biomolecules move and function freely. This mimics the natural organization of lipid based compartments, but offers improved mechanical stability (Figure 18)[129].

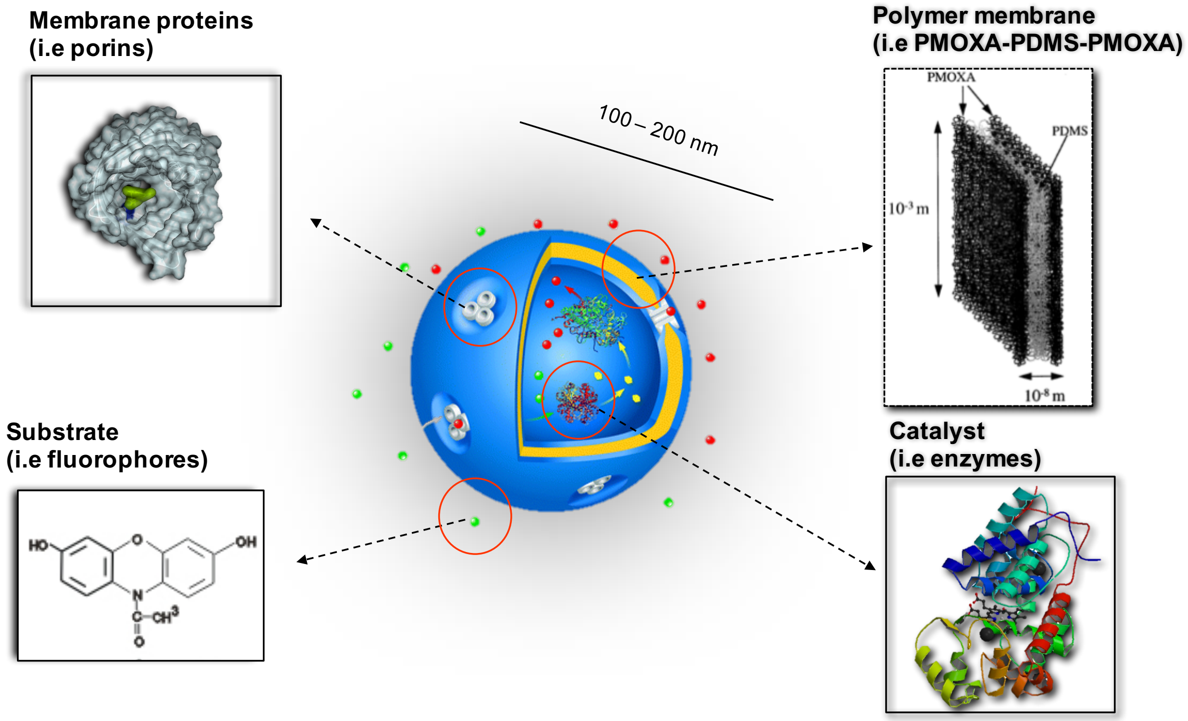

Figure 18. Schematic representation of biomimetic modifications done on polymersomes. Topological regions of interest: Aqueous cavity of polymersomes where hydrophilic molecules can be encapsulated, hydrophobic region of the polymersome membrane and membrane surface. Adapted from *Ref*[130] with permission.

ENCAPSULATION OF BIOMOLECULES

Entrapment of biomolecules in the hydrophilic compartment of polymersomes protects them from their environment and represents a key approach for the design of functional biomimetics that are closer to natural cellular or subcellular compartments[1].

Catalytically functional biomolecules, such as enzymes and their mimics are of particular interest as encapsulation introduces a specific functionality and converts the polymersome into a catalytic nanocompartment (nanoreactor). Examples of previously encapsulated biomolecules include enzymes (i.e β-lactamase, horseradish peroxidase, nucleoside hydrolase or acid phosphatase, superoxide dismutase), photosensitizers (Rose Bengal bovine serum albumin conjugate), oxygen carriers (haemoglobin) and others[99,131-134]. Systems that are more complex rely on the simultaneous encapsulation of a set of enzymes that work in tandem and mimic the crowded molecular environment of cellular compartment spaces[5].

MEMBRANE FUNCTIONALIZATION

A key requirement for the function of biomolecules encapsulated inside polymersomes is that the polymersome membrane is permeable for a molecular exchange of substrates/products between the polymersome inner cavity and the polymersome environment[49,135].

Various methods have been developed to induce permeability to polymersome membranes, such as using polymers, which spontaneously form porous membranes, inducing membrane permeability with organic solvents, or incorporation of stimuli responsive polymer chains into the membrane[136,137]. However, a drawback of these methods is that they do not allow a defined control of the membrane permeability, essential in preventing the escape of encapsulated biomolecules from the polymersomes cavity.

An elegant method to overcome the issue of membrane permeability is a bioinspired approach that renders the membrane permeable by the incorporation of biopores and membrane proteins [138,139]. In this way selective membrane permeability of polymer membranes towards protons and ions has been achieved by insertion of small pore forming peptides like gramicidin and ionophores like ionomycin[139,140]. Membrane permeabilization by the latter is straight forward as they are usually added directly to pre-formed polymersomes using trace amounts of organic solvents, such as EtOH. In contrast, a more complex scenario of membrane functionalization is presented by the functional reconstitution of larger membrane associated proteins, which have to remain functional despite the large hydrophobic mismatch between synthetic block-copolymer membranes (9-13 nm) and the size of the proteins (3.3-7.1 nm)[141]. Functional reconstitution is possible only if the type of polymer chains forming the polymersomes present a high flexibility and and adapt to the hydrophobic parts of membrane proteins by coiling[4]. In addition, harsh conditions such as extreme temperatures and organic solvents have to be avoided, since they readily lead to protein denaturation. Functional protein reconstitution is achieved by either addition of the desired membrane protein during the polymersome formation or by the post-hoc insertion of membrane proteins in destabilised polymersome membranes [4]. In both cases, the removal of the detergent (i.e. OG, Triton X, SDS), used in the membrane protein isolation from cellular membranes, plays a vital role as it is not only allows the membrane protein to be inserted in polymersome membrane but can also influence on polymersome stability[142]. Previously functional reconstitutions of bacterial membrane porines such as, Outer membrane protein F (OmpF), FhuA and LamB induced a size-dependent cut-off permeability of polymersome membranes: only molecules smaller than the respective pore diameter (i.e 600 Da in the case of OmpF) can diffuse across the membrane[139,138,143-145]. Similarly, insertion of selective membrane proteins, such as GlpF or Aquaporin Z allowed a step further in controlling membrane permeability by allowing the diffusion of specific molecules, such as water and ribitol, through the polymersome membrane[121,116]. Significant efforts have been made in obtaining stimulus-responsive polymersomes by the reconstitution of chemically and/or genetically modified membrane proteins that act as "gates", however up to date only few examples remain. In this way histidine residues, which induced a pH dependent permeability to OmpF, were introduced to the OmpF pore by point mutations of native amino acids[146], whilst chemical modifications of key amino acid residues of FhuA{Onaca:2008tt} and MscL[147] resulted in reduction or pH responsive behaviour of porins. Once reconstituted in polymersome membranes, these modified membrane proteins allowed a pH or redox potential triggered permeability of polymersome membranes.

In addition to inducing passive membrane permeability, biomimetic modification of the polymersome membrane opens possibilities of utilizing membrane proteins that do not act as passive pores but have membrane associated catalytic activity. As for example, NADH:ubiquinone reductase (complex I) a mitochondrial membrane associated protein was reconstituted in PMOXA-*b*-PDMS-*b*-PMOXA polymersomes, in order to mediate electron transfer from NADH to ubiquinone[142] (Figure 19.). Further such examples include alpha-helical model proteins bacteriorhodopsin (BR) / proteorhodopsin that acted as light mediated proton pumps and the F_0F_1-ATP synthase photon pump[148,149].

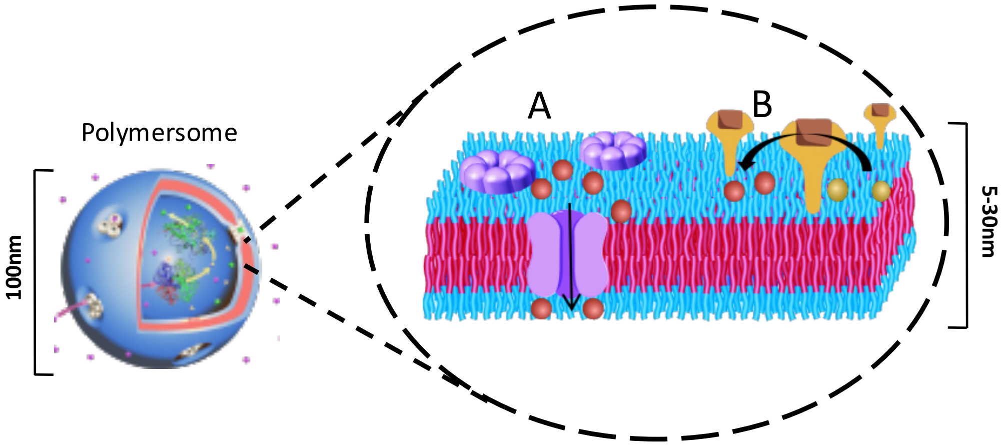

Figure 19. Biomimetic engineering of polymersome membranes. A. Functional reconstitution of channel proteins that allow enhanced membrane permeability. B. Functional reconstitution of catalytically active membrane proteins. Adapted from *Ref*[1] with permission.

Another approach lies in modifying the polymersomes by attaching molecules at their external interface. This imitates the plethora of proteins, glycoproteins that act as catalysts, receptors or ligands on the surface of natural cell membranes[6,8]. In this way polymersomes can be engineered to allow molecular recognition, which is of great importance in biomedical applications. Furthermore, molecular networks can be formed by connecting multiple polymersomes through DNA recognition[6]. Attachment is achieved by covalent attachment of biomolecules, such as heparin chains, antibodies and DNA to functional end groups of polymer chains [6,7] but could also be achieved by electrostatic attachment of biomolecules to charged polymer endgroups.

1.8 APPLICATION OF BIOMIMETICALLY ENGINEERED COLLOIDAL NANOARCHITECTURES

1.8.1 APPLICATION OF MICELLES AND SOFT NANOPARTICLES

One of the main applications of micelles and soft nanoparticles is as carriers for therapeutic molecules or contrast agents. Entrapment of active compounds within their nanoarchitecture ensures they are protected from degradation and loss of activity through enzymatic attack[150]. If the hydrophilic corona is appropriately selected, micelles injected in the circulation of mammals avoid protein absorption, and thus systemic elimination[151]. Due to their size, micelles accumulate in solid tumor tissues via an enhanced permeability and retention effect[152] (Figure 20). In addition functionalization of the micelle corona with specific ligands allows targeted delivery of active compounds to desired tissues or cell types[31]. Once micelles reach the intracellular environment, the molecular cargo is released either by diffusion from the carrier, or by change of micelle morphology in the presence of different stimuli such as temperature, acidic pH, or light[153]. For example, poly(ethylene oxide)-b-poly(eta-caprolactone) (PEO-PCL) was used for filomicelle formation, providing a biodegradable and compatible system for paclitaxel delivery[154]. Polymeric micelles can entrap contrast agents, for magnetic resonance imaging (MRI), and x-ray computed tomography (CT)[31]. The applications of micelles as carriers for therapeutic agents have recently been supported by phase I clinical trials delivering anti-cancer drugs. [155,156].

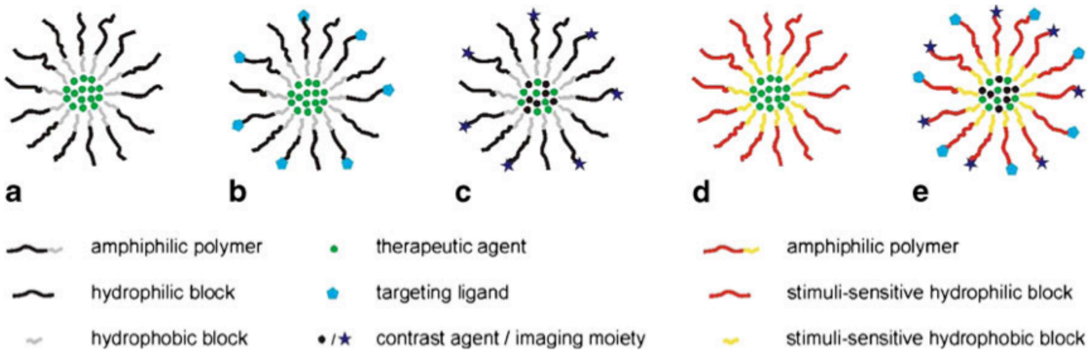

Figure 20. Polymer micelles as delivery agents. Schematic representation of a.) Polymeric micelles. b.) Micelle conjugated with a targeting moiety. c.) Micelle loaded with a contrast

agent or imaging moieties. d.) Micelle designed for triggered drug release. e) Stimuli responsive block-copolymer micelles for targeted delivery. Adapted from *Ref*[31] with permission.

1.8.2 APPLICATION OF POLYMERSOMES

Polymersomes have the advantage of allowing the encapsulation/entrapment of both hydrophilic and hydrophobic molecules in the same vesicle due to their intrinsic architecture. This allows for the construction of complex systems beyond traditional drug delivery vehicles [24,157], such as catalytic nanocompartments (nanoreactors), artificial organelles [24,150,157-161], active surfaces (e.g. biosensors)[150], and multicompartment systems that mimic cellular functions and provide deeper understanding of biology[162].

DELIVERY AGENTS

The robustness large size of their hydrophilic compartment, and their chemical versatility are main advantages of polymersomes compared to other delivery carriers and diagnostic agents[163]. By an appropriate selection of the copolymers to contain stimuli-responsive blocks, it is possible to release cargo “on demand” [164]. Common triggers used for stimuli-responsive release from polymersomes are pH, temperature, redox-potential, and concentration gradients of certain molecules (e.g. glucose) [54,55,165]. Another advantage of polymersomes for drug delivery is their long *in vivo* circulation time, 47.3h half-life compared to 10.6h for PEGylated liposomes in mice [55]. The long circulation time was achieved by using the hydrophilic domain PEG, known to reduce adsorption of proteins and subsequent opsonisation by cells[166]. Other factors that support the use of polymersomes for biomedical applications are the biocompatibility/biodegradability of the polymers, their size, shape and surface properties[24]. Especially surface modificiation of polymersomes with targeting ligands offers unprecedented possibilities of achieving disease targeted drug delivery. Two prominent examples include antibody-polymersome conjugates that were applied to target and overcome the blood-brain barrier, which is an essential obstacle for successful delivery of drugs into the human brain and nanomimics – polymersomes presenting receptors required for parasite attachment to host cells, that served to interrupt the parasite life cycle of *P.falciparum*[7,8].

CATALYTIC NANOCOMPARTMENTS

Catalytic nanocompartments, commonly referred to as nanoreactors, are engineered by encapsulation of active compounds (proteins, enzymes, mimics, or combinations thereof) that perform chemical/biochemical reactions inside the cavity of polymersomes. The membrane permeability allows an exchange of substrates/products with the environment and can be specifically tuned by the chemical nature of copolymers by chemical modifications[167,168] or by incorporation of natural channel proteins, as discussed above[158,159]. Catalytic nanocompartments evolved from one-step reactions inside the polymersome cavity[134,169], to two-step ATP synthesis[149] or more complex reactions such as three-enzyme cascade reactions [170,171]. Another example of such a complex system includes the transcription of DNA to mRNA and the subsequent translation to yield fluorescent proteins[172]. Immobilized catalytic nanocompartments were also used as precise biosensors or to synthesize antibiotics on demand and on site. For example bacterial growth was inhibited by antibiotics (cephalexin), locally produced by catalytic nanocompartments containing penicillin acylase, and having a permeable membrane due to the insertion of bacterial outer membrane protein F (OmpF) to allow substrate and product permeation. To mimic the crowded environment found in cell organelles, catalytic nanocompartments were generated that had channel proteins reconstituted in their membranes and encapsulated enzymes along with a crowding agents (Ficoll or polyethylene glycol) inside their cavity[103] .

ARTIFICIAL ORGANELLES

The concept of artificial organelles was introduced by reports of catalytic nanocompartments performing their enzymatic reactions *in situ* inside cells (Figure 21)[5,25,158]. Different examples of systems that have the potential to act as artificial organelles have been recently developed based on liposomes, porous silica nanoparticles, and polymer compartments in combination with biomacromolecules [5,173,174]. One example of polymersome based artificial organelles is the detoxification of reactive oxygen species (ROS) by artificial peroxisomes. Two enzymes (superoxide dismutase and catalase) acting in tandem inside the cavity of polymersomes equipped with channel proteins for membrane permeabilization, detoxified superoxide radicals and hydrogen peroxide in cells that were exposed to reactive oxygen species. These artificial organelles protected cells from oxidative stress to the same extent as natural peroxisomes[5].

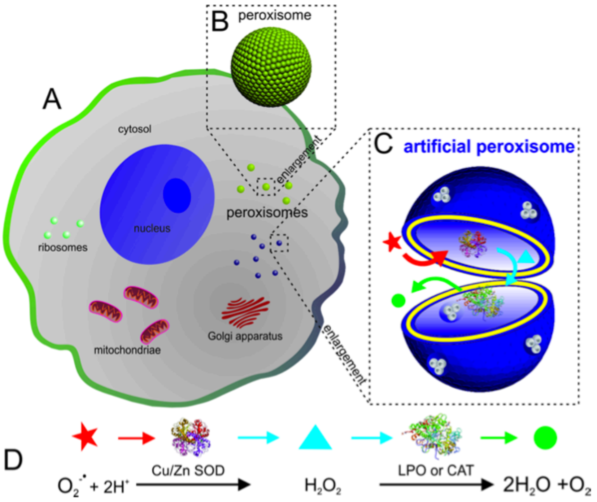

Figure 21. Design of artificial cell organelles. Panel A.) Schematic representation of a cell including various organelles. Panel B.) Naturally occurring peroxisomes, which are nanometer-sized organelles involved in ROS regulation. Panel C.) Artificial peroxisome containing antioxidant enzymes and membrane-bound channel proteins for detoxification of ROS. Panel D.) Cascade reaction of superoxide radicals and hydrogen peroxide that takes place inside artificial peroxisomes. Adapted from *Ref*[5], with permission.

MULTICOMPARTMENT SYSTEMS AND CELL MIMICS

Another direction of polymersome research is to establish multicompartment systems that act as simple cell models. First attempts have been made by engineering polymersome cavities that mimicked the crowded molecular space of the cytosol[122,162,172]. Controlled production and loading of giant polymersomes was realized by microfluidic techniques[172], filling the polymersomes with a whole transcription- and translation machinery in order to synthesize fluorescent proteins from DNA plasmids (Figure 8)[172]. Other attempts produced multicompartment polymersome systems that mimicked cytosol properties within giant polymersomes [162,175,176]. In this manner small polymersomes (100-200nm) were encapsulated in big polymersomes (2-10μm) together with a crowding agent (alginate)[175]. Alginate completely arrested movement of the small polymersomes, whereas the addition of dextran only slowed down the polymersome diffusion. Cascade reactions were also implemented in a multicompartment polymersome systems[171]. Two kinds of catalytic nanocompartments (containing two different kinds of enzymes) were encapsulated in micrometer-sized polymersomes together with a third enzyme ("cytosolic" enzyme), enabling cascade reactions in this compartmentalized structure with participation of all three enzymes.

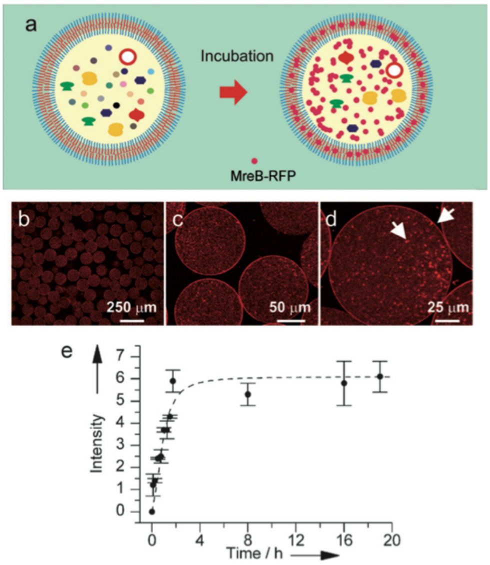

Figure 22. Polymersomes as Multicompartment models and nanofactories. Cell-free expression of fusion protein membrane-related bacterial protein-red fluorescent protein (MreB-RFP) in polymersomes by DNA transcription and translation. Panel a.) Schematic representation of the expression system. Panels b-d.) Confocal microscope images showing production of MreB-RFP (red spots) in PEG-*b*-PLA polymersomes. Panel e.) Fluorescence intensity increase over time due to protein expression adapted from *Ref*[122], with permission.

Chapter 2.

PEG-*b*-PMCL-*b*-PDMAEMA NANOPARTICLES FOR CONTROLLED LOCALIZATION AND pH SENSITIVE RELEASE OF BIOMACROMOLECULES [⊥]

In this chapter, PEG-b-PMCL-b-PDMAEMA copolymer nanoparticles are biomimetically engineered such as to act as carriers for therapeutic proteins. To do this, the positively charged nature of the PDMAEMA block, forming the corona of the nanoparticles, which allows controlled localization and release of negatively charged biomolecules is made use of. The chapter provides an insight into the synthesis and self assembly of PEG-b-PMCL-b-PDMAEMA copolymers, the behavior of self-assembled PEG-b-PMCL-b-PDMAEMA nanoparticles in response to pH and particle interactions with small molecular weight and large biomacromolecules. Finally, the potential application of PEG-b-PMCL-b-PDMAEMA copolymer nanoparticles biomimetically engineered with a therapeutic protein, acid sphingomyelinase, is demonstrated in human epithelial HeLa cells.

[⊥] This study has been published: D.Vasquez[*], T. Einfalt[*], W. Meier, C. G Palivan PEG-b-PMCL-b-PDMAEMA copolymer nanoparticles for controlled localization and pH sensitive release of biomacromolecules, *Langmuir*, **32**, 10235-10243 (2016)

[*] Both authors contributed equally.

2.1 MOTIVATION AND PROBLEM DEFINITION

Protein therapy, an essential part of treating several diseases, aims to increase the levels of deficient proteins, displace dysfunctional proteins or inhibit biological processes by delivering functional proteins into cells[177]. In this respect, therapy via direct administration of proteins is limited and ineffective because of low bioavailability, rapid degradation through enzymatic attack or immonogenity[178]. The need to develop novel solutions for protein administration has led to the design of colloidal carriers with sizes in nanometer range that serve as efficient transporters and enhance the protein bioavailability in specific spatial and time conditions. In particular these carriers include a variety of polymer nanoarchitectures (particles, capsules, micelles, or vesicles) in which specific proteins are entrapped, encapsulated or attached[24]. The nature of protein entrapment depends on the chemical nature of the copolymer, its molecular weight, the presence of functional end groups, and protein-polymer interactions[179]. Hence careful selection of components that build the supramolecular assembly is vital for protein localization,[180] and controlled protein release[180,181]. In this respect, copolymer assemblies based on PCL-PEG-PCL[182,183], PEO-PCL-PAA[184] and PEG-PCL-PAA[185] have been used to study their interactions with model proteins, such as bovine serum albumin (BSA) and therapeutic proteins, such as insulin (REF). Of particular interest are nanoarchitectures that present responsiveness to various stimuli, such as pH, temperature or the presence of chemical or biological compounds[186]. Responsive behavior is important as it allows the release of proteins in the presence of a stimulus, either by degradation of the assembly or by detachment of the biomolecules induced by a change in protein-polymer interactions[186]. For example, pH responsive assemblies have high potential for medical applications because pH is an essential signaling factor that accompanies pathological conditions (e.g. inflammation, cancerous tissue) [187]. Various pH responsive polymer assemblies such as polyionic complex micelles[188], nanocapsules[189], or aldehyde displaying silica nanoparticles[190] have been used to deliver therapeutic drugs. In particular, PEG-*b*-PCL-*b*-PDMAEMA assemblies have been reported as delivery carriers for RNA[191], DNA[192] and siRNA[184], but not yet for proteins.

The motivation behind chapter two of this thesis is to demonstrate that biomimetically engineered PEG-*b*-PMCL-*b*-PDMAEMA asymmetric copolymer nanoparticles can allow controlled localization and subsequent pH dependent release of therapeutic proteins. The protein binding efficiency of PEG-*b*-PMCL-*b*-PDMAEMA is evaluated both with a model protein, BSA fluorescein isothiocyanate conjugate (BSA-FITC) and the therapeutic protein acid sphingomyelinase (ASM), known for its role in catalyzing the breakdown of sphingomyelin to ceramide in the treatment of Niemann-Pick disease[193]. Asymmetric tri-block copolymers PEG-*b*-PMCL-*b*-PDMAEMA were selected to self-assemble into biocompatible and biodegradable nanoparticles that can support a specific localization of biomacromolecules on their surface[194]. The presence of the positively charged PDMAEMA block induces pH responsiveness, whilst poly(methylcaprolactone) (PMCL) favors the formation of more stable colloidal assemblies, because it is fluid at room temperature, and more hydrophobic than poly caprolactone [195] .Formation and stability of PEG-*b*-PMCL-*b*-PDMAEMA nanoparticles in PBS, as relevant environment for attachment of proteins, have been characterized by a combination of light scattering, transmission electron microscopy (TEM and cryo-TEM), and fluorescence correlation spectroscopy (FCS). The effect of the ratio between the hydrophobic block and the pH-sensitive block on the entrapment/release of ASM allowed improvements in the system efficiency for protein delivery. Enzyme activity assays were performed to establish whether protein entrapment affected its activity once released from the nanoparticles, whilst up-take and toxicity in HeLa cells were evaluated by a combination of [3-(4,5-dimethylthiazol-2-yl)-5-(3-carboxymethoxyphenyl)-2-(4-sulfophenyl)-2H-tetrazolium (MTS) assay and fluorescence activated cell sorting (FACS). Stimuli-responsive nanoparticles with controlled localization of proteins represent a smart solution for protein therapy, serving to improve the release as a key parameter for efficient therapeutic solutions.

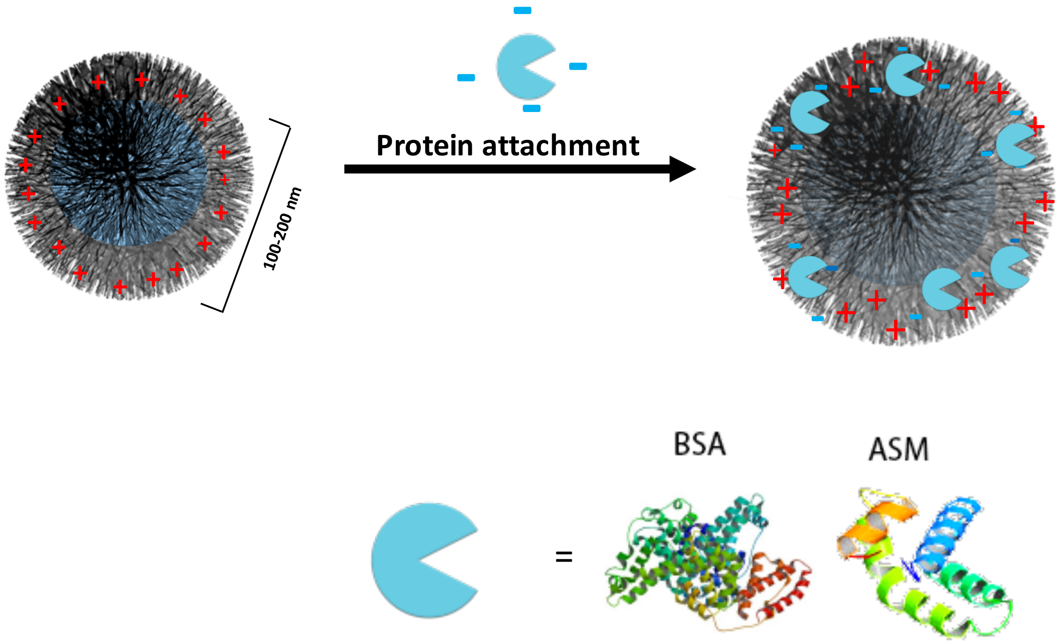

Scheme 2. Schematic illustration of the self-assembly of PEG-*b*-PMCL-*b*-PDMAEMA copolymers before and after interaction with a charged protein at pH 7.2. The BSA or ASM are attached to the positively charged particles through electrostatic interactions. Adapted from *Ref*[9] with permission.

2.2 PEG-*b*-PMCL-*b*-PDMAEMA COPOLYMER SYNTHESIS

PEG-*b*-PMCL-*b*-PDMAEMA tri-block copolymers were obtained by a three step synthesis: (*i*) ring-opening polymerization of γ-methyl-ε-caprolactone (MCL), (*ii*) functionalization of PEG-PMCL with an ATRP-initiating group, and (*iii*) ATRP of DMAEMA with mPEG-b-PMCL-Br as macronitiator[194]. Tri-block copolymers were assigned as $A_{45}B_mC_n$ where *m* and *n* represent the chain length of PMCL and PDMAEMA groups respectively determined from the ^{1}H NMR spectra (Figure S1, SI).

2.3 SELF-ASSEMBLY OF PEG-*b*-PMCL-*b*-PDMAEMA SUPRAMOLECULAR NANOSTRUCTURES

Self-assembly of PEG-*b*-PMCL-*b*-PDMAEMA (PEG$_{45}$-*b*-PMCL$_{110}$-*b*-PDMAEMA$_{37}$ and PEG$_{45}$-*b*-PMCL$_{101}$-*b*-PDMAEMA$_{27}$) copolymers was performed at various pH values in the range 3.5 - 10 in order to analyze both the 3D assemblies generated in dilute solutions, and their pH responsiveness. Nanoarchitectures formed by copolymers were characterized by a combination of light scattering (dynamic and static), and TEM. TEM micrographs of self-assembled nanostructures of copolymers show the coexistence of two populations of spherical objects with different sizes (Figure 21 A, B).

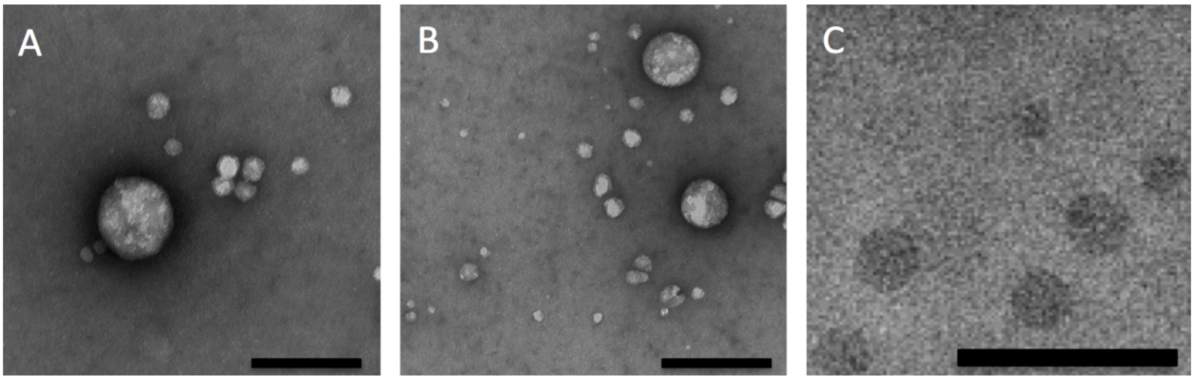

Figure 23. **TEM micrographs nanoarchitectures generated by PEG-*b*-PMCL-*b*-PDMAEMA copolymers at physiological pH.** A. $A_{45}B_{110}C_{37}$ copolymer, B. $A_{45}B_{101}C_{27}$ copolymer. Scale bars: 200nm. C. Cryo-TEM micrograph of 3D supramolecular assemblies of $A_{45}B_{110}C_{37}$ copolymer after 2 months. Scale bar: 200 nm. Adapted from *Ref*[9] with permission.

In this particular case, the size distribution of the spherical objects was measured by DLS to analyze the predominance of populations. According to the CONTIN algorithm, there are two populations of spherical objects: a population of particles with R_H~ 100 nm, and a second one with smaller particles of R_H~ 50 nm (Figure S2, SI). However, the existence of two separated populations allows us to analyze the data by taking into account only the population of particles with larger size. The ratio (ρ) between the radius of gyration (R_g), obtained from SLS, and the hydrodynamic radius (R_H), from DLS experiments ($\rho = R_g/R_H$) was calculated, because it is known to be a specific parameter for identification of the morphology of spherical nano-objects

(Table 1). ρ values of the copolymer assemblies were 1.19 - 1.23, which characterize an architecture of soft spherical nanoparticles with a hydrophilic corona, in agreement with previous reports[196]. A value for R_H larger than that obtained from TEM was expected, because the R_H from DLS experiments is the sum of the particle size and its surrounding hydration sphere.

Table 1. Physico-chemical parameters of PEG-*b*-PMCL-*b*-PDMAEMA copolymers in physiological conditions (PBS, pH 7.2 at 25 °C).

Copolymer	**Mw (g/mol)^a**	**ζ potential (mV)***	**R_H (nm)**	**R_g (nm)**	**R_g/R_H**	**PDI**
$A_{45}B_{110}C_{37}$	22100	20.2 ± 0.3	88 ± 10	112 ± 8	1.27	1.50
$A_{45}B_{101}C_{27}$	18167	12.9 ± 0.2	50 ± 12	66 ± 6	1.32	1.30

R_H: hydrodynamic radius; R_g: radius of gyration; *a. M_W, weight-average molar mass

At pH = 7.2, the radius of nanoparticles increased from 50 nm up to 88 nm as the length of the B and C blocks was increased (from 101 to 110 units for the B block and from 27 to 37 units for the C block). Under physiological pH, nanoparticles were stable for more than two months, as indicated by cryo-TEM and TEM micrographs (Fig. 1 C, S3, SI). In addition, cryo-TEM micrographs indicate a soft-core particle morphology for these assemblies, in the self-assembly conditions used here, specifically selected for attachment of proteins relevant for bio-applications.

Particle architecture and size are influenced by various factors such as: chemical nature of the blocks, chain length of each block and the ratio between them, the domain of the polymer exposed to the environment, pH and temperature. Therefore, the changes in the architecture and size of nanopoarticles were analysed at different pH values. By varying the pH, the particle size for each copolymer changed, indicating a pH sensitive behavior (Figure 24, Figure S3). The hydrodynamic radius, R_H, was affected both by the pH (3.5 – 12.0), and the molecular properties of the copolymers: D_H increased from 50±8 to 150±22 nm for $A_{45}B_{101}C_{27}$, and from 72±11 to 174±26 nm for $A_{45}B_{110}C_{37}$ nanoparticles. While the size of $A_{45}B_{101}C_{27}$ nanoparticles did not change for pH values 6.0 - 7.4, $A_{45}B_{110}C_{37}$ nanoparticles increased their size in this pH range. The increase of the hydrodynamic radius upon increase of the pH is associated with the decrease of the electrostatic repulsions, which initiates an aggregation process of the small nanoparticles[197,198]. The aggregation process can lead to a probable sedimentation of large aggregates as indicated by the SLS experiments (Figure S4). The equilibrium between the two fractions of nanoparticles is shifted towards the smaller nanoparticles (Figure S2, SI). With increasing pH, the particles lose their charge and the equilibrium shifts to larger nanoparticles, due to the start of a particle-particle aggregation process.

The pH sensitive behavior of PEG-*b*-PMCL-*b*-PDMAEMA soft nanoparticles indicates that the polymer domain exposed at the interface with the environment is predominantly PDMAEMA with possible PEG chains as well. Whereas there is no power to separate PEG and PDMAEMA, by taking into account the molecular characteristics of PEG and PDMAEMA monomers, PEG is not likely to be located at the external surface of the corona because of the bulky conformation of PDMAEMA for both copolymers. The resulting nanoparticle morphology is therefore based on PEG mainly embedded in the hydrophilic domain, and the branched PDMAEMA exposed at the particle surface. This privileged orientation of the PDMAEMA domain is exactly the one necessary to support attachment of biomolecules based on electrostatic interactions. In addition, note that only a small number of PEG chains can be located at the exterior domain with the environment to not obstruct protein attachment because of the repellent property of PEG[199,200] .

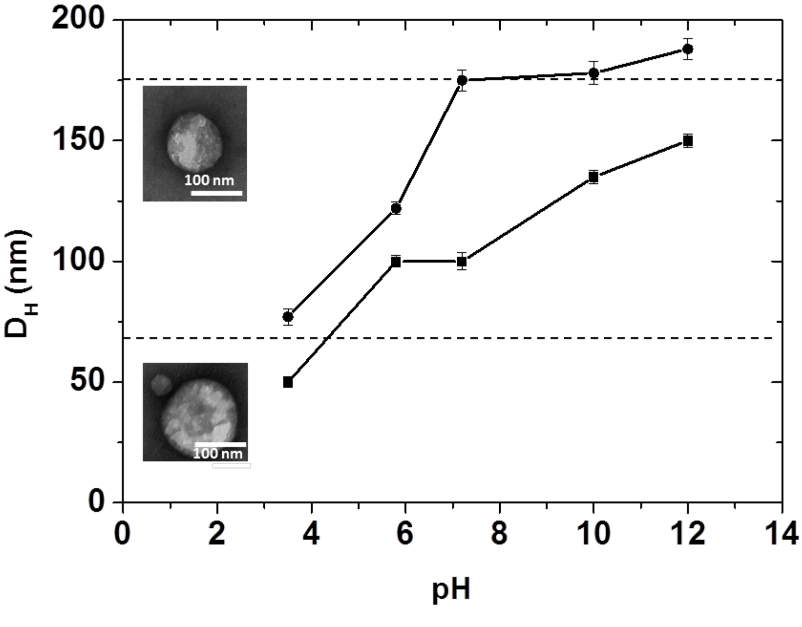

Figure 24. **Hydrodynamic diameter (D_H) of PEG-*b*-PMCL-*b*-PDMAEMA NP.** $A_{45}B_{110}C_{37}$ nanoparticles (circles), and $A_{45}B_{101}C_{27}$ nanoparticles (squares) at different pH values. Dashed lines represent a transition domain where both small and large nanoparticles co-exist. Adapted from *Ref*[9] with permission.

The effect of temperature on the hydrodynamic diameter of nanoparticles was assessed between 25°C and 40°C, a range relevant for medical applications. There was only a small change in nanoparticle diameter between 25°C and 40ºC, which would not affect the possible medical application of the nanoparticles (Figure S5, SI).

2.4 INTERACTION OF PEG-*b*-PMCL-*b*-PDMAEMA NANOPARTICLES WITH SMALL MOLECULAR WEIGHT MOLECULES

Sodium fluorescein (Mw = 376.27 Da) was used as a model molecule to establish whether small molecular mass molecules can be attached to the surface of nanoparticles. In this respect fluorescence correlation spectroscopy (FCS) was used to examine the interaction of sodium fluorescein with the soft nanoparticles, by measuring the diffusion time of free sodium fluorescein, and sodium fluorescein-nanoparticles, respectively. By using FCS, as discussed in depth in the introduction, the laser-induced fluorescence of the excited fluorescent molecules that pass through a very small probe volume is auto-correlated in time to give information about the diffusion times of the molecules. These provide information about interactions of the fluorescent molecules with larger target molecules, including encapsulation/attachment of proteins in/to nanoparticles due to their proportionality to the R_H of the fluorescent object (according to the Stokes-Einstein equation). The change of the diffusion time for the free dye of $\tau_D = 38\ \mu s$ to 5.5 ms (for $A_{45}B_{101}C_{27}$ nanoparticles), and 5.9 ms (for $A_{45}B_{110}C_{37}$ nanoparticles) indicates that the dye interacts with both types of nanoparticle. Electrostatic interactions represent the driving force for the attachment of sodium fluorescein, and attachment efficiencies (A.E) of 40% and 67%, respectively were obtained when the hydrophobic/hydrophilic ratio between the C and B blocks was increased (SI, Table S1). As expected, nanoparticles with a longer positively charged C block are able to attach more molecules (67%) than those with a shorter positively charged C block (40%).

2.5 INTERACTION OF PEG-*b*-PMCL-*b*-PDMAEMA NANOPARTICLES WITH BIOMACROMOLECULES

A further step was to select model proteins and analyze whether they bind to PEG-b-PMCL-b-PDMAEMA soft nanoparticles. Water soluble BSA was selected due to its negatively charged protein backbone for pH > PI (isoelectric point PI = 4.7 at 25°), which favours its binding to the positively charged nanoparticles. The isoelectric point of the copolymers was determined by titration (Figure S6, SI), and attachment of BSA labelled with fluorescein isothiocyanate (FITC) to the nanoparticles was studied by FCS. The diffusion time (τ_d) for the free BSA-FITC at room temperature was τ_D = 82 μs (Figure S7 A-a and B-a, SI), and the autocorrelation curve for BSA-FITC-nanoparticles (Figure S7 A-b and B-b, SI) indicates the presence of slowly diffusing particles for both copolymers. This population with a reduced diffusion time, τ_D = 5.71 ms (for $A_{45}B_{110}C_{37}$), and τ_D = 5.53 ms (for $A_{45}B_{101}C_{27}$) represents more than 73 % of the total number of fluorescent particles that passed through the confocal volume during the measurement time, and corresponds to BSA-FITC-nanoparticles. The remaining diffusing fluorescent particles correspond to free BSA-FITC molecules, which were not attached to nanoparticles, and were detected due to their high quantum yield, and the high sensitivity of FCS. Upon interaction with BSA-FITC, the hydrodynamic radius of protein-nanoparticles changed compared to the values obtained from light scattering data (Table 2). However, it is known that there are differences between the hydrodynamic radius determined by FCS and DLS[201], and therefore this difference is not considered as relevant. Light scattering of labelled protein-loaded nanoparticles was excluded because of the interference of the fluorophore with the laser used in light scattering experiments.

The attachment efficiency was calculated as the number of fluorescent labeled proteins per nanoparticle in comparison with the theoretical maximum number of fluorescent labeled proteins per nanoparticle (SI). The maximum number is calculated by dividing the volume of the vesicle with the volume of the fluorescent protein. Due to the preparation method of the particles (co-solvent method), the radius used for calculations for A.E. were the R_H. The attachment efficiency of the nanoparticles indicates that the proteins are present in the outer corona of the nanoparticles because of the PDMAEMA domain predominantly exposed at their external surface. Nanoparticles morphology, which combines the molecular specificity of PEG and PDMAEMA with the results of the proteins attachment, is indeed based on PEG mainly forming the outer part of the nanoparticle core of PMCL, which is embedded into the domain of the branched PDMAEMA as the particle surface. The presence of the PDMAEMA domain at the interface of the nanoparticles with the environment favored both a controlled localization of charged biomolecules, and their pH-sensitive release.

Note that the protein-ABC fraction represents the overall bound protein-nanoparticle population in a two-populations FCS fit (free protein fraction and bound-protein fraction), without distinguishing between different numbers of nanoparticles or different number of proteins/nanoparticle in various samples. A.E. values are the key parameters used to analyze the differences between the protein binding to different copolymers nanoparticles.

Table 2. Attachment efficiency of BSA-FITC to PEG-b-PMCL-b-PDMAEMA nanoparticles.

Copolymer	**IEP**	**τ_D free protein (μs)**	**τ_D protein-ABC (μs)**	**D_H^* (nm)**	**D_H^{**} (nm)**	**free protein fraction (%)**	**protein-ABC fraction (%)**	**A. E (%)**
$A_{45}B_{110}C_{37}$	9.16	82	5533	140	126	27	73	22
$A_{45}B_{101}C_{27}$	7.5	82	3189	113	119	4	96	13

IEP: Isoelectric point; D_H: hydrodynamic radius (*) by FCS (**) by DLS; A.E: attachment efficiency; τ_D: diffusion time

The A.E. of BSA-FITC increased from 13 to 22 % when the size of the hydrophilic block PDMAEMA increased (Table 2). This effect is attributed to electrostatic interactions between the positively charged hydrophilic block and the negatively charged protein at pH 7.2, in agreement with reports indicating that positively charged nanoparticles entrap proteins with isoelectric points lower than pH 5.5[202]. The release of BSA-FITC protein as a function of time was evaluated by FCS (Figure S8, SI). At pH = 5.8, PEG-b-PMCL-b-PDMAEMA nanoparticles released up to 70 % of BSA-FITC independent of the hydrophobic/hydrophilic ratio of the copolymers.

A step further towards the development of a product for therapeutic applications was to produce sphingomyelinase-bound nanoparticles, and the fraction of sphingomyelinase labeled with OregonGreen 488 succinimidyl ester (o-ASM) bound to polymer nanoparticles was evaluated in a similar manner to that described in the preceding paragraph. The autocorrelation curve for the free labeled enzyme resulted in a diffusion time of τ_D = 126 μs, whereas a significant increase was observed when the enzyme was added to nanoparticles: τ_D = 4.15 ms for $A_{45}B_{110}C_{37}$, and τ_D = 3.33 ms for $A_{45}B_{101}C_{27}$ nanoparticles, respectively (Figure 25 A and B). Similar to the BSA attachment, this significant increase in diffusion time is attributed to interaction of the enzyme with the nanoparticles. The hydrodynamic diameter of protein-nanoparticles increased compared to that of BSA-nanoparticles as a result of both the differences in molecular masses of the biomolecules, and higher attachment efficiency for ASM (Table 2 and 3). The stronger interaction of the enzyme molecules with both types of nanoparticle is indicated by the fraction of enzyme-nanoparticles of > 89%.

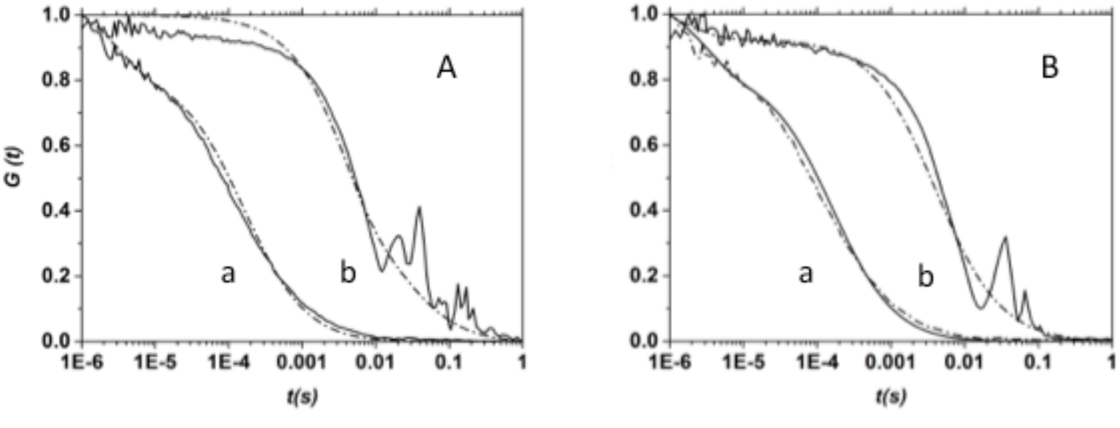

Figure 25. **FCS analysis of PEG-b-PMCL-b-PDMAEMA NP interaction with ASM.** FCS autocorrelation curves (continuous lines) and their fits (dotted lines) Panel A.) free o-ASM (a) and o-ASM-nanoparticles of $A_{45}B_{110}C_{37}$ (b). Panel B.) free o-ASM (a), and o-ASM-nanoparticles of$A_{45}B_{101}C_{27}$ (b). Curves are normalized to 1 to facilitate comparison. Adapted from *Ref*[9] with permission.

Table 3. Attachment efficiency of o-ASM to PEG-b-PMCL-b-PDMAEMA (ABC) nanoparticles

Copolymer	**τ_D free enzyme (µs)**	**τ_D enzyme-ABC (µs)**	**D_H (nm)**	**free protein fraction (%)**	**protein-ABC fraction (%)**	**N° molec/part**	**A.E (%)**
$A_{45}B_{110}C_{37}$	126	4146	199	9	91	17	38
$A_{45}B_{101}C_{27}$	126	3326	143	11	89	11	13

The A.E. of molecules to polymer nanoparticles can be affected by several factors, such as method of preparation, size of the nanoparticles, hydrophilic/hydrophobic ratio, or concentration of molecules to be attached[203]. In the case of PEG-b-PMCL-b-PDMAEMA nanoparticles, the particle size and the hydrophilic/hydrophobic ratio play an important role in the A.E., and results in an increase of > 50% when the sizes of the B and C blocks are increased. TEM micrographs (Figure S9, SI) show that attachment of proteins to PEG-b-PMCL-b-PDMAEMA nanoparticles does not affect the architecture of nanoparticles compared to those without attached proteins (Figure 1).

Localization of proteins upon interaction with polymer nanoparticles is a key factor affecting the release profile. In the case of BSA-FITC attached to the outer interface of nanoparticles of PEO-PCL-PDMAEMA copolymers, protein localization at the external interface has been reported to improve the release behavior[185]. In order to get more insight into the localization of ASM upon interaction with the copolymer nanoparticles, a combination of zeta potential characterization and FCS was used. Zeta potential was measured for PEG-b-PMCL-b-PDMAEMA nanoparticles with and without enzyme (Figure S10, SI). Nanoparticles without ASM were positively charged (+15 mV), but upon ASM addition, the charge of biomolecule-nanoparticles decreased dramatically (to -2 mV). This significant charge difference indicates that ASM molecules interact with the outer shell of the nanoparticles, in agreement with the morphology of the nanoparticles with the PDMAEMA domain exposed towards the environment. Localization of ASM molecules at the external hydrophobic domain of the soft nanoparticles was assessed by comparing the fraction of o-ASM-nanoparticles with the fraction of o-ASM molecules interacting with nanoparticles already attached to non-labeled ASM.

First, copolymer nanoparticles ($A_{45}B_{101}C_{27}$ or $A_{45}B_{101}C_{37}$) without protein are prepared, then mixed with a solution of o-ASM during 50 minutes and measured by FCS (Figure S11, SI). The change in the autocorrelation function of the mixture of o-ASM with nanoparticle compared with that of the free o-ASM indicated that the proteins interacted with the outer corona of nanoparticles for both copolymers (Figure S11, SI), and an A.E of around 13 % was calculated for $A_{45}B_{101}C_{27}$. Second, nanoparticles were prepared in the presence of unlabeled ASM and measured by FCS both before and after addition of a solution of o-ASM for 50 minutes (Figure S11, SI). A significant decrease of the A.E to < 3% indicates that unlabeled-ASM molecules are already attached to the nanoparticles and hinder supplementary interaction of o-ASM with the nanoparticles. Therefore, ASM is mainly localized in the outer hydrophilic domain of nanoparticles, a location which favors protein release under appropriate environment conditions.

2.6 STIMULI RESPONSIVE BEHAVIOUR OF PEG-*b*-PMCL-*b*-PDMAEMA NANOPARTICLES

A key parameter for potential medical applications is the activity of ASM upon interaction with the nanoparticles. Since ASM is stable in acidic conditions[193] ,its activity was measured at pH 7.2 both for ASM-$A_{45}B_{110}C_{37}$ nanoparticles kept at this pH value, and for those previously exposed to acidic conditions for 60 min (pH = 5.5) (Figure 26). The activity of ASM-$A_{45}B_{110}C_{37}$ kept at pH 7.2 was lower than that of ASM-particles previously exposed to acidic conditions due to the lower accessibility of ASM molecules at pH 7.2, being protected in the hydrophilic corona of the nanoparticles. The location of the proteins at the external hydrophilic domain of the nanoparticles is clearly supported by the residual enzymatic activity of the protein-loaded nanoparticles at pH 7.2. If the proteins would have been located in the inner domain of the nanoparticles, their accessibility would have been completely inhibited and they should have no activity. The residual activity proves that the ASM proteins are located in the external hydrophilic domain and are still able to convert the substrate into product. In the case of ASM-nanoparticles exposed to acidic pH, the more positively charged environment favors ASM release, which results in a significantly increase of the ASM activity.

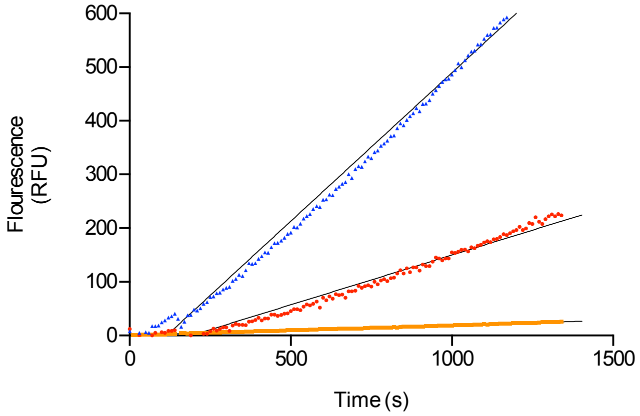

Figure 26: **Enzymatic activity of ASM modified NP**. ASM-$A_{45}B_{110}C_{37}$ nanoparticles kept at pH 7.2 (Red), and ASM-$A_{45}B_{110}C_{37}$ nanoparticles exposed at pH 5.5 for 60 min (Blue); $A_{45}B_{110}C_{37}$ nanoparticles (Yellow). Adapted from *Ref*[9] with permission.

Release of o-ASM was monitored by FCS for $A_{45}B_{110}C_{37}$ (Figure 27A) and $A_{45}B_{101}C_{27}$ (Figure 27B) as a function of time and pH. At pH 5.5, the release profile of ASM- $A_{45}B_{110}C_{37}$ nanoparticles shows a fast ASM release within 240 min (70 %), followed by a plateau (around 85 % release). The fast release profile is due to favored diffusion of ASM from the corona of the nanoparticles, because of the combined effect of the decreased charge of the protein molecules (pH < I.P) and the increased positive change of the environment. The fast release can be correlated with the increased activity of ASM-nanoparticles in acidic pH conditions (see above). At pH 7.2, as the proteins are negatively charged, electrostatic interactions favor their attachment to the nanoparticles, which results in a significantly slower release (30 % release in 240 min). A similar release of ASM molecules was observed at pH = 7.2 for nanoparticles based on copolymers with a shorter C block. However, a slower release profile was observed at pH = 5.5 in the case of $A_{45}B_{101}C_{27}$ nanoparticles compared to that resulting from $A_{45}B_{110}C_{37}$ nanoparticles: the decreased fraction of the released protein molecules from nanoparticles based on a shorter C block is due to a different balance in the electrostatic interactions, because of the different amount of attached proteins (Table 3).

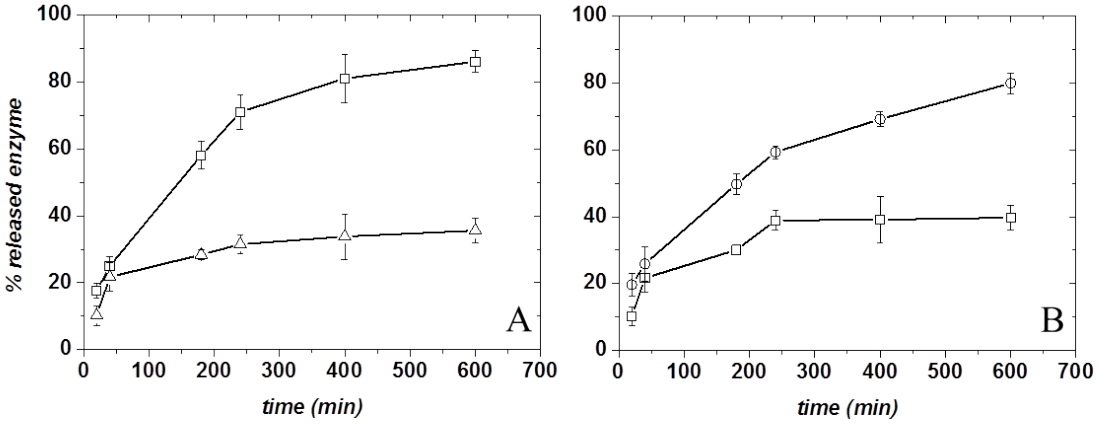

Figure 27. Release behavior of o-ASM from ABC nanoparticles as a function of time. Panel A.) $A_{45}B_{110}C_{37}$ nanoparticles at pH 7.2 (triangles), and at pH 5.5 (squares). Panel B.) $A_{45}B_{101}C_{27}$ nanoparticles at pH 7.2 (squares) and at pH 5.5 (circles). Adapted from *Ref*[9] with permission.

2.7 APPLICATION OF BIOMIMETICALLY ENGINEERED NANOPARTICLES AS DELIVERY AGENTS

The toxicity of nanoparticles was assessed in human epithelial HeLa cell line using the MTS assay by incubating for 24 hours with nanoparticles, BSA- or ASM-nanoparticles (concentrations up to 50 µg/ml). The nanoparticles and both protein-loaded nanoparticles all showed >70% cell viability (Figure 28).

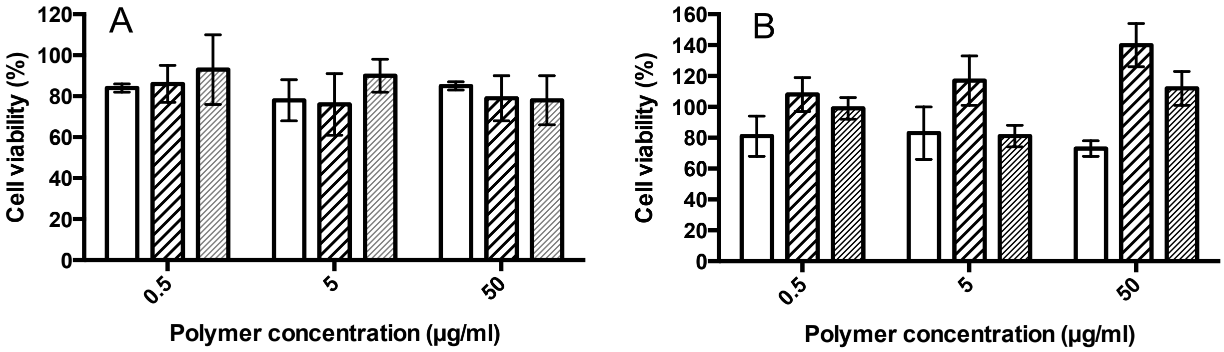

Figure 28. **HeLa cell viability after 24 h incubation with protein modified nanoparticles.** Panel A.) $A_{45}B_{110}C_{37}$ nanoparticles (empty), $A_{45}B_{110}C_{37}$ nanoparticles with BSA-FITC (stripes),

$A_{45}B_{110}C_{37}$ nanoparticles with o-ASM (dense stripes). (B) $A_{45}B_{101}C_{27}$ nanoparticles (empty), $A_{45}B_{101}C_{27}$ nanoparticles with BSA-FITC (stripes), and $A_{45}B_{101}C_{27}$ nanoparticles with o-ASM (dense stripes). Adapted from *Ref*[9] with permission.

At the highest concentration $A_{45}B_{101}C_{27}$ nanoparticles present a slightly lower cell viability (73%) than $A_{45}B_{110}C_{37}$ nanoparticles (78%), due to a lower overall positive charge (ESI), in agreement with previous reports on cationic polymer nanoparticles[204]. However, upon attachment of protein molecules, both $A_{45}B_{101}C_{27}$ and $A_{45}B_{110}C_{37}$ nanoparticles at the highest concentration have a lower cytotoxicity (the effect is, due to the decrease in the overall positive charge, as indicated by zeta-potential measurements (Fig. S8, SI). The effect is seen for both copolymers, but it is more pronounced for $A_{45}B_{11}0C_{37}$-based nanoparticles. BSA-FITC loaded $A_{45}B_{110}C_{37}$ nanoparticles presented a viability > 100%, due to the stimulatory effect of BSA on cell proliferation[205] .Overall, the low cytotoxicity of protein-nanoparticles supports their further development for therapeutic applications.

To be applied as a therapeutic agent, cellular uptake of ASM-nanoparticles is critical and therefore was investigated in HeLa cells using confocal laser scanning microscopy (CLSM). In HeLa cells incubated with the o-ASM/ABC nanoparticles for 24 h, the presence of a fluorescent signal for o-ASM/$A_{45}B_{110}C_{37}$ nanoparticles, and o-ASM/$A_{45}B_{101}C_{27}$ nanoparticles clearly indicated uptake of o-ASM loaded nanoparticles (Figure 29).

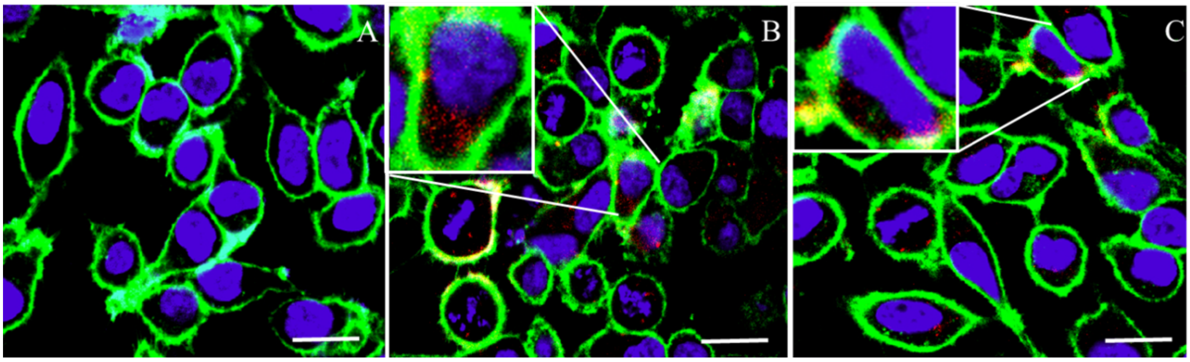

Figure 29. Confocal laser scanning micrographs of HeLa cells incubated with ASM modified NP. The cellular membrane was visualized by Cell Mask Deep Red (green), nuclei with Hoechst 33342 (violet), and o-ASM (red). Panel A.) Untreated cells, Panel B.) Cells treated with 50μg/ml o-ASM-$A_{45}B_{110}C_{37}$ nanoparticles, Panel C.) cells treated with 50μg/ml o-ASM-$A_{45}B_{101}C_{27}$ nanoparticles. Insets: zoomed regions of HeLa cells treated with 50μg/ml o-

ASM-$A_{45}B_{110}C_{37}$ and 50μg/ml o-ASM-$A_{45}B_{101}C_{27}$ nanoparticles. Scale bar: 50 µm. Adapted from *Ref*[9] with permission.

In addition, up-take by HeLa cells after incubation for 24h of nanoparticles containing fluorescently labeled BSA-FITC (1:12 labeling efficiency) and o-ASM (1:3 labeling efficiency) respectively, was measured by fluorescence-activated cell sorting (FACS). A significant shift of the peaks corresponding to the cells incubated with nanoparticles compared to normal cells confirms uptake (Figure 30). The difference in fluorescence shift between nanoparticles loaded with BSA-FITC and o-ASM is attributed to the lower labeling efficiency of o-ASM. The stimulating effect of BSA is considered only as a minor factor, because the coating of nanoparticles with BSA has been reported to have little or no influence on the cellular uptake of nanoparticles[206].

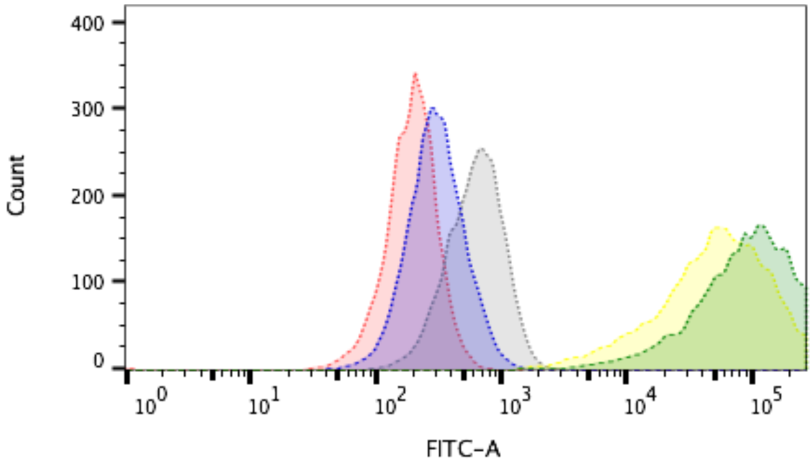

Figure 30. Flow cytometry analysis of cellular uptake of HeLa cells for labeled proteins in nanoparticles: Untreated HeLa cells (red); HeLa cells treated with 50μg/ml o-ASM-$A_{45}B_{101}C_{27}$ (blue); HeLa cells treated with 50μg/ml o-ASM-$A_{45}B_{110}C_{37}$ (grey); HeLa cells treated with 50μg/ml BSA-FITC-$A_{45}B_{101}C_{27}$ (yellow), and HeLa cells treated with 50μg/ml BSA-FITC-$A_{45}B_{110}C_{37}$ (green). Adapted from *Ref*[9] with permission.

2.8 CONCLUSION

This chapter focused on the self-assembly of poly(ethylenegycol)-b-poly(methyl caprolactone)-b-poly(2-(N,N-diethylamino) ethyl methacrylate) copolymers with two different ratios of the hydrophobic to hydrophilic blocks generated soft nanoparticles to which proteins could be attached at a desired location in order to develop an efficient protein delivery platform. The asymmetry of the block copolymers favored a specific location for proteins and small molecular mass molecules: the PDMAEMA block predominantly present at the external interface favored attachment of proteins and small molecular mass molecules with the opposite charge, while PEG was mainly embedded inside the hydrophilic domain. The combination of the methods used in this study (LS, TEM, cryo-TEM, FCS, activity assays of the proteins) allowed for a deeper understanding of the nanoparticles' morphology and behavior in the presence of proteins as key factors for future translational applications. Attachment of biomolecules was favored by a triggered effect of electrostatic interactions between the PDMAEMA domain and negatively charged molecules. Both BSA and o-ASM were successfully attached, and subsequently released from the self-assembled nanoparticles (>80%) when the pH was decreased to acidic values. This is the first system based on electrostatic attachment and release of therapeutic proteins (ASM), whilst preserving their activity. The protein-polymer nanoparticles showed low toxicity at concentrations up to 50μg/ml, and were up-taken by HeLa cells. PEG-*b*-PMCL-*b*-PDMAEMA nanoparticles can attach a variety of biomolecules with charge opposite to that of the PDMAEMA domain, and then release them in a pH-responsive manner, which supports their further optimization for potential therapeutic applications. This study is the first one showing that it is possible to deliver proteins in a pH responsive manner by their controlled localisation in the nanoparticle interface with the environment.

Chapter 3.

BIOMIMETICALLY ENGINEERED PH TRIGGERED PMOXA-*b*-PDMS-*b*-PMOXA CATALYTIC NANOCOMPARTMENTS[⊥]

In this chapter, the concept of pH triggered catalytic nanocompartments designed by biomimetic engineering of PMOXA-b-PDMS-b-PMOXA polymersomes is introduced. pH responsive catalytic nanocompartments are developed by simultaneous equipment of polymersomes with both a responsive protein gate - a chemically modified version of Outer membrane protein F (OmpF) and a catalyst - horseradish peroxidase. Insight is given into how chemical modifications of key amino acid residues, located at the constriction site of the OmpF pore affect the function of OmpF, the self-assembly of PMOXA-b-PDMS-b-PMOXA polymersomes and the functional reconstitution of OmpF into polymersome membranes. Finally, we demonstrate how the chemically modified OmpF affects the functionality of the self-assembled biomimic by acting as a pH responsive gate, thereby allowing controlled access of enzymatic substrates to the enzyme encapsulated in PMOXA-b-PDMS-b-PMOXA polymersomes.

[⊥] This study has been published: T. Einfalt, R. Goers, I. A. Dinu, A. Najer, M Spulber, O. Onaca-Fischer and C. G. Palivan Stimuli-Triggered Activity of Nanoreactors by Biomimetic Engineering Polymer Membranes, Nano Letters **11**, 7596 – 7603, (2015)

BIOMIMETICALLY ENGINEERED PH TRIGGERED PMOXA-*b*-PDMS-*b*-PMOXA CATALYTIC NANOCOMPARTMENTS

3. 1 MOTIVATION AND PROBLEM DEFINITION

The need to introduce new systems that can provide reaction spaces at the nano-scale level with high space and time precision responses is present in various domains, such as biomedicine, environmental sciences and chemical engineering. As discussed in chapter one, emerging concepts of molecular factories, artificial organelles and artificial cell mimics are already opening new frontiers in medicine. Inspired by biosynthetic processes in nature, researchers have become increasingly interested in designing reaction spaces based on vesicular supramolecular assemblies (polymersomes, PICsomes, or LBL capsules), with sizes in the nanometer range and containing active compounds so that they can function as catalytic nanocompartments[13]. The advantage of polymersome based nanocompartments, in respect to soft polymer nanoparticles discussed in chapter two, is their unique ability to simultaneously protect encapsulated biomolecules from their environment, while preserving their activity inside the aqueous cavity of the supramolecular assembly [13,134].

Of particular interest in the generation of catalytic nanocompartments are polymersomes, because of their greater stability compared to liposomes,[48] and the ability to modulate their properties (size, permeability, polarity, stimuli responsiveness) by changing the chemical nature of the copolymers or their functionalisation[130,207]. The unique nanoarchitecture of polymersomes offers three topologic regions: the inner cavity, the membrane, and their exterior surface. These regions can be used to support the simultaneous loading of both hydrophilic and hydrophobic molecules, which can range from small molecular weight molecules (i.e. drugs and fluorophores) to macromolecules (i.e proteins)[130]. An essential molecular parameter that needs to be controlled for an *in situ* reaction inside the cavity of a catalytic nanocompartment is a membrane permeability that allows transport of the substrates required for the reaction, and the products generated by the reaction. To maximize the effectiveness of catalytic nanocompartments, especially when they are intended to serve as artificial organelles or simple mimics of cells, an additional step in design should be triggered activity. Significant efforts have been made to obtain stimulus-responsive polymersomes for use as drug carriers with enhanced efficacy by providing a homogenous spatial distribution, and increasing the localization of drugs in desired regions through triggered release[54]. Polymersomes serving as drug delivery carriers were designed to respond to specific stimuli, such as pH[208], temperature[209], light[210], enzyme[211] or a combination of thereof[212]. The release from the carrier has been mainly obtained by dissociation or degradation of polymersomes into polymer chains or small molecules. However, this strategy involving the dissociation of the polymer supramolecular assembly upon the presence of stimulus(i) is not compatible with the concept of a catalytic nanocompartment, in which the enzymatic reactions should take place *in situ*, inside their inner cavity. There are a few examples of stimuli responsive catalytic nanocompartments (to light[117,131], to pH changes[167,213]), but they are either permeable only to reactive oxygen species[117,131], or lack controlled permeability[167,213]. Therefore alternative strategies are required to design stimuli-triggered catalytic in which polymersomes both preserve their integrity, and an *in situ* reaction is triggered by the presence of a stimulus.

The aim here was to develop catalytic nanocompartments with triggered activity based on the encapsulation of enzymes inside polymersomes with a membrane that is rendered selectively permeable by inserting chemically engineered channel porins to act as “gates”. The protein “gates” reconstituted in the polymersome membrane are partially closed, and open at different pH values: thus pH-controlled enzymatic activity inside the catalytic nanocompartments is mediated by the blockage/free diffusion of molecules through the porin channel (Scheme 1). Our biomimetic approach is inspired by protein function that is commonly found in nature, as for example the pH-gated M2 protein found in the capsid of the Influenza B virus, which has very low conductance at physiological pH values, but increases 50 fold at lower pH[214]. Change in pH presents as a model stimulus for our triggered catalytic nanocompartments, because it is an essential signaling factor that accompanies pathological conditions[187]. In medicine differences in pH are exploited by specific diagnostics or therapeutic agents[215,216].

Catalytic nanocompartments were generated by encapsulating a model enzyme, horseradish peroxidase (HRP), inside the inner cavity of poly(2-methyloxazoline)-block-poly(dimethylsiloxane)-block-poly(2-methyloxazoline) ($PMOXA_6$–$PDMS_{44}$–$PMOXA_6$) polymersomes with a membrane in which modified Outer membrane protein F, OmpF served as a protein “gate”.

In order to obtain a responsive protein gate, OmpF was chemically modified with a “molecular cap” to be partially blocked/blocked/open depending on the pH values of the surrounding environment of the catalytic nanocompartment. Differences in accessibility of the OmpF pore for molecules (substrates and products of the *in situ* enzymatic reaction) represent key factors for triggering the activity of catalytic nanocompartments. Use of the bottom-up approach of combining polymersome membranes with protein gates allows the optimization of catalytic nanocompartments with respect to: (i) membrane permeability, (ii) the mass of the molecules transported, and (iii) overall catalytic nanocompartment functionality. In contrast to polymersomes with membranes containing genetically modified OmpF, which served for pH-sensitive release of a payload[146], our catalytic nanocompartments represent an additional step in terms of functionality, because of the controlled modulation of the *in situ* enzymatic reaction. Developments in the design of catalytic nanocompartments with triggered activity, such as our system, will support the production of complex reaction spaces at the nanoscale in which the functionality is modulated in an analogous manner to that in cell membranes, and ultimately in the creation of artificial cells (Scheme 3.). In addition, the strategy introduced here will provide solutions for personalized medicine by a simple change of combinations of active compounds (enzymes, proteins, mimics) encapsulated inside the catalytic nanocompartments.

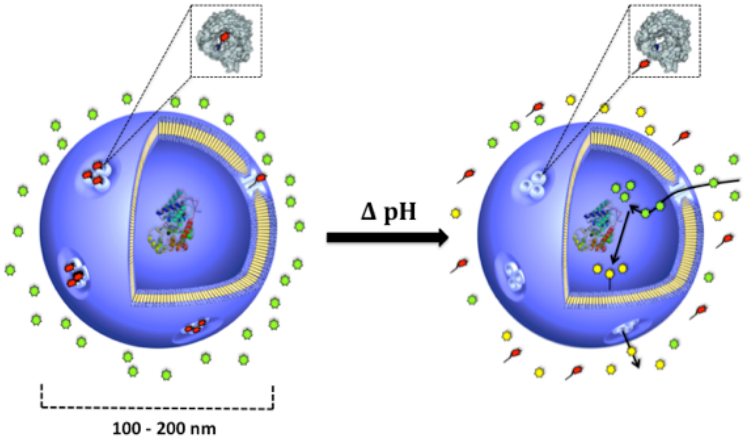

Scheme 3. Concept of a catalytic nanocompartment with triggered activity based on a chemically engineered protein "gate" inserted in a polymersome membrane. A change in pH induces the release of the sensitive molecular cap (green dots) from the protein "gate" allowing the entrance of substrates (red dots), and the release of the products of the enzymatic reaction (yellow dots). Adapted from *Ref*[12] with permission.

3.2 ENGINEERING OF THE OMPF WILD TYPE PORE TO DEVELOP A PH GATE

OmpF has already been used in its wild type form (trimer with a pore diameter that allows transport of molecules < 600 Da[217]) to render permeable the membrane of PMOXA-PDMS-PMOXA polymersomes, and to develop catalytic nanocompartments for various applications[5,134,218]. In order to design a pH responsive "gate" that triggers the *in-situ* activity of catalytic nanocompartments, the OmpF pore was chemically modified by attaching a molecular cap to reduce accessibility of the pore at pH = 7.4 (Figure 31). The cap is cleaved when the pH decreases to 5.5, and the "open gate" allows diffusion of molecules, and initiation or increase in activity of catalytic nanocompartments depending on the degree of pore blockage.

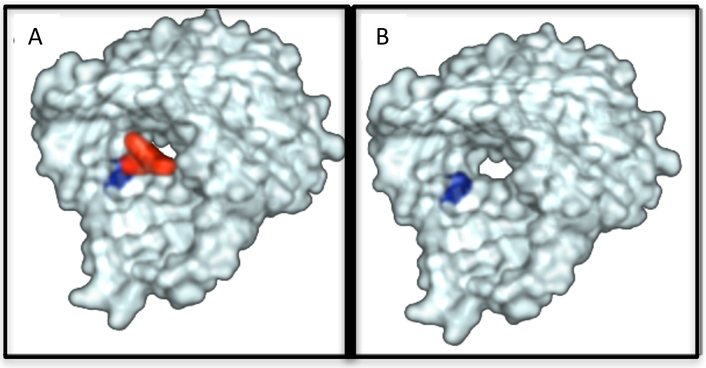

Figure 31. Molecular representation of the pH responsive OmpF. A. OmpF with a pH responsive cap (red molecular region) in the "closed state", and B. OmpF after release of the pH responsive cap, in the "open state". Image shown is a static representation. Adapted from *Ref*[12] with permission.

There are various methods to modify the pores of channel proteins in order to reduce transport, such as replacement of native amino acids with ones selected to allow chemical modification (e.g. cysteins), modification of the amino acid sequence via trans-splicing, or introduction of novel amino acids at the genetic level[219]. Here chemical modification of OmpF wildtype presented the most straightforward approach.

OmpF contains a constriction site with two amino acid half rings, which creates an electrostatic field that modulates solute fluxes and pore properties[217,220]. Diffusion of molecules through the OmpF pore is determined by six amino acid residues located inside of the constriction zone of the pore[221]. Since accessibility of the K16 and K46 residues located inside the pore cavity favours interactions with small molecular weight molecules, a binding of the pH sensitive cap to the these residues was expected. Such an approach for the design of a pH responsive OmpF, has the advantage of being able to bind different porin "caps" that can block the pore to different degrees depending on their properties.

We decided to first couple the lysine residues with levulinic acid by a simple sulfo-NHS/EDC reaction (Scheme 4.), and removed unreacted levulinic acid was by filtration and dialysis. This step was necessary to introduce reactive carbonyl groups, which favour the binding of a pH responsive cap cyanine5-hydrazide (Cy5-Hydrazide). Acid-liable chemical bonds, such as acetal, orthoester, hydrazone, imine and cis-aconyl bonds are well known to introduce pH responsiveness, and their degradation or hydrolysis under acidic conditions leads to the release of attached molecules[222]. Cy5-hydrazide was selected as the second part of the pH responsive linker, because its molecular weight (569.6 g/mol) matches with the pore size at the constriction region (Figure 31). In addition, as the fluorescence intensity of Cy5 is not influenced by a change in pH, the Cy5 fluorophore could be used for an efficient assessment of the "gate" functionality by fluorescence correlation spectroscopy (FCS) (see below).

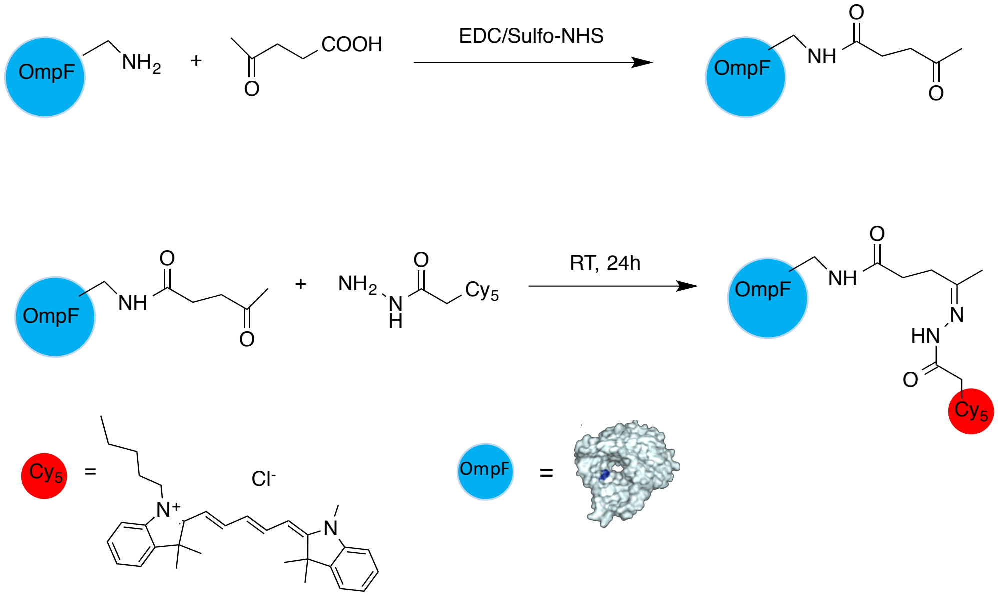

Scheme 4. Chemical modification of wild type OmpF. EDC/Sulfo-NHS coupling is used to attach levolunic acid. Subsequently pH sensitive molecular cap Cy5 hydrazide is attached to carbonyl groups. Adapted from *Ref*[12] with permission.

After coupling Cy5-hydrazide to the carbonyl groups (referred to in the manuscript as “CA”) and the formation of a pH responsive hydrazone bond, any unreacted Cy5-hydrazide was removed by centrifugal filtration. To avoid the possible formation of multimers, and sedimentation in a non-amphiphilic environment, OmpF was stored in 3% octyl-glucopiranoside (OG). However, as the presence of OG interferes with the purification of Cy5-hydrazide, further purification through dialysis was necessary to lower the OG concentration below the critical micellar concentration. In this way residual Cy5-hydrazide entrapped in OG micelles was removed in addition to avoiding any influence of OG on polymersome formation. In order to prove the introduction of CA, carbonylated OmpF (OmpF-CA) was compared with: wild type OmpF (OmpF-WT), wild type OmpF with added Cy5-hydrazide (OmpF-WT-Cy5) and carbonylated OmpF with added Cy5-hydrazide (OmpF-CA-Cy5). After completion of the purification procedure, all these subsets of OmpF were tested with 2,4-dinitrophenylhydrazine (DNPH), a specific reagent to assess the presence of carbonyl groups. Successful introduction of carbonyl groups was found for OmpF-CA and a value of 56.5+/-16.8 nmol carbonyl groups per mg of protein was obtained by UV-Vis spectroscopy (Figure 32a). In contrast, OmpF-WT, OmpF-WT-Cy5, and OmpF-CA-Cy5 did not react with DNPH either because of the lack of CA (OmpF-WT and OmpF-WT-Cy5), or successful binding of Cy5-hydrazide to CA groups, which blocked further reactivity in the case of OmpF-CA-Cy5.

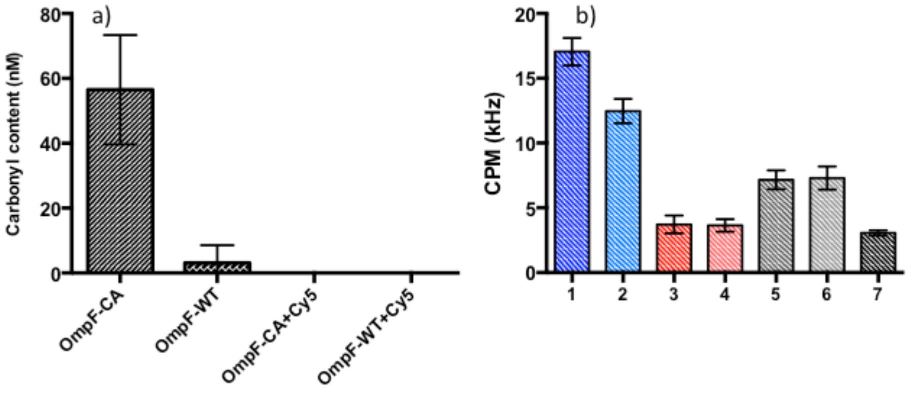

Figure 32. Characterisation of OmpF modification. a) carbonyl content determination of OmpF-CA, OmpF-WT, OmpF-CA+Cy5 and OmpF-WT+Cy5 protein pores. s determined by a DNPH protein carbonylation kit, and b.) Molecular brightness (CPM) of OG micelles with various OmpFs and/or free dye in 3% OG or PBS: (1) OmpF-CA+Cy5, 3% OG pH 7.2 (Dark blue), (2) OmpF-CA+Cy5, 3% OG pH 5.5 (Blue), (3) OmpF-WT+Cy5, 3% OG pH 7.2 (Dark

red), (4) OmpF-WT+Cy5, 3% OG pH 5.5 (Red), (5) Cy5, 3% OG pH 7.2 (Dark grey), (6) Cy5, 3% OG pH 5.5 (Grey), and (7) Cy5 pH 7.4 in PBS (Black). Adapted from *Ref*[12] with permission.

The binding of Cy5-hydrazide to the carbonylated OmpF was investigated by native page (Figure S12, S13, SI). Lower electrophoretic migration of OmpF CA-Cy_5 (35.9 ± 0.01 pixels) compared with OmpF-CA (37.7 ± 0.03 pixels) results from the trimer having a higher molecular weight when bound to Cy5-hydrazide. The modification did not affect the stability of the OmpF trimer, because no dissociation into mono or dimers was observed (Figure S12, SI).

An important aspect of a functional pH-responsive protein gate is the release of its sensitive cap upon the pH change. To observe this FCS was used, because it is able to assess the binding of fluorescent molecules to molecules with significantly higher molecular weight (protein, DNA, antibody), or to supramolecular assemblies (polymersome, nanoparticles)[8,223], and their encapsulation/entrapment in such supramolecular assemblies[224]. In addition, FCS has already been used to determine the release of small molecules through modified porins[146].

FCS allows analysis of the binding of fluorescent molecules to molecules/assemblies with significantly higher molecular weight by comparing their diffusion property and molecular brightness (counts per molecule, CPM) in the free and bound states.[224] In order to follow the release of Cy5 from OmpF-CA-Cy5 the brightness of OmpF-CA-Cy5 was compared with that of OmpF-WT+Cy5, and Cy5-hydrazide at different pH values, and in 3% OG to avoid aggregation and precipitation of OmpF. The presence of OG micelles complicated data interpretation because of interactions of dye molecules with the detergent micelles. Once solubilized in OG micelles, OmpF-CA-Cy5 had a diffusion time of $\tau_D = 350 \pm 27\ \mu s$; both Cy5 in OG micelles with $\tau_D = 249 \pm 34\ \mu s$, and OmpF-WT+Cy5 with $\tau_D = 266 \pm 50\ \mu s$ diffused similarly (Table S2, SI). Nevertheless, OmpF-CA+Cy5 micelles had a higher molecular brightness (CPM = 17 ± 1 kHz) compared to OmpF-WT+Cy5, (CPM = 4 ± 1 kHz) and therefore, on average, contained more dye molecules per micelle; this indicates additional interaction of the membrane protein with the dye, as expected for modified OmpF-CA (Figure S14, Table S2, SI). A decrease of brightness from 17 ± 1 kHz to 12 ± 1 kHz was observed after keeping OmpF-CA-Cy5 at pH 5.5 for 1 h, which indicates cleavage of the pH-responsive hydrazone bond leading to the release of Cy_5-hydrazide into the environment (Table S3, SI). Complete recovery of the free dye by FCS was not possible due to the aforementioned interaction of the dye with the detergent micelles. No significant change in brightness was observed in OG micelles both for OmpF-WT-Cy_5 and for Cy5-hydrazide at pH = 5.5 or pH = 7.2 (Figure 2b, Table S2, SI).

3.3 SELF-ASSEMBLY OF pH TRIGGERED BIOMIMETIC CATALYTIC NANOCOMPARTMENTS

In order to generate catalytic nanocompartments with pH triggered activity, simultaneous encapsulation of HRP and reconstitution of OmpF-CA-Cy5 was achieved during the self-assembly of $PMOXA_6$–$PDMS_{44}$–$PMOXA_6$ copolymers by thin film rehydration method. This preparation method has the advantage of avoiding organic solvents, which are difficult to be remove completely, and can also affect the biomacromolecules or be problematic in a later application of this system *in vivo*[150]. In addition, the film rehydration method is known as a mild method of enzyme encapsulation, as already reported for catalytic nanocompartments based on encapsulation of HRP[13]. Reconstitution of OmpF-WT and encapsulation of HRP in supramolecular assemblies of $PMOXA_6$–$PDMS_{44}$–$PMOXA_6$ copolymers served to create a non-pH responsive catalytic nanocompartment control.

$PMOXA_6$–$PDMS_{44}$–$PMOXA_6$ copolymers were selected here because they have an appropriate hydrophilic-to-hydrophobic ratio, and have been reported to self-assemble into polymersomes with sizes of 100-200 nm[139,140]. In order to establish whether the insertion of modified or non-modified OmpF, as well as the decrease in pH, affects polymersome morphology and stability, light scattering experiments were performed. The results indicated the formation of spherical nano-objects with a R_H of 77 nm for assemblies containing OmpF-WT and HRP, and 79 nm for those with-CA-Cy5 and HRP. At pH 7.2 the structural parameter ϱ ($\varrho = R_G/R_H$) has values of 0.90 – 0.96 for un-permeabilised HRP-loaded polymersomes, OmpF-CA-Cy5 permeabilised HRP-loaded polymersomes, and OmpF-WT permeabilised HRP-loaded polymersomes, whereas at pH 5.5 ϱ values are 0.96 - 1.05. These values are all close to 1.0, which is typical for hollow spheres; therefore the polymersome self-assembly process was not affected by the presence of HRP and/or OmpF reconstitution (Table 4, Table S3, SI).

TEM and cryo-TEM micrographs indicate the formation of spherical structures, with radii around 70 nm at pH = 7.2, both after self-assembly of $PMOXA_6$–$PDMS_{44}$–$PMOXA_6$ copolymers, and upon insertion of OmpF and encapsulation of HRP in the polymer assemblies (Figure 33 and Figure S15b, SI). Therefore, insertion of OmpF-WT / OmpF-CA-Cy5 and simultaneous encapsulation of HRP did not affect the self-assembly process of $PMOXA_6$–$PDMS_{44}$–$PMOXA_6$ copolymers into polymersomes. A slight decrease in size compared to un-permeabilised polymersomes was observed, as already reported for such copolymers[139,140]. The decrease of pH to 5.5 neither affected the architecture nor the size of OmpF-WT and OmpF-CA-Cy5 equipped catalytic nanocompartments (Table S3, SI). After 14 days OmpF-WT- and OmpF-CA-Cy5-equiped catalytic nanocompartments still preserved their structures, and did not aggregate.

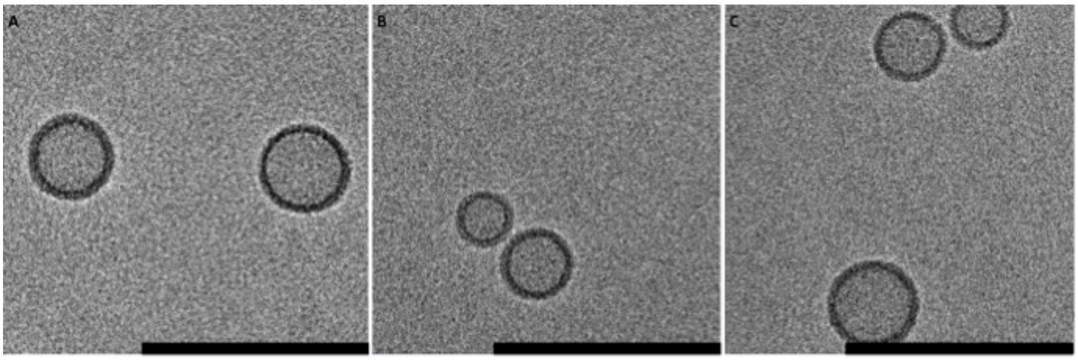

Figure 33. Cryo-TEM micrographs of catalytic nanocompartments. Panel A.) catalytic nanocompartments without OmpF, Panel B.) catalytic nanocompartments with reconstituted OmpF-WT, and Panel C.) catalytic nanocompartments with reconstituted OmpF-CA-Cy5. Scale bar = 200 nm. Adapted from *Ref*[12] with permission.

Table 4. Molecular characteristics of $PMOXA_6$–$PDMS_{44}$–$PMOXA_6$ assemblies without and with reconstituted OmpF at pH 7.2. M_w = 4500 g/mol, PDI = 1.8 $f_{hydrophilic}$ = 25 %.

Nano-assemblies	DLS/SLS		
	R_g [nm]	R_h [nm]	$\varrho = R_g/R_h$
HRP-loaded nano-assemblies	95	106	0.90
HRP-loaded nano-assemblies with OmpF-CA-Cy5	77	80	0.96
HRP loaded nano-assemblies with OmpF-WT	79	84	0.95

FCS was used to evaluate the insertion and calculate the number of OmpF gates/polymersome (OmpF-CA-Cy5/vesicle). FCS autocorrelation curves show a significant difference in τ_d values between freely diffusing Cy5-hydrazide (τ_d = 67 μs), OmpF-CA-Cy5 in 3% OG micelles (τ_d = 266 μs) and polymersomes with reconstituted OmpF-CA-Cy_5 (τ_d = 2914 μs) (Figure 34). The large increase in τ_d of OmpF-CA-Cy5-equipped polymersomes indicates that the modified protein gate was inserted in the polymer membrane. Furthermore by means of FCS it was possible to calculate a mean value of 55 OmpF-CA-Cy5 pores per polymersome by comparing the molecular brightness (CPM) of OmpF-CA-Cy5 in OG micelles (CPM = 17+/-1 kHz) with the molecular brightness of OmpF-CA-Cy_5 equipped polymersomes (CPM = 945 +/-33 kHz).

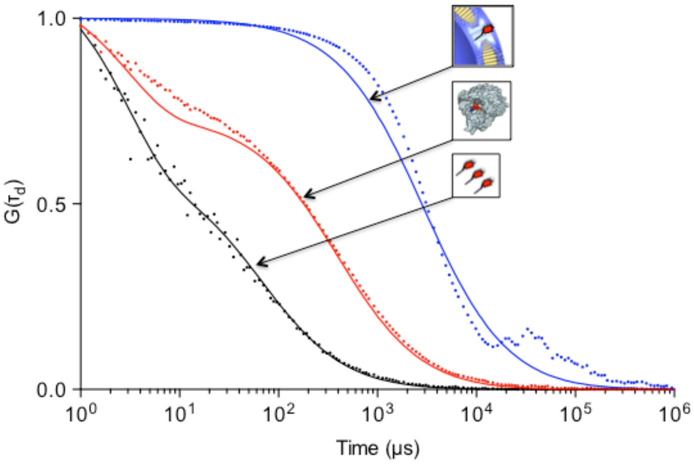

Figure 34. FCS autocorrelation curves of Cy5, OmpF-CA-Cy5 and reconstituted OmpF-CA-Cy5. 100 nM Cy5-hydrazide in PBS (Black), OmpF-CA-Cy5 in 3% OG (Red) and OmpF-CA-Cy5 in the membrane of polymersomes (Blue). Experimental autocorrelation curves

(dotted line), and their fit (full line). Curves normalized to 1 to facilitate comparison. Adapted from *Ref*[12] with permission.

The hydrodynamic radius (R_H) of the OmpF-CA-Cy_5 catalytic nanocompartments at pH 7.2 was calculated by Stokes-Einstein equation to be 47+/- 4 nm, in agreement with the values obtained from TEM, Cryo-TEM, and light scattering experiments.

3.4 FUNCTION OF pH TRIGGERED BIOMIMETIC CATALYTIC NANOCOMPARTMENTS

A crucial point in demonstrating that a catalytic nanocompartment has triggered activity is to evaluate its activity as function of pH. In this respect two different enzymatic assays were used, the TMB (3,3',5,5'- tetramethylbenzidine) colorimetric assay and the Amplex Red® fluorimetric assay. Amplex Red and TMB were selected because they differ in their molecular properties, as for example the charge or geometrical arrangement, and therefore serve as models to asses pore closure towards different types of molecule. It has been already reported that the molecular influx inside OmpF pores strongly depends on the properties of the molecules passing through them, which support an interaction, especially with the constriction zone.[47] Therefore pore closing of a modified OmpF is based on two factors, which have to be considered together: the closing of the pore due to modification with a specific molecular cap (for example in our case CA-Cy5), and interaction of the molecules penetrating the pore with the constriction region.

First, free HRP was tested to establish whether exposure to pH 5.5 affects its activity. No significant change in HRP activity was observed between incubation at pH 5.5 and pH 7.4 when TMB and Amplex Red were used as substrates (Figure S16, S17 SI);[47] thus any change in HRP activity inside catalytic nanocompartments is due to a triggered diffusion of substrates through the modified OmpF pore.

When TMB (predicted polar surface area = 52 A^2, M_W = 240 g mol^{-1}, Log P = 3.40, neutral at pH 7.4) was the substrate used to penetrate the modified OmpF gate, a smaller enzymatic turnover (around 38%) was obtained in catalytic nanocompartments equipped with OmpF-CA-Cy_5 at pH = 7.4, compared with the OmpF-WT catalytic nanocompartments at the same pH value (Figure 35, Figure S19). This decrease in *in situ* enzymatic activity of HRP for catalytic nanocompartments equipped with OmpF-CA-Cy5 indicates a partial closing of the pore, which decreases the molecular influx of TMB molecules. As TMB has M_w = 240g mol^{-1}, it is expected that this partial closing of the OmpF pore serves as a barrier, and thus will block molecules with higher M_w.

At pH = 5.5, the activity of catalytic nanocompartments equipped with OmpF-CA-Cy5 increased by 23%, indicating successful hydrolysis of the hydrazone bond, and the release of the Cy5-hydrazide molecular cap. The increase in the influx of TMB through the pore resulted in an increase in *in situ* catalytic nanocompartment activity. This allowed a comparable transport through the pore to that with carbonylated OmpF, and therefore a similar value for the *in situ* enzymatic reaction rate.

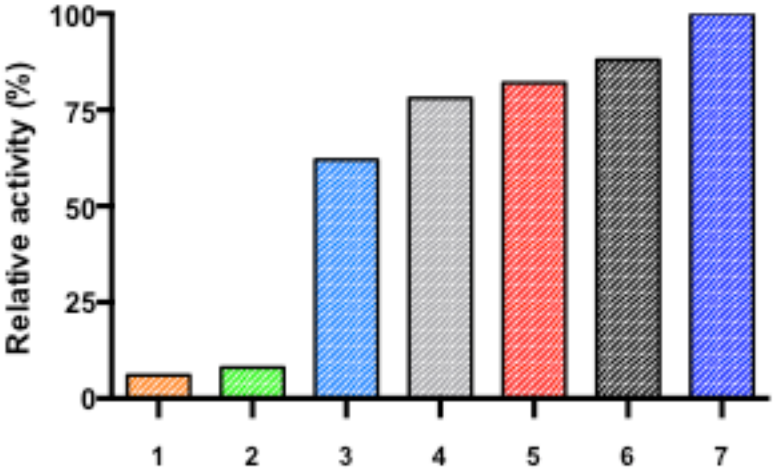

Figure 35. TMB conversion kinetics measured at pH = 7.4 of catalytic compartments prepared with different OmpF subsets. (1) unpermeabelised catalytic compartments incubated at pH = 5.5 (Orange), (2) unpermeabelised catalytic nanocompartments incubated at pH 7.4 (Green), (3) OmpF-CA-Cy5 catalytic nanocompartments incubated at pH 7.4 (Blue), (4) OmpF-CA-Cy5 catalytic nanocompartments incubated at pH 5.5 (Gray), (5) OmpF-CA catalytic nanocompartments incubated at pH 5.5 (Red), (6) OmpF-WT catalytic nanocompartments incubated at pH 5.5 (Black), (7) OmpF-WT catalytic nanocompartments incubated at pH 7.4 (dark Blue). Adapted from *Ref*[12] with permission.

The enzymatic turnover of the Amplex Red substrate (predicted polar surface area 72 A^2, M_W = 257 g mol^{-1}, Log P = 0.89, charge = -0.1 at pH 7.4) was drastically reduced (down to 14%), compared to OmpF-WT catalytic nanocompartments acting in similar conditions at pH = 7.4.

The blockage of Amplex Red influx through the pore is considered to be due to a combination of effects: (i) closing of the pore by the molecular cap, and (ii) electrostatic interaction of Amplex Red with the molecular cap. Such interactions of charged molecules with the positively charged constriction region of OmpF have been already reported for ampicillin.[48] After decreasing the pH to 5.5, the activity of nanoractors equipped with OmpF-CA-Cy5 increased to 74% in one hour. This indicates a successful pore opening, which allowed a significant increase in the influx of substrates through the pore (Figure 36, Figure S17). The slight increase in activity of the catalytic nanocompartments equipped with OmpF-CA with time is explained by the concentration gradient of the substrate at the beginning of the enzymatic reaction.

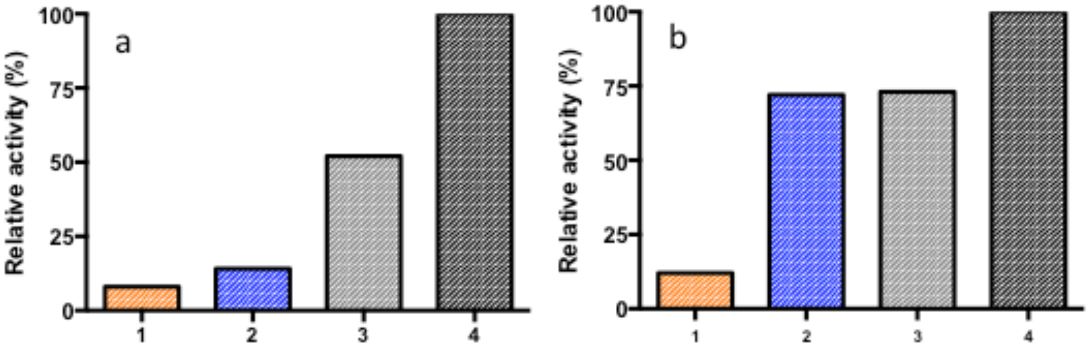

Figure 36. Amplex red conversion kinetics of catalytic nanocompartments equipped with different OmpFs (1) unpermeabilised catalytic nanocompartments (orange), (2) OmpF-CA-Cy5 (blue), (3) OmpF-CA (grey), and (4) Ompf-WT (black) at pH 5.5, at time 0 (a) and after 1 hour (b). Adapted from *Ref*[12] with permission.

Catalytic nanocompartments without inserted OmpF had a very low enzymatic turnover for both substrates at pH = 5.5, probably due to the presence of traces of HRP not removed by dialysis. As expected, no increase in activity was observed in catalytic nanocompartments without reconstituted OmpF at pH 5.5. This indicates that the permeability of polymersomes was not affected by the change in pH (Figure 35 Figure 36, Table S3, SI), in agreement with previous reports on the stability of PMOXA-*b*-PDMS-*b*-PMOXA polymersomes at different pH values[139] .

The difference in the decrease of the *in situ* activity of catalytic nanocompartments equipped with OmpF-CA-Cy5 at pH = 7.4 as function of the molecular nature of the substrates results from a modulation of the influx through the pore due to the combined effect of pore closing and intermolecular interactions of the substrates in the “spatially reduced” constriction region. Whilst the influx of the neutral TMB is only reduced by the pore closing, that of the slightly negatively charged Amplex red is blocked by intermolecular interactions with the positively charged Cy5 fluorophore. Our results are in agreement with previously reported data, in which mutations of key OmpF residues (K16 and K46) substantially altered the diffusion of molecules through the pore[47,48].

Therefore, depending on the desired application, the “gate” can be partially or fully closed at pH = 7.4, and opened at pH = 5.5, resulting in a modulation of the enzymatic activity inside the cavity of catalytic nanocompartments. The decrease in the functional diameter of the OmpF pore defining the size exclusion limit for diffusion represents the driving force for a triggered *in situ* activity of these catalytic nanocompartments. Our stimuli-responsive switch is one-time stimulus responsive, especially designed to be released and open the pore upon a pH change. Reversible control of opening/closing the OmpF channel could be engineered by a gating moiety, near the constriction site of the protein, which should be covalently attached, stable in acidic pH, and present specific properties dependent on the pH of the environment. Ongoing experiments are dedicated to engineer this type of sensitive molecular cap, which could influence in a reversible manner the influx of substrates through the pore.

3.5 CONCLUSION

In cellular and subcellular environments, reaction catalysts (enzymes or small molecular weight compounds) are often protected in specific compartments where they act *in situ* when necessary, as for example in the presence of a stimulus. Here a new biomimetic strategy for developing catalytic nanocompartments possessing triggered activity is presented. Modulation of enzyme activity inside catalytic nanocompartments was successfully implemented by inserting chemically-modified channel proteins to act as pH-controlled “gates” in the membrane of enzyme-loaded polymersomes. Together with a preserved architecture of the polymersomes, the decrease/blocking of the flow of substrates through the membrane at neutral pH, and its unblocking at a lower pH resulted in very efficient stimulus-driven active catalytic nanocompartments. This system produces pH-triggered enzymatic activity, and therefore represents an additional step in the design of active systems capable of responding “on demand”. In, addition, an example of chemical modification of OmpF that results in both tuning the pore cut-off size (from 600Da in the case of OmpF- WT to around 240Da for OMPF-CA-Cy5) and molecular selectivity is presented.

The design of catalytic nanocompartments with triggered activity opens new possibilities for advanced control of reactions at the molecular level, and is expected to have a significant impact in domains such as medicine or controlled catalysis.

Chapter 4.

BIOMIMETIC ENGINEERING OF RESPONSIVE ARTIFICIAL ORGANELLES WITH IN VITRO AND IN VIVO FUNCTIONALLITY[⊥]

The final experimental chapter of this thesis builds on the knowledge of developing a responsive catalytic nanoarchitecture, acquired in the second and third chapter, in order to design an artificial organelle with in vitro and in vivo functionality. To develop an artificial organelle, a responsive catalytic PMOXA-b-PDMS-b-PMOXA nanocompartment, capable of interacting with the intracellular environment of living cells, is designed. For this purpose, a cysteine double mutant of OmpF is chemically modified to act as a reduction responsive gate in polymersome membranes. Through the functional reconstitution of the modified OmpF, in horseradish peroxidase loaded PMOXA-b-PDMS-b-PMOXA polymersomes, a biomimetic system is created that is capable of acting in response to small intracellular signalling molecules, such as glutathione. The function of the designed biomimic as an artificial organelle is demonstrated by the "in vitro" application in human epithelial HeLa cells and "in vivo" in zebrafish embryos. Surisingly, even after being recognised by the zebrafish embryo early immune system, it remains responsive and functional, due to the robust nature of the polymersomes.

[⊥] This study has been submitted to Nature Communications: T. Einfalt, D. Witzigmann, C. Edlinger, S. Sieber, R. Goers, A. Najer, M Spulber, O. Onaca-Fischer and J. Huwyler, C. G. Palivan, Biomimetic artificial organelles with *in vitro* and *in vivo* reduction triggered activity

4.1 MOTIVATION AND PROBLEM DEFINITION

Nanoscale biomimics designed as artificial organelles (AOs) are particularly appealing in biomedicine because of their ability to act as cellular implants by providing a required compound/signal, detoxifying harmful compounds, or changing cellular conditions and reactions[129]. AOs are based on nanoscale compartmentalisation of active compounds (enzymes, proteins, catalysts, mimics) within an artificial compartment that can reach, survive and function in the intracellular environment, thereby acting as a simplified mimic of nature's own organelles. AOs compartmentalisation permits the compartmentalised compounds to perform a specific *in situ* reaction, whilst being protected from the environment in the synthetic compartment[129]. Different examples of systems that have the potential to act as AO have been recently developed. They are based on liposomes, porous silica nanoparticles, and polymer compartments (polymersomes) in combination with biomacromolecules[5,173,174]. *In vitro* and *in vivo* preserved integrity and activity of the system represent essential requirements for a functional AO. However, only very few of such systems with AO potential have been tested *in vitro* to assess their cellular functionality and none have been assessed *in vivo*[5,113,173,174,225]. Polymer-based compartments named polymersomes are ideal candidates for the creation of AOs, due to their hollow sphere architecture with a membrane serving as a border to the inner environment, combined with an improved mechanical stability compared with the lipid-based compartments i.e. liposomes[49,226]. The encapsulation of active compounds in polymersomes represents a key approach for the design of AOs if the synthetic membrane is permeable for a molecular exchange of substrates/products with the environment to support the *in situ* reaction [49,135]. Previous examples of AO are exciting because they show the ability of AOs to emulate cellular pathways (e.g. ROS detoxification or glucose oxidation) as a potent strategy for the substitution of decreased or absent cellular activity[5]. Stability, biocompatibility and low toxicity of AOs represent real advantages favouring AOs when compared to existing solutions for enzyme replacement, such as direct enzyme delivery and transfection[227]. However, none of the first reported AOs were evaluated *in vivo*, to indicate their functionality in living organisms. Another essential factor to tune AOs functionality and applicability is a triggered response to environmental factors, as for example the redox state of the cell, which regulates various processes involved in cellular signalling pathways[228,229]. Mitochondria, for example, can act as critical mediators of cellular redox homeostasis[230], since their membranes contain proteins responsive to changes in glutathione (GSH), reactive oxygen species (ROS) or reactive nitrogen species (RNS) levels[231,232,233]. As biological systems are required to respond to constant changes in the cellular microenvironment, triggered permeability of AOs membrane is essential to assure precise control of the *in-situ* reactions, and resulting products.

Here a strategy to design biomimetic AOs with an *in-situ* enzymatic reaction triggered by the presence of an external cellular stimulus is presented *in vitro* and *in vivo*. Polymersomes were equipped with genetically modified OmpF porines to induce redox responsiveness to the membrane while simultaneously encapsulating a model enzyme, HRP inside their cavity as core of the AO functionality. Amphiphilic block-copolymers poly(2-methyloxazoline)-block-poly(dimethylsiloxane)-block-poly(2-methyloxazoline) ($PMOXA_6$–$PDMS_{44}$–$PMOXA_6$) have been used to self-assemble into polymersomes because they have already been shown to form membranes in which biopores and membrane proteins were successfully inserted and they preserved their functionality[4]. Once inserted in the polymersome membrane, the modified OmpF porines act as protein "gates" and trigger the *in situ* HRP enzymatic reaction. The molecular flow through the membrane is controlled in an open/closed state of the protein gate, directly related to changes in the environment of the polymersomes. A previously developed double cysteine mutant of OmpF[234] is used as it opens the possibility of attaching molecular caps to the genetically introduced cysteine residues. By attaching the molecular cap using disulphide bonds the OmpF pore is blocked/unblockunblocked depending on changes in redox potential, which occur when the system enters the intracellular microenvironment. In contrast to polymersomes with membranes containing genetically modified OmpF, which served for release of a payload in reductive conditions[235], the system presented here has an increased functionality, because it serves to control an *in situ* enzymatic reaction, and therefore the overall functionality of the AOs. Inspired by cellular membranes, this strategy provides stimuli-responsiveness to the polymersome membranes without affecting the membrane integrity, as is the case of stimuli-responsive synthetic membranes of compartments[236], nor the size and architecture of the polymersomes. Therefore, encapsulated HRP can fulfil its activity when the protein gate allows the specific molecular diffusion of substrates/products through the membrane and is simultaneously protected from proteolytic attack. A combination of spectroscopic methods (fluorescence correlation spectroscopy, electron paramagnetic resonance), LC-MS-MS analysis, light scattering (static and dynamic LS), transmission electron microscopy (TEM and cryoTEM) and enzymatic assays served to characterise the system in solution, and evaluate its triggered functionality. Crucial steps were to evaluate AOs toxicity and functionality in human epithelial HeLa cells, and then *in vivo* tolerability, preservation of the AOs architecture, and *in situ* regulation of the encapsulated enzymes activity in a vertebrate model (Scheme 4).

Developments in the design of AOs with triggered activity result in complex reaction spaces at the nanoscale with functionalities modulated in an analogous manner to that of cell membranes, and represent a necessary step towards the creation of artificial cells. In addition, the strategy of engineering AOs acting as cellular implants in living organisms will provide solutions for personalized medicine by a straightforward change of the encapsulated biomolecules to cope with the specificity of the pathologic conditions.

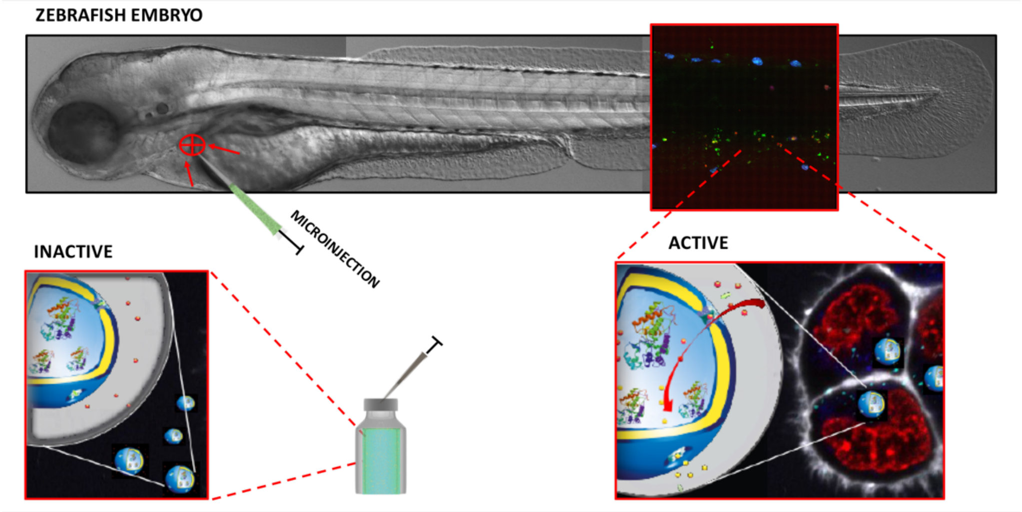

Scheme 4. In *vivo* functionality of AO. Functionality of AO was tested by injection into zebrafish embryos. After being recognised by the early immune system of zebfarish embryos, the biomimetic systems remains highly active.

4.2 ENGINEERING THE OMPF CYSTEINE MUTANT PORE

The key factor in engineering AOs - with activity triggered by changes in environmental conditions – is the "on-demand" permeability of the compartment towards enzymatic substrates/products. In addition, the structural integrity of the polymersome architecture, which mimics the architecture of the organelle, is required for enzyme protection, and generation of a confined reaction space. In a biomimetic approach $PMOXA_6$-$PDMS_{44}$-$PMOXA_6$ polymersome membranes were equipped with protein "gates" responsive to changes in GSH concentrations present in intracellular environments, while preserving the architecture of the nanocompartment (Scheme 5A, B).

To construct the responsive "protein gate", a cysteine double mutant of OmpF (OmpF-M)[234] was chosen, because cysteine residues, replacing the amino acids K89 and R270, are expected to form reduction-sensitive disulphide bonds with molecules selected to serve as "molecular caps". As demonstrated in the previous chapter molecular caps block the OmpF pore under specific conditions, and unblock them when changes in the environment occur.

The ability of cysteine residues of OmpF-M to form disulphide bonds with thiol groups of small molecular weight molecules was examined using a suitable spin probe (bis-(2,2,5,5-Tetramethyl- 3-imidazoline-1-oxyl-4-yl)disulfide)[237] and the fluorescent dye SAMSA fluorescein (SAMSA-CF) (Scheme 5C, B)[238].

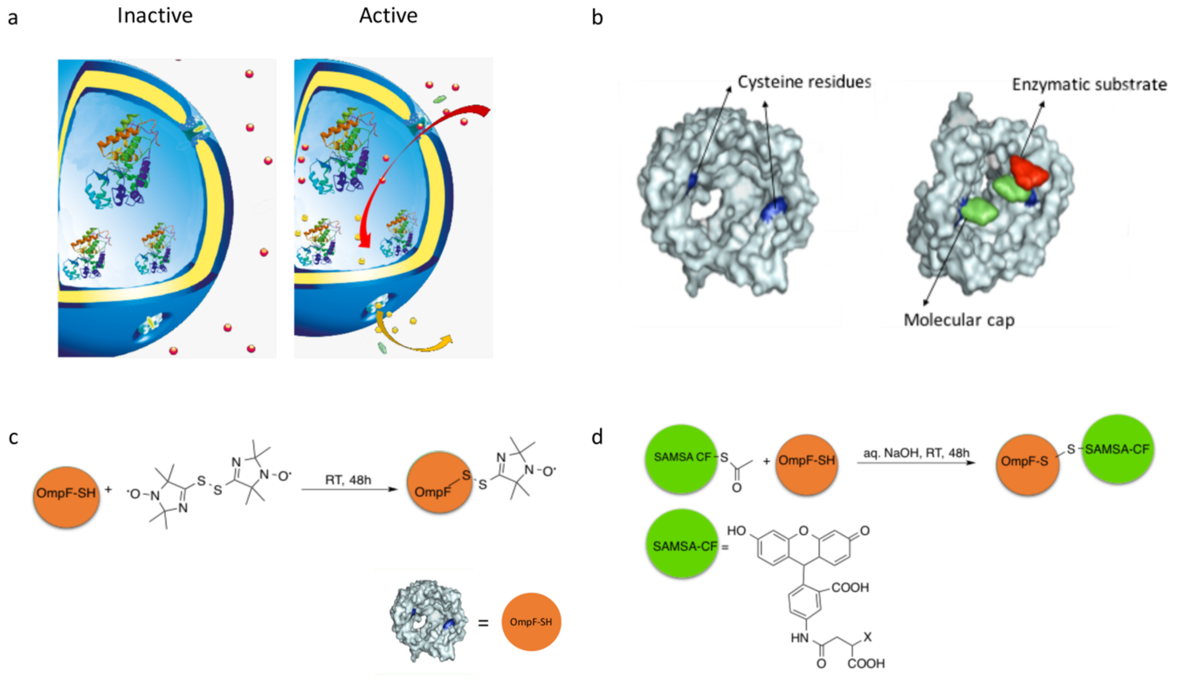

Scheme 5. Engineering of stimuli stimuli-responsive OmpF A. Schematic representation of modified OmpF acting as a gate in catalytic nanocompartments. B. Molecular representation of the OmpF-M cysteine mutant[234]. C. Chemical modification of OmpF-M cysteine mutant with the spin probe bis-(2,2,5,5-Tetramethyl- 3-imidazoline-1-oxyl-4-yl)disulfide, D. Chemical modification of OmpF-M cysteine mutant with the fluorophore SAMSA-CF .

Coupling reaction of the molecular caps with the cysteine residues of OmpF-M resulted in the formation of OmpF conjugates (OmpF-S-S-CF for OmpF conjugated with SAMSA-CF and

OmpF-S-S-NO$^{\bullet}$ for OmpF conjugated with bis-(2,2,5,5-Tetramethyl- 3-imidazoline-1-oxyl-4-yl)disulphide) respectively. Unreacted reagents were removed by centrifugal filtration and dialysis. Modified OmpF-M conjugates were purified by extensive centrifugal filtration and dialysis to remove all unbound reagents.

Binding of the thiol-reactive spin probe was evaluated by LC-MS-MS, and electron paramagnetic resonance (EPR). Upon in-gel digestion of the porin[239], LC-MS-MS analysis of the peptide fragments indicated a 96 ± 4% labelling efficiency of the spin probe to cysteine residues of the OmpF-M. EPR spectrum of the bis-(2,2,5,5-Tetramethyl- 3-imidazoline-1-oxyl-4-yl)disulphide in PBS at 298K consists of an isotropic triplet pattern (Figure S20, SI), with a hyperfine coupling a_N value of 15.8 G, similar to reported values for analogous nitroxide probes with no aggregation present (15.8 G for 5 DSA in 0.1 M NaOH and 15.9 G for 16 DSA in 0.1 M NaOH [240,241]. A very weak second component is present as well, because of spin-spin interaction resulting in an additional broadening of the third line[237]. In case of OmpF-S-S-NO$^{\bullet}$, a broad anisotropic EPR spectrum with no additional isotropic component was obtained. This is similar to that reported for 5-DSA in lipid bilayers or cholesterol aqueous solutions, with typical g and A values ($g(x) = 2.009$, $g(y) = 2.0065$, $g(z) = 2.0039$, and $A(x) = 6.0$ G, $A(y) = 6.0$ G, $A(z) = 34$ G)[242]. This spectrum results from a hindered rotation of the nitroxide probe[243] upon binding to the OmpF mutant (OmpF-S-S-NO$^{\bullet}$), and indicates the successful binding of the bis-(2,2,5,5-Tetramethyl- 3-imidazoline-1-oxyl-4-yl)disulphide to modified OmpF mutant at the cysteine level (Figure 37a).

When OmpF-S-S-NO$^{\bullet}$ was exposed to 10 mM DTT (Figure 37b) an isotropic EPR spectrum with a_N value of 15.7 G – characteristic for the spin probe free rotation in PBS pH 7.4 – was obtained, demonstrating that the reaction is reversible. This is a clear indication that the nitroxide spin probe bound to thiol groups of the OmpF under oxidative conditions is cleaved from OmpF in a reductive environment.

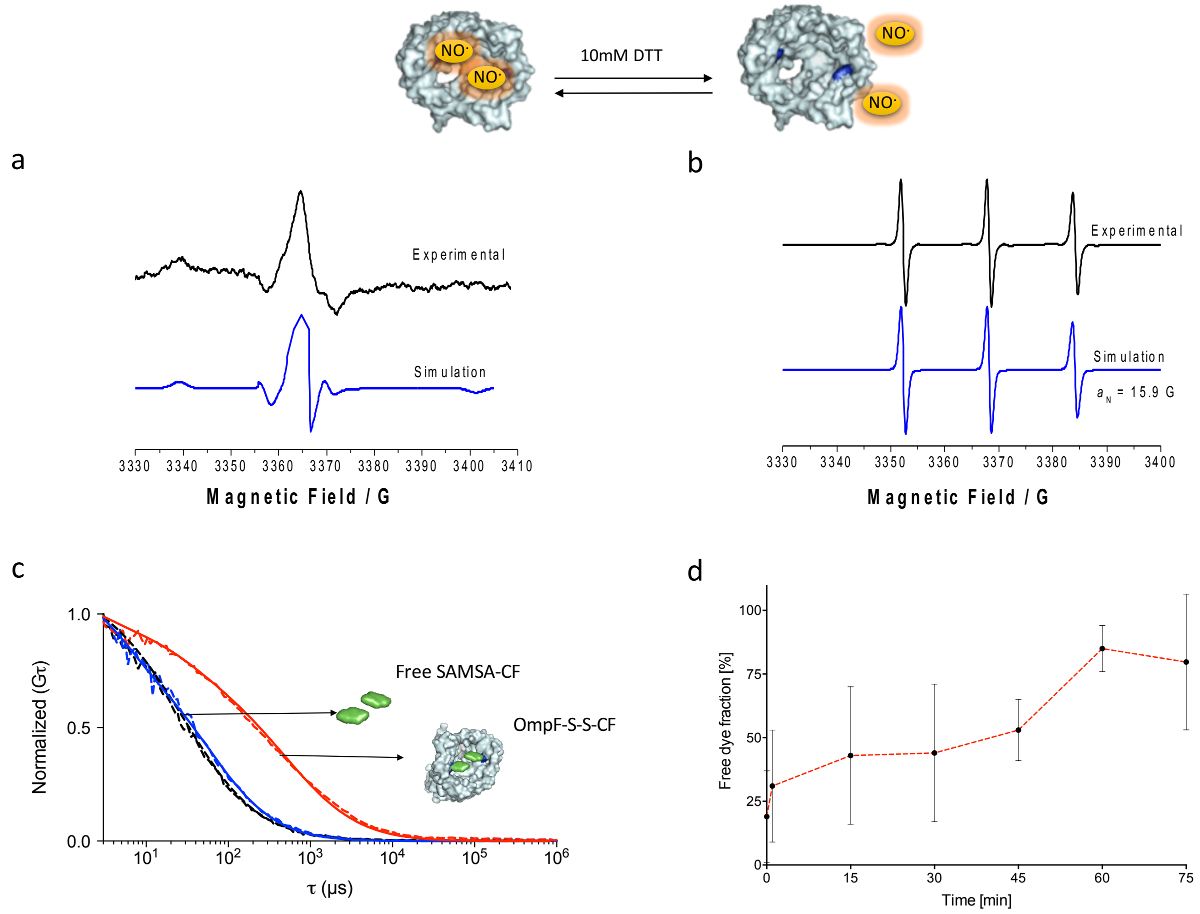

Figure 37. **Characterisation of stimuli-responsive OmpF** Panel a.) EPR spectra of bis-(2,2,5,5-Tetramethyl- 3-imidazoline-1-oxyl-4-yl)disulfide labelled OmpF-M experimental (black) and simulated (blue). Panel b.) 3-imidazoline-1-oxyl-4-yl)disulfide labelled OmpF-M in 1% OG incubated with 10 mM DTT experimental (black) and simulated (blue). Panel c.) Normalized FCS autocorrelation curves for SAMSA-CF in PBS (black), SAMSA-CF in 1% OG (blue) and OmpF-S-S-CF in 1% OG (Red). Dotted line – experimental autocorrelation curves, full line – fit. Panel d.) SAMSA-CF release kinetics from OmpF-M in 30 mM GSH, 1% OG, as measured by FCS and analyzed with a two-component fit.

SAMSA-CF was selected as a molecular cap to block the pore, due to its molecular weight (521.49 Da) expected to block the OmpF-M pore, and ability to form cleavable disulphide bonds[244]. Attachment of SAMSA-CF to OmpF-M introduces a stimuli-responsiveness to the pore, and therefore to the polymersome membrane when OmpF-S-S-CF is inserted. In addition, the fluorescent properties of SAMSA-CF served to analyze pore modification by a combination of SDS-PAGE and fluorescence correlation spectroscopy (FCS).

LC-MS-MS analysis of the peptide fragments indicated a labelling degree of OmpF-M of 81 ± 31%. Furthermore, a fluorescent band appeared in the SDS-PAGE gel when SAMSA-CF was conjugate to OmpF-M compared to the OmpF wild type, which did not interact with the fluorophore. This fluorescent band in SDS-PAGE supports the formation of OmpF-S-S-CF (Figure S2, SI). To mimic the intracellular reductive environment, where the glutathione concentration is kept at a constantly high level (10mM GSH) by cytosolic enzymes[245], such as glutathione reductase, the behaviour of the reduction responsive molecular caps in a similar environment was studied. Due to lack of a steady state concentration, and constant regeneration of GSH, an excess concentration of 30mM GSH was used to mimic the intracellular steady state of glutathione. In SDS-PAGE the fluorescent band disappeared when the OmpF-S-S-CF was mixed with 30mM GSH, indicating a successful cleavage of the molecular cap in reductive conditions. (Figure 37c, 37d, Figure S21, SI).

The binding of SAMSA-CF to OmpF-M cysteine residues was also evaluated by FCS. Molecular brightness and diffusion times of SAMSA-CF in PBS (pH 7.4), SAMSA-CF in 1% OG PBS (pH 7.4) and SAMSA-CF bound to OmpF (OmpF-S-S-CF) in 1% OG PBS (pH 7.4) were compared (Figure 37c). A labelling efficiency of an average of two SAMSA-CF molecules per monomer was calculated by comparing the molecular brightness (counts per molecule, CPM in kHz) of SAMSA-CF (2.2 ± 0.7 kHz) with that of protein bound to SAMSA-CF (4.8 ± 0.6 kHz) (Figure 37c). On contrary, wild type OmpF treated similarly as the cysteine mutant OmpF-M did not present any fluorescence after purification, therefore there was no binding of SAMSA-CF to OmpF-WT. To determine the kinetics of OmpF pore opening, the cleavage of SAMSA-CF from labelled OmpF-M upon addition of 30mM GSH at pH 7.4 was evaluated by FCS and an analysis by a two component fit. Due to cleavage of the disulphide bonds between the dye and the OmpF-M, the percentage of the free dye increased over time to 85 ± 9 %, plateauing after one hour (Figure 1D, Figure S22, SI).

4.3 SELF-ASSEMBLY OF REDUCTION TRIGGERED CATALYTIC NANOCOMPARTMENTS

In order to obtain stimuli-responsive catalytic polymersomes simultaneously encapsulated HRP in the inner cavity, and had inserted OmpF-S-S-CF or OmpF-S-S-NO$^{\bullet}$ into the membrane. PMOXA$_6$-PDMS$_{44}$-PMOXA$_6$ copolymers formed vesicles (as shown below) and spontaneously self-assembled in the presence of HRP or of both biomolecules (HRP and OmpF-S-S-CF or OmpF-S-S-NO$^{\bullet}$). Spherical vesicles between 100 – 200 nm were identified by cryo-TEM for polymer assemblies formed in the presence of HRP, polymer assemblies formed in the presence of HRP and OmpF-S-S-CF, and polymer assemblies formed in the presence of HRP and OmpF-SH (Figure 38A, Figure S23). These spherical polymer assemblies were demonstrated by light scattering to be polymersomes with: R_H of 99 ± 2 nm for HRP-loaded polymersomes containing OmpF-S-S-CF, R_H of 89 ± 4 nm for polymersomes loaded with HRP and equipped with OmpF-SH and R_H 101 ± 1 nm for HRP loaded polymersomes (Table S4, Table S5, SI). In the presence of 30 mM glutathione the polymersome architecture was not affected, with structural parameters ρ ($\rho=R_G/R_H$) values of 0.90 - 0.96 (all close to 1) confirming a hollow sphere morphology[93]. (Table S4, Table S5 SI). After 2 weeks of storage at 4°C in dark, HRP-loaded polymersomes, HRP-loaded polymersomes equipped with OmpF-SH and HRP-loaded polymersomes equipped with OmpF-S-S-CF preserved their size and did not aggregate (Figure S24, Figure, S25, Figure S26, SI).

The insertion of channel proteins into enzyme-loaded PMOXA$_6$–PDMS$_{44}$–PMOXA$_{6.}$ polymersomes is critical for the *in situ* functionality of the encapsulated enzyme because the channels allow substrates and products of the enzymatic reaction to pass through the membrane. OmpF-S-S-CF and OmpF-S-S-NO$^{\bullet}$ insertion into the polymersome membrane using was evaluated by FCS and EPR. A diffusion time of τ_d = 2573 ± 960 μs, was obtained for polymersomes with reconstituted OmpF-S-S-CF, indicating that the modified protein gates were successfully inserted into the polymer membranes. Four OmpF-S-S-CF porins / vesicle were calculated by comparing the molecular brightness of free fluorophore (2.2 ± 0.7 kHz) and the OmpF-S-S-CF equipped polymersomes (18.9 ± 11.1 kHz) OmpF-S-S-CF porins / vesicle), similar to values reported previously for the wild type OmpF[12] (Figure 38b).

HRP-loaded polymersomes equipped with OmpF-S-S-NO$^{\bullet}$ have an EPR spectrum with a broad single peak (g value 2.0065 and linewidth of 10G) (Figure 38c). As no additional peaks characteristic for the parallel and perpendicular component of the spin labelled OmpF EPR spectrum were present, the nitroxide polar group has a low mobility due resulting from its insertion in the dense polymer membrane. A similar behaviour was reported for 5-DSA and 16-DSA when inserted in the membrane of polymersomes[246]. When polymersomes equipped with the spin labelled OmpF-S-S-NO$^{\bullet}$ were exposed to reductive conditions (10 mM DTT), an isotropic characteristic EPR spectrum (a_N = 15.9 G) superposed on the broad peak was obtained. The isotropic spectrum indicates a successful cleavage of the nitroxide spin probe from the OmpF, whilst the broad EPR component resulted from a fraction of spin label cleaved and located in the polymersome membrane, with the nitroxide polar group pointing towards the environment (Figure 38c).

4.4 FUNCTIONAL CHARACTERSIATION OF REDUCTION TRIGGERED BIOMIMETIC CATALYTIC NANOCOMPARTMENTS

The functionality of the HRP-loaded polymersomes equipped with OmpF-S-S-CF in response to external stimuli was assessed before and after the addition of 30 mM GSH, by following the fluorescent signal associated with conversion of Amplex Ultra Red to theResorufin-like product (RLP) during the *in situ* enzymatic reaction of HRP[247]. Enzymatic turnover of the AR substrate was reduced for HRP-loaded polymersomes equipped with OmpF-S-S-CF - 36±4% relative activity compared to HRP-loaded polymersomes equipped with OmpF-SH. The very low activity of HRP-loaded polymersomes without OmpF was taken into account for a background correction. The reduced activity of HRP-loaded polymersomes equipped with OmpF-S-S-CF suggests that this molecular cap is sufficient to reduce the passage of small molecules through the pore. The addition of 30 mM GSH to the system increased the activity of HRP-loaded polymersomes equipped with OmpF-S-S-CF equal to that of HRP-loaded polymersomes equipped with OmpF-SH. Therefore, in the presence of GSH the reduction of the disulphide bridge between the attached SAMSA-CF cap and cysteine residues of the OmpF-M successfully restored the OmpF-M pore permeability to the substrate of the enzyme by releasing the cap from the pore. (Figure 38D, Figure S27, SI).

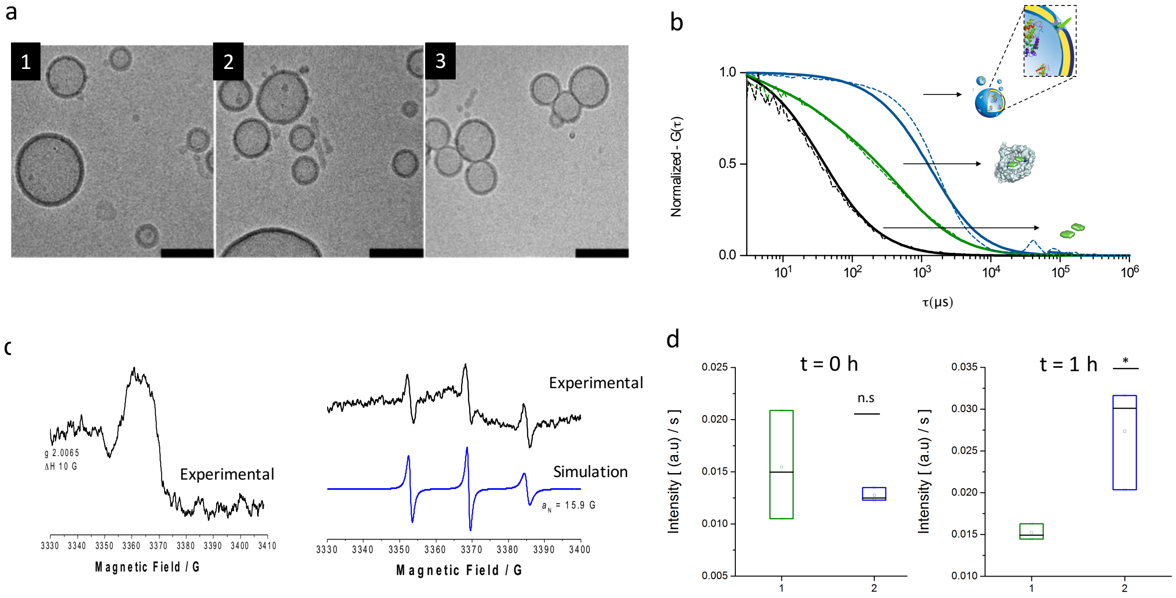

Figure 38. **Characterisation of stimuli-responsive catalytic nanocompartments** Panel a.) Cryo-TEM micrographs of: (1) Polymersomes loaded with HRP and equipped with OmpF-S-S-CF, (2) polymersomes loaded with HRP and equipped with OmpF-SH, and (3) polymersomes loaded with HRP without OmpF. Scale bar = 100 nm. Panel b.) Normalised FCS autocorrelation curves of SAMSA-CF in PBS (Black), and OmpF-S-S-CF in the membrane of polymersomes (Blue). Dotted line = experimental auto correlation curves, solid line = fitted curve. Curves normalized to 1 to facilitate comparison. Panel c.), left panel: EPR spectrum of bis-(2,2,5,5-Tetramethyl- 3-imidazoline-1-oxyl-4-yl)disulfide labelled OmpF reconstituted in PMOXA$_6$–PDMS$_{44}$–PMOXA$_6$ polymersomes (black line). Panel C, right panel: 3-imidazoline-1-oxyl-4-yl)disulfide labelled OmpF reconstituted in PMOXA$_6$–PDMS$_{44}$–PMOXA$_6$ polymersomes and incubated with 10mM DTT experimental (black line) and simulated (blue line). Panel d.) Enzymatic activity of HRP-loaded polymersomes: OmpF-S-S-CF equipped polymersomes (green, left panel), OmpF-SH equipped polymersomes (blue, left panel), OmpF-S-S-CF equipped HRP-loaded polymersomes (green, right panel), OmpF-

SH equipped HRP-loaded polymersomes (blue, right panel). Left panel: Directly after addition of 30mM GSH, Right panel: 1 hour after addition of 30 mM GSH.

4.5 STIMULI-RESPONSIVE ARTIFICIAL ORGANELLES

Previously designed catalytically active $PMOXA_{12}$–$PDMS_{56}$–$PMOXA_{12}$ polymersomes as artificial peroxisomes by our group successfully overcame the first barrier of cell membranes and escaped from endosomes[5]. Here one step further is achieved by developing a triggered AO system, whose functionality is modulated by the responsive OmpF porins. Several PMOXA-*b*-PDMS-*b*-PMOXA based polymersomes have already shown high cytocompatibility in various cell lines [5,7]. In order to study the intracellular activation and enzymatic activity of AOs, the cytocompatibility was evaluated, by testing their cellular toxicity using the 3-(4,5-dimethylthiazol-2-yl)-5-(3-carboxymethoxyphenyl)-2-(4-sulfophenyl)-2H-tetrazolium (MTS) assay. Notably, the AO did not show any decrease in cell viability in HeLa cells even after 48h (i.e. polymer concentration ranging from 0.25-0.75 mg ml^{-1}), confirming biocompatibility of these AOs at the cellular level (Figure S29, SI).

In order to study cellular internalisation and intracellular localization of polymersomes, polymersomes equipped with OmpF-S-S-CF, and polymersomes equipped with OmpF-SH, HRP conjugated with Atto-488 (HRP-Atto488) was encapsulated inside the cavity (Figure S30, SI). Cellular uptake assays in HeLa cells indicated successful internalization resulting in a particulate intracellular staining pattern with increasing intensity in a time dependent manner from 8 up to 24h (Figure 9a, Figure S31, Figure S32). After 24 h AO did not colocalize with early endosomes (PCC=0.101 ± 0.028; M1=0.026 ± 0.008, M2=0.003 ± 0.001; Costes=0.047 ± 0.017) or lysosomes (PCC=0.214 ± 0.015; M1=0.029 ± 0.010, M2=0.010 ± 0.005; Costes=0.037 ± 0.008), confirming a successful intracellular endosomal escape (Figure S12, SI) (Figure S33, SI). Localized HRP-Atto488 signals confirmed the intracellular integrity of polymersomes. In sharp contrast, if cells were treated by with a membrane disrupting agent (i.e. 0.1 % saponin) (Figure S34, SI), polymersomes were destroyed resulting in an intracellular cytoplasmic distribution of HRP-Atto488.

The capacity of the AOs to act within target cells in a stimuli-responsive manner was investigated by a combination of confocal laser scanning microscopy (CLSM) and flow cytometry. Thus, it was thus possible to evaluate the potential of AOs to respond to increased intracellular GSH levels. HeLa cells were incubated with HRP-loaded polymersomes without OmpF or HRP-loaded polymersomes equipped with either OmpF-S-S-CF or OmpF-SH to promote cellular uptake. Extracellular polymersomes were removed by washing before imaging the intracellular activity of AO. Cells were incubated with a 1:1 substrate mixture of H_2O_2 and AR to allow the intracellular deposition and finally the conversion of AR into its RLP by AO. In contrast to control cells, or those incubated with HRP loaded polymersomes without OmpF, a significant increase of intracellular fluorescence was observed with AOs equipped with OmpF-S-S-CF or OmpF-SH (Figure 39b, Figure S35). The same trend was observed when AR turnover was quantified by flow cytometry (Figure S36). The strong fluorescent signal for OmpF-S-S-CF equipped, HRP loaded polymersomes confirmed successful intracellular cleavage of the molecular cap. Thus, AOs were successfully activated within the intracellular environment of the target cells through reductive opening of the OmpF pores.

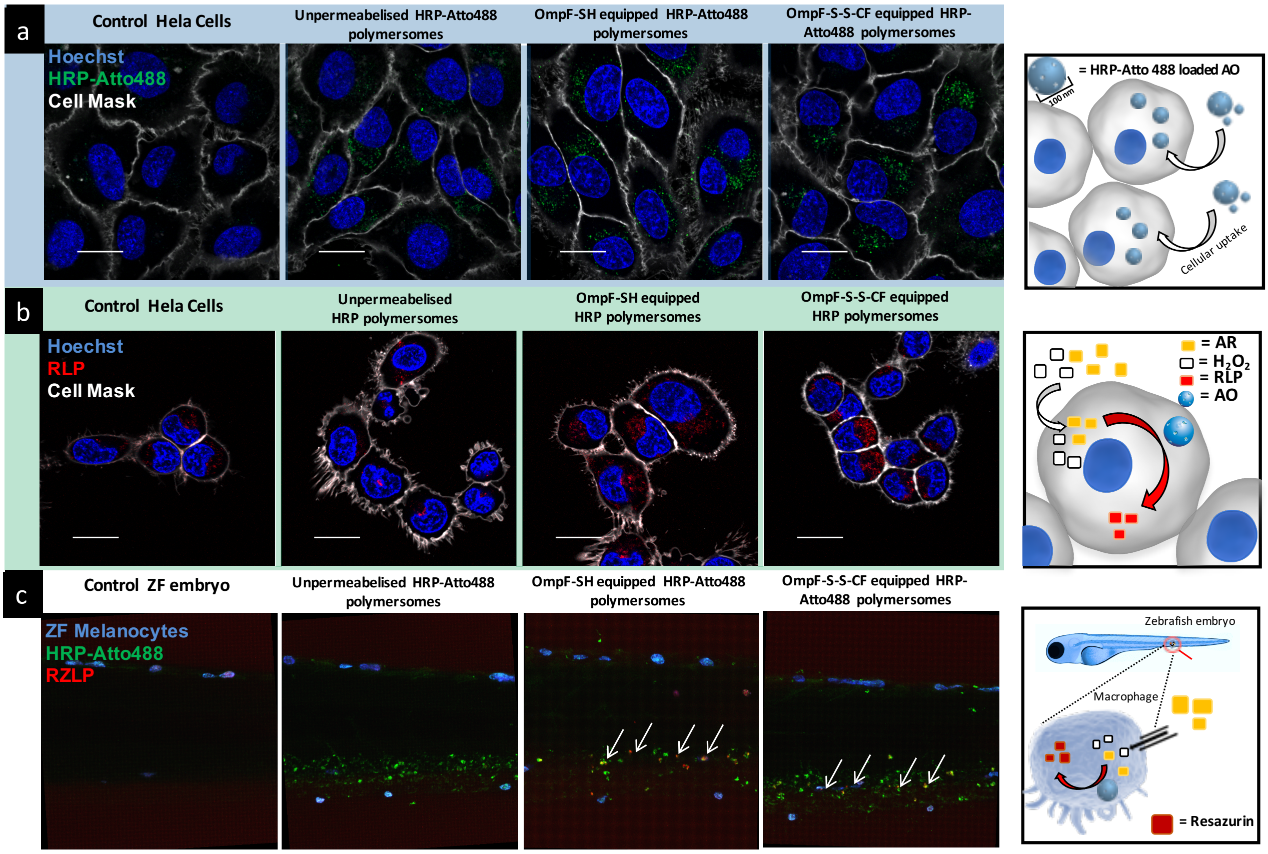

Figure 39. Cellular uptake, intracellular activation and *in vivo* activity of AOs.

Panel a: Confocal fluorescence micrographs of Hela cells showing cellular uptake of AOs loaded with fluorescently labelled HRP. Scale bar: 10μm

Panel b: Cellular uptake and intracellular activation of enzyme loaded AOs Blue signal: Hoechst 33342 nucleus stain. Grey signal: CellMask Deep Red-Plasma membrane stain. Green signal: Atto-488 HRP. Red signal: Resorufin like product (RLP). Scale bar 20μm

Panel c: *In vivo* ZFE biodistribution and activity of AOs – lateral view of the ZFE cross-section. Blue signal: ZFE melanocytes. Green signal: HRP-Atto488. Red signal: Resazurin like product (RZLP). Arrows show regions of enzymatic activity of AOs.

As a step further, the AOs in the present study were evaluated *in vivo* in the zebrafish embryo (ZFE) model to assess their safety and tolerability and to get a first insight into their performance *in vivo*. ZFEs were selected due to their recognition as a complimentary vertebrate animal model for applications such as compound screening in drug discovery, toxicological studies and recombinant disease models [248] [249] [250]. Due to their optical transparency, ZFEs open the possibility of imaging fluorescently-tagged objects and fluorescent processes *in vivo* at a high resolution over time [251] (Figure S37, SI). In order to follow the biodistribution of AOs, HRP-Atto488 loaded polymersomes with membranes without or with either OmpF-S-S-CF or OmpF–SH were injected intravenously into ZFE via the duct of Cuvier. No acute toxicity such as change in behaviour i.e. mobility, seizures, heart failure or other toxic effects such as malformations, denaturation of tissue fluids or yolk mass was observed in ZFE injected with AOs after 24h. ZFE analysed two hours post intravenous injection of all types of AOs containing Atto-488 conjugated HRP, showed a distinct fluorescent staining pattern (Figure S38, SI) in the posterior cardinal vein region of ZFE. The recognition of polymersome based AOs by the ZFE immune system was confirmed by the colocalization of AOs loaded with Atto647 conjugated HRP (Atto647-HRP) injected into transgenic ZFE specifically expressing eGFP in macrophages[252]. (Figure S30, S39, SI). In strong contrast to AOs loaded with Atto647-HRP, the free Atto647-HRP enzyme did not show significant macrophage colocalisation after 24h, even when Atto647-HRP was injected at concentrations of 0.2 mg ml^{-1}. In order to assess *in vivo* stability, integrity, and functionality of AOs when exposed to the conditions in the macrophage microenvironment, a second injection of AOs together with the enzyme substrate Amplex Ultra Red (AR) was performed. Injection of the co-substrate H_2O_2 in combination with AR was not necessary, since macrophages have the ability of producing H_2O_2. In addition, coinjection of H_2O_2 resulted in a red colouring of the whole blood volume, presumably due to haemolysis and thus interaction of AR with erythrocyte enzymes or haemoglobin [253] (Figure S40, SI). In these experiments, distinct colocalization within macrophages of the converted AR oxidation product was found only for HRP-Atto488 loaded AOs equipped with either OmpF-SH or OmpF-S-S-CF. This showed that the molecular cap of OmpF-S-S-CF is cleaved *in vivo* leading to activation of the catalytic AOs. In sharp contrast, HRP-Atto488 loaded polymersomes without OmpF remained inactive demonstrating that the polymersome membrane is robust enough to stay intact in ZFE macrophages (Figure 39C).

4.6 CONCLUSION

The bioinspired strategy of creating AO presented here is based on incorporation of stimuli-responsive SAMSA-CF modified OmpF in the membranes of PMOXA-*b*-PDMS-*b*-PMOXA polymersomes. The stimuli-responsive modification of OmpF acts as an efficient strategy to include life-like responsiveness in the synthetic polymersome membranes and allows the biomolecules (HRP) encapsulated in the polymersome cavity to fulfil their catalytic role only when the protein gate is open. By micking the dynamic processes present in membranes of cellular organelles, such as the mitochondria, this shows that the developed system can act as an artificial organelle (AO) once it reaches the cellular microeinvironment. Using the vertebrate zebrafish embryo model *in vivo* tolerability was proven along with a successful preservation of the AOs architecture and *in situ* regulation of the encapsulated enzymes activity. Developments in the design of AOs with triggered activity, such as the system presented here, results in nanoscale reaction spaces with functionality modulated in an analogous manner to that of cell membranes, and represent a necessary step towards the creation of artificial cells.

Chapter 5.

5. CONCLUSIONS AND OUTLOOK

5.1 CONCLUSION

Bioinspired approaches of modifying properties of synthetic materials by their combination with biomolecules, such as the combination of polymeric supramolecular nanoarchitectures with proteins, DNA or polysaccharides, serve to design new hybrid materials that mimic structures and processes found in living organisms. Compared to entirely synthetic materials, biomimics possess new properties, like an enhanced catalytic activity or selective responsiveness to changes in their environment, while retaining the robustness of their synthetic backbone.

This thesis focused on biomimetic engineering of colloidal polymer supramolecular nanoarchitectures, namely soft nanoparticles and polymersomes. In this regard different approaches of biomimetic engineering have been applied in order to demonstrate controlled enzyme localisation of proteins on PEG-PMCL-PDMAEMA soft nanoparticles for the design of a smart protein delivery agent, controlled transport of enzymatic substrates through the membranes of enzyme loaded PMOXA-*b*-PDMS-*b*-PMOXA polymersomes for the design of triggered catalytic compartment and finally *in vitro and in vivo* validation of controlled transport of enzymatic substrates through the membrane of enzyme loaded PMOXA-*b*-PDMS-*b*-PMOXA polymersomes equipped with a chemically and genetically modified OmpF.

In the following paragraphs the most important results of chapters 2, 3 and 4, along with the conceptual contribution of the individual chapters to nanosciences and the further development of biomimetic engineering of nanoarchitectures are concluded.

Chapter 2 demonstrates how nanoparticles self-assembled from asymmetric PEG-*b*-PMCL-*b*-PDMAEMA copolymers can be biomimetically engineered by controlled attachment of proteins on their polymeric corona. By applying characterization methods, the biomimetically engineered nanoparticles are shown to possess a well-defined morphology, specific protein localization and a pH responsive protein release behavior. We demonstrate that the ability of nanoparticles to attach and release proteins is a direct result of electrostatic interactions between the positively charged PDMAEMA domain and negatively charged protein biomolecules. The process of protein attachment and release through electrostatic interactions does not appear to interact with functional properties of the immobilized protein biomolecules. Once self-assembled in solution, the hybrid system shows low toxicity at therapeutic concentrations and can be taken up by human epithelial HeLa cells. These findings implicate, that the nature of PEG-*b*-PMCL-*b*-PDMAEMA nanoparticles opens a new possibility of responsive biomimetic modification through electrostatic interactions. In the future, the approach of modifying PEG-*b*-PMCL-*b*-PDMAEMA nanoparticles with negatively charged proteins presented in this study could be extended to other therapeutic proteins, such as insulin, DNA/RNA/mRNA or negatively charged polysaccharides.

In chapter 3, the concept of biomimetically engineering colloidal polymer nanoarchitectures was extended to PMOXA-*b*-PDMS-*b*-PMOXA polymersomes. In contrast to the electrostatic attachment of enzyme biomolecules on the corona of polymer nanoparticles described in Chapter 2, here a model enzyme horseradish peroxidase is encapsulated in the inner aqueous cavities of polymersome nanocompartments. Permeability of the polymersome membrane and thereby access of small molecular weight molecules to the the encapsulated enzyme is achieved by the functional reconstitution of OmpF in polymersome membranes. In order to develop a pH responsive catalytic nanocompartment, we investigated how a chemical modification, done on key amino acids located at the constriction site of OmpF, blocks the OmpF pore and introduces a selective pH triggered permeability. Once reconstituted in biomimetically engineered catalytic nanocompartments, this pH responsive behavior of OmpF affects the enzymatic activity of the encapsulated enzyme. This chapter demonstrates, how a combination of synthetic polymersomes, a catalyst and a modified membrane protein can be used to design biomimics that can provide desired catalytic activity that can act on demand.

Chapter 4 builds on the knowledge of engineering biomimetic colloidal nanoarchitectures acquired in Chapters 2 and 3, with the purpose of designing a functional artificial organelle. Since artificial organelles need to mimic the natural compartmentalization found in cells, we decided to build a polymersome based biomimetic system by advancing the one designed in Chapter 3. In order to allow the catalytic polymersome nanocompartments to interact with cytoplasmic signaling molecules, we equipped polymersome membranes with a genetically and chemically modified OmpF. Two cysteine residues, replacing amino acids K89 and R270, were introduced at the rim of the OmpF pore opening the possibility to limit the pore permeability by binding molecular caps through disulfide bonds. Functional reconstitution of the modified OmpF pore allowed us to build a catalytic nanocompartment with a functionality that can be modulated by the intracellular glutathione and redox potential. Once the system was fully characterized in terms of structure and function, we showed that our biomimetically designed AO can reach and function inside cells. Furthermore, we demonstrated their applicability and function *in vivo* in zebrafish embryos. This proof of concept demonstrates that life-like nanostructures with *in vivo* and *in cellulo* functionality can be designed by taking a biomimetic path in designing novel nanoscale architectures. These findings represent a new powerful approach for enzyme therapy, and the design of artificial cells.

5.2 OUTLOOK

The bioinspired strategies applied to develop biomimeitc nanoarchitectures presented in this thesis have important implications for future development of nano-scale biomimetical engineering. First – the developed biomimics serve as proof of concepts, they demonstrate that biomimetically engineered nanoarchitectures have a tremendous translational value in fields such as medicine and technology. Novel systems could in the future be fine tuned to develop patient tailored therapeutic and diagnostic agents or to serve as the first artificial cell implants. Second – by studying the interactions between synthetic systems and biomacromolecules we deepend our understanding of the fundamental principles of self-assembly. This is important as it not only allows us to better understand evolution of non-living systems to living, but also to make use of this knowledge in the design of future custom made biomimics that could serve very specific applications. Finally – the work highlights the importance of a multidisciplinary approach and teamwork. As demonstrated by the diverse backgrounds of scientists, that have helped to design the biomimetic nanoarchitectures presented in this thesis, upcoming biomimetically engineered nanoarchitectures will without doubt require the combined knowledge of fields such as syntetic chemistry, biology, pharmaceutical sciences, biophysics, nanotechnology and many others.

5.3 AUTHORS COMMENT

Despite the tremendous technological, biomedical, and environmental applications of nanoscale biomimetical engineering, the real importance of working in natural sciences is the realization that, in our day and age, science is just incredibly addictive. I suppose that discovering new things has always been fulfilling, even centuries ago, hence the human progress. New discoveries spark a craving for more and more knowledge. However, what makes our time so special is that we are able to rationally understand how little we actually know about the world that surrounds us, which opens unlimited possibilities for new discoveries and innovation. Nowadays, scientific knowledge progresses with astonishing speed and discoveries on the nanoscale level are just beginning to scratch the surface of how the world that surrounds us functions. Not only does that help us understand what is happening around us, it also enables us to design new materials by modifying what nature already created. Richard Feynman's quote "There is plenty of room at the bottom" has never been more relevant as it is today. Moreover, the space is there for us to be filled with new materials and molecular systems. In the end, I guess this is what makes me so happy about being a scientist.

Chapter 6.

MATERIALS AND METHODS

6.1 MATERIALS

All chemicals and solvents were purchased from Sigma-Aldrich or Fluka (Sigma Chemical Co., US) and used as received, unless otherwise stated.

6.2 METHODS: CHAPTER 2

SYNTHESIS OF PEG-*b*-PMCL-*b*-PDMAEMA TRIBLOCK COPOLYMERS

PEG-b-PMCL-PDMAEMA triblock copolymers were synthesized according to the procedure described by Matter et al. [194], by using poly (ethyleneglycol) monomethylether (mPEG) with a molar mass of 2000 Da (Aldrich), copper (I) chloride (Reagent plus > 99 %, Sigma Aldrich), N, N, N′, N″, N″-pentamethyldiethylenetriamine (PMDETA) (> 99%, Aldrich), THF (Fluka), methanol, 2-bromoisobutyrylbromide (BIBB > 98%, Sigma Aldrich), triethylamine (> 99.5%, Fluka) and dichloromethane (Baker, HPLC grade).

SELF-ASSEMBLY OF PEG-B-PMCL-B-PDMAEMA TRIBLOCK COPOLYMERS

Supramolecular assemblies of PEG-*b*-PMCL-*b*-PDMAEMA triblock copolymers were prepared by the co-solvent method[194]. Block copolymer was dissolved in ethanol, and then a phosphate buffer saline solution (PBS) was added drop-wise to produce a copolymer concentration of 5 mg mL^{-1}. The average size of the self-assembled nanoparticles was reduced by repeated extrusions (9 times) through filters (0.4 μm pore diameter) using a mini extruder from Avanti-Polar Lipidics Inc. Biomolecule-copolymer assemblies were prepared in a similar manner. The block copolymer was dissolved in ethanol, and then a solution of the biomolecule (BSA or ASM) in PBS at physiological pH was added drop-wise to the copolymer solution to reach a copolymer concentration of 5 mg mL^{-1}, and a biomolecule concentration of 0.058 mg mL^{-1}. The final mixture was stirred overnight at room temperature and then dialyzed for 48 h in buffer, changing the buffer (pH = 7.2) 6 times in order to remove protein excess.

LIGHT SCATTERING

Dynamic light scattering (DLS) and static light scattering (SLS) were measured using an ALV laser goniometer with a linearly-polarized He-Ne laser operating at a wavelength of 632.8 nm (JDS Uniphase). Copolymer solutions were maintained at a constant temperature of 20 ± 0.1 °C. Measurements were carried out by varying the scattering angle (θ) from 30 to 150° in 10° steps. The viscosity of the solutions was assumed equal to that of pure water at 20 °C ($\eta = 1.0$ cP). The time correlation function $G(t)$ was determined with an ALV/LSE-5004 correlator. Diffusion coefficients at zero deviation (D_0) were evaluated from $G(t)$ using both nonlinear decay-time analysis and the Laplace inversion method (CONTIN).

TEM

TEM micrographs were obtained with a Phillips EM400 electron microscope operating at 100 kV. Nanoparticles were negatively stained by adding 5 μL of 2 % uranyl acetate solution and deposited on a carbon-coated copper grid. Excess uranyl acetate was removed under vacuum.

CRYOGENIC-TEM

Nanoparticle suspensions in buffer (10 mM PBS, pH 7.2, 50 mM NaCl) (1 mg mL^{-1}) were deposited on glow-discharged carbon grids (Quantifoil, Germany) and blotted before quick-freezing in liquid ethane using a Vitribot plunge-freezing device (FEI Co.). The grids were stored in liquid nitrogen before transferring them into a cryo-holder (Gatan). Imaging was performed on a Philips CM200 FEG TEM at 200 kV accelerating voltage in low-dose mode with a defocus value of about -4 μm

FLUORESCENCE CORRELATION SPECTROSCOPY

FCS was performed with a Zeiss LSM 510-META/Confcor2 laser-scanning microscope equipped with an Ar laser (488 nm) and a 40× water-immersion objective (Zeiss C/Apochromat 40X, NA 1.2), with the pinhole adjusted to 70 μm. Solutions of copolymers (5 mg/ml) with entrapped protein (BSA-FITC, $\lambda_{excitation}$ 495 nm) or enzyme (o-ASM, $\lambda_{excitation}$ 496 nm) were measured at room temperature in special chambered quartz-glass holders (Lab-Tek; 8-well, NUNC A/S), which provide optimal conditions for measurement while reducing evaporation of the solutions. Intensity fluctuations were analyzed using an autocorrelation function with the LSM 510/Confocor software package (Zeiss, AG). Spectra were recorded over 10 s, and each measurement was repeated ten times; results are reported as the average of three independent experiments. Adsorption and bleaching effects were reduced by exchanging the sample droplet after 2 minutes of measurement. The excitation power of the Ar laser was P_L = 200 mW, and the excitation transmission at 495 nm was 25 %. To reduce the number of fitting parameters, the diffusion times for free labeled protein (τ_D BSA-FITC = 82 μs) and for free labeled enzyme (τ_Do-ASM = 126μs) were independently determined, and fixed in the fitting procedure.

Experimental auto correlation curves were fitted using a one-component (EQ1) or two-component model (EQ2) including triplet state:

$$EQ1 : G(\tau)_{fit} = 1 + (1 + \frac{T}{1-T} e^{-\frac{\tau}{\tau trip}}) \frac{1}{N} \left[\frac{1}{1+\frac{\tau}{\tau D}} \frac{1}{\sqrt{1+R^2 \frac{\tau}{\tau D}}} \right]$$

EQ2: $G(\tau)fit = 1 + \left(1 + \frac{T}{1-T} e^{-\frac{\tau}{\tau trip}}\right) \frac{1}{N} \left[\frac{f_1}{1+\frac{\tau}{\tau D1}} \frac{1}{\sqrt{1+R^2 \frac{\tau}{\tau D1}}} \right] + \left(1 + \frac{T}{1-T} e^{-\frac{\tau}{\tau trip}}\right) \frac{1}{N} \left[\frac{f_2}{1+\frac{\tau}{\tau D2}} \frac{1}{\sqrt{1+R^2 \frac{\tau}{\tau D2}}} \right]$

τ_D represents the diffusion time, T the fraction of fluorophores in triplet state with triplet time τ_{trip}, N is the number of particles and R the structural parameter. R and τ_D of free dye were determined independently, and subsequently fixed in the fitting procedure.

CELL TOXICITY ASSAY

The [3-(4,5-dimethyl-2-yl)-5-(3-carboxymethoxyphenyl)-2-(4-sulfophenyl)-2H-tetrazolium (MTS) assay (Promega) was used to determine cell viability after treatment of cells with ABC nanoparticles. Hela cells were cultured at a density of $2.5x10^3$ cells/well in a 96-well plate. After 24 hours, the medium was removed and 100 μl aliquots containing the corresponding concentration of samples [0.5; 5 and 50 μg/ml] were added to the cell medium. Cells incubated only in medium served as controls. After 24 hours of incubation 20μl of MTS solution was added to each well. The plates were incubated for 2 hours at 37 ºC, and the absorption measured at λ = 490 nm. The quantity of formazan product as measured by absorbance at 490 nm is directly proportional to the number of living cells in culture. Absorption of cells where no nanoparticles were added served as 100 %.

CLSM ANALYSIS OF SPHINGOMYELINASE LOADED NANOPARTICLES IN HELA CELLS

HeLa cells were cultured at a density of $5x10^4$ cells per well in an 8-well Lab-Tek (NalgeNunc International, USA) for 24 h in Dulbelcco's Modified Eagle's Medium (DMEM) containing 10% fetal calf serum (FCS) growth medium to allow attachment to the surface. After attachment, the medium was removed and nanoparticles containing fluorescent labeled Sphingomyelinase (o-ASM) at a final polymer concentration of 0.05 mg/ml were incubated for an additional 24 h in DMEM growth medium. The pre-treated HeLa cells containing the o-ASM-nanoparticles were further incubated at 37 °C for 10 min with freshly prepared Deep Red (Cellmask) plasma membrane stain (5 mg ml^{-1}), and Hoechst 3342 (5 mg ml^{-1}) DNA stain. Cells washed three times with PBS were visualized with a CLSM (Carl Zeiss LSM510, Germany) equipped with a 63x water emulsion objective (Olympus, Japan). The measurements were performed in multitrack mode and the intensity of each fluorescent dye was adjusted individually: Hoechst 3342 was excited at 405 nm in channel 1, Deep Red at 633 nm in channel

2 and Alexa-488 at 488 nm in channel 3. The micrographs were recorded using Carl Zeiss LSM software (version 4.2 SP1).

FLOW CYTOMETRY ANALYSIS OF THE UPTAKE OF LABELED-SPHINGOMYELINASE LOADED NANOPARTICLES

$8x10^4$ HeLa cells were cultured in a well of a 24-well plate and cultured in DMEM containing 10% FCS for 24 h at 37 °C in a humidified CO_2 incubator. Then the medium was exchanged and polymer solution with entrapped biomolecule was added and incubated for another 24 h. Cells were washed with PBS, trypsinized, centrifuged, washed, centrifuged, suspended in PBS and put on ice. Flow cytometry was measured with a BD FACSCanto II flow cytometer (BD Bioscience, USA) using FSC and SSC detectors as well as a fluorescence channel o-ASM. A total of 10,000 events for each sample were analyzed, and data processed using Flow Jo VX software (TreeStar, Ashland, OR).

SPHINGOMYELINASE ENZYME ACTIVITY ASSAY

ASM release kinetics from PEG-*b*-PMCL-*b*-PDMAEMA nanoparticles incubated at physiological pH and acidic pH 5.5 (corresponding to lysosomal pH) were studied at room temperature. Nanoparticles containing no enzyme were served as a control for the background signal of the enzymatic assay. The enzyme kinetics of ASM was followed immediately after mixing the sample with the Sphingomyelinase Assay Kit (Abcam®) in Microtiter® 96-Well FluorescenceMicroplates (Thermo Scientific) as described by the manufacturer. $20 \mu l$ of ABC ASM-nanoparticle solution incubated at pH 5.5 or 7.4 was tansferred to $200 \mu l$ of the reaction mixture provided by the manufacturer. ASMase hydrolysed sphingomyelin to yield ceramide and phosphorylcholine, followed by hydrolysis of phosphorylcholine by alkaline phosphatase to form choline. In the next step choline is oxidized by choline oxidase to yield betaine and oxygen peroxide. In the final step horseradish peroxidase reacts H_2O_2 with 10-acetyl-3,7-dihydroxyphenoxazine (ADHP) in a 1:1 stoichiometry to generate the highly fluorescent product resorufin. The fluorescence intensity of resorurfin (λ_{ex} =530 nm, λ_{em} =580 nm), as the final reaction product was recorded using the Spectramax M5e microplate reader (Molecular Devices)

TITRATION OF NANOPARTICLES

Nanoparticles for titration were prepared by the same method used for self-assembly at pH 7.2. A Zetasizer NANO with a multi-purpose titrator MPT-2 from Malvern was used, and NaOH (0.5 M), HCl (0.5 M) and HCl (0.05 M) solutions were used to adjust the pH between 3 and 10.

DETERMINATION OF ENTRAPMENT EFFICIENCY (E.E) INSIDE NANOPARTICLES

In order to determine the entrapment efficiency by FCS, it is necessary first to calculate the average number of molecules in the confocal volume, which is obtained from the amplitude of the FCS curve. The lower the number of molecules in the confocal volume, the higher is the correlation amplitude. Therefore, the number of molecules contributing to a certain detected signal can be extracted by fitting a diffusion model to the FCS curve. Having obtained the correct number of molecules (*N*), the molecular brightness (*mB*) can be calculated as:

$$mB = \frac{count\ rate}{N\ x\ excitation\ power}$$

Using the count rate per molecule of a two component model, we determine the population of free dye or protein and the population of dye or protein containing in nanoparticles (NP):

$$N(molec/NP) = \quad V(NP) \times C \times Na$$

Where $V(NP) = 4/3\pi R_H^3$, C is the concentration (mol/L) and *Na* is Avogadro's number. *N(molec/NP)* represents the maximum number of molecules that can be entrapped in a nanoparticle.

In order to determine E.E, it is necessary to calculate the count rate per molecule of *NP* (CPM_{NP}):

$$CPM_{exp} = f_{dye}CPM_{dye} + f_{NP}CPM_{NP}$$

Entrapment efficiency is determined according to:

$$E = \frac{N(molec/NP)exp}{N(molec/NP)} x\ 100$$

Here, the term *N (molec/NP)exp* = CPM_{NP}/CPM_{dye} represents the number of molecules calculated by using the count rate per molecule of dye divided by the count rate per molecule of NP by FCS.

SPHINGOMYELINASE LABELING

A 2 mg mL^{-1} solution of Sphingomyelinase from Bacilus cerus (Sigma Aldrich) was prepared with 0.1M Na_2CO_3 buffer. 4μL of 15mM Oregon Green 488 succinimidyl ester (Life Technologies^{Tm}) in DMSO solution was added to 175μL of the enzyme solution and mixed for 1h at room temperature. The free dye was removed by size exclusion chromatography (SEC) on a Sephadex G25 (300 mm) desalting column, equilibrated with PBS.

6.3 METHODS: CHAPTER 3

OMPF EXPRESSION, EXTRACTION

The outer membrane protein F (OmpF) was expressed in BL21 (DE3) Omp8 *Escherichia coli* cells following a protocol described previously *Ref*[103] with the following modifications: During the purification OmpF was solubilized in a 3% Octyl-glucopiranoside solution (OG, Anatrace) to remove residual lipids, as described below in detail. The extracted fraction was analyzed by 12% SDS-PAGE (CBB stained) to confirm the protein purity, and the protein concentration was determined using a BCA kit (Pierce Chemical Co, Rock- ford, USA). OmpF was stored at 4ºC in 3% OG at a concentration of 1.2mg/ml for several weeks.

Under aseptic conditions, a loopful of cells from an Ampicillin resistant *E. Coli* strain BL21 stock culture that overexpressed OmpF-WT was smeared onto the surface of LB, ampicillin agar plate. After overnight incubation at 37 °C, a single colony was transferred from the plate to 10 mL of TB liquid medium with 100 mg mL^{-1}ampicillin (total 3 flasks). 3 Liters of TB medium with 100 mg mL^{-1} ampicillin was inoculated with 10 mL of the overnight culture. The optical density of the growing culture was followed by measuring the absorbance at 600 nm. When the absorbance reached an OD of 0.5, IPTG was added to a final concentration of 1 mM into each flask in order to start the expression of the OmpF gene. The bacteria were grown for 3 more hours at 37 ºC, then the *E. Coli* cells were pelleted at 7.000 x *g* for 8 min at 4 ºC. Pellets were stored at -25 ºC, and on the following day were re-suspended in 50 mL of 25 mM Tris-HCl pH 7.4. Then 10 mg DNase and 10 mg RNase were added, and the cell suspension French pressed three times at 1,000 bar. 1 mL of 20% SDS was added per 10 mL of cell suspension and incubated for 1 h at 60 ºC. The suspension was then centrifuged at 50.000 x *g* at 4 ºC. The supernatant was removed and the cell pellet incubated in 0.125% OG for 1 h. The suspension was centrifuged at 50.000 x *g* at 4 ºC. Finally, the cell pellet was re-suspended in 3% OG in 10 mM phosphate buffer and homogenized. The suspension was centrifuged at 50.000 x *g* and the protein concentration in the supernatant was determined by UV-Vis at 280 nm.

OMPF MODIFICATION BY LEVOLUNIC ACID AND CYANINE5-HYDRAZIDE

Levolunic acid was activated by sulfo/NHS and EDC (Sigma Aldrich) at pH 5.5 and then 75μL of 9.4mM activated levolunic acid was added to 600μL 1 mg mL^{-1} OmpF solution. OmpF was incubated with activated levolunic acid for 3h at pH 7.2. The OmpF-CA was immediately washed 10 times by 3% OG in PBS pH 7.2 in Amicon Ultra-0.5 mL centrifugal filters for protein purification and concentration, molecular cutoff: 30kDA (Millipore). The volume was adjusted to 475μL PBS pH 7.2 and 75μL of 877μM DMSO solution of Cyanine5-hydrazide (Cy5-hydrazide) (Lumiprobe) was added. The mixture was incubated in the dark for 24h at RT. The volume was adjusted to 1ml and the reaction mixture washed 25 times in Amicon Ultra-0.5 ml centrifugal filters with 3% OG to remove excess dye. The volume was adjusted to 500μL and the protein dialysed overnight against 1L of 0.05 % OG using Membra-Cel^{TM} dialysis membranes. The protein was dialysed for additional 4 hours against PBS pH 7.4 to further reduce the OG concentration. The protein concentration was determined by UV-Vis spectroscopy and adjusted to 0.5 mg mL^{-1} with PBS 7.4.

CARBONYLATION ASSAY OF OMPF

A commercially available protein carbonyl content assay kit (Sigma Aldrich) was used to determine the carbonyl content of OmpF subsets.

100 μL of DNPH solution provided by the manufacturer (Sigma Aldrich) was mixed with 100 μL of a subset of OmpF and incubated at room temperature for 10 min. 30 μL of 100% TCA solution was added to each sample, vortexed and incubated on ice for 5 min. The samples were centrifuged at 13,000 x *g* for 2 min and the supernatant was carefully removed. 500 μL of ice-cold acetone mixture was added to each protein pellet and incubated for 5 min on ice. The samples were then centrifuged at 13,000 x *g* for 2 min and the acetone was carefully removed together with any free DNPH. 200 μL of 6 M guanidine solution was added to the pellet to re-solubilize the protein. 100 μL of the sample was transferred to a 96-well plate and the absorbance measured at 370 nm with a Spectramax M5e microplate reader (Molecular Devices). The protein concentration was determined using a BCA protein assay kit (0.1 mg mL^{-1}). The theoretical calculation is based on the starting protein concentration of the assay (0.1 mg mL^{-1}), assuming that each monomoer has 2 accessible lysine residues.

CHARACTERISATION OF OMPF

A 20% SDS polyacrylamide gel was cast. OmpF-CA-Cy5 and OmpF-CA were mixed with BN-PAGE loading buffer and 15μL of the final OmpF solution was added to the gel. The gels were run at 300V for 6 hours.

The Native-Page image was evaluated by using the image analysis module from OriginPro 9.1 (OriginLab) to show an expected difference in band migration. The intensity per pixel was recorded along the migration lane and normalized. A Gaussian function was fitted to the data and their x-axis peak positions compared. R^2 was 0.98 for OmpF-CA-Cy5 and 0.91 for OmpF-CA, and the peak positions were 35.9 ± 0.015 and 37.7 ± 0.031.

FLUORESCENCE CORRELATION SPECTROSCOPY

All FCS measurements were carried out using the ConfoCor2 instrument (Carl Zeiss, Germany) with a HeNe laser (633nm) using a 40x, 1.2 N.A. water immersion C-Apochromat objective lens. The measurements were carried out at room temperature using a sample volume of 20μl on a covered eight-well Lab-Tek chambered borosilicate cover glass (Nalage Nunc International). Measurements were recorded over 10sec and each measurement was repeated 30 times. The structural parameter and diffusion time of the free dye (100nM Cy5-hydrazide) and measured probes were determined independently. The autocorrelation function was calculated using a software correlator and fitted with a one component fit (LSM 510 META-ConfoCor 2 System).

PREPARATION OF PH TRIGGERED CATALYTIC NANOCOMPARTMENTS

pH-responsive catalytic nanocompartments were prepared at 23 ºC from the ABA triblock copolymer, $PMOXA_6$-$PDMS_{44}$-$PMOXA_6$, $A_6B_{44}A_6$ and a subset of modified or native OmpF. The synthetic procedure and the polymer characterization are presented in [53]. pH-responsive catalytic nanocompartments were generated using the film rehydration technique in the presence of native or modified OmpF (OmpF-WT-Cy5, OmpF-WT, OmpF-CA-Cy5, OmpF-CA) in 0.05% OG. Films were rehydrated to a final polymer concentration of 5 mg mL^{-1}, HRP concentration of 0.2 mg mL^{-1}, and OmpF concentration of 80 μg mL^{-1}, respectively. Unpearmebilised polymersomes were also prepared in the absence of OmpF. Rehydrated films were stirred overnight at 23 ºC. All samples were extruded through an Avanti mini-extruder (Avanti Polar Lipids, Alabama, USA) using a 100 nm diameter pore-size polycarbonate membrane (11 times) in order to obtain size homogeneity. Non-encapsulated enzyme was removed from the catalytic nanocompartments by dialysis against PBS at pH 7.4 at RT for 5 days, exchanging the buffer every 8 hours during the day and leaving the buffer unchanged overnhight, using Spectrapore dialysis tubes, MWCO 300 kDa from Spectrum Laboratories Inc. The dialysis buffer was kept at pH 7.4 in order to maintain the hydrazine bond stability during enzyme removal. All incubation experiments and activity measurements were performed on the following day.

LIGHT SCATTERING

Dynamic and static light scattering (DLS and SLS) experiments were performed at 20 °C using an ALV/CGS–8F goniometer (Langen/Hessen, Germany) equipped with a frequency-doubled He-Ne laser (JDS Uniphase, $\lambda = 632.8$ nm). pH-responsive catalytic nanocompartments were serially diluted to polymer concentrations ranging from 0.05 mg mL^{-1} down to 0.025 mg mL^{-1}, and measured at scattering angles between 30° and 150°, with an angular step of 10°, in 10 mm diameter cylindrical quartz cells mounted in a thermostatted optical matching bath (toluene bath). The photon intensity auto-correlation function, $g^2(t)$, was determined with an ALV/LSE–5004 digital correlator. A nonlinear decay-time analysis supported by regularized inverse Laplace transform of $g^2(t)$ (CONTIN algorithm) was used to analyze the DLS data. The angle-dependent apparent diffusion coefficient was extrapolated to zero momentum transfer (q^2) using the ALV/Static and dynamic FIT and PLOT 4.31 software. Angle and concentration-dependent SLS data are presented as Guinier plots[254].

TRANSMISSION ELECTRON MICROSCOPY

Vesicle- and cell-samples containing catalytic nanocompartments for TEM imaging studies were negatively stained with 1.5% uranyl acetate solution and deposited on carbon-coated copper grids. A transmission electron microscope (Philips Morgagni 268D) at 293 K was used.

CRYOGENIC-TEM

Catalytic nanocompartment suspensions in buffer (10 mM PBS, pH 7.4, 50 mM NaCl) at high concentrations (1 mg mL^{-1}) were deposited on glow-discharged carbon grids (Quantifoil, Germany) and blotted before quick-freezing in liquid ethane using a Vitribot plunge-freezing device (FEI Co.). The grids were stored in liquid nitrogen before transferring them into a cryo-holder (Gatan). Imaging was performed on a Philips CM200 FEG TEM at 200 kV accelerating voltage in low-dose mode with a defocus value of about $-4\ \mu$m.

FLUORESCENCE CORRELATION SPECTROSCOPY

All FCS measurements were carried out using a ConfoCor2 instrument (Carl Zeiss, Germany) with a 40x, 1.2. water immersion C-Apochromat objective lens. Measurements were carried out at room temperature using a sample volume of 20 μL on a covered eight-well Lab-Tek chambered borosilicate cover glass (Nalage Nunc International). A HeNe laser was used for excitation of the Cy-5 fluorophore the 633 nm. The fluorescence signal was measured in real time and the autocorrelation function was calculated by a software correlator (LSM 510 META-ConfoCor 2 System). Measurements were recorded over 10 s and each measurement was repeated 30 times. Experimental auto correlation curves were fitted using a one-component model including triplet state:

$$G(\tau)fit = 1 + (1 + \frac{T}{1-T} e^{-\frac{\tau}{\tau trip}}) \frac{1}{N} \left[\frac{1}{1+\frac{\tau}{\tau D}} \frac{1}{\sqrt{1+R^2 \frac{\tau}{\tau D}}} \right]$$

τ_D represents the diffusion time, T the fraction of fluorophores in triplet state with triplet time τ_{trip}, N is the number of particles and R the structural parameter. R and τ_D of free dye (Cy5 – hydrazine) were determined independently, and subsequently fixed in the fitting procedure for Cy5-bound OmpF and vesicles with reconstituted OmpF.

ENZYMATIC ASSAY TMB

The final catalytic nanocompartment solutions incubated at pH 7.4 or 5.5 were added to a preprepared TMB/H_2O_2 PBS solution at pH 7.4 and measured in 96-well plates. The absorbance of each well mixture was measured with a Spectromax M5e microplate reader (Molecular Devices) at 370 nm.

The enzymatic reaction speeds of catalytic nanocompartments were determined by comparing TMB slopes of linear regions of the TMB kinetic graphs of catalytic nanocompartments as a direct measure for the relative reaction speed. The time dependence of the conversion of TMB into its first oxidation product, which absorbs at 370nm was measured at pH 7.4. Linear regression was performed using Graphpad Prism software, in order to determine the best linear section. Slopes determined from the linear regression are a direct measure of the relative reaction speed, as the difference in absorbance over time is directly liked to the difference in concentration of the first TMB oxidation product. The actual conversion rate of TMB (nmol/sec) could not be determined, as ε of the first TMB oxidation product measured at 370nm is unknown. For % of activity, slopes were compared to those for TMB conversion of OmpF-WT catalytic nanocompartments incubated at pH 5.5.

ENZYMATIC ASSAY AMPLEX RED

The emission fluorescence intensity was determined using a LS 55 Flourescence Spectrometer (Perkin Elmer). Samples containing the catalytic nanocompartments were excited at 535 nm and the emission intensity was monitored at 590 nm (15nm slits). Final catalytic nanocompartment solutions equipped with different OmpFs were adjusted to pH 5.5. Immediately and after 1 hour of incubation time, the samples were injected into a freshly prepared Amplex Red/H_2O_2 PBS solution and measured in PBS at pH 7.4. 20μl of the samples were transferred to 440μl of the reaction mixture (4.5 μM H_20_2 and 3.4 μM Amplex Red) PBS pH 7.4. Fluorescence was expressed as arbitrary fluorescence units (AU) and was measured at the same instrument setting in all experiments. The detailed procedure and calculation of enzyme kinetics are described below

HRP kinetic assays carried out with Amplex Red concentrations ranging from 0.011 to 0.41 mM provided apparent Michaelis-Menten parameters, K_m, by fitting the Michaelis-Menten equation to plots of the initial reaction rate vs. Amplex Red concentration. HRP used in our study exhibited K_m of 0.11and 0.12 mM at pH 7.4 and 5.5, respectively. These values are higher than reported for Amplex Red 0.36, and indicate a better affinity for the substrate at 7.4[255].

Conversion of Amplex red into its fluorescent product resorufin was determined by observing fluorescence intensity at pH 7.4 as a function of time. Linear regression was performed using Graphpad Prism software, in order to identify the best linear section. Similarly to the TMB assaay, slopes determined from the linear regression of Amplex red conversion are a direct measure for the relative reaction speed, as the difference in fluorescence over time is directly liked to the difference in concentration of the fluorescent resurfin. For % of activity, slopes were compared to Amplex red conversion of OmpF-WT catalytic nanocompartments.

6.4 METHODS: CHAPTER 4

OMPF EXPRESSION, EXTRACTION

The outer membrane protein F (OmpF) K89 R270 cysteine mutant and the outer membrane protein F wild type were expressed in BL21 (DE3) Omp8 *Escherichia coli* cells following a protocol described previously [234]. The detailed procedure is described in below. The extracted fraction was analysed by a 4-15% Mini-PROTEAN® TGX™ Precast SDS (Bio-Rad Laboratories, USA) gel to confirm the protein purity and the protein concentration was determined using a BCA assay kit (Pierce Chemical Co, Rock- ford, USA). OmpF was stored at 4ºC in 3% OG at a concentration of 1.2mg/ml for several weeks.

Under aseptic conditions, cells from an ampicillin resistant *Escherichia Coli* strain BL21 stock culture overexpressing the cysteine OmpF K89 R270 mutant were smeared onto the surface of LB, ampicillin agar plate. After 16h incubation at 37 °C, a single bacterial colony was transferred from the plate to 15 mL of TB liquid medium with 100 mg mL^{-1} ampicillin (total 5 flasks). 5 times 1 L of TB medium with 100 mg mL^{-1} ampicillin was inoculated with 15 mL of the overnight culture. The optical density of the growing culture was followed by measuring the absorbance at 600 nm. Once the absorbance reached an optical density (OD) of 0.6, IPTG was added to a final concentration of 1 mM into each flask in order to start the over-expression of the OmpF K89 R270 gene. Bacteria were grown for 16 more hours at 25 ºC with vigorous shaking. Then the *E. Coli* cells were pelleted at 7.000 x *g* for 8 min at 4 ºC. Pellets were stored at -25 ºC, and on the day following the harvesting re-suspended in 50 mL of 25 mM Tris-HCl at pH 7.4. 10 mg DNase and 10 mg RNase were added, and the cell suspension was french pressed five times at 1,000 bar. 1 mL of 20% SDS was added per 10 mL of cell lysate and incubated for 1 h at 60 ºC. The suspension was centrifuged at 50.000 x *g* at RT. The supernatant was removed and the cell pellet incubated in 0.125% OG for 1 h at 37ºC. The suspension was centrifuged at 50.000 x *g* at RT. Finally, the cell pellet was re-suspended in 3% n-octyl-β-Dglucopyranoside (OG) (Anatrace, USA) in 10 mM phosphate buffer and homogenized. The suspension was centrifuged at 50.000 x *g* and the protein concentration in the supernatant was determined by UV-Visible absorption spectroscpy at 280 nm.

OMPF MODIFICATION WITH SAMSA FLUORESCEIN; OMPF-S-S-CF

The OmpF K89 R270 double cysteine mutant was modified by disulphide binding of SAMSA fluorescein to the free cysteine residues. The same reaction was also performed in presence of OmpF wild type in 3% Octyl-glucopyranoside (OG) (Anatrace, USA) and 3% OG in order to serve as controls. 20μl of 959μM SAMSA-CF (5-((2-(and-3)-S-(acetylmercapto) succinoyl) amino) Fluorescein) (Thermofischer Scientific) dissolved in 5% DMSO, 1% OG in PBS buffer was added to 400μl of 0.5mg/ml OmpF and mixed. The mixture was shaken in dark conditions for 30min. After 30min, the deprotection of SAMSA-CF was initiated by adjusting the pH of the solution to pH 8.5 with 0.5M NaOH. The reaction was incubated and shaken protected from light for 24 hours at RT. After 24 hours another 5μl of 959μM SAMA fluorescein was added. 24 hours after the second addition of SAMSA fluorescein the protein was purified from the reaction mixture by washing it 25 times with 1% OG in PBS pH 7.2 in Amicon Ultra-0.5 mL centrifugal filters for protein purification and concentration, molecular cutoff: 30kDA (Millipore) (10min at 13 000 RPM). Volume was adjusted to 475μL PBS pH 7.2 and protein concentration was determined by UV-Vis spectroscopy. 40μl of the purified protein fraction was taken for FCS analysis and SDS gel electrophoresis. The volume was adjusted to 500μL and the protein was dialysed against 1L of 0.05 % OG in PBS for 16 hours and twice against PBS for 2 hours using 14kDa Membra-Cel$^{\text{TM}}$ (Carl Roth, Germany) dialysis membranes. The protein concentration was verified by UV-VIS (A280) (Thermofischer Scientific, Switzerland).

OMPF MODIFICATION WITH (BIS-(2,2,5,5-TETRAMETHYL- 3-IMIDAZOLINE-1-OXYL-4-YL)DISULFIDE); OMPF-S-S-NO*

The OmpF K89 R270 double cysteine mutant was modified by disulphide binding of (bis-(2,2,5,5-Tetramethyl- 3-imidazoline-1-oxyl-4-yl)disulfide) (Noxygen, Germany) to the free cysteine residues. The same reaction was also done in presence of OmpF wild type in 3% OG PBS and 3% OG PBS in order to serve as controls for unspecific binding of (bis-(2,2,5,5-Tetramethyl- 3-imidazoline-1-oxyl-4-yl)disulfide) to wild type OmpF and unspecific interactions with OG micelles. 20μl of dissolved (bis-(2,2,5,5-Tetramethyl- 3-imidazoline-1-oxyl-4-yl)disulfide) (1.4 mM) in 4% DMSO, 1% OG in PBS Buffer was added to 400μl of 0.5mg/ml OmpF and mixed. The reaction was shaken protected from light for 24 hours at RT. 24 hours after the second addition of (bis-(2,2,5,5-Tetramethyl- 3-imidazoline-1-oxyl-4-yl)disulfide) the conjugated protein was purified from the reaction mixture by washing it 25 times with 1% OG in PBS pH 7.2 in Amicon Ultra-0.5 mL centrifugal filters for protein purification and concentration, molecular cutoff: 30kDA (Millipore). Volume was adjusted to 475μL PBS pH 7.2 and protein concentration was determined by UV-Vis spectroscopy. 40μl of the purified protein fraction was taken for EPR analysis. The volume was adjusted to 500μL and the protein dialysed against 1L of 0.05 % OG in PBS for 16 hours and twice against PBS for 2 hours using 14kDa Membra-Cel™ (Carl Roth, Germany) dialysis membranes. The protein concentration was verified by UV-VIS (A280) (Thermofischer Scientific, Switzerland).

CHARACTERISATION OF SAMSA FLUORESCEIN CONJUGATED OMPF

A 4-12% SDS polyacrylamide gel was cast. Samples were mixed with BN-PAGE loading buffer and 15μL of the final OmpF solution was added to the gel. To show the effect of GSH, separate probes were incubated with the loading buffer supplemented with 30mM GSH. The gels were run at 200V for 45min. Gels were scanned unstained and stained with Brilliant blue.

PREPARATION OF OMPF EQUIPPED POLYMERSOMES

OmpF equipped polymersomes were prepared at RT from the ABA triblock copolymer, $PMOXA_6$-$PDMS_{44}$-$PMOXA_6$, ($A_6B_{44}A_6$) and a subset of modified or unmodified OmpF (OmpF-SH, OmpF-S-S-NO$^{\bullet}$ and OmpF-S-S-CF). The synthetic procedure and the polymer characterization are presented in [53]. Polymersomes were generated using the film rehydration technique where the polymer was dried in the presence of native or modified OmpF K89 R270 cysteine mutant (OmpF-SH, OmpF-S-S-CF or OmpF-S-S-NO$^{\bullet}$). Horseradish peroxidase (HRP), Atto-488 conjugated HRP (Atto488-HRP) or Atto-647 conjugated HRP (Atto647-

HRP) in PBS buffer pH=7.4 at RT were used as rehydration solutions. Films were rehydrated to a final polymer concentration of 2.5 mg mL^{-1}, HRP concentration of 0.2 mg mL^{-1}, and OmpF concentration of 50 μg mL^{-1}, respectively. Control polymersomes were also prepared in the absence of OmpF. Rehydrated films were stirred overnight at RT, protected from light. All samples were extruded through an Avanti mini-extruder (Avanti Polar Lipids, USA) using a 100 nm diameter pore-size polycarbonate membrane (11 times) at RT in order to obtain size homogeneity. Non-encapsulated enzyme was removed from the polymersomes by dialysis against PBS at pH 7.4 at RT for 5 days, exchanging the buffer every 3 hours during the day and leaving the buffer unchanged overnight, using Spectrapore dialysis tubes, MWCO 300 kDa (Spectrum Laboratories Inc., USA) Steps involving the generation of catalytic nanocompartments were preformed protected from light in order to avoid photodegradation of fluorophores. Incubation experiments and activity measurements were performed on the day following the last dialysis step.

LC-MS-MS

Mass spectrometry was applied in order to determine the degree of labelling of the OmpF conjugates [234]. The spectrometer consisted of a LC-MS column ReproSil-Pur C18–AQ, 1.9 µm resin Dr. Maisch GmbH, Ammerbuch-Entringen, Germany combined with a dual pressure LTQ-Orbitrap Elite mass spectrometer connected to an electrospray ion source (Thermo Fisher Scientific). The in gel digestion was based on[256]. Briefly, the band of interest was cut out of the SDS-gel and the sample was cut to tiny cubes. The coomassie blue staining was rinsed out and the protein was alkylated with iodoacetamide and digested using Trypsine. The peptides were then washed out and desalted with C18 reversed phase spin columns Microspin, Harvard Apparatus. After drying, the samples were dissolved and subjected to LC–MS analysis using a linear gradient from 95% solvent A (0.15% formic acid, 2% acetonitrile) and 5% solvent B (98% acetonitrile, 0.15% formic acid) to 28% solvent B over 40 min at a flow rate of 0.2 µl/min. The 20 most intense ions were released from the linear ion trap and subjected to a MS-MS analysis. The intensity of the mutation carrying fragment was put into relation with another fragment of the same sample to eliminate the dependence on the concentration and the ratio was then compared to the same ratio of OmpF with free thiol groups (EQ1).

Eq. 1: $\left(\frac{I_{SH-fragment}}{I_{other-fragment}}\right)_{conjugate} \Big/ \left(\frac{I_{SH-fragment}}{I_{other-fragment}}\right)_{mutant}$

For three separately measured samples a labeling degree of 96+/-4% (100%, 95%, 100%) degree of labelling of OmpF was determined for $NO^{\bullet}$ labelling and 81+/-31% (100%, 100%, 46%) for labelling with SAMSA-CF.

FLUORESCENCE CORRELATION SPECTROSCOPY

All FCS measurements were carried out using a ConfoCor2 instrument (Carl Zeiss, Germany) with a 40x, 1.2. water immersion C-Apochromat objective lens. Measurements were carried out at room temperature using a sample volume of 20 μL on a covered eight-well Lab-Tek chambered borosilicate cover glass (Nalage Nunc International, USA). An Argon 488 laser was used for excitation of the SAMSA-CF fluorophore at 488 nm (Laser power output 20%, 8mW) with the appropriate filter sets. The fluorescence signal was measured in real time and the autocorrelation function was calculated by a software correlator (LSM 510 META-ConfoCor 2 System). Measurements were recorded over 3s and each measurement was repeated 60 times. Correlation curves that could not be fitted were excluded (<10%).

For determining the binding of SAMSA-CF to OmpF-SH and the successful reconstitution of OmpF-S-S-CF into HRP loaded PMOXA-PDMS-PMOXA polymersomes, experimental auto correlation curves were fitted using a one component model including triplet state (Eq1):

$$G(\tau)_{fit} = 1 + \left(1 + \frac{T}{1-T} e^{-\frac{\tau}{\tau_{trip}}}\right) \frac{1}{N} \left[\frac{1}{1 + \frac{\tau}{\tau_D}} \frac{1}{\sqrt{1 + R^2 \frac{\tau}{\tau_D}}} \right]$$

τ_D represents the diffusion time, T the fraction of fluorophores in triplet state with triplet time τ_{trip}, N is the number of particles and R the structural parameter. R and τ_D of free dye SAMSA-CF were determined independently. Number of SAMSA-CF molecules per OmpF was determined based on the molecular brightness (CPM) of SAMSA-CF (2.2 ± 0.7 kHz) in comparison with SAMSA-CF covalently attached to OmpF K89 R270 (4.8 ± 0.6 kHz). The number of OmpF-S-S-CF monomers per vesicle was determined by comparing the molecular brightness of SAMSA-CF (2.2 ± 0.7 kHz) to the molecular brightness of OmpF-S-S-CF in 1% OG (18.9 ± 11.1 kHz), taking into consideration that every OmpF monomer is modified by two SAMSA-CF molecules.

For determining the release kinetics of SAMSA-fluorescein from OmpF-S-S-CF experimental auto correlation curves were fitted using a two-component model including triplet state (Eq. 2.):

$$G(\tau)fit = 1 + \left(1 + \frac{T}{1-T} e^{-\frac{\tau}{\tau trip}}\right)\frac{1}{N}\left[\frac{f_1}{1+\frac{\tau}{\tau D1}}\frac{1}{\sqrt{1+R^2\frac{\tau}{\tau D1}}}\right]$$
$$+ \left(1 + \frac{T}{1-T} e^{-\frac{\tau}{\tau trip}}\right)\frac{1}{N}\left[\frac{f_2}{1+\frac{\tau}{\tau D2}}\frac{1}{\sqrt{1+R^2\frac{\tau}{\tau D2}}}\right]$$

τ_D represents the diffusion time, T the fraction of fluorophores in triplet state with triplet time τ_{trip}, N is the number of particles and R the structural parameter.

R and τ_D of free dye (SAMSA-CF) were determined independently in 30mM GSH, PBS pH 7.4, and subsequently fixed in the fitting procedure in order to determine the % of free dye fraction, which represented SAMSA-CF released from OmpF-S-S-CF in 1% OG 30mM GSH, PBS pH 7.4.

EPR MEASUREMENTS OF OMPF-S-S-NO$^{\bullet}$

EPR measurements were performed on a Bruker CW EPR Elexsys-500 spectrometer equipped with a variable temperature unit. The spectra were recorded at 298 K with the following parameters: 100 KHz magnetic field modulation, microwave power 2 mW, conversion time 61.12 ms, number of scans up to 200, resolution 2048 points, modulation amplitude 0.5 G for the samples containing the free nitroxide and 1 G for the samples containing spin labeled OmpF (OmpF-S-S-NO.), sweep width 150 G. Note: the EPR spectra presented in the figures were zoomed to a maximum of 80G sweep width for better resolution of the peaks. Isotropic EPR spectra were simulated using the WINSIM (NIEHS/NIH) simulation package, while the anisotropic spectra were simulated with Bruker WinEpr SimFonia package.

For the free nitroxide spin probe (bis-(2,2,5,5-tetramethyl- 3-imidazoline-1-oxyl-4-yl) disulfide), aN values correspond to half the distance (in Gauss) between the low-field and high-field lines of the isotropic spectra (triplets).

CRYOGENIC-TEM

Polymersome suspensions in buffer (10 mM PBS, pH 7.4, 50 mM NaCl) at high concentrations (2.5 mg mL^{-1}) were deposited on glow-discharged carbon grids (Quantifoil, Germany) and blotted before quick-freezing in liquid ethane using a Vitribot plunge-freezing device (FEI Co.). The grids were stored in liquid nitrogen before transferring them into a cryo-holder (Gatan). Imaging was performed on a Philips CM200 FEG TEM at 200 kV accelerating voltage in low-dose mode with a defocus value of about -4 μm.

LIGHT SCATTERING

Dynamic and static light scattering (DLS and SLS) experiments were performed at 20 °C using an ALV/CGS–8F goniometer (Langen/Hessen, Germany) equipped with a frequency-doubled He-Ne laser (JDS Uniphase, $\lambda = 632.8$ nm). Reduction-responsive polymer nanocompartments were serially diluted to polymer concentrations ranging from 0.05 mg mL^{-1} down to 0.025 mg mL^{-1}, and measured at scattering angles between 30° and 150°, with an angular step of 10°, in 10 mm diameter cylindrical quartz cells mounted in a thermostatted optical matching bath (toluene bath). The photon intensity auto-correlation function, $g^2(t)$, was determined with an ALV/LSE–5004 digital correlator. A nonlinear decay-time analysis supported by regularized inverse Laplace transform of $g^2(t)$ (CONTIN algorithm) was used to analyze the DLS data. The angle-dependent apparent diffusion coefficient was extrapolated to zero momentum transfer (q^2) using the ALV/Static and dynamic FIT and PLOT 4.31 software. Angle and concentration-dependent SLS data are presented as Guinier plots [93].

AMPLEX ULTRA RED ENZYMATIC ASSAY

The emission fluorescence intensity was determined using a a Spectromax M5e microplate reader. Samples were incubated with a final concentration of 30mM GSH in PBS pH 7.4. The pH was kept at pH 7.4. For the measurement 10μl of the samples mixed with GSH were transferred to 220μl of the reaction mixture (4.5 μM H_20_2 and 3.4 μM Amplex Ultra Red) PBS pH 7.4. The reaction mixture was excited at 530 nm and the emission intensity was monitored at 590 nm. Fluorescence was expressed as relative fluorescence units (RFU) and was measured at the same instrument setting in all experiments.

The reacting rate at which catalytic HRP-loaded polymersomes, equipped with different OmpFs, perform in solution was studied by employing the Amplex Ultra Red enzymatic assay. Conversion of Amplex Ultra Red into its fluorescent product was determined by observing fluorescence intensity in PBS pH 7.4 as a function of time in the presence of GSH. Linear regression was performed using Origin software, in order to identify the best linear section. Substrate turnover of OmpF-S-S-CF equipped, HRP-loaded polymersomes, OmpF-SH equipped HRP-loaded polymersomes and unpermeabelized HRP-loaded polymersomes was averaged between three separately prepared samples. Slopes determined from the linear regression of Amplex Ultra red conversion are a direct measure for the relative reaction speed, as the difference in fluorescence over time is directly linked to the difference in concentration of the fluorescent product [257]. For % of relative activity, slopes were compared to Amplex Ultra red conversion of OmpF-SH catalytic nanocompartments in presence and absence of GSH. The minor decrease in total HRP substrate turnover in the presence of GSH is expected due to noncompetitive inhibiton of the enzyme and previously reported by *Ref*[258]. The significant difference between the slopes of OmpF-S-S-CF equipped HRP loaded polymersomes and OmpF-SH equipped polymersomes immediately after addition of 30mM GSH was verified by two sample t-test ($p < 0.02$, n=3).

HRP CONJUGATION WITH ATTO-488 AND ATTO-647

Atto-488 carboxylic acid succinimidyl ester (Atto-488 NHS ester) (Atto-TEC, Germany). A 0.2 mg ml^{-1} HRP solution was prepared in 0.2 M sodium bicarbonate buffer pH = 8.1. 10μL of 10mM Atto-488 NHS ester was added per 1 mL of enzyme solution. The final solution was mixed protected from light for 24h. Upon labelling the Atto-488 HRP conjugate was purified by dialysis against PBS pH 7.4 for 72 hours, exchanging the buffer 3 times daily (MWCO: 10-14 kDa). Samples were further purified using Amicon Ultra-15mL Centrifugal Filters for DNA and protein concentration (MWCO: 10kDa) (EMD Millipore, USA). Labeling was confirmed by SDS-PAGE.

Atto-647 carboxylic acid succinimidyl ester (Atto 647 NHS ester) (Atto-TEC, Germany). A 0.2mg ml^{-1} HRP solution was prepared in 0.2 M sodium bicarbonate buffer pH = 8.1. 10μL of 10mM Atto-647 NHS ester was added per 1 mL of enzyme solution. The final solution was mixed protected from light for 24h. Upon labelling the Atto-647 HRP conjugate was purified by dialysis against PBS pH 7.4 for 72 hours, exchanging the buffer 3 times daily (MWCO: 14 kDa). Samples were further purified using Amicon Ultra-15mL Centrifugal Filters for DNA and protein concentration (MWCO: 10kDa) (EMD Milipore, USA). Labeling was confirmed by SDS-PAGE.

CELL TOXICITY ASSAY OF CATALYTIC NANOCOMPARTMETNS

The [3-(4,5-dimethyl-2-yl)-5-(3-carboxymethoxyphenyl)-2-(4-sulfophenyl)-2H-tetrazolium (MTS) assay (Promega) was used to determine cell viability. Hela cells were seeded at a density of $2.5x10^3$ cells/well in a 96-well plate. Cells were cultured for 24 h in DMEM growth medium (supplemented with 10% fetal calf serum, penicillin (100 units ml^{-1}) and streptomycin (100 μg ml^{-1})). After 24 hours, the medium 100 µl aliquots containing the corresponding concentration of catalytic nanocompartments [0.25, 0.5 and 0.75 mg ml^{-1}] were added to the cell medium in triplicate. Cells incubated only in medium served as control (100%). After 24 hours of incubation 20μl of MTS solution was added to each well. The plates were incubated for 1 hour at 37°C, and the absorption was measured at λ = 490nm. The quantity of formazan product as measured by absorbance at 490nm is directly proportional to the number of living cells in culture. Absorption of cells where no formulation was added served as 100%.

FLOW CYTOMETRY ANALYSIS OF ARTIFICIAL ORGANELLE IN CELLULO ACTIVITY

HeLa cells were seeded in a well of a 24-well plate (8×10^4 cells / well) and cultured in Dulbelcco's Modified Eagle's Medium (DMEM) containing 10% fetal calf serum, penicillin (100 units ml^{-1}) and streptomycin (100 μg ml^{-1})) for 24 h at 37°C in a humidified CO_2 incubator. Then the medium was exchanged and polymersome solution was added to a final concentration of 0.5 mg ml^{-1} for another 24 h. Cells were washed 3 times with PBS, trypsinized, centrifuged, washed, centrifuged, suspended in 1ml PBS. AR/H_20_2 was added to a final concentration of 10μM. After 2 hours, flow cytometry analysis was performed using a BD FACSCanto II flow cytometer (BD Bioscience, USA). Doublets were excluded using FSC and SSC detectors, single cells were excited at 561 nm and the emission was detected in FL5 (586/15; Resorufin Channel). A total of 10'000 single cells for each sample were analyzed, and data processed using Flow Jo VX software (TreeStar, Ashland, OR).

INTRACELLULAR STABILITY OF AO

HeLa cells were seeded at a density of 3×10^4 cells ml^{-1} onto poly-D-lysine-coated glass coverslips. Cells were cultured for 24 h in DMEM growth medium (supplemented with 10% fetal calf serum, penicillin (100 units ml^{-1}) and streptomycin (100 μg ml^{-1})). After attachment to the surface, the medium was removed and catalytic nanocompartments were added to a final polymer concentration of 0.5 mg ml^{-1}. Cells were incubated for an additional 24 h in medium. Then cells were washed trice with PBS and fixed with 4% PFA for 15min. After a neutralization step using 50mM NH_4Cl, cells were either treated with PBS (control) or 0.1% Saponin for 10 min at room temperature. After additional washing steps, cell nuclei were counterstained for 10 min using Hoechst 33342 (0.5 μg mL^{-1}). Finally cells were embedded in Vectashield antifade mounting media. Confocal laser scanning microscopy was performed using an Olympus FV-1000 inverted microscope (Olympus Ltd., Tokyo, Japan) equipped with a 60x UPlanFL N oil-immersion objective (numerical aperture 1.40). Cells were excited at 405 nm (Hoechst 33342) and 488 nm (Atto488-HRP), and the fluorescence signal was collected using Kalman modus between 425-475 nm and 500-600 nm, respectively. To minimize spectral cross talk the samples were scanned using sequential mode. The laser settings were adjusted depending on the treatment. Images were processed using Fiji open source image processing package of ImageJ.

INTRACELLULAR LOCALIZATION OF ARTIFICIAL ORGANELLES

HeLa cells were seeded at a density of $3x10^4$ cells/well onto poly-D-lysine-coated glass coverslips. Cells were cultured for 24 h in DMEM growth medium (supplemented with 10% fetal calf serum, penicillin (100 units ml^{-1}) and streptomycin (100 μg ml^{-1})) to allow attachment to the surface. After attachment, the medium was removed and catalytic nanocompartments were added to a final polymer concentration of 0.5 mg ml^{-1}. For images taken of non fixated cells after 24h, the cells were washed trice with PBS and imaged directly. For fixated cells, after 24 h cells were washed trice with PBS and then fixed for 15 min using 4% PFA. After a neutralization step using 50 mM NH_4Cl cells, cells were incubated with either rabbit polyclonal anti-EEA1 (ab2900, Abcam) or anti-LAMP1 (ab24170, Abcam) antibody (1:1000) for early endosome or lysosome staining, respectively[7]. The cells were washed with PBS, followed by staining with the secondary goat anti-rabbit polyclonal Dylight633-labelled antibody (1:1000; #35562, ThermoFisher Scientific). Cell nuclei were counterstained for 10 min using Hoechst 33342 (0.5 μg ml^{-1}). Finally, cells were embedded in Vectashield antifade mounting media. Confocal laser scanning microscopy was performed using an Olympus FV-1000 inverted microscope (Olympus Ltd., Tokyo, Japan) equipped with a 60x UPlanFL N oil-immersion objective (numerical aperture 1.40). Z-stacks were taken using Kalman modus and a step size of 450 nm. Cells were excited at 405 nm (Hoechst 33342), 488 nm (Atto488-HRP), and 633 nm (Early Endosome/Lysosome). The fluorescence signal was collected between 425-475 nm, 500-600 nm and 655-755 nm, respectively. To minimize spectral cross talk the samples were scanned using sequential mode. Images were processed using Fiji open source image processing package of ImageJ and Imaris image analysis software.

Colocalization of polymersomes with markers of early endosome (EEA1) or lysosome (LAMP1) were carried out using JaCoP plug-in in Fiji. Pearson's correlation coefficient (PCC), Mander's coefficients (M1/M2, using thresholds of A=200 and B=180) and Costes' randomization based colocalization (200 randomization rounds) were used to assess extend of colocalization [259].

CELLULAR ACTIVITY OF ARTIFICIAL ORGANELLES BY CLSM

HeLa cells were cultured at a density of 3×10^4 cells per well in an 8-well Lab-Tek (NalgeNunc International, USA) for 24 h in DMEM growth medium (supplemented with 10% fetal calf serum, penicillin (100 units ml^{-1}) and streptomycin (100 $\mu g\ ml^{-1}$) to allow attachment to the surface. After attachment, the medium was removed and catalytic nanocompartments were added to a final polymer concentration of 0.25mg ml^{-1}. Cells were incubated for an additional 24 h in medium. After 24 h cells were washed twice with PBS, and AR/H_2O_2 were added in the ratio of 1:1 to a final concentration of 10μM. After 30min, cells washed three times with PBS. Cell nuclei were counterstained for 10 min using Hoechst 33342 (0.5 $\mu g\ ml^{-1}$). Cells were washed twice with D-PBS and cultured in DMEM. CellMask Deep Red Plasma membrane stain (0.5 $\mu l\ ml^{-1}$) was added and cells were analyzed after 5 min. Confocal laser scanning microscopy was performed using an Olympus FV-1000 inverted microscope (Olympus Ltd., Tokyo, Japan) equipped with a 60x UPlanFL N oil-immersion objective (numerical aperture 1.40). Cells were excited at 405 nm (Hoechst 33342), 559 nm (RLP), and 635 nm (CellMask Deep Red Plasma membrane stain) and the fluorescence signal was collected between 425-475 nm, 575-620 nm, and 655-755 nm, respectively. To minimize spectral cross talk the samples were scanned using sequential mode. The laser settings for RLP, the photomultiplier tube gain, and the pinhole settings were kept constant during the analysis. Images were processed using Olympus FluoView software (v3.1, Olympus).

IN VIVO ACTIVITY OF ARTIFICIAL ORGANELLES

Standard zebrafish embryo (ZFE) culture medium at pH 7.4 was prepared at final concentrations of 5 mM sodium chloride, 0.25 mM potassium chloride, 0.5 mM magnesium sulfate, 0.15 mM potassium dihydrogen phosphate, 0.05 mM sodium phosphate dibasic, 0.5 mM calcium chloride, 0.71 mM sodium bicarbonate, and 0.001 % (w/v) methylene blue.

Collected eggs from adult ABC/TU ZFE (Wildtype) and EGFPs843 ZFE (GFP-macrophage line) were kept in ZFE culture medium at 28°C. PTU (0.03 mg ml^{-1}) was added 1-day post fertilization (dpf) in order to avoid pigment cell formation. Three different enzyme loaded polymersomes were injected into 2 dpf ZFE according to an adapted protocol originally designed for microangiography. ZFE were anesthetized using 0.01% tricaine (w/v) and casted into 0.3% (w/v) agarose containing the same amount of tricaine. Immobilized ZFE were injected with either with 3 nL of 0.2 mg ml^{-1} free HRP or 3 nL AO solution (5mg ml^{-1}), removed from the agarose and kept in ZFE culture medium containing PTU for 24 hours. Then, a second injection of 1 nL AR (78μM) was performed following the same procedure. As control experiments, ZFE were injected with the enzymatic substrate AR and AR mixed with H_2O_2 without previous AO injection. Fluorescence imaging of injected ZFE was performed using an Olympus FV1000 confocal microscope (Olympus Schweiz AG, Volketswil, Switzerland). ZFE were excited at 488 nm (Atto 488 HRP), 559 nm (Melanocytes), and 635 nm (Resazurin like product) and the fluorescence signal was collected between 500-530 nm, 575-620 nm, and 655-755 nm, respectively.

Chapter 7.

APENDIX – SUPPLEMENTARY INFORMATION

7.1 Chapter 2

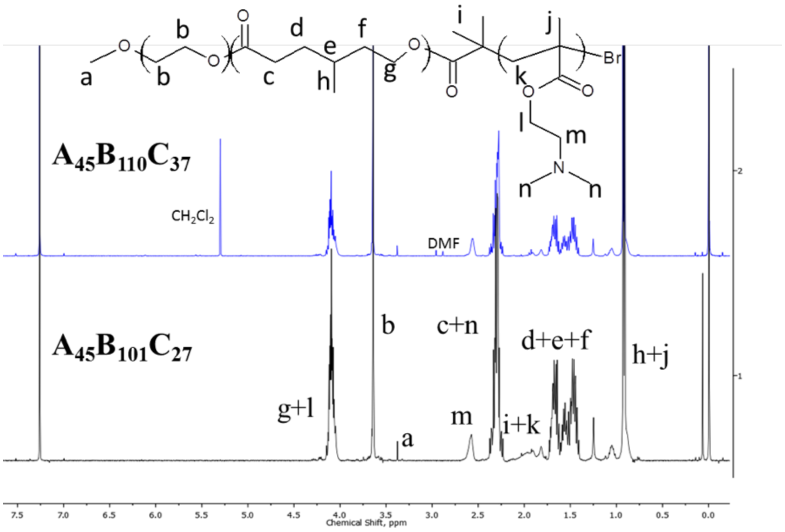

Figure S1. **^{1}H NMR spectra of ABC tri-block copolymers.** Blue line $A_{44}B_{110}C_{37}$, Black line: $A_{45}B_{101}C_{27}$

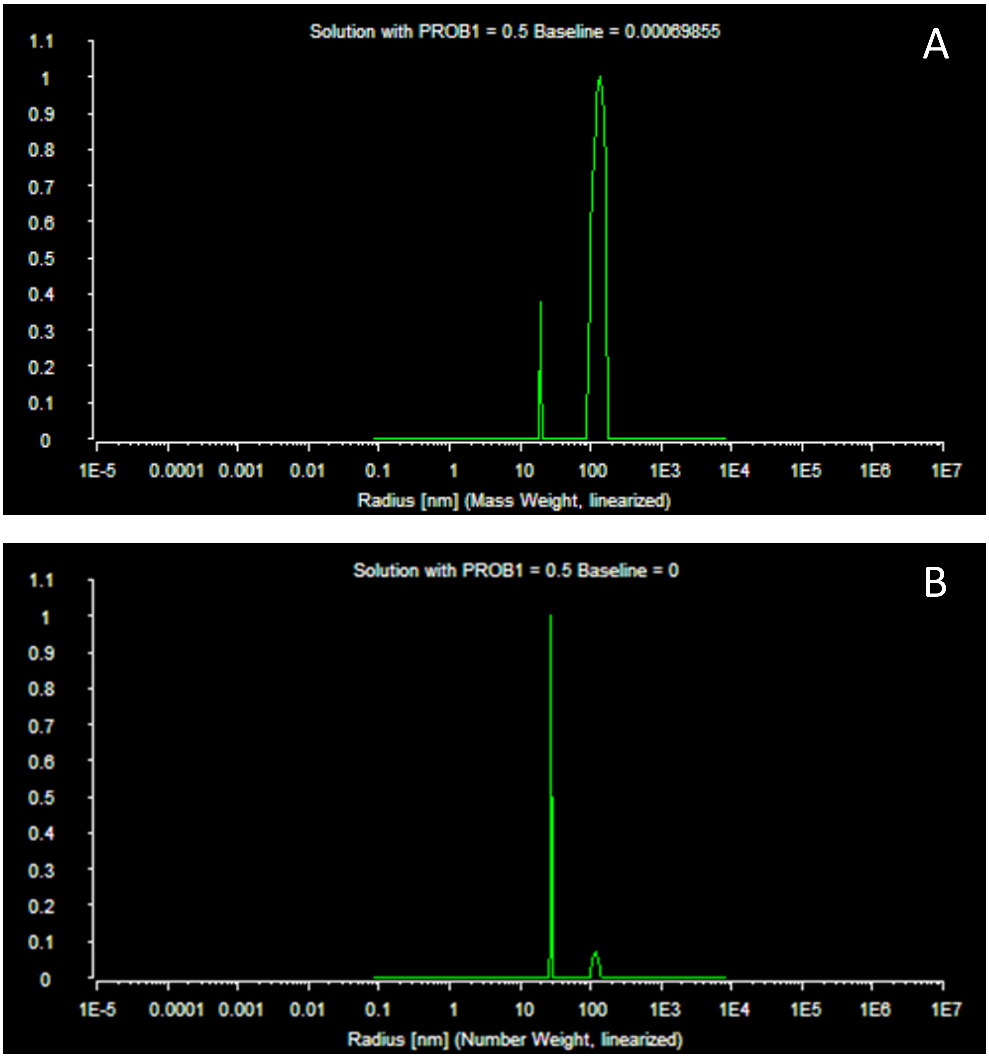

Figure S2. **Particle size distribution of $A_{45}B_{110}C_{37}$ tri-block copolymers.** Panel a.) Mass weighted distribution. Panel b.) Number weighted distribution.

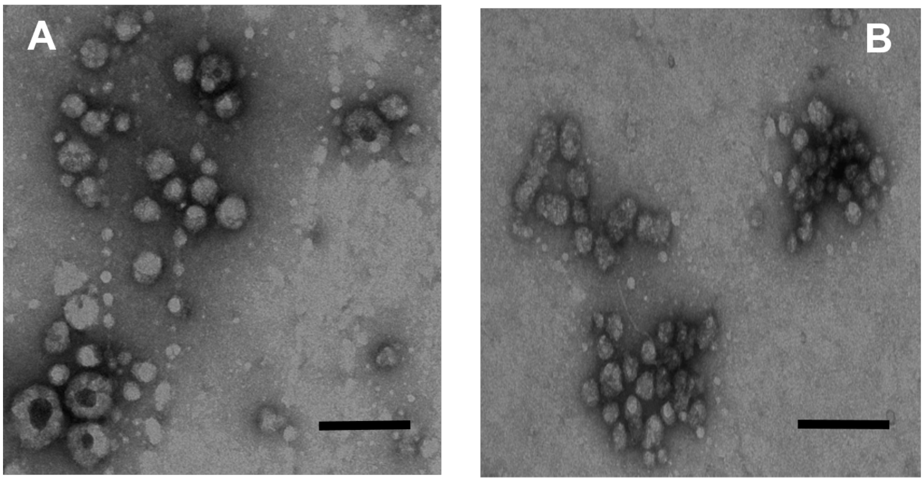

Figure S3. Transmision Electron Microscopy of $A_{45}B_{110}C_{37}$ copolymer Panel A.) sample prepared at first day Panel B.) sample after 60 days. Scale bar: 500 nm

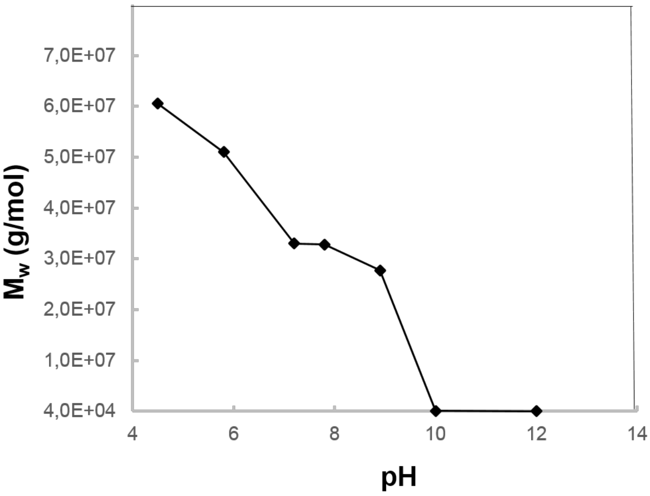

Figure S4. Influence of pH on molecular weigth (Mw) of $A_{45}B_{110}C_{37}$ copolymers

The decrease of Mw with pH increase is supposed to be related to the aggregation process (supported by Rh increase). Big aggregates can interact with the cuvette walls or sediment in the SLS experiment, which influences the measurement (only small particles that do not sediment remain suspended in the solution).

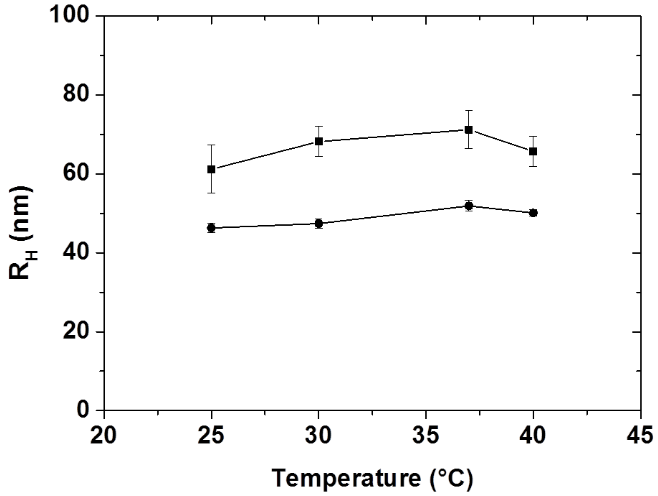

Figure S5. **Effect of temperature on particle size of ABC copolymers.** (squares) $A_{45}B_{110}C_{37}$; (circles) $A_{45}B_{101}C_{27}$.

Copolymer	IEP	τ_D free dye (µs)	τ_D dye-ABC (µs)	D_H (nm)	free dye fraction (%)	dye-ABC fraction (%)	N° molec/part	Bound fraction (%)	A. E (%)
$A_{45}B_{110}C_{37}$	9.16	38	5996	104	4	96	9	**38**	**67**
$A_{45}B_{101}C_{27}$	7.5	38	5533	96	5	95	7	**31**	**40**

Table S1. Attachment efficiency for sodium fluorescein to ABC nanoparticles.

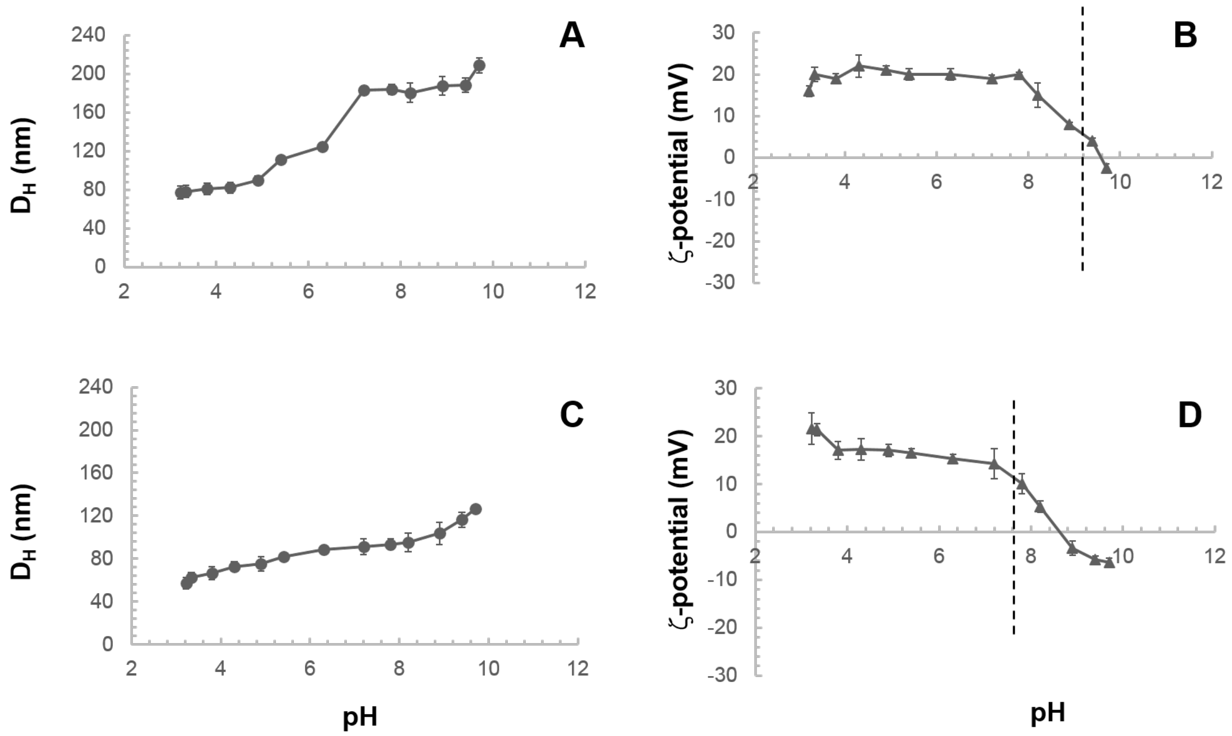

Figure S6. **Zeta-potential titration measurements of ABC copolymers**. Panels A.) and B.) $A_{45}B_{110}C_{37}$ Circles: Hydrodynamic diameter (D_H) Triangles: ζ-potential. Panels C.) and D.) $A_{45}B_{101}C_{27}$ Circles: Hydrodynamic diameter (D_H) Triangles: ζ-potential. Dash lines: Isoelectric point.

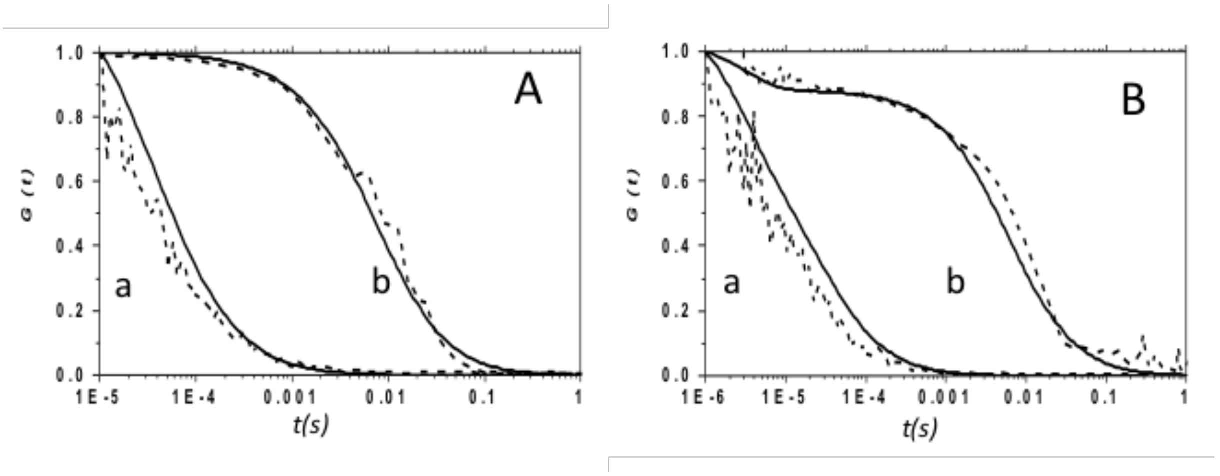

Figure S7. **Fluorescence correlation spectroscopy of BSA-FTIC modified nanoaprticles** Panel A.) FCS autocorrelation curves (continuous lines) and their fit (dashed lines) of: Free BSA-FITC (a) and BSA-FITC-$A_{45}B_{110}C_{37}$ (b). Panel B.) BSA-FITC (a) and BSA-FITC $A_{45}B_{101}C_{27}$ (b). Curves normalized to 1 to facilitate comparison.

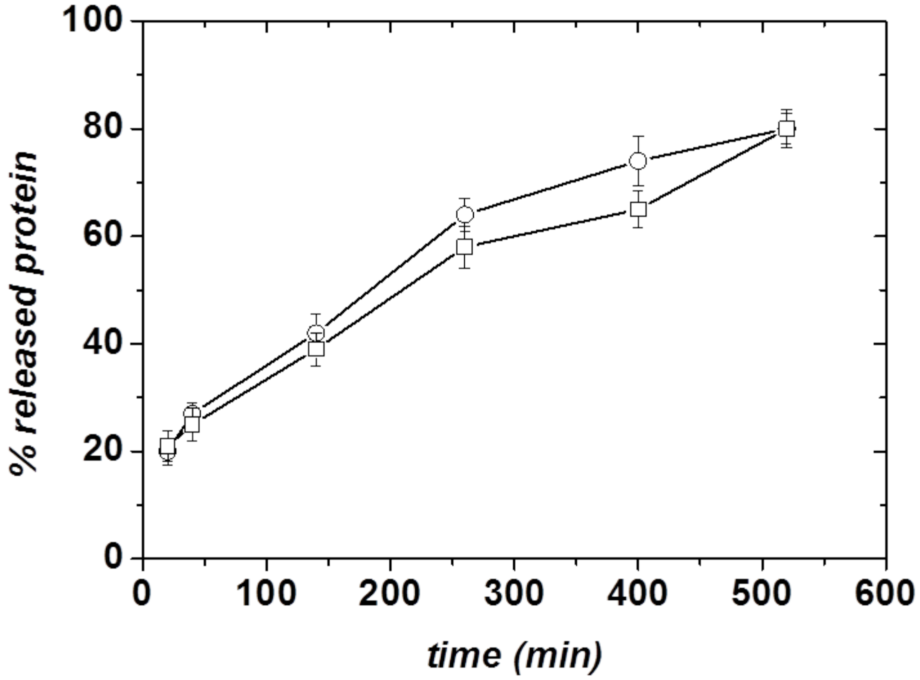

Figure S8. **BSA-FITC release from ABC nanoparticles as a function of time at pH = 5.8**. (diamonds) $A_{45}B_{31}C_{44}$; (triangles) $A_{45}B_{84}C_{85}$; (circles) $A_{45}B_{101}C_{27}$; (squares) $A_{45}B_{101}C_{20}$ followed by FCS.

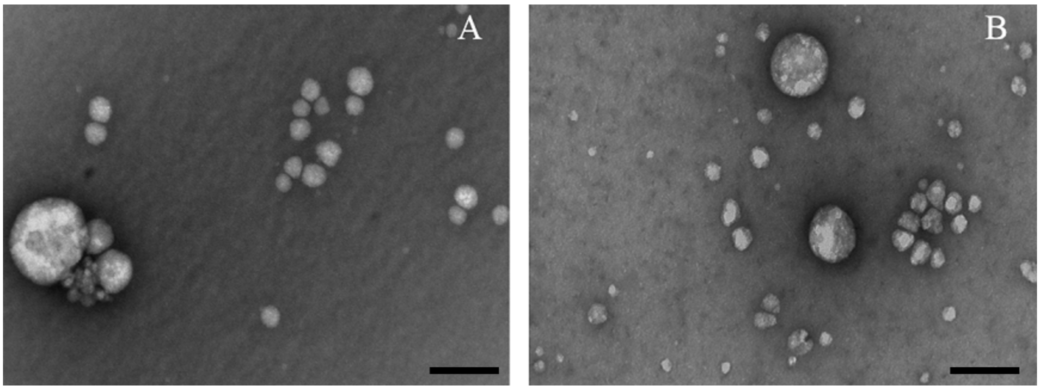

Figure S9. **TEM micrographs after attachment of o-ASM to ABC nanoparticles.** Panel A.) o-ASM/$A_{45}B_{101}C_{27}$; Panel B.) o-ASM/$A_{45}B_{110}C_{37}$. Scale bar: 200 μm.

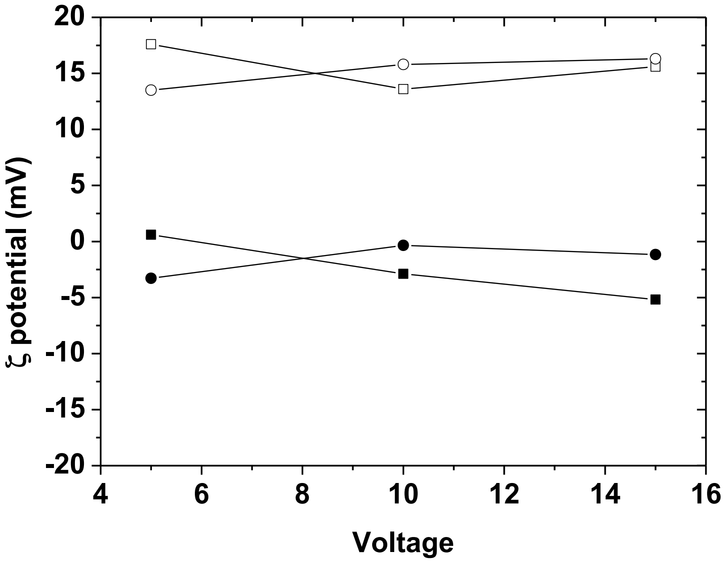

Figure S10. **Zeta potential measurements of ABC nanoparticles at pH 7.4.** (empty squares) $A_{45}B_{110}C_{37}$ without protein; (empty circles) $A_{45}B_{101}C_{27}$ without protein; (filled squares) $A_{45}B_{110}C_{37}$ with protein; (filled circles) $A_{45}B_{101}C_{27}$ with protein.

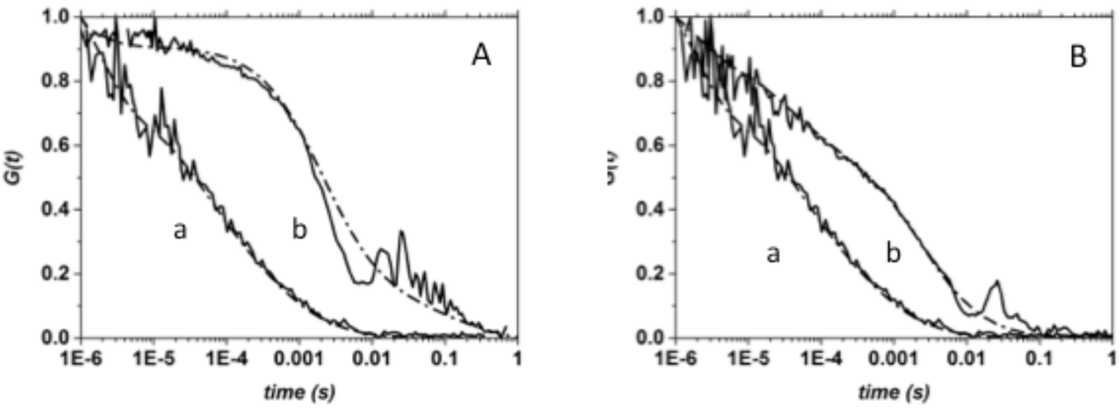

Figure S11. **Fluorescence correlation spectroscopy of o-ASM modified ABC nanoaprticles.** FCS autocorrelation curves (continuous lines) and their fit (dash lines). Panel A.) Free o-ASM protein (a), and $A_{45}B_{110}C_{37}$ nanoparticles attached with non-labelled ASM 50 min after mixing with a solution of free o-ASM (b). Panel B.) free o-ASM (a), and $A_{45}B_{101}C_{27}$ nanoparticles attached with non labelled ASM 50 min after mixing with a solution of o-ASM (b). Curves normalized to 1 to facilitate comparison.

7.2 Chapter 3 - SI

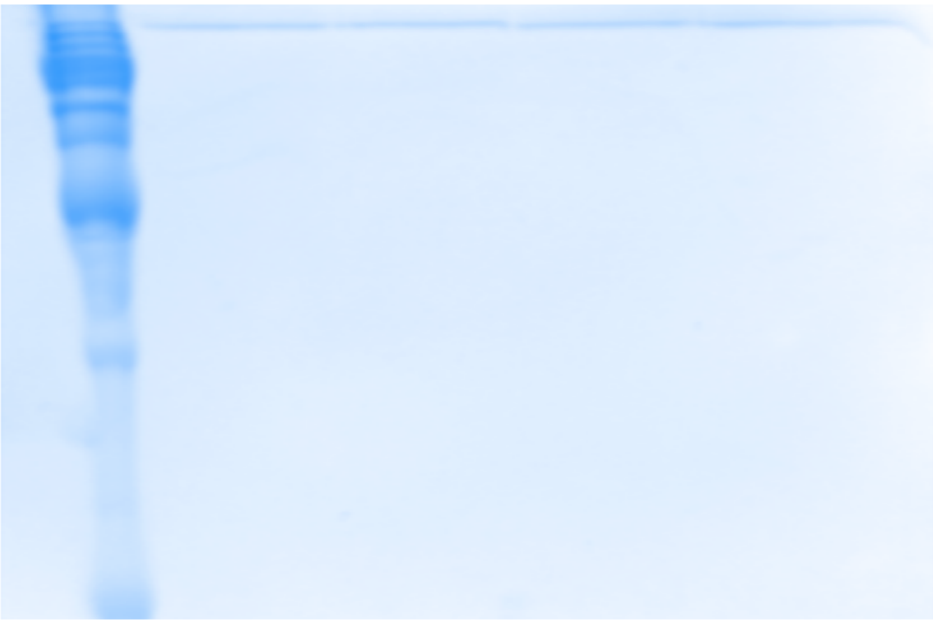

Figure S12. 20% SDS Native gel of OmpF. Lane 1. Benchmark Protein Ladder. Lane 2-3 OmpF-CA-Cy5, Lane 4-5 OmpF-CA.

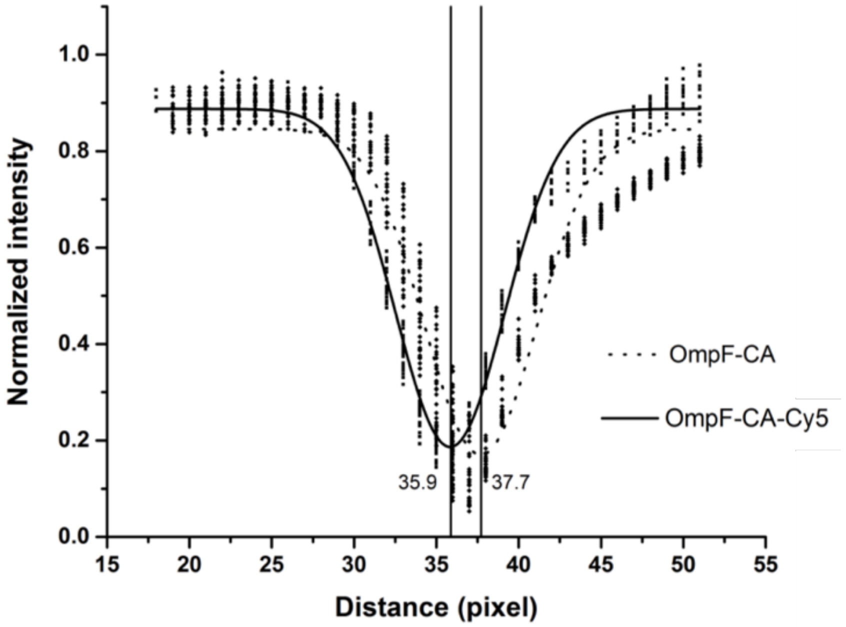

Figure S13. **Analysis of 20% native page electrophoresis.** Electrophoretic mobility of carbonylated OmpF (OmpF-CA) and OmpF modified with Cy5 (OmpF-CA-Cy5).

Table S2. Molecular brightness and diffusion times for OmpF-CA+Cy5, OmpF-WT+Cy5, and Cy5 in 3% OG measured at pH 7.4 and 5.5 respectively.

OmpF subset	CPM (kHz)	τ[μs]
OmpF-CA+Cy5, 3% OG pH 7.2	17±1	350±27
OmpF-WT+Cy5, 3% OG pH 7.2	4±1	266±51
Cy5 , 3% OG pH 7.2	7±1	249±34
OmpF-CA+Cy5, 3% OG pH 5.5	12±1	445±40
OmpF-WT+Cy5, 3% OG pH 5.5	4±1	324±30
Cy5 in 3% OG pH 5.5	7±1	297±29
Cy5 in PBS	3±1	67±1

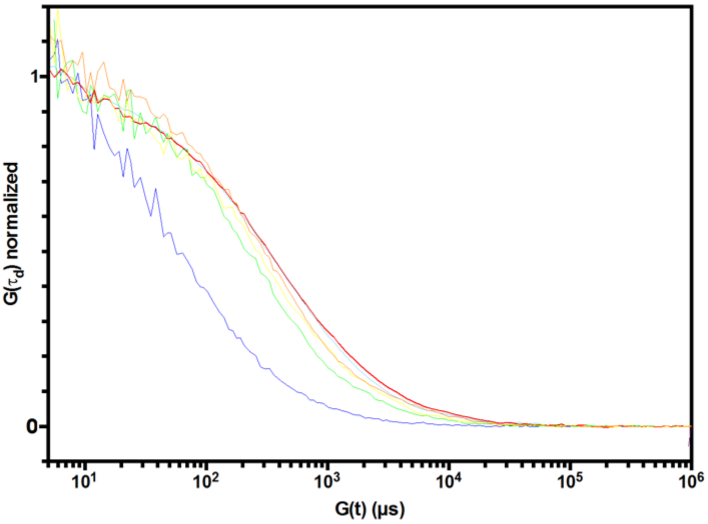

Figure S14. FCS autocorrelation curves of Cy5. 100 nM Cy_5-hydrazine in PBS solution (Blue), OmpF-CA-Cy5 at pH 7.4 (Cyan), OmpF-WT-Cy5 at pH 7.4 (Green), OmpF-WT+Cy5 pH 5.5 (Yellow), 3% OG + Cy5 pH 7.2 (Orange), 3% OG + Cy5 pH 5 (Violet), OmpF-CA+Cy5 pH 5.5 (Red).

Table S3. Size of nano-assemblies based on $PMOXA_6$–$PDMS_{44}$–$PMOXA_6$ without and with reconstituted OmpF, pH 5.5.

Size and stability of nano-assemblies	DLS/SLS		
	R_g [nm]	R_h [nm]	$\varrho = R_g/R_h$
Non-permeabelised Polymersomes	89	86	1.04
OmpF-CA-Cy5 Polymersomes	85	81	1.05
OmpF-WT Polymersomes	84	88	0.96

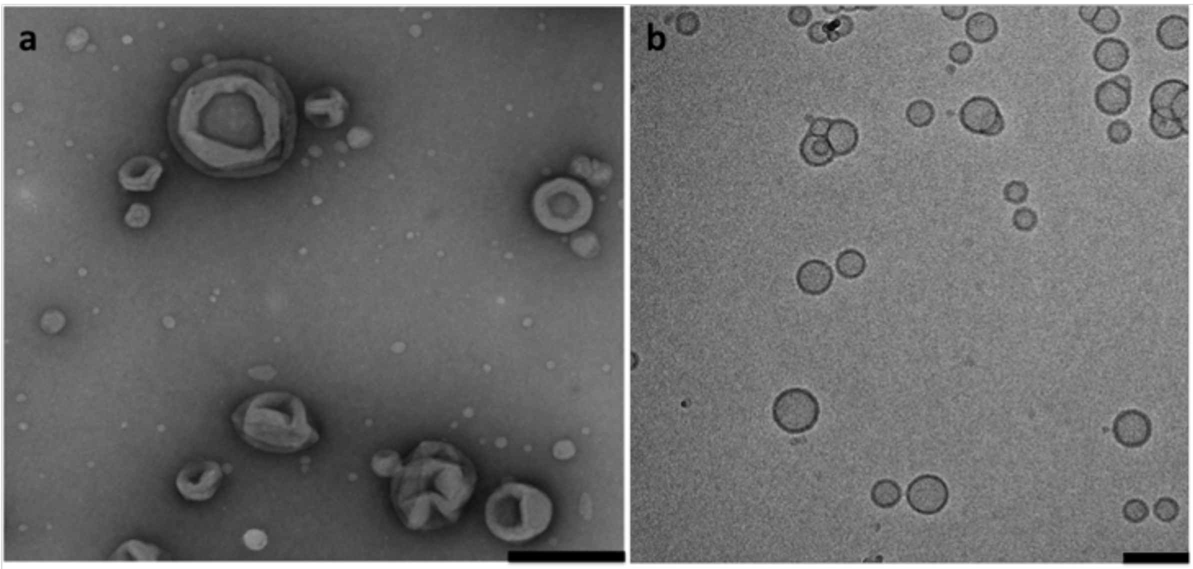

Figure S15. TEM and Cryo-TEM micrographs of OmpF-WT catalytic nanocompartments. Panel a.) Overview TEM picture of a 0.5mg/ml OmpF-WT catalytic nanocompartment solution. Scale bar 50nm. Panel b.) Overview Cryo-TEM picture of a 2.5mg/ml OmpF WT catalytic nanocompartment solution. Scale bar: 100nm.

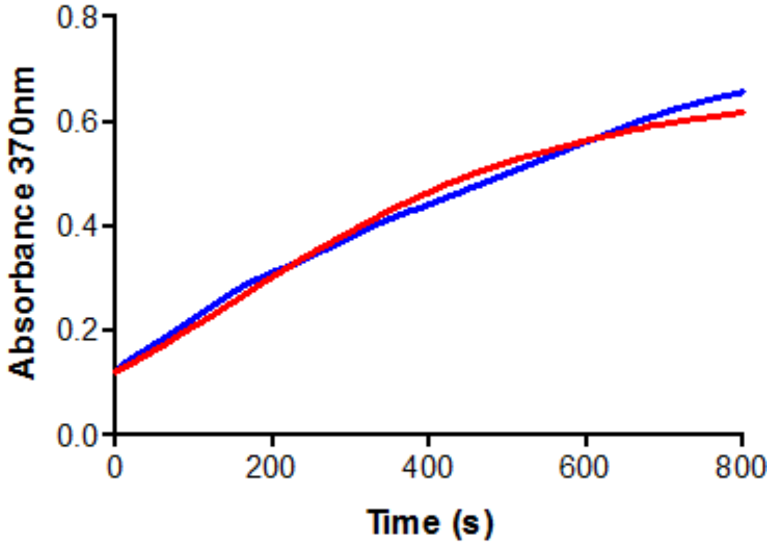

Figure S16. TMB conversion kinetics of free HRP. HRP incubated at pH 7.4 (Blue) and 5.5 (Red) and measured at pH 7.4.

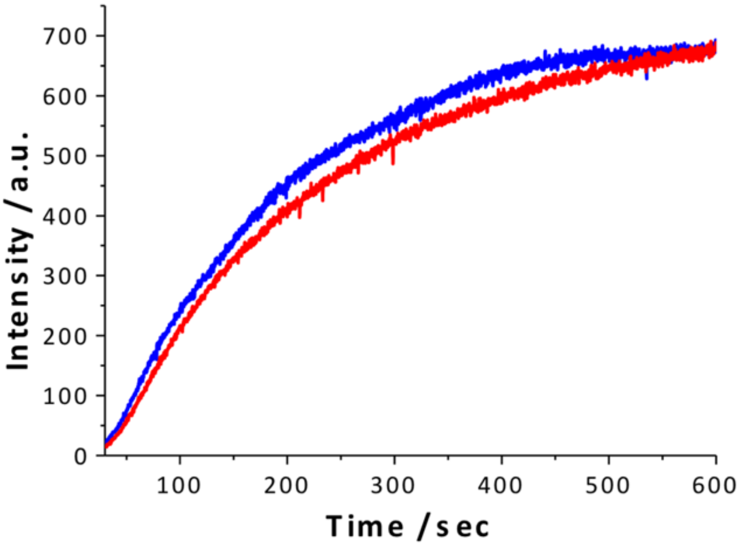

Figure S17. **Amplex red conversion kinetics of Free HRP measured at pH 5.5 and 7.4.** Amplex red conversion at pH 7.4 (Blue), Amplex red Conversion at pH 5.5 (Red).

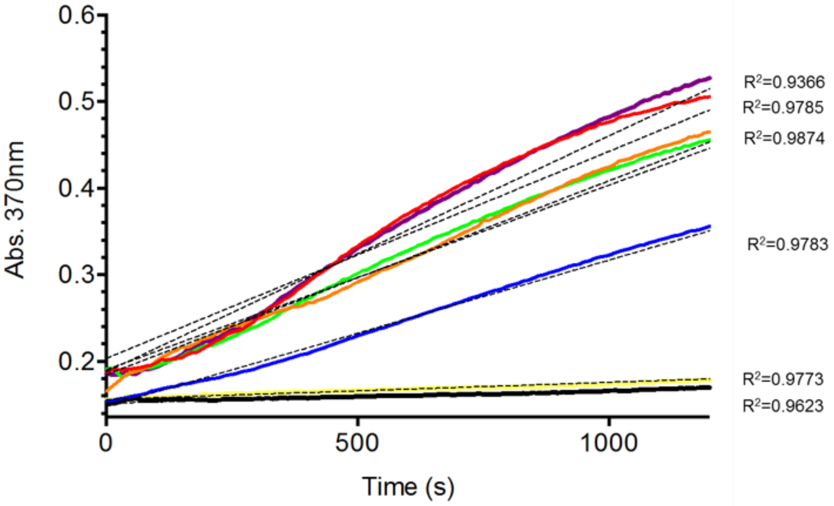

Figure S18. **TMB conversion kinetics at pH 7.4 of HRP loaded polymersomes modified with different OmpF subsets.** TMB conversion kinetics measured at pH 7.4 of catalytic nanocompartments prepared with different OmpF subsets. Red: OmpF-WT catalytic nanocompartments incubated at pH 7.4, Blue: OmpF-CA-Cy5 catalytic nanocompartments incubated at 7.4, Grey: OmpF-CA catalytic nanocompartments incubated at pH 5.5, Black: OmpF-CA-Cy5 catalytic nanocompartments incubated at 5.5, Yellow: OmpF-CA-Cy5 catalytic nanocompartments incubated at 5.5.

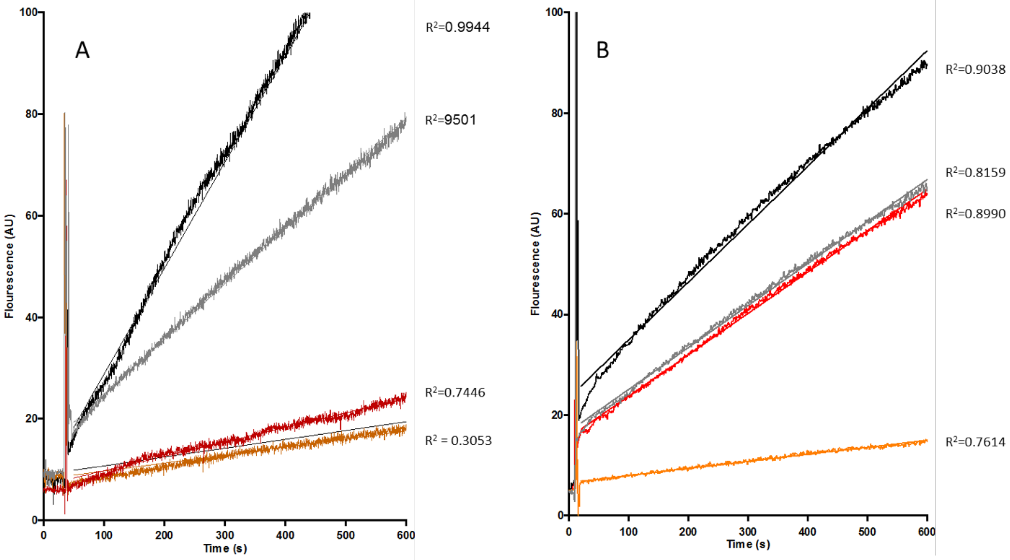

Figure S19. Amplex red conversion kinetics of catalytic nanocompartments equipped with different OmpFs. Incubaton time at pH 5.5 0h Panel A.) and after 1 hour Panel B.). Red: OmpF-CA-Cy5 catalytic nanocompartments, Grey: OmpF-CA catalytic nanocompartments, Black: OmpF-WT catalytic nanocompartments, Orange: Unpermeabelised HRP loaded polymersomes.

7.3 Chapter 4

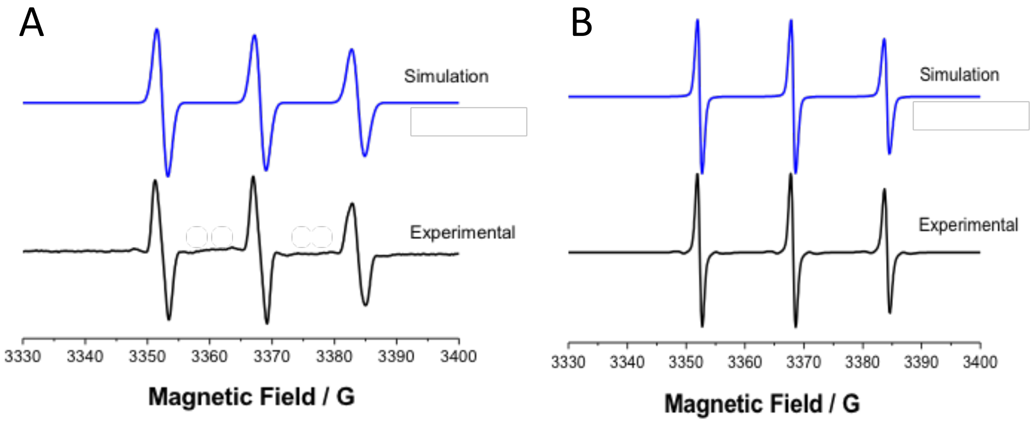

Figure S20. EPR measurement of free bis-(2,2,5,5-Tetramethyl- 3-imidazoline-1-oxyl-4-yl)disulfide Panel A.) EPR signal of bis-(2,2,5,5-Tetramethyl- 3-imidazoline-1-oxyl-4-yl)disulfide in PBS, experimental (black) and simulated (blue) Panel B.) EPR signal of bis-(2,2,5,5-Tetramethyl- 3-imidazoline-1-oxyl-4-yl)disulfide in presence of 10mM DTT experimental (black) and simulated (blue).

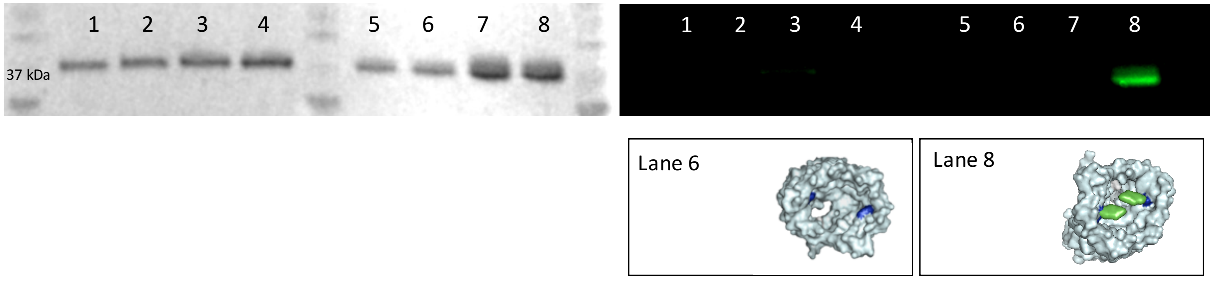

Figure S21: **4-15% SDS-PAGE of modified and unmodified OmpF**. Left: Coomassie blue stained gel. Right: Fluorescent image. Lane 1. OmpF Wild type exposed to 30mM GSH, Lane 2. OmpF Wild Type exposed to SAMSA- CF and 30mM GSH, Lane 3. OmpF K89 R270 exposed to 30mM GSH, Lane 4. OmpF K89 R270 exposed to SAMSA- fluorescein and 30mM GSH Lane 5. OmpF Wild type, Lane 6. OmpF Wild Type exposed to SAMSA- fluorescein, Lane 7. OmpF K89 R270, Lane 8. OmpF K89 R270 exposed to SAMSA-fluorescein

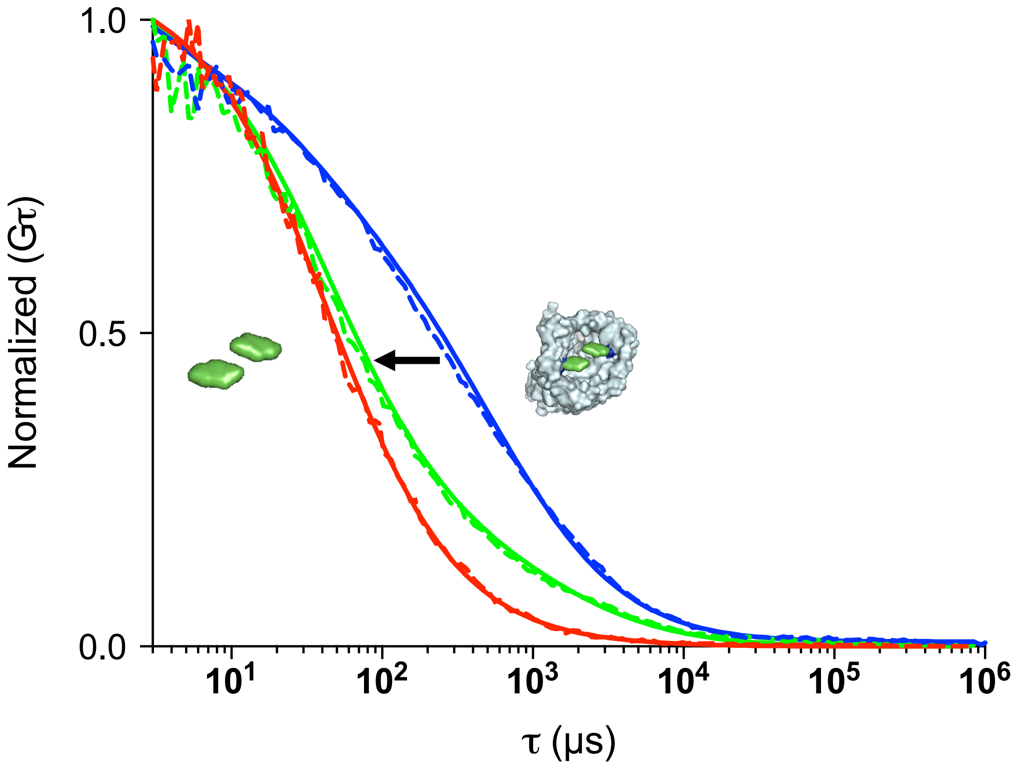

Figure S22*:* FCS analysis of OmpF-S-S-CF stimuli responsiveness. FCS autocorrelation curves of SAMSA-CF in 1% OG 30mM GSH (red), OmpF-S-S-CF mixed with 30mM GSH in 1% OG Time 1h (green) and OmpF-S-S-CF in 1% OG Time 0h, PBS (blue). Dotted line – experimental auto correlation curves, Full line – fit. Curves normalized to 1 to facilitate comparison.

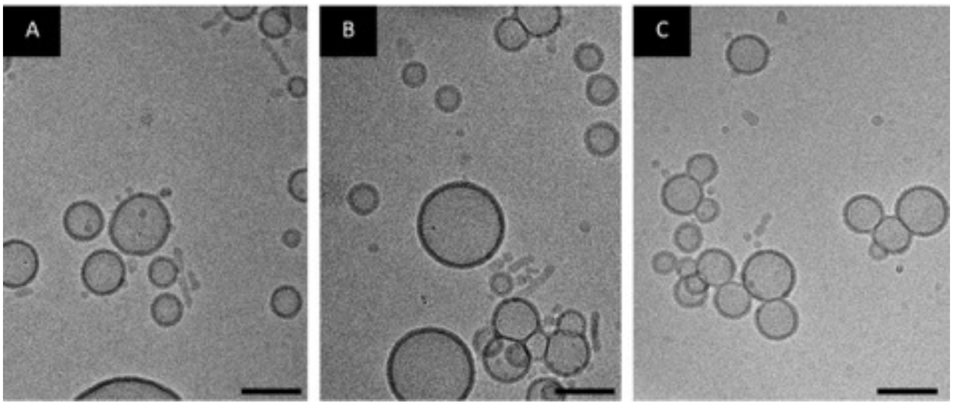

Figure S23*: *Cryo-TEM overview micrographs of Panel a.) Polymersomes loaded with HRP and equipped with OmpF-S-S-CF. Panel b.) polymersomes loaded with HRP and equipped OmpF-SH. Panel c.) polymersomes loaded with HRP. Scale bar:100 nm

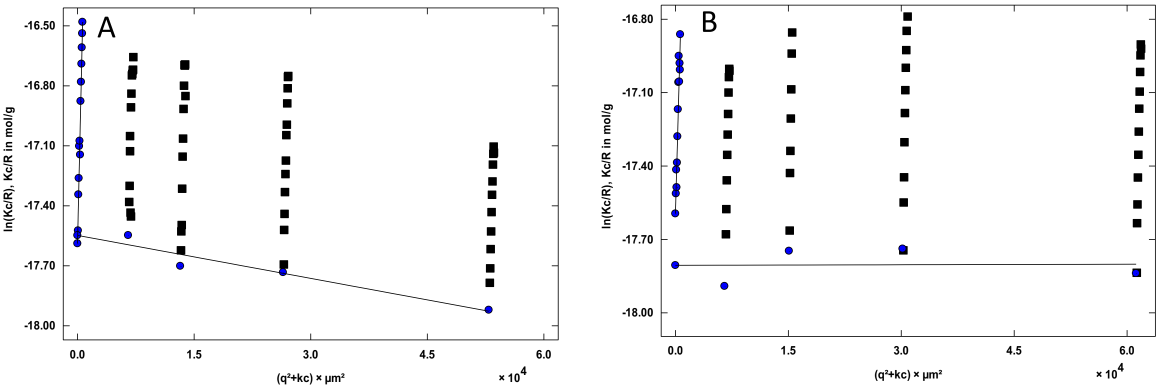

Figure S24: **Guinier plot representation of SLS data.** HRP-loaded polymersomes equipped with OmpF-S-S-CF in PBS pH 7.4 (A), in presence 30mM GSH in PBS 7.4 (B).

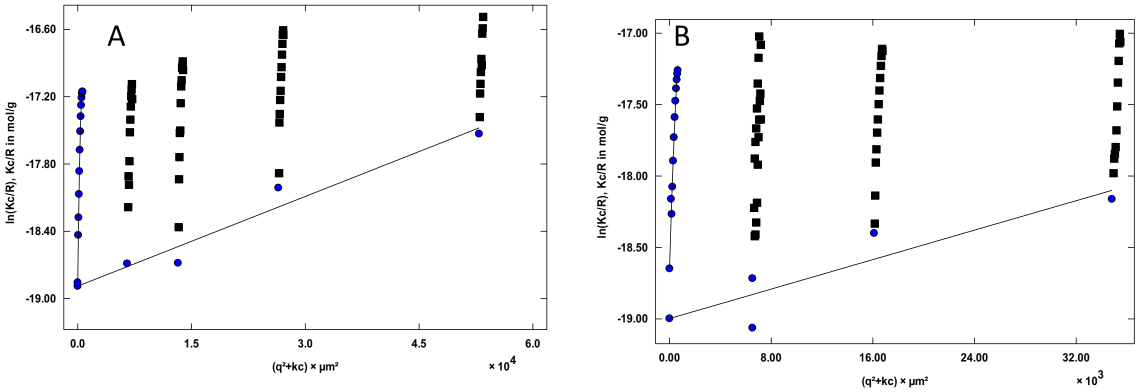

Figure S25: Guinier plot representation of SLS data. HRP-loaded polymersomes equipped with OmpF-SH in PBS pH 7.4 (A), in presence 30mM GSH in PBS pH 7.4 (B).

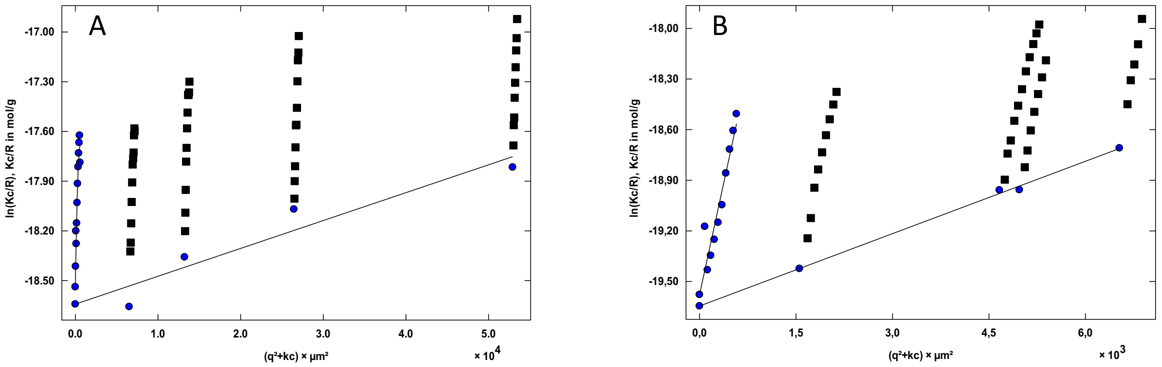

Figure S26: Guinier plot representation of SLS data. HRP-loaded polymersomes in PBS (A), in presence 30mM GSH in PBS (B).

Nanocompartments	**$\varrho = R_g/R_h$**
HRP-loaded polymersomes	0.97 ± 0.01
HRP-loaded polymersomes equipped with OmpF-S-S-CF	0.93 ± 0.02
HRP loaded polymersomes equipped with OmpF-SH	0.98 ± 0.04

Tale S2: Molecular Characteristics of PMOXA$_6$–PDMS$_{44}$-PMOXA$_6$ assemblies in PBS pH 7.4. Mw = 4500 g/mol, PDI = 1.8, fhydrophylic = 25%

Nanocompartments	**$\varrho = R_g/R_h$**
HRP-loaded polymersomes	0.95 ± 0.01
HRP-loaded polymersomes equipped with OmpF-S-S-CF	0.96 ± 0.02
HRP loaded polymersomes equipped with OmpF-SH	0.95 ± 0.04

Table S3: Molecular Characteristics of $PMOXA_6$–$PDMS_{44}$-$PMOXA_6$ assemblies in PBS pH 7.4 + 30mM GSH. Mw = 4500 g/mol, PDI = 1.8, fhydrophylic = 25%

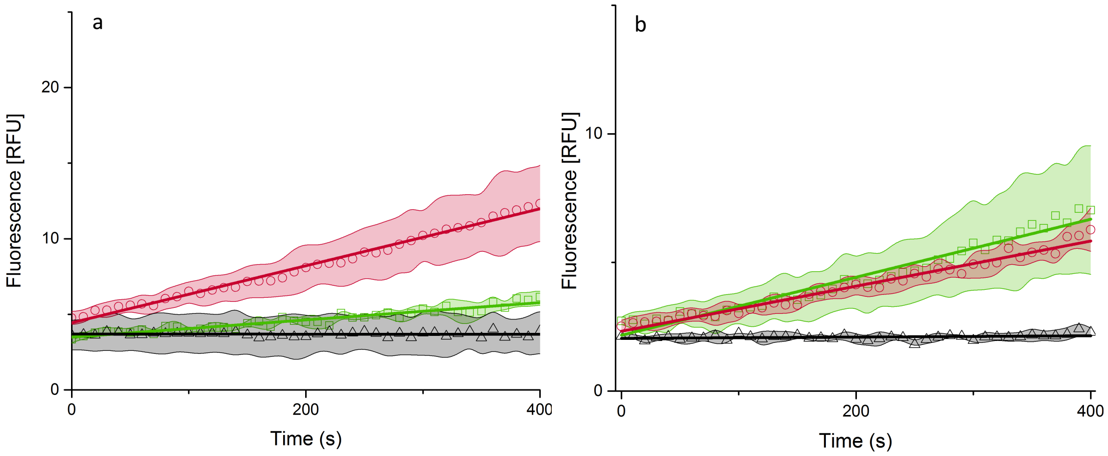

Figure S27. **Enzymatic Amplex Ultra red conversion by catalytic nanocompartments.** OmpF-SH permeabilised catalytic nanocompartments (red), OmpF-S-S-CF permeabelized catalytic nanocompartments (green), unpermeabilised HRP-loaded polymersomes (black) in the presence of 30mM GSH in PBS pH 7.4. Panel a.) t=0, Panel b.) t=1h.

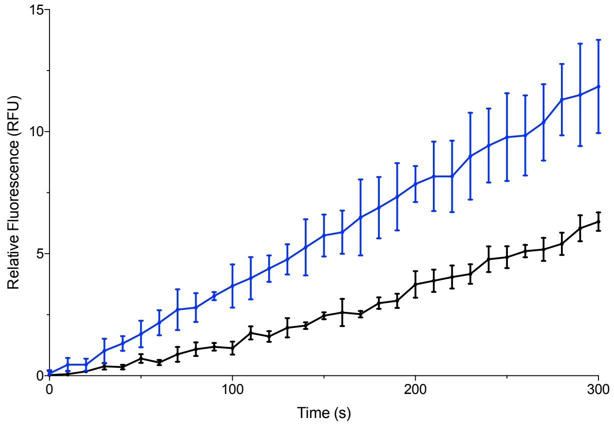

Figure S28: **Amplex Ultra Red conversion of free HRP in presence of 30mM GSH.** Immediately after mixing with 30mM GSH (blue) and 1 hour after mixing with 30mM GSH in PBS pH 7.4 (black).

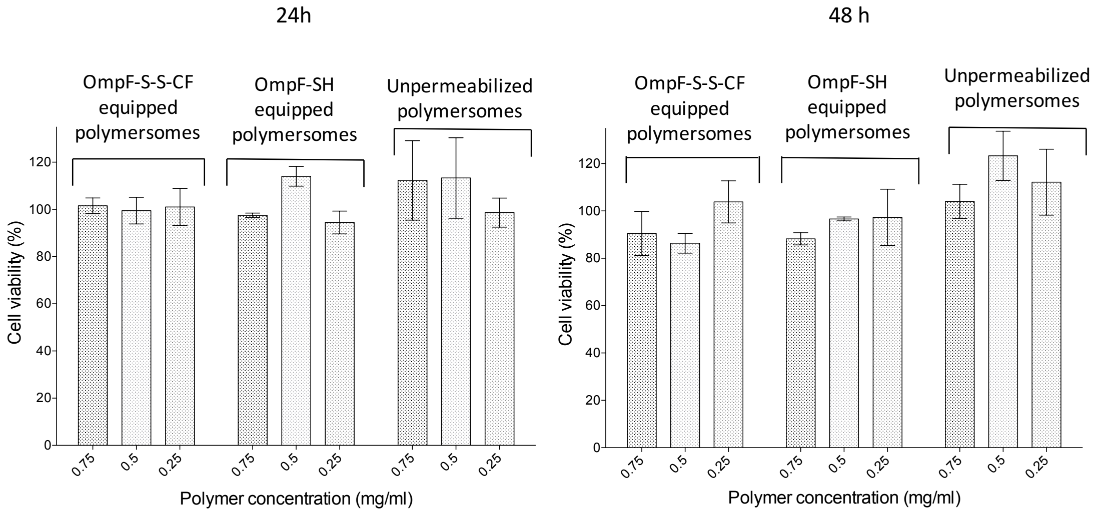

Figure S29. **Cytototxicity of catalytic nanocompartments.** 24h (left) and 48h (right) cell viability of HeLa cells incubated with HRP-loaded polymersomes, HRP-loaded polymersomes equipped with OmpF-SH and HRP-loaded polymersomes equipped with OmpF-S-S-CF.

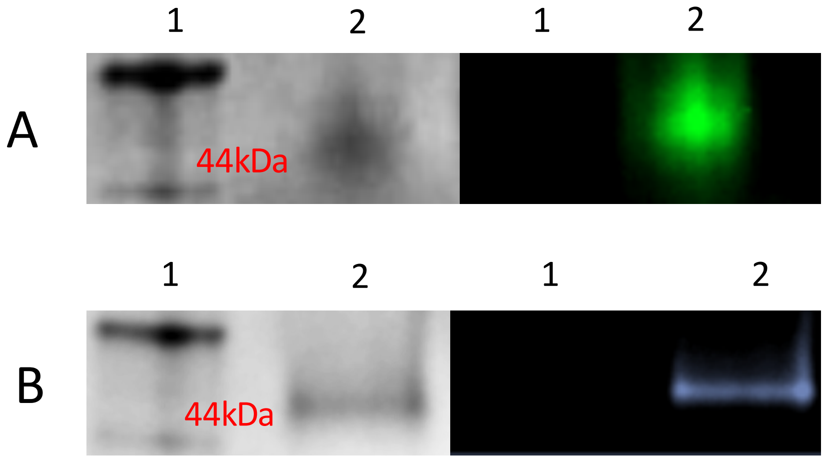

Figure S30: 4-20% SDS-PAGE of Atto-488 conjugated HRP and Atto-647 conjugated HRP. Panel A.) Left: Coomassie blue stained gel. Right: Fluorescent image. Lane 1: Protein ladder. Lane 2. Atto-488 Conjugated HRP. Panel B.) 4-20% SDS-PAGE. Left: Coomassie blue stained gel. Right: Fluorescent image. Lane 1: Protein ladder. Lane 2: Atto-647 conjugated HRP.

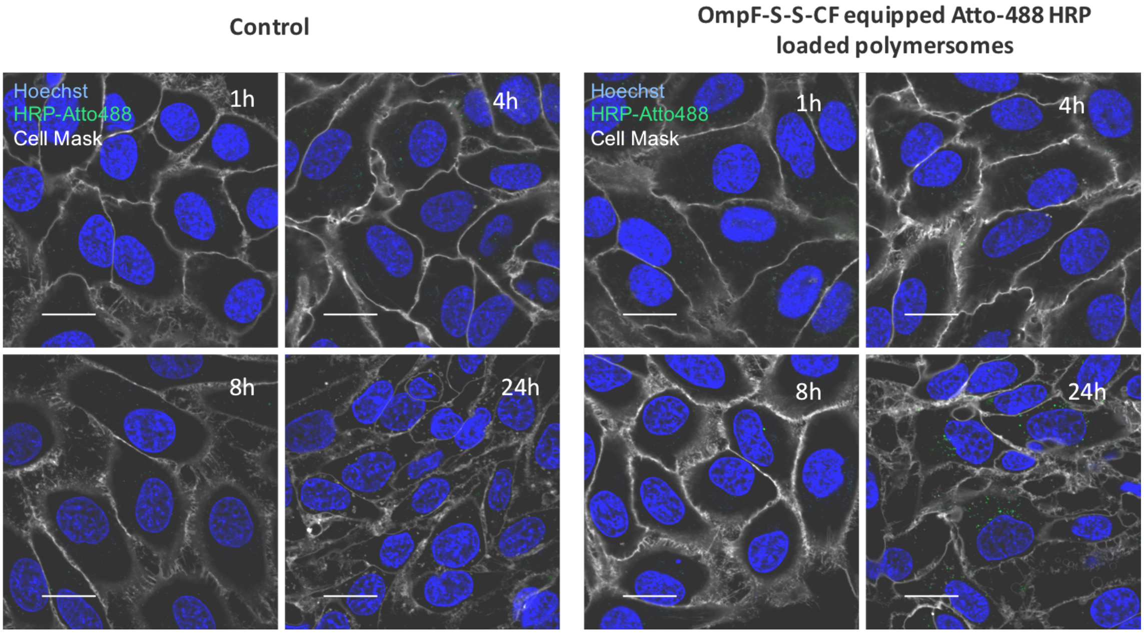

Figure S31. Time dependent cellular uptake of Atto-488 conjugated HRP-loaded polymersomes equipped with OmpF-S-S-CF over 24 hours. CLSM micrographs of HeLa cells treated with PBS (Control) or 0.25 mg/ml Atto-488 HRP-loaded polymersomes equipped with OmpF-S-S-CF. Blue: Hoechst 33342 nucleus stain, Gray: CellMask Deep Red Plasma membrane stain, Green: Atto-488. scale bars: 20 μm

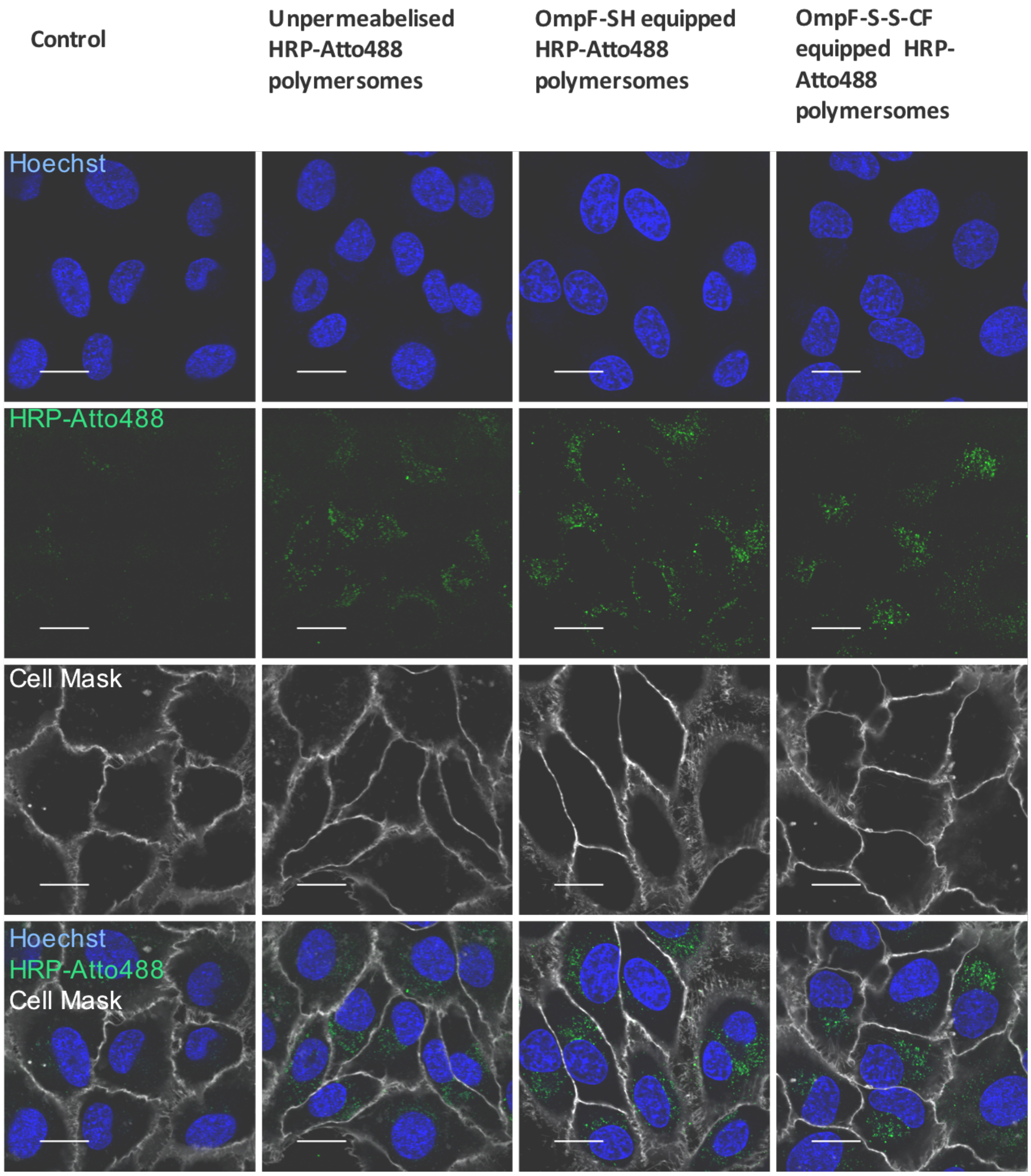

Figure S32. Cellular uptake of different HRP-loaded polymersomes after 24 hours. CLSM micrograph of HeLa cells treated with PBS (Control), HRP-Atto488 loaded polymersomes, HRP-Atto488loaded polymersomes equipped with OmpF-SH and HRP-Atto488 loaded polymersomes equipped with OmpF-S-S-CF. Blue: Hoechst 33342 nucleus stain, Gray: CellMask Deep Red Plasma membrane stain, Green: Atto-488. Scale bar: 20μm

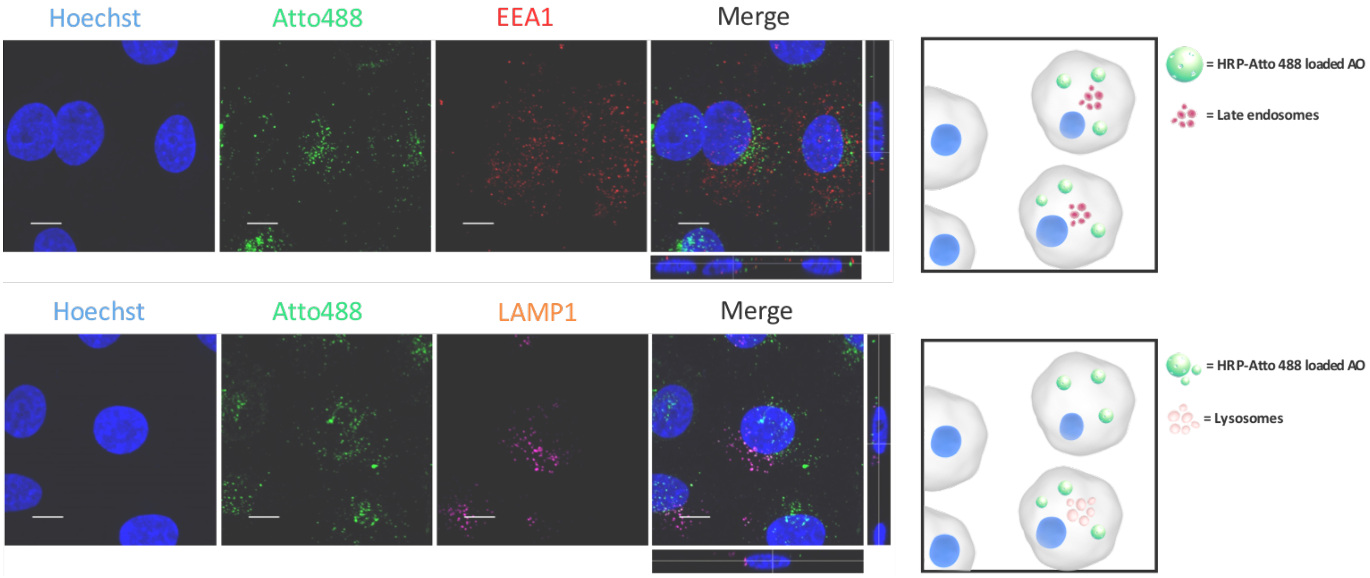

Figure S33. Intracellular localization of HRP-loaded polymersomes. Maximum intensity projections including lateral view of HeLa cells treated with HRP-Atto488 loaded polymersomes equipped with OmpF-S-S-CF for 24 hours. Endosomes were visualized with EEA1 staining, and lysosomes with LAMP1 staining. Blue: Hoechst 33342 nucleus stain, Green: Atto-488, Red: Early Endosome. Magenta: Lysosome. Scale bar: 10μm

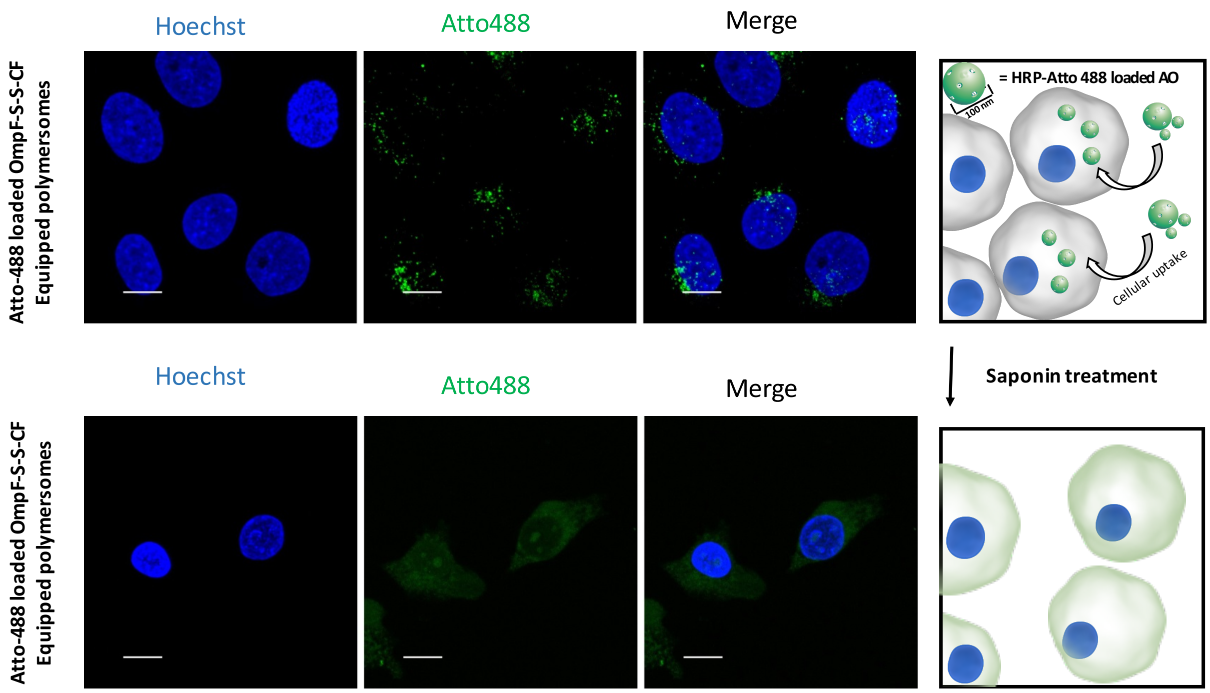

Figure S34. Effect of saponin treatment on localization of polymersome encapsulated HRP-Atto488. CLSM maximum intensity projection micrograph of uptake experiments in HeLa cells with HRP-Atto488 loaded polymersomes equipped with OmpF-S-S-CF. After 24 hours cells were treated with PBS (control) or 0.1% saponin. Blue: Hoechst 33342 nucleus stain, Green: Atto-488. Scale bar: 10μm

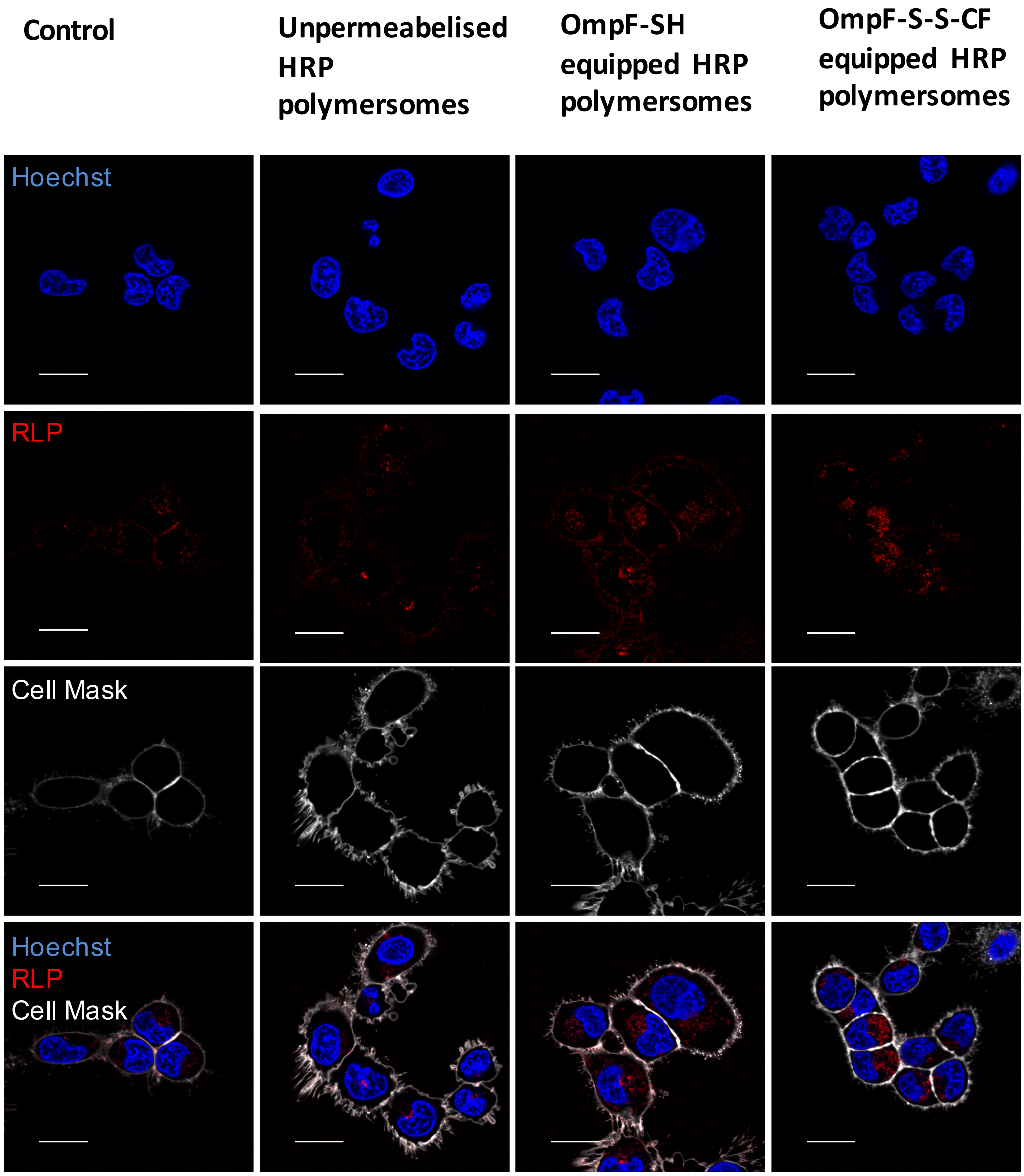

Figure S35. Intracellular conversion of Amplex Ultra Red by HRP loaded polymersomes. CLSM micrograph of HeLa cells treated with PBS (Control), Unpermeabilised HRP loaded polymersomes, OmpF-SH permeabelised HRP loaded polymersomes and HRP loaded polymersomes equipped with OmpF-S-S-CF. Blue: Hoechst 33342 nucleus stain, Cyan: CellMask Deep Red Plasma membrane stain, Red: converted Amplex Red product. Scale bar: 20μm

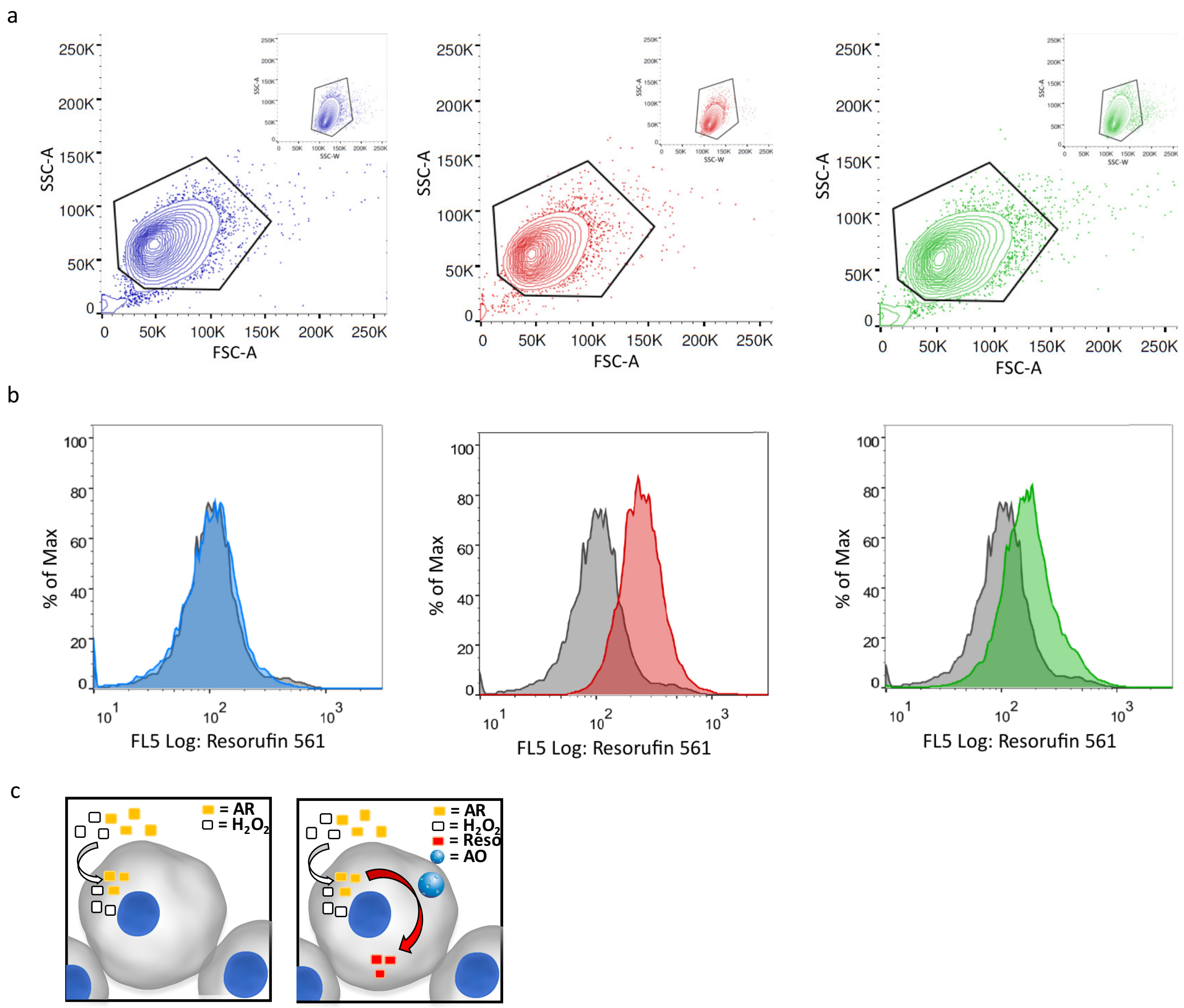

Figure S36. Flow cytometry analysis of Amplex Ultra Red Conversion in HeLa cells. Panel a.) Dot plots of FSC area against SSC area are shown. Inserts show the doublet exclusion for the SSC Panel b.) Analysis of Hela cells incubated with: PBS (Blue), Unequipped HRP loaded polymersomes (Gray), OmpF-SH equipped polymersomes (Red), OmpF-S-S-CF equipped polymersome (Green). Panel c.) Shematic representation of artificial organelle activity.

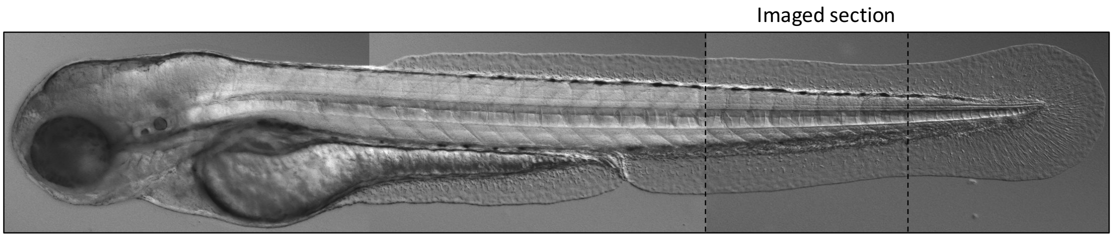

Figure S37. Lateral view of the ZFE cross-section used for fluorescent imaging.

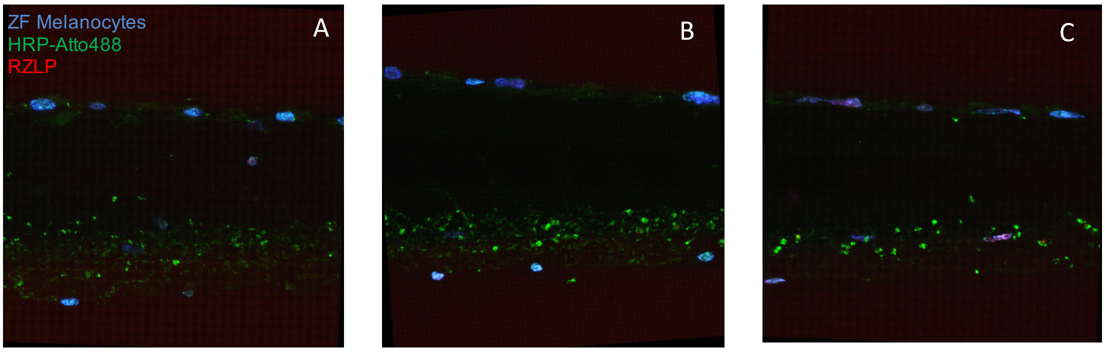

Figure S38. Biodistribution of HRP loaded catalytic nanocompartments in ZFE. Lateral view of the ZFE embryo cross-section. Panel a.) ZFE injected with HRP loaded polymersomes. Panel b.) ZFE injected with HRP-Atto488 loaded polymersomes equipped with OmpF-S-S-CF, Panel c.) ZFE injected with HRP loaded polymersomes equipped with OmpF-SH.

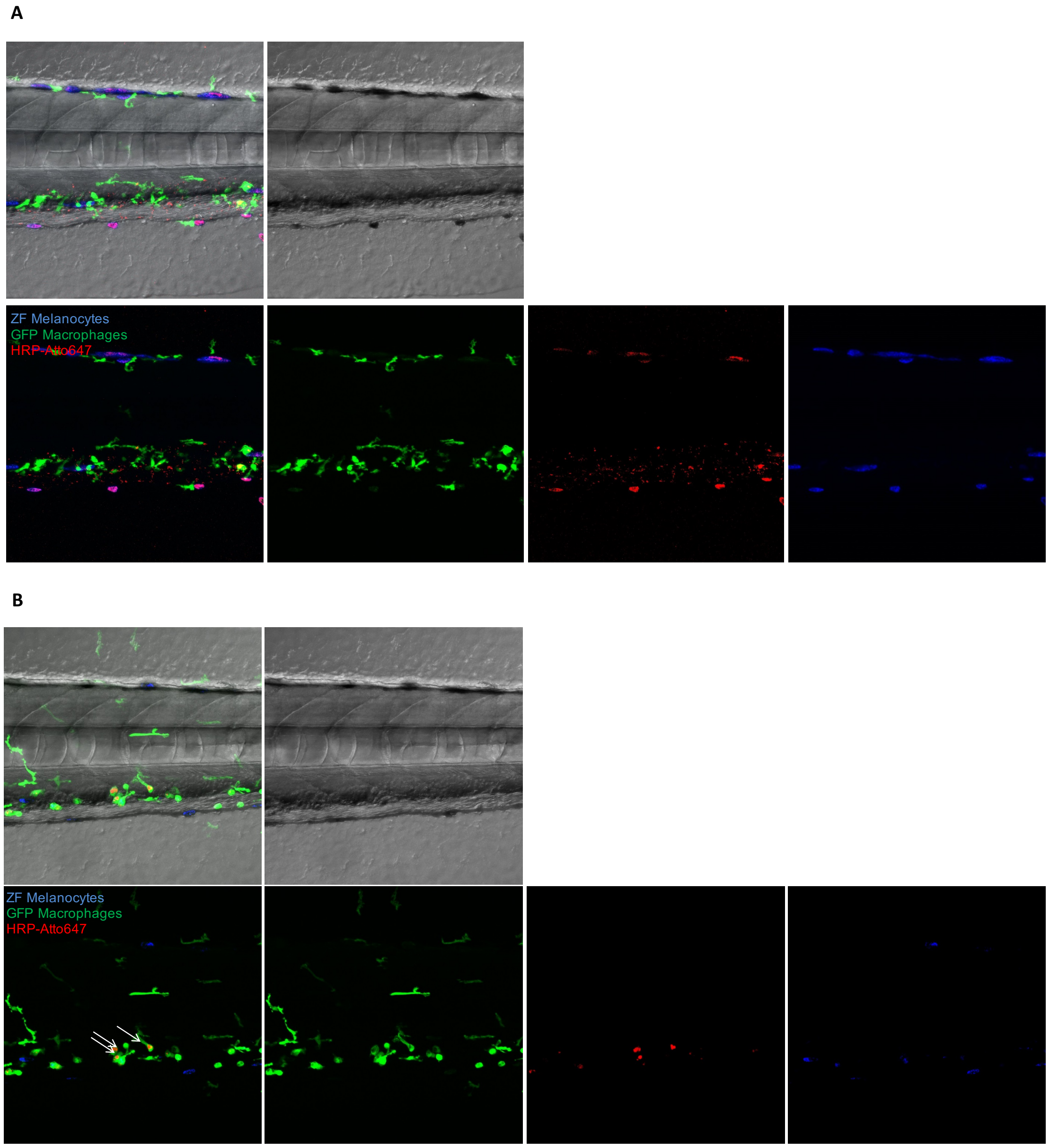

Figure S39. Localisation of AO in ZFE. Lateral view of the ZFE cross-section. Panel A: ZF injected with HRP-Atto647 Panel B: ZF injected with HRP-Atto488 loaded polymersomes equipped with equipped with OmpF-S-S-CF. Arrowheads: Localization of AO.

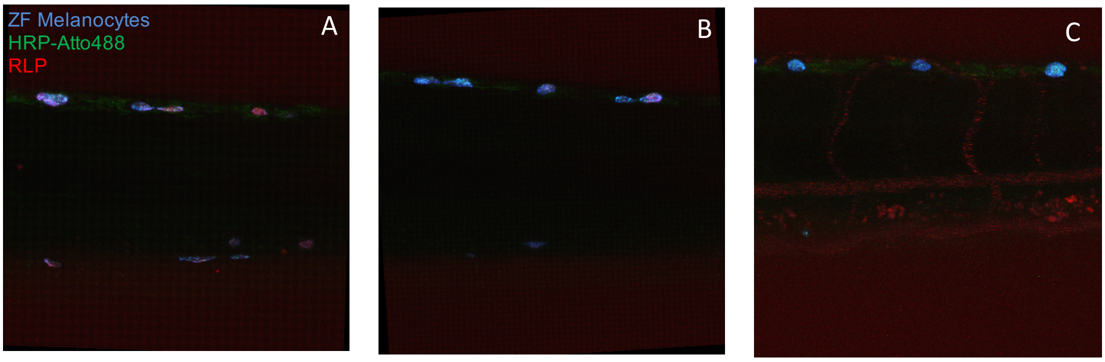

Figure S40. Injection of Amplex Ultra Red in ZFE Lateral view of the ZFE cross-section. Panel A.) ZFE control. B.) ZFE injected with only Amplex Red, C.) ZFE injected with Amplex Red and H_2O_2.

No Resorufin like product (RLP) or Resazurin like product (RZLP) was observed in ZFE control or in ZFE injected with only AR. Injection of AR and H_2O_2 resulted in a staining pattern of the erythrocytes.

REFERENCES

1. Palivan, C. G. *et al.* Bioinspired polymer vesicles and membranes for biological and medical applications. *Chem. Soc. Rev.* **45,** 377–411 (2016).
2. Yoo, J.-W., Irvine, D. J., Discher, D. E. & Mitragotri, S. Bio-inspired, bioengineered and biomimetic drug delivery carriers. *Nat. Rev. Drug Discovery* **10,** 521–535 (2011).
3. Mai, Y. & Eisenberg, A. Self-assembly of block copolymers. *Chem. Soc. Rev.* **41,** 5969 (2012).
4. Garni, M., Thamboo, S., Schoenenberger, C.-A. & Palivan, C. G. Biopores/membrane proteins in synthetic polymer membranes. *Biochim. Biophys. Acta* **1859,** 619–638 (2017).
5. Tanner, P., Balasubramanian, V. & Palivan, C. G. Aiding Nature's Organelles: Artificial Peroxisomes Play Their Role. *Nano Lett.* **13,** 2875–2883 (2013).
6. Liu, J. *et al.* DNA-Mediated Self-Organization of Polymeric Nanocompartments Leads to Interconnected Artificial Organelles. *Nano Lett.* (2016).
7. Dieu, L.-H., Wu, D., Palivan, C. G., Balasubramanian, V. & Huwyler, J. Polymersomes conjugated to 83-14 monoclonal antibodies: in vitro targeting of brain capillary endothelial cells. *Eur. J. Pharm. Biopharm.* **88,** 316–324 (2014).
8. Najer, A. *et al.* Nanomimics of Host Cell Membranes Block Invasion and Expose Invasive Malaria Parasites. *ACS Nano*
9. Vasquez, D., Einfalt, T., Meier, W. & Palivan, C. G. Asymmetric Triblock Copolymer Nanocarriers for Controlled Localization and pH-Sensitive Release of Proteins. *Langmuir* (2016).
10. Walker, H. K., Hall, W. D., Hurst, J. W., Cox, R. A. & García-Palmieri, M. R. Cholesterol, Triglycerides, and Associated Lipoproteins. *Edition:3rd* (1990).
11. Jutz, G., van Rijn, P., Santos Miranda, B. & Böker, A. Ferritin: A Versatile Building Block for Bionanotechnology. *Chem. Rev.* **115,** 1653–1701 (2015).
12. Einfalt, T. *et al.* Stimuli-Triggered Activity of Nanoreactors by Biomimetic Engineering Polymer Membranes. *Nano Lett.* **15,** 7596–7603 (2015).
13. Gunkel-Grabole, G. *et al.* Polymeric 3D nano-architectures for transport and delivery of therapeutically relevant biomacromolecules. *Biomaterials Sci.* **3,** 25–40 (2015).
14. Mai, Y. & Eisenberg, A. Self-assembly of block copolymers. *Chem. Soc. Rev.* **41,** 5969–5985 (2012).
15. Fu, C., Xu, J., Kokotovic, M. & Boyer, C. One-Pot Synthesis of Block Copolymers by Orthogonal Ring-Opening Polymerization and PET-RAFT Polymerization at Ambient Temperature. *ACS Macro Lett.* (2016).
16. Koide, A. *et al.* Semipermeable Polymer Vesicle (PICsome) Self-Assembled in Aqueous Medium from a Pair of Oppositely Charged Block Copolymers: Physiologically Stable Micro-/Nanocontainers of Water-Soluble Macromolecules. *J. Am. Chem. Soc.* **128,** 5988–5989 (2006).
17. Blanazs, A., Armes, S. P. & Ryan, A. J. Self-Assembled Block Copolymer Aggregates: From Micelles to Vesicles and their Biological Applications. *Macromo. R. Comm.* **30,** 267–277 (2009).
18. Braunecker, W. A. & Matyjaszewski, K. Controlled/living radical polymerization: Features, developments, and perspectives. *Prog. Polym. Sci.* **32,**

93–146 (2007).

19. Aoshima, S. & Kanaoka, S. A Renaissance in Living Cationic Polymerization. *Chem. Rev.* **109,** 5245–5287 (2009).

20. Dechy-Cabaret, O., Martin-Vaca, B. & Bourissou, D. Controlled Ring-Opening Polymerization of Lactide and Glycolide. *Chem. Rev.* **104,** 6147–6176 (2004).

21. Matyjaszewski, K. Atom Transfer Radical Polymerization: From Mechanisms to Applications. *Isr. J. Chem.* **52,** 206–220 (2012).

22. Lowe, A. B. & McCormick, C. L. Reversible addition–fragmentation chain transfer (RAFT) radical polymerization and the synthesis of water-soluble (co)polymers under homogeneous conditions in organic and aqueous media. *Prog. Polym. Sci.* **32,** 283–351 (2007).

23. Wakamatsu, J., Kawasaki, M., Zetterlund, P. B. & Okubo, M. Nitroxide-Mediated Radical Polymerization in Microemulsion. *Macromol. Rapid Commun.***28,** 2346–2353 (2007).

24. Najer, A., Wu, D., Vasquez, D., Palivan, C. G. & Meier, W. Polymer nanocompartments in broad-spectrum medical applications. *Nanomedicine (Lond)* **8,** 425–447 (2013).

25. Tanner, P. *et al.* Can polymeric vesicles that confine enzymatic reactions act as simplified organelles? *FEBS Lett.* **585,** 1699–1706 (2011).

26. Won, Y. Y., Brannan, A. K. & Davis, H. T. Cryogenic transmission electron microscopy (Cryo-TEM) of micelles and vesicles formed in water by poly (ethylene oxide)-based block copolymers. *J. Phys. Chem.* ***106,*** *3354-3364, B* (2002).

27. Allen, C., Maysinger, D. & Eisenberg, A. Nano-engineering block copolymer aggregates for drug delivery. *Colloids and Surfaces B: Biointerfaces* **16,** 3–27 (1999).

28. Singh, V., Khullar, P., Dave, P. N. & Kaur, N. Micelles, mixed micelles, and applications of polyoxypropylene (PPO)-polyoxyethylene (PEO)-polyoxypropylene (PPO) triblock polymers. *Int. J. Ind. Chem.* **4,** 1–18 (2013).

29. Jones, M.-C. & Leroux, J.-C. Polymeric micelles – a new generation of colloidal drug carriers. *Eur. J. Pharm. Biopharm.* **48,** 101–111 (1999).

30. Torchilin, V. P. Targeted pharmaceutical nanocarriers for cancer therapy and imaging. *AAPS J* **9,** E128–E147 (2007).

31. Oerlemans, C. *et al.* Polymeric Micelles in Anticancer Therapy: Targeting, Imaging and Triggered Release. *Pharm. Res.* **27,** 2569–2589 (2010).

32. Qian, J., Zhang, M., Manners, I. & Winnik, M. A. Nanofiber micelles from the self-assembly of block copolymers. *Trends in Biotechnology* **28,** 84–92 (2010).

33. Ekaterina B Zhulina, Mireile Adam, Isaac LaRue, Sergei S Sheiko, A.Michael Rubinstein. Diblock Copolymer Micelles in a Dilute Solution. Pharmaceutical Biotechnology. *Macromolecules* **38,** 5330-5351, (2005)

34. Y Lauw, F A M Leermakers, A., Stuart, M. A. C., O V Borisov, A. & Zhulina, E. B. Coexistence of Crew-Cut and Starlike Spherical Micelles Composed of Copolymers with an Annealed Polyelectrolyte Block. Pharmaceutical Biotechnology. *Macromolecules* **39,** (2006)

35. Shaoliang Lin, Naoko Numasawa, Takuhei Nose, A. & Lin, J. Brownian Molecular Dynamics Simulation on Self-Assembly Behavior of Rod−Coil Diblock Copolymers. *Macromolecules,* **40**, (2007)

36. Weiwei Ding, Shaoliang Lin, Jiaping Lin, A. & Zhang, L. Effect of Chain Conformational Change on Micelle Structures: Experimental Studies and Molecular Dynamics Simulations. *J. Phys. Chem. B.* **112**, 776-783, (2008)

37. Chu, Z., Dreiss, C. A. & Feng, Y. Smart wormlike micelles. *Chem. Soc. Rev.* **42,** 7174–7203 (2013).
38. Dan, N. & Safran, S. A. Junctions and end-caps in self-assembled non-ionic cylindrical micelles. *Adv. Colloid Interface Sci.* **123-126,** 323–331 (2006).
39. Nicolas, J., Mura, S., Brambilla, D., Mackiewicz, N. & Couvreur, P. Design, functionalization strategies and biomedical applications of targeted biodegradable/biocompatible polymer-based nanocarriers for drug delivery. *Chem Soc Rev* **42,** 1147–1235 (2013).
40. Capretto, L. *et al.* Production of polymeric micelles by microfluidic technology for combined drug delivery: Application to osteogenic differentiation of human periodontal ligament mesenchymal stem cells (hPDLSCs). *Int. J. Pharm.* **440,** 195–206 (2013).
41. Oltra, N. S. *et al.* Polymersomes and Filomicelles. *Fundamentals of Pharmaceutical Nanoscience,* 183–210 (2013).
42. Won, Y.-Y., Davis, H. T. & Bates, F. S. Giant Wormlike Rubber Micelles. *Science* **283,** 960–963 (1999).
43. Wang, X. *et al.* Shell-Cross-Linked Cylindrical Polyisoprene- b-Polyferrocenylsilane (PI- b-PFS) Block Copolymer Micelles: One-Dimensional (1D) Organometallic Nanocylinders. *J Am Chem Soc* **129,** 5630–5639 (2007).
44. Cho, H. K., Cheong, I. W., Lee, J. M. & Kim, J. H. Polymeric nanoparticles, micelles and polymersomes from amphiphilic block copolymer. *Korean J. Chem. Eng.* **27,** 731–740 (2010).
45. Huo, M. *et al.* Single-chain polymer nanoparticles: Mimic the proteins. *Polymer* **66,** 11–21 (2015).
46. Johnson, B. K. & Prud'homme, R. K. Mechanism for rapid self-assembly of block copolymer nanoparticles. *Phys. Rev. Lett.* **91,** 118302 (2003).
47. Xu, Z., Lu, C., Riordon, J., Sinton, D. & Moffitt, M. G. Microfluidic Manufacturing of Polymeric Nanoparticles: Comparing Flow Control of Multiscale Structure in Single-Phase Staggered Herringbone and Two-Phase Reactors. *Langmuir* **32,** 12781–12789 (2016).
48. Discher, B. M. Polymersomes: Tough Vesicles Made from Diblock Copolymers. *Science* **284,** 1143–1146 (1999).
49. Discher, D. E. Polymer Vesicles. *Science* **297,** 967–973 (2002).
50. Smith, A. E., Xu, X. & McCormick, C. L. Stimuli-responsive amphiphilic (co)polymers via RAFT polymerization. *Prog. Polym. Sci.* **35,** 45–93 (2010).
51. Hadjichristidis, N., Iatrou, H., Pitsikalis, M. & Sakellariou, G. Synthesis of Well-Defined Polypeptide-Based Materials via the Ring-Opening Polymerization of α-Amino Acid N-Carboxyanhydrides. *Chem. Rev.* **109,** 5528–5578 (2009).
52. LoPresti, C., Lomas, H., Massignani, M., Smart, T. & Battaglia, G. Polymersomes: nature inspired nanometer sized compartments. *J. Mat. Chem.***19,** 3576–3590 (2009).
53. Itel, F. *et al.* Molecular Organization and Dynamics in Polymersome Membranes: A Lateral Diffusion Study. *Macromolecules* **47,** 7588–7596 (2014).
54. Onaca, O., Enea, R., Hughes, D. W. & Meier, W. Stimuli-Responsive Polymersomes as Nanocarriers for Drug and Gene Delivery. *Macromol. Biosci.* **9,** 129–139 (2009).
55. Lee, J. S. & Feijen, J. Polymersomes for drug delivery: design, formation and characterization. *J. Control. Release* **161,** 473–483 (2012).
56. Schatz, C. & Lecommandoux, S. Polysaccharide-Containing Block Copolymers: Synthesis, Properties and Applications of an Emerging Family of

Glycoconjugates. *Macromol. Rapid Commun.* **31,** 1664–1684 (2010).

57. Schatz, C., Louguet, S., Le Meins, J.-F. & Lecommandoux, S. Polysaccharide-block-polypeptide Copolymer Vesicles: Towards Synthetic Viral Capsids. *Angew. Chem. Int. Ed.* **48,** 2572–2575 (2009).
58. Zhao, L. *et al.* Biomaterials. *Biomaterials* **35,** 1284–1301 (2014).
59. Egli, S., Schlaad, H., Bruns, N. & Meier, W. Functionalization of Block Copolymer Vesicle Surfaces. *Polymers* **3,** 252–280 (2011).
60. Pawar, P. V., Gohil, S. V., Jain, J. P. & Kumar, N. Functionalized polymersomes for biomedical applications. *Polym. Chem.* **4,** 3160 (2013).
61. Messager, L., Gaitzsch, J., Chierico, L. & Battaglia, G. Novel aspects of encapsulation and delivery using polymersomes. *Curr. Opin. Pharmacol.* **18,** 104–111 (2014).
62. Kita-Tokarczyk, K., Grumelard, J., Haefele, T. & Meier, W. Block copolymer vesicles—using concepts from polymer chemistry to mimic biomembranes. *Polymer* **46,** 3540–3563 (2005).
63. Martino, C., Lee, T. Y., Kim, S.-H. & deMello, A. J. Microfluidic generation of PEG-b-PLA polymersomes containing alginate-based core hydrogel. *Biomicrofluidics* **9,** 024101 (2015).
64. Salva, R. *et al.* Polymersome shape transformation at the nanoscale. *ACS Nano* **7,** 9298–9311 (2013).
65. Stuart, M. A. C. *et al.* Emerging applications of stimuli-responsivepolymer materials. *Nat. Mater.* **9,** 101–113 (2010).
66. Sullivan, T. P. & Huck, W. T. Reactions on monolayers: organic synthesis in two dimensions. *Eur. J. Org. Chem.* **2003,** 17–29 (2003).
67. Vericat, C., Vela, M. E., Benitez, G., Carro, P. & Salvarezza, R. C. Self-assembled monolayers of thiols and dithiols on gold : new challenges for a well-known system. *Chem. Soc. Re.v* **39,** 1805–1834 (2010).
68. Whitesides, G. M. *et al.* Organized Molecular Assemblies. **3,** 49–65 (1993).
69. Yan, L., Huck, W. T. S. & Whitesides, G. M. Self-Assembled Monolayers (SAMs) and Synthesis of Planar Micro- and Nanostructures. *J. Macrom. Sci. C: Polymer Reviews* **44,** 175–206 (2004).
70. Zhang, X., Tanner, P., Graff, A., Palivan, C. G. & Meier, W. Mimicking the cell membrane with block copolymer membranes. *J. Polym. Sci. A Polym. Chem.* **50,** 2293–2318 (2012).
71. Kowal, J., Zhang, X., Dinu, I. A., Palivan, C. G. & Meier, W. Planar Biomimetic Membranes Based on Amphiphilic Block Copolymers. *ACS Macro Lett.* **3,** 59–63 (2014).
72. Ariga, K. *et al.* Challenges and breakthroughs in recent research on self-assembly. *Sci. Technol. Adv. Mater.* **9,** 014109 (2008).
73. Ariga, K., Yamauchi, Y., Mori, T. & Hill, J. P. 25th Anniversary Article: What Can Be Done with the Langmuir-Blodgett Method? Recent Developments and its Critical Role in Materials Science. *Adv. Mat.* **25,** 6477–6512 (2013).
74. Wang, H. *et al.* Highly Permeable and Selective Pore-Spanning Biomimetic Membrane Embedded with Aquaporin Z. *Small* **8,** 1185–1190 (2012).
75. Milner, S. T. Polymer brushes. **251,** 905–914 (1991).
76. Zhao, B. & Brittain, W. J. Polymer brushes: surface-immobilized macromolecules. *Prog. Polym. Sci.* **25**, 677-710, (2000).
77. Edmondson, S., Osborne, V. L. & Huck, W. T. S. Polymer brushes via surface-initiated polymerizations. *Chem Soc Rev* **33,** 14 (2004).
78. Barbey, R. *et al.* Polymer Brushes via Surface-Initiated Controlled Radical

Polymerization: Synthesis, Characterization, Properties, and Applications. *Chem. Rev.* **109,** 5437–5527 (2009).

79. Juang, A., Scherman, O. A., Grubbs, R. H. & Lewis, N. S. Formation of Covalently Attached Polymer Overlayers on Si(111) Surfaces Using Ring-Opening Metathesis Polymerization Methods. *Langmuir* **17,** 1321–1323 (2001).
80. Sakai, N. *et al.* Self-Organizing Surface-Initiated Polymerization: Facile Access to Complex Functional Systems. *J Am Chem Soc* **133,** 15224–15227 (2011).
81. Rühe, J. *et al.* in *Filler-Reinforced Elastomers/Sanning Force Microscopy* **165,** 79–150 (Springer Berlin Heidelberg, 2004).
82. Amin, I. *et al.* Polymer Carpets. *Small* **6,** 1623–1630 (2010).
83. Estillore, N. C. & Advincula, R. C. Stimuli-Responsive Binary Mixed Polymer Brushes and Free-Standing Films by LbL-SIP. *Langmuir* **27,** 5997–6008 (2011).
84. Mallwitz, F. & Laschewsky, A. Direct Access to Stable, Freestanding Polymer Membranes by Layer-by-Layer Assembly of Polyelectrolytes. *Advanced Materials* **17,** 1296–1299 (2005).
85. Kissel, P. *et al.* A two-dimensional polymer prepared byorganic synthesis. *Nat. Chem.* **4**, 287-291, (2014).
86. Turchanin, A. & Gölzhäuser, A. Progress in Surface Science. *P. Surf. Sci.* **87,** 108–162 (2012).
87. Norrman, K., Ghanbari-Siahkali, A. & Larsen, N. B. 6 Studies of spin-coated polymer films. *Annu. Rep. Prog. Chem., Sect. C* **101,** 174 (2005).
88. Decher, G. Fuzzy Nanoassemblies: Toward Layered Polymeric Multicomposites. *Science* **277,** 1232–1237 (1997).
89. Becker, A. L., Johnston, A. P. R. & Caruso, F. Layer-By-Layer-Assembled Capsules and Films for Therapeutic Delivery. *Small* **6,** n/a–n/a (2010).
90. Edmondson, S. & Armes, S. P. Synthesis of surface-initiated polymer brushes using macro-initiators. *Polym. Int.* **58,** 307–316 (2009).
91. Krebs, F. C. Fabrication and processing of polymer solar cells: A review of printing and coating techniques. *Solar Energy Materials and Solar Cells* **93,** 394–412 (2009).
92. Nishimura, K. *et al.* Population Analysis of Structural Properties of Giant Liposomes by Flow Cytometry. *Langmuir* (2009).
93. Stauch, O., Schubert, R., Savin, G. & Burchard, W. Structure of artificial cytoskeleton containing liposomes in aqueous solution studied by static and dynamic light scattering. *Biomacromolecules* **3,** 565–578 (2002).
94. Anderson, W., Kozak, D., Coleman, V. A., Jämting, Å. K. & Trau, M. A comparative study of submicron particle sizing platforms: Accuracy, precision and resolution analysis of polydisperse particle size distributions. *Journal of Colloid and Interface Science* **405,** 322–330 (2013).
95. Joset, A., Grammenos, A., Hoebeke, M. & Leyh, B. Small-Angle Neutron Scattering investigation of cholesterol-doped DMPC liposomes interacting with β-cyclodextrin. *J Incl Phenom Macrocycl Chem* **84,** 153–161 (2016).
96. Xiao, Q. *et al.* Bioactive cell-like hybrids coassembled from (glyco)dendrimersomes with bacterial membranes. *Proc. Natl. Acad. Sci. U.S.A.* **113,** 1134–1141 (2016).
97. Patterson, G. H. Fluorescence microscopy below the diffraction limit. *Seminars in Cell & Developmental Biology* **20,** 886–893 (2009).
98. Carr, R. *et al.* The real-time, simultaneous analysis of nanoparticle size, zeta potential, count, asymmetry and fluorescence. *Nanotechnology* (2008).
99. Axthelm, F. *et al.* Antioxidant Nanoreactor Based on Superoxide Dismutase

Encapsulated in Superoxide-Permeable Vesicles. *J. Phys. Chem. B* **112,** 8211–8217 (2008).

100. Rigler, R., Mets, Ü., Widengren, J. & Kask, P. Fluorescence correlation spectroscopy with high count rate and low background: analysis of translational diffusion. *Eur. Biophys. J.,* **22,** 169–175 (1993).

101. Dertinger, T. *et al*. Two-Focus Fluorescence Correlation Spectroscopy: A New Tool for Accurate and Absolute Diffusion Measurements. *Chem. Phys. Chem.* **8,** 433–443 (2007).

102. Najer, A. *et al*. An amphiphilic graft copolymer-based nanoparticle platform for reduction-responsive anticancer and antimalarial drug delivery. *Nanoscale* **8,** 14858–14869 (2016).

103. Baumann, P., Spulber, M., Fischer, O., Car, A. & Meier, W. Investigation of Horseradish Peroxidase Kinetics in an 'Organelle-Like' Environment. *Small* (2017). doi:10.1002/smll.201603943

104. Kim, S. A. & Schwille, P. Intracellular applications of fluorescence correlation spectroscopy: prospects for neuroscience. *Curr. Opin. Neurobiol.* **13,** 583–590 (2003).

105. Slavin, S. & Haddleton, D. M. An investigation into thiol–ene surface chemistry of poly(ethylene glycol) acrylates, methacrylates and CCTP polymers via quartz crystal microbalance with dissipation monitoring (QCM-D). *Soft Matter* **8,** 10388 (2012).

106. Gunkel, G. & Huck, W. T. S. Cooperative Adsorption of Lipoprotein Phospholipids, Triglycerides, and Cholesteryl Esters Are a Key Factor in Nonspecific Adsorption from Blood Plasma to Antifouling Polymer Surfaces. *J. Am. Chem. Soc.* **135,** 7047–7052 (2013).

107. Mrksich, M. Mass Spectrometry of Self-Assembled Monolayers: A New Tool for Molecular Surface Science. *ACS Nano* **2,** 7–18 (2008).

108. Erath, J., Schmidt, S. & Fery, A. Characterization of adhesion phenomena and contact of surfaces by soft colloidal probe AFM. *Soft Matter* **6,** 1432 (2010).

109. Zimmermann, R., Dukhin, S. S., Werner, C. & Duval, J. F. L. Current Opinion in Colloid & Interface Science. *Curr. Opin. Colloid Interface Sci.* **18,** 83–92 (2013).

110. Küchler, A., Yoshimoto, M., Luginbühl, S., Mavelli, F. & Walde, P. Enzymatic reactions in confined environments. *Nat. Nanotech.* **11,** 409–420 (2016).

111. Grzybowski, B. A. & Huck, W. T. S. The nanotechnology of life-inspired systems. *Nat. Nanotech.* **11,** 585–592 (2016).

112. Xiao, K., Wen, L. & Jiang, L. Biomimetic Solid-State Nanochannels: From Fundamental Research to Practical Applications. *Small* **12,** 2810–2831 (2016).

113. Balasubramanian, V. *et al*. Biomimetic Engineering Using Cancer Cell Membranes for Designing Compartmentalized Nanoreactors with Organelle-Like Functions. *Adv. Mat.* **29,** (2017).

114. Parodi, A. *et al*. Synthetic nanoparticles functionalized with biomimetic leukocyte membranes possess cell-like functions. *Nat. Nanotec.* **8,** 61–68 (2013).

115. Brea, R. J., Rudd, A. K. & Devaraj, N. K. Nonenzymatic biomimetic remodeling of phospholipids in synthetic liposomes. *Proc. Natl. Acad. Sci. U.S.A.* **113,** 8589–8594 (2016).

116. Zhang, X. *et al*. Active surfaces engineered by immobilizing protein-polymer nanoreactors for selectively detecting sugar alcohols. *Biomaterials* **89,** 79–88 (2016).

117. Baumann, P., Balasubramanian, V., Onaca-Fischer, O., Sienkiewicz, A. &

Palivan, C. G. Light-responsive polymer nanoreactors: a source of reactive oxygen species on demand. *Nanoscale* **5,** 217–224 (2013).

118. Burns, J. R., Seifert, A., Fertig, N. & Howorka, S. A biomimetic DNA-based channel for the ligand-controlled transport of charged molecular cargo across a biological membrane. *Nat. Nanotech.* **11,** 152–156 (2016).
119. Jin, Y. *et al.* Bioengineered Extracellular Membranous Nanovesicles for Efficient Small-Interfering RNA Delivery: Versatile Platforms for Stem Cell Engineering and In Vivo Delivery. *Adv Funct Mater* **26,** 5804–5817 (2016).
120. Anraku, Y. *et al.* Systemically Injectable Enzyme-Loaded Polyion Complex Vesicles as In Vivo Nanoreactors Functioning in Tumors. *Angew. Chem. Int. Ed. Engl.* **55,** 560–565 (2016).
121. Kumar, M., Grzelakowski, M., Zilles, J., Clark, M. & Meier, W. Highly permeable polymeric membranes based on the incorporation of the functional water channel protein Aquaporin Z. *Proc. Natl. Acad. Sci. U.S.A* **104,** 20719–20724 (2007).
122. Hammer, D. A. & Kamat, N. P. Towards an artificial cell. *FEBS Lett.* **586,** 2882–2890 (2012).
123. Roodbeen, R. E. & van Hest, J. C. M. Synthetic cells and organelles: compartmentalization strategies. *BioEssays* **31,** 1299–1308 (2009).
124. Bolisetty, S. & Mezzenga, R. Amyloid–carbon hybrid membranes for universal water purification. *Nat.e Nanotech.* **11,** 365–371 (2016).
125. Kumar, M., Grzelakowski, M. Z., Clark, J. & Meier, M. *W.* Highly permeable polymeric membranes based on the incorporation of the functional water channel protein Aquaporin Z. *Proc. Natl. Acad. Sci. U.S.A.* **104,** 20719-20724 (2016)
126. Pace, C. N., Treviño, S., Prabhakaran, E. & Scholtz, J. M. Protein structure, stability and solubility in water and other solvents. *Philos. Trans. R. Soc. Lond., B, Biol. Sci.* **359,** 1225–1235 (2004).
127. Ahmad, Z., Shah, A., Siddiq, M. & Kraatz, H.-B. Polymeric micelles as drug delivery vehicles. *RSC Adv.* **4,** 17028–17038 (2014).
128. Chen, H. *et al.* Thermally Responsive Reversed Micelles for Immobilization of Enzymes. *Adv. Funct. Mater.* **18,** 95–102 (2008).
129. Garni, M. *et al.* Artificial Organelles: Reactions inside Protein–Polymer Supramolecular Assemblies. **70,** 424–427 (2016).
130. Tanner, P. *et al.* Polymeric vesicles: from drug carriers to nanoreactors and artificial organelles. *Acc. Chem. Res.* **44,** 1039–1049 (2011).
131. Baumann, P., Spulber, M., Dinu, I. A. & Palivan, C. G. Cellular Trojan Horse Based Polymer Nanoreactors with Light-Sensitive Activity. *J. Phys. Chem. B* **118**, 9361–9370 (2014)
132. Egli, S. *et al.* Biocompatible Functionalization of Polymersome Surfaces: A New Approach to Surface Immobilization and Cell Targeting Using Polymersomes. *J. Am. Chem. Soc.* ***133**, 4476-83,* (2011).
133. Dobrunz, D., Toma, A. C., Tanner, P., Pfohl, T. & Palivan, C. G. Polymer Nanoreactors with Dual Functionality: Simultaneous Detoxification of Peroxynitrite and Oxygen Transport. *Langmuir* **28,** 15889–15899 (2012).
134. Nardin, C., Thoeni, S., Widmer, J., Winterhalter, M. & Meier, W. Nanoreactors based on (polymerized) ABA-triblock copolymer vesicles. *Chem. Comm.* ***15*** 1433–1434 (2000).
135. Dzieciol, A. J. & Mann, S. Designs for life: protocell models in the laboratory. *Chem. Soc. Rev.* **41,** 79–85 (2012).
136. Ahmed, F. & Discher, D. E. Self-porating polymersomes of PEG–PLA and

PEG–PCL: hydrolysis-triggered controlled release vesicles. *J. Cont. Release* **96,** 37–53 (2004).

137. Yu, Y. *et al*. The proton permeability of self-assembled polymersomes and their neuroprotection by enhancing a neuroprotective peptide across the blood–brain barrier after modification with lactoferrin. *Nanoscale* **6,** 3250–3258 (2014).
138. Nardin, C., Widmer, J., Winterhalter, M. & Meier, W. Amphiphilic block copolymer nanocontainers as bioreactors. *Eur. Phys. J. E* **4,** 403–410 (2001).
139. Lomora, M. *et al*. Polymersomes with engineered ion selective permeability as stimuli-responsive nanocompartments with preserved architecture. *Biomaterials* **53,** 406–414 (2015).
140. Lomora, M., Itel, F., Dinu, I. A. & Palivan, C. G. Selective ion-permeable membranes by insertion of biopores into polymersomes. *Phys. Chem. Chem. Phys* .**17,** 15538–15546 (2015).
141. Itel, F., Najer, A., Palivan, C. G. & Meier, W. Dynamics of Membrane Proteins within Synthetic Polymer Membranes with Large Hydrophobic Mismatch. *Nano Lett*. **15**, 7596-7603 (2015).
142. Graff, A. *et al*. Amphiphilic Copolymer Membranes Promote NADH:Ubiquinone Oxidoreductase Activity: Towards an Electron-Transfer Nanodevice. *Macromol. Chem. Phys*. **211,** 229–238 (2010).
143. Graff, A., Sauer, M., Van Gelder, P. & Meier, W. Virus-assisted loading of polymer nanocontainer. *Proc. Natl. Acad. Sci. U.S.A*. **99,** 5064–5068 (2002).
144. Kumar, M., Habel, J. E. O., Shen, Y.-X., Meier, W. P. & Walz, T. High-density reconstitution of functional water channels into vesicular and planar block copolymer membranes. *J Am Chem. Soc*. **134,** 18631–18637 (2012).
145. Muhammad, N., Dworeck, T., Fioroni, M. & Schwaneberg, U. Engineering of the E. coli Outer Membrane Protein FhuA to overcome the Hydrophobic Mismatch in Thick Polymeric Membranes. *J. Nanobiotechnology* **9,** 8 (2011).
146. Ihle, S. *et al*. Nanocompartments with a pH release system based on an engineered OmpF channel protein. *Soft Matter* **7,** 532 (2011).
147. Koçer, A., Walko, M. & Ben L Feringa. Synthesis and utilization of reversible and irreversible light-activated nanovalves derived from the channel protein MscL. *Nat. Protoc*. **2,** 1426–1437 (2007).
148. Choi, H.-J. & Montemagno, C. D. Light-Driven Hybrid Bioreactor Based on Protein-Incorporated Polymer Vesicles. *IEEE Trans. Nanotechnology* **6,** 171–176 (2007).
149. Choi, H.-J. & Montemagno, C. D. Artificial Organelle: ATP Synthesis from Cellular Mimetic Polymersomes. *Nano Lett*. **5,** 2538–2542 (2005).
150. Palivan, C. G., Fischer-Onaca, O., Delcea, M., Itel, F. & Meier, W. Protein-polymer nanoreactors for medical applications. *Chem. Soc. Rev*. **41,** 2800–2823 (2012).
151. Lin, W.-J. *et al*. Pegylated Polyester Polymeric Micelles as a Nano-carrier: Synthesis, Characterization, Degradation, and Biodistribution. *J Exper. & Clin. Med*. **2,** 4–10 (2010).
152. Hamad, I., Hunter, A. C. & Moghimi, S. M. Complement monitoring of Pluronic 127 gel and micelles: Suppression of copolymer-mediated complement activation by elevated serum levels of HDL, LDL, and apolipoproteins AI and B-100. *J. Cont. Release* **170,** 167–174 (2013).
153. Rapoport, N. Physical stimuli-responsive polymeric micelles for anti-cancer drug delivery. *Prog. Polym. Sci*. **32,** 962–990 (2007).
154. Cai, S., Vijayan, K., Cheng, D., Lima, E. M. & Discher, D. E. Micelles of

Different Morphologies—Advantages of Worm-like Filomicelles of PEO-PCL in Paclitaxel Delivery. *Pharm. Res.* **24,** 2099–2109 (2007).

155. Kim, D. W. *et al.* Multicenter phase II trial of Genexol-PM, a novel Cremophor-free, polymeric micelle formulation of paclitaxel, with cisplatin in patients with advanced non-small-cell lung cancer. *Ann. Oncol.* **18,** 2009–2014 (2007).
156. Verschraegen, C. F. *et al.* A phase I and pharmacokinetic study of paclitaxel poliglumex and cisplatin in patients with advanced solid tumors. *Cancer Chemother. Pharmacol.* **63,** 903–910 (2009).
157. De Oliveira, H., Thevenot, J. & Lecommandoux, S. Smart polymersomes for therapy and diagnosis: fast progress toward multifunctional biomimetic nanomedicines. *WIREs Nanomed. Nanobiotechnol.* **4,** 525–546 (2012).
158. Tanner, P., Onaca, O., Balasubramanian, V., Meier, W. & Palivan, C. G. Enzymatic cascade reactions inside polymeric nanocontainers: a means to combat oxidative stress. *Chemistry* **17,** 4552–4560 (2011).
159. Renggli, K. *et al.* Selective and Responsive Nanoreactors. *Adv. Funct. Mater.* **21,** 1241–1259 (2011).
160. Peters, R. J. R. W., Louzao, I. & van Hest, J. C. M. From polymeric nanoreactors to artificial organelles. *Chem. Sci.* **3,** 335–342 (2012).
161. van Oers, M., Rutjes, F. & van Hest, J. Cascade reactions in nanoreactors. *Curr. Op. Biotech.* **28,** 10–16 (2014).
162. Marguet, M., Bonduelle, C. & Lecommandoux, S. Multicompartmentalized polymeric systems: towards biomimetic cellular structure and function. *Chem. Soc. Rev.* **42,** 512 (2012).
163. Meng, F. & Zhong, Z. Polymersomes Spanning from Nano- to Microscales: Advanced Vehicles for Controlled Drug Delivery and Robust Vesicles for Virus and Cell Mimicking. *J. Phys. Chem. Lett.* **2,** 1533–1539 (2011).
164. Hu, X. *et al.* Stimuli-Responsive Polymersomes for Biomedical Applications. *Biomacromolecules* (2017).
165. Cabane, E., Zhang, X., Langowska, K., Palivan, C. G. & Meier, W. Stimuli-Responsive Polymers and Their Applications in Nanomedicine. *Biointerphases* **7,** 1–27 (2012).
166. Immordino, M. L., Dosio, F. & Cattel, L. Stealth liposomes: review of the basic science, rationale, and clinical applications, existing and potential. *Int. J. nanomedicine.* **1**, 297-315 (2006).
167. Gaitzsch, J., Appelhans, D., Wang, L., Battaglia, G. & Voit, B. Synthetic Bio-nanoreactor: Mechanical and Chemical Control of Polymersome Membrane Permeability. *Angew. Chem. Int. Ed. Engl.* **51,** 4448–4451 (2012).
168. Spulber, M. *et al.* Photoreaction of a Hydroxyalkyphenone with the Membrane of Polymersomes: A Versatile Method To Generate Semipermeable Nanoreactors. *J. Am. Chem. Soc.* **135,** 9204–9212 (2013).
169. Ranquin, A., Versées, W., Meier, W., Steyaert, J. & Van Gelder, P. Therapeutic nanoreactors: combining chemistry and biology in a novel triblock copolymer drug delivery system. *Nano Lett.* **5,** 2220–2224 (2005).
170. van Dongen, S., de Hoog, H. & Peters, R. Biohybrid polymer capsules. *ChemRev.* **109**, 6212-6274 (2009).
171. Peters, R. J. R. W. *et al.* Cascade Reactions in Multicompartmentalized Polymersomes. *Angew. Chem. Int. Ed.* **53,** 146–150 (2013).
172. Martino, C. *et al.* Protein Expression, Aggregation, and Triggered Release from Polymersomes as Artificial Cell-like Structures. *Angew. Chem. Int. Ed.* **51,** 6416–6420 (2012).

173. Thingholm, B., Schattling, P., Zhang, Y. & Städler, B. Subcompartmentalized Nanoreactors as Artificial Organelle with Intracellular Activity. *Small* **12,** 1806–1814 (2016).
174. Godoy Gallardo, M., Labay, C., Jansman, M. M. T., Ek, P. K. & Hosta-Rigau, L. Intracellular Microreactors as Artificial Organelles to Conduct Multiple Enzymatic Reactions Simultaneously. *Adv. Healthc. Mater.* **6,** (2017).
175. Marguet, M., Sandre, O. & Lecommandoux, S. Polymersomes in 'Gelly' Polymersomes: Toward Structural Cell Mimicry. *Langmuir* **28,** 2035–2043 (2012).
176. Marguet, M., Edembe, L. & Lecommandoux, S. Polymersomes in Polymersomes: Multiple Loading and Permeability Control. *Angew. Chem. Int. Ed.* **51,** 1173–1176 (2011).
177. *Therapeutic Proteins.* (Humana Press, 2005).
178. Pisal, D. S., Kosloski, M. P. & Balu-Iyer, S. V. Delivery of Therapeutic Proteins. *J. Pharm. Sci.* **99,** 2557–2575 (2010).
179. Govender, T., Stolnik, S., Garnett, M. C., Illum, L. & Davis, S. S. PLGA nanoparticles prepared by nanoprecipitation: drug loading and release studies of a water soluble drug. *J. Cont. Release* **57,** 171–185 (1999).
180. Jahanshahi, M. & Babaei, Z. Protein nanoparticle: A unique system as drug delivery vehicles. *Afr. J. Biotechnol.* **7,** 4926–4934 (2008).
181. Saptarshi, S. R., Duschl, A. & Lopata, A. L. Interaction of nanoparticles with proteins: relation to bio-reactivity of the nanoparticle. *J. Nanobiotech.* **11,** 26–1 (2013).
182. Zhang, Y. & Zhuo, R.-X. Synthesis and in vitro drug release behavior of amphiphilic triblock copolymer nanoparticles based on poly (ethylene glycol) and polycaprolactone. *Biomaterials* **26,** 6736–6742 (2005).
183. Guo, S. *et al.* Amphiphilic and biodegradable methoxy polyethylene glycol-block-(polycaprolactone-graft-poly(2-(dimethylamino)ethyl methacrylate)) as an effective gene carrier. *Biomaterials* **32,** 879–889 (2011).
184. Wittemann, A. & Ballauff, M. Interaction of proteins with linear polyelectrolytes and spherical polyelectrolyte brushes in aqueous solution. *Phys Chem Chem Phys* **8,** 5269–5275 (2006).
185. Wittemann, A., Azzam, T. & Eisenberg, A. Biocompatible Polymer Vesicles from Biamphiphilic Triblock Copolymers and Their Interaction with Bovine Serum Albumin. *Langmuir* **23,** 2224–2230 (2007).
186. Lu, Y., Sun, W. & Gu, Z. Stimuli-responsive nanomaterials for therapeutic protein delivery. *J.Cont. Release* **194,** 1–19 (2014).
187. Chu, X.-P., Papasian, C. J., Wang, J. Q. & Xiong, Z.-G. Modulation of acid-sensing ion channels: molecular mechanisms and therapeutic potential. *Int. J. Physiol. Pathophysiol. Pharmacol.* **3,** 288–309 (2011).
188. Lee, Y. *et al.* Charge-Conversional Polyionic Complex Micelles-Efficient Nanocarriers for Protein Delivery into Cytoplasm. *Angew. Chem. Int. Ed.* **48,** 5309–5312 (2009).
189. Yan, M. *et al.* A novel intracellular protein delivery platform based on single-protein nanocapsules. *Nature Nanotech.* **5,** 48–53 (2010).
190. Wu, X., Wu, S., Yang, L., Han, J. & Han, S. Cytosolic delivery of proteins mediated by aldehyde-displaying silica nanoparticles with pH-responsive characteristics. *J. Mat. Chem.* **22,** 17121–17127 (2012).
191. Cheng, C., Convertine, A. J., Stayton, P. S. & Bryers, J. D. Multifunctional triblock copolymers for intracellular messenger RNA delivery. *Biomaterials* **33,**

6868–6876 (2012).

192. Guo, S. *et al.* Ternary complexes of amphiphilic polycaprolactone-graft-poly (N,N-dimethylaminoethyl methacrylate), DNA and polyglutamic acid-graft-poly(ethylene glycol) for gene delivery. *Biomaterials* **32,** 4283–4292 (2011).

193. Schuchman, E. H. & Edward H. Schuchman. Acid sphingomyelinase, cell membranes and human disease: Lessons from Niemann-Pick disease. *FEBS Lett.* **584,** 1895–1900 (2009).

194. Matter, Y. *et al.* Amphiphilic PEG-b-PMCL-b-PDMAEMA Triblock Copolymers: From Synthesis to Physico-Chemistry of Self-Assembled Structures. *Macromol. Chem. Phys.* **212,** 937–949 (2011).

195. Zupancich, J. A., Bates, F. S. & Hillmyer, M. A. Aqueous Dispersions of Poly(ethylene oxide)- b-poly(γ-methyl-ε-caprolactone) Block Copolymers. *Macromolecules* **39,** 4286–4288 (2006).

196. Schillén, K. *et al.* Characterization of Polyisoprene- b-Poly(methyl methacrylate) Diblock Copolymer Micelles in Acetonitrile *J. Phys. Chem. B* **103,** 9090–9103 (1999).

197. Car, A. *et al.* pH-Responsive PDMS- b-PDMAEMA Micelles for Intracellular Anticancer Drug Delivery. *Biomacromolecules* **15,** 3235–3245 (2014).

198. Tebaldi, M. L. *et al.* Specific thermoresponsiveness of PMMA-block-PDMAEMA to selected ions and other factors in aqueous solution. *Colloid Polym Sci* **290,** 1285–1291 (2012).

199. Allen, C. *et al.* Controlling the physical behavior and biological performance of liposome formulations through use of surface grafted poly(ethylene glycol). *Biosci Rep* **22,** 225–250 (2002).

200. Elbert, D. L. & Hubbell, J. A. Surface treatments of polymers for biocompatibility. *Annual Review of Materials Science* **26,** 365–394 (1996).

201. Wu, B., Chen, Y. & Müller, J. D. Fluorescence Correlation Spectroscopy of Finite-Sized Particles. *Biophys. J.* **94,** 2800–2808 (2008).

202. Rahman, M., Laurent, S., Tawil, N., Yahia, L. & Mahmoudi, M. in *Protein-Nanoparticle Interactions* **15,** 21–44 (Springer Berlin Heidelberg, 2013).

203. Hu, Y., Xie, J., Tong, Y. W. & Wang, C.-H. Effect of PEG conformation and particle size on the cellular uptake efficiency of nanoparticles with the HepG2 cells. *J. Cont. Release* **118,** 7–17 (2007).

204. van de Wetering, P. *et al.* Relation between transfection efficiency and cytotoxicity of poly(2-(dimethylamino)ethyl methacrylate)/plasmid complexes. *J. Cont. Release* **49,** 59–69 (1997).

205. Bedotti, R., Borghetti, A. F. & Favilla, R. Stimulatory effect of serum albumin on the proliferation of serum-free SV40-transformed Balb/c 3T3 cells. *Biochim. Biophys. Acta* **1053,** 74–80 (1990).

206. Baier, G. *et al.* BSA Adsorption on Differently Charged Polystyrene Nanoparticles using Isothermal Titration Calorimetry and the Influence on Cellular Uptake. *Macromol. Biosci.* **11,** 628–638 (2011).

207. Antonietti, M. & Förster, S. Vesicles and Liposomes: A Self-Assembly Principle Beyond Lipids. *Adv. Mat.* **15,** 1323–1333 (2003).

208. Lane, D. D. *et al.* Dynamic intracellular delivery of antibiotics via pH-responsive polymersomes. *Polym. Chem.* **6,** 1255–1266 (2015).

209. Agut, W., Brûlet, A., Schatz, C., Taton, D. & Lecommandoux, S. pH and Temperature Responsive Polymeric Micelles and Polymersomes by Self-Assembly of Poly[2-(dimethylamino)ethyl methacrylate]- b-Poly(glutamic acid) Double Hydrophilic Block Copolymers. *Langmuir* **26,** 10546–10554 (2010).

210. Cabane, E., Malinova, V., Menon, S., Palivan, C. G. & Meier, W. Photoresponsive polymersomes as smart, triggerable nanocarriers. *Soft Matter* **7,** 9167–9176 (2011).

211. Guo, D.-S., Wang, K., Wang, Y.-X. & Liu, Y. Cholinesterase-Responsive Supramolecular Vesicle. *J. Am. Chem. Soc.* **134,** 10244–10250 (2012).

212. Jeong, E. S., Park, C. & Kim, K. T. Doubly responsive polymersomes towards monosaccharides and temperature under physiologically relevant conditions. *Polym. Chem.* **6,** 4080–4088 (2015).

213. Gräfe, D., Gaitzsch, J., Appelhans, D. & Voit, B. Cross-linked polymersomes as nanoreactors for controlled and stabilized single and cascade enzymatic reactions. *Nanoscale* **6,** 10752–10761 (2014).

214. Mould, J. A. *et al.* Mechanism for Proton Conduction of the M2 Ion Channel of Influenza A Virus. *Journal of Biological Chemistry* **275,** 8592–8599 (2000).

215. Liu, J. *et al.* pH-Sensitive nano-systems for drug delivery in cancer therapy. *Biotechnol. Adv.* **32**, 693-710 (2013).

216. Kato, Y., Ozawa, S., Miyamoto, C. & Maehata, Y. Acidic extracellular microenvironment and cancer. *Cancer Cell, 89, 1475- 2867* (2013).

217. Koebnik, R., Locher, K. P. & Van Gelder, P. Structure and function of bacterial outer membrane proteins: barrels in a nutshell. *Mol. Microbiol.* **37,** 239–253 (2000).

218. Langowska, K., Palivan, C. G. & Meier, W. Polymer nanoreactors shown to produce and release antibiotics locally. *Chem. Commun. (Camb.)* **49,** 128 (2012).

219. Grosse, W., Essen, L.-O. & Koert, U. Strategies and Perspectives in Ion-Channel Engineering. *Chem. Bio. Chem* .**12,** 830–839 (2011).

220. Miedema, H. *et al.* Ca2+ Selectivity of a Chemically Modified OmpF with Reduced Pore Volume. *Biophy. J.* **91,** 4392–4400 (2006).

221. Miedema, H. *et al.* Permeation Properties of an Engineered Bacterial OmpF Porin Containing the EEEE-Locus of Ca2+ Channels. *Biophys. J.* **87,** 3137–3147 (2004).

222. Kale, A. A. & Torchilin, V. P. Design, Synthesis, and Characterization of pH-Sensitive PEG−PE Conjugates for Stimuli-Sensitive Pharmaceutical Nanocarriers: The Effect of Substitutes at the Hydrazone Linkage on the pH Stability of PEG−PE Conjugates. *Bioconjugate Chem.* **18,** 363–370 (2007).

223. Tanner, P. *et al.* Specific His6-tag attachment to metal-functionalized polymersomes relies on molecular recognition. *J. Phys. Chem. B* **116,** 10113–10124 (2012).

224. Rigler, P. & Meier, W. Encapsulation of Fluorescent Molecules by Functionalized Polymeric Nanocontainers: Investigation by Confocal Fluorescence Imaging and Fluorescence Correlation Spectroscopy. *J. Am. Chem. So.c* **128,** 367–373 (2006).

225. Zhang, Y., Baekgaard Laursen, M. & Städler, B. Small Subcompartmentalized Microreactors as Support for Hepatocytes. *Adv. Healthc. Mat.* (2016).

226. Discher, B. M., Hammer, D. A., Bates, F. S. & Discher, D. E. Polymer vesicles in various media. *Curr. Opin. Colloid Interface Sci.* **5,** 125–131 (2000).

227. Breunig, M., Lungwitz, U., Liebl, R. & Goepferich, A. Breaking up the correlation between efficacy and toxicity for nonviral gene delivery. *Proc. Natl. Acad. Sci. U.S.A.* **104,** 14454–14459 (2007).

228. Hatori, Y. *et al.* Neuronal differentiation is associated with a redox-regulated increase of copper flow to the secretory pathway. *Nat. Comm.* **7,** 10640 (2016).

229. Dunnill, C. J., Ibraheem, K., Mohamed, A., Southgate, J. & Georgopoulos, N. T.

A redox state-dictated signalling pathway deciphers the malignant cell specificity of CD40-mediated apoptosis. *Oncogene* (2016). doi:10.1038/onc.2016.401

230. Ježek, P. & Hlavatá, L. Mitochondria in homeostasis of reactive oxygen species in cell, tissues, and organism. *Int. J. Biochem. Cell Biol,* **37,** 2478–2503 (2005).
231. Marí, M. *et al.* Mitochondrial glutathione: Features, regulation and role in disease. *BBA - General Subjects* **1830,** 3317–3328 (2013).
232. Chen, C.-A. *et al.* S-glutathionylation uncouples eNOS and regulates its cellular and vascular function. *Nature* **468,** 1115–1118 (2010).
233. Beer, S. M. *et al.* Glutaredoxin 2 Catalyzes the Reversible Oxidation and Glutathionylation of Mitochondrial Membrane Thiol Proteins implications for mitochondrial redox regulation and antioxidant defense. *J. Biol. Chem.* **279,** 47939–47951 (2004).
234. Edlinger, C., Fischer-Onaca, O., Meier, W. & Palivan, C. Switchable transport across modified membrane channel proteins in *Int. Sym. Nanopart./Nanomat. App., 319-320* (2014).
235. Onaca, O. *et al.* Functionalized Nanocompartments (Synthosomes) with a Reduction-Triggered Release System. *Angew. Chem. Int. Ed.* **47,** 7029–7031 (2008).
236. Sun, H., Meng, F., Cheng, R., Deng, C. & Zhong, Z. Reduction-responsive polymeric micelles and vesicles for triggered intracellular drug release. *Antioxidants & Redox Signaling* **21,** 755–767 (2014).
237. Weiner, L. M., Hu, H. & Swartz, H. M. EPR method for the measurement of cellular sulfhydryl groups. *FEBS Lett.* **290,** 243–246 (2001).
238. Hapuarachchi, S. & Aspinwall, C. A. Design, characterization, and utilization of a fast fluorescence derivatization reaction utilizing o-phthaldialdehyde coupled with fluorescent thiols. *Electrophoresis* **28,** 1100–1106 (2007).
239. Shevchenko, A., Tomas, H., Havlis, J., Olsen, J. V. & Mann, M. In-gel digestion for mass spectrometric characterization of proteins and proteomes. *Nat Protoc* **1,** 2856–2860 (2006).
240. Zhou, L. & Schlick, S. Electron spin resonance (ESR) spectra of amphiphilic spin probes in the triblock copolymer EO13PO30EO13 (Pluronic L64): hydration, dynamics and order in the polymer aggregates. *Polymer* **41,** 4679–4689 (2000).
241. Beghein, N. *et al.* Characterization of self-assembling copolymers in aqueous solutions using Electron Paramagnetic Resonance and Fluorescence spectroscopy. *J. Cont. Release* **117,** 196–203 (2007).
242. Deo, N., Somasundaran, P., Subramanyan, K. & Ananthapadmanabhan, K. P. Electron Paramagnetic Resonance Study of the Structure of Lipid Bilayers in the Presence of Sodium Dodecyl Sulfate. *J. Colloid. Interface. Sci.* **256,** 100–105 (2002).
243. Nakagawa, K. Spin-Probe Investigations of Head Group Behavior in Aqueous Dispersions of a Nonionic Amphiphilic Compound. *Lipids* **42,** 457–462 (2007).
244. Serban, M. A., Yang, G. & Prestwich, G. D. Synthesis, characterization and chondroprotective properties of a hyaluronan thioethyl ether derivative. *Biomaterials* **29,** 1388–1399 (2008).
245. Circu, M. L. & Aw, T. Y. Reactive oxygen species, cellular redox systems, and apoptosis. *Free Radic. Biol. Med* **48,** 749–762 (2010).
246. Wu, D. *et al.* Effect of Molecular Parameters on the Architecture and Membrane Properties of 3D Assemblies of Amphiphilic Copolymers. *Macromolecules* **47,** 5060–5069 (2014).

247. Siti, W. *et al.* An intercompartmental enzymatic cascade reaction in channel-equipped polymersome-in-polymersome architectures. *J. Mater. Chem. B* **2,** 2733–2737 (2014).

248. Ali, S., Champagne, D. L., Spaink, H. P. & Richardson, M. K. Zebrafish embryos and larvae: a new generation of disease models and drug screens. *Birth Defects Res. C Embryo Today* **93,** 115–133 (2011).

249. Rizzo, L. Y. *et al.* In Vivo Nanotoxicity Testing using the Zebrafish Embryo Assay. *J Mater Chem. B Mater. Biol. Med.* **1,** 3918–3925 (2013).

250. MacRae, C. A. & Peterson, R. T. Zebrafish as tools for drug discovery. *Nat. Rev. Drug Discovery* **14,** 721–731 (2015).

251. Fenaroli, F. *et al.* Nanoparticles as drug delivery system against tuberculosis in zebrafish embryos: direct visualization and treatment. *ACS Nano* **8,** 7014–7026 (2014).

252. Torraca, V., Masud, S., Spaink, H. P. & Meijer, A. H. Macrophage-pathogen interactions in infectious diseases: new therapeutic insights from the zebrafish host model. *Dis. Model. Mech.* **7,** 785–797 (2014).

253. Hale, J. P., Winlove, C. P. & Petrov, P. G. Effect of Hydroperoxides on Red Blood Cell Membrane Mechanical Properties. *Biophys. J.* **101,** 1921–1929 (2011).

254. Brown, S. D. *et al.* Gold Nanoparticles for the Improved Anticancer Drug Delivery of the Active Component of Oxaliplatin. *J. Am. Chem. So.c* **132,** 4678–4684 (2010).

255. Gi Hun Seong, Jinseok Heo, A. & Crooks, R. M. Measurement of Enzyme Kinetics Using a Continuous-Flow Microfluidic System. *Anal. Chem.* **75**, 3161-3167 (2003).

256. Glatter, T. *et al.* Large-Scale Quantitative Assessment of Different In-Solution Protein Digestion Protocols Reveals Superior Cleavage Efficiency of Tandem Lys-C/Trypsin Proteolysis over Trypsin Digestion. *J. Proteome Res.* **11,** 5145–5156 (2012).

257. Güven, A., Fioroni, M., Hauer, B. & Schwaneberg, U. Molecular understanding of sterically controlled compound release through an engineered channel protein (FhuA). *J Nanobiotechnology* **8,** 14 (2010).

258. Sariri, R., Sajedi, R. H. & Jafarian, V. Inhibition of horseradish peroxidase activity by thiol type inhibitors. *Journal of Molecular Liquids* **123,** 20–23 (2006).

259. Bolte, S. & Cordelières, F. P. A guided tour into subcellular colocalization analysis in light microscopy. *J Microsc* **224,** 213–232 (2006).

ABBERVATIONS

%	Percent
AO	Artificial organelle
AqpZ	Aquaporin Z
AR	Amplex Red or Amplex Ultra Red in Chapter 4
Ar	Argon
ASM	Acid sphingomyelinase
ATRP	Atom transfer radical polymerization
BCA	Bicinchoninic acid assay
BSA	Bovine serum albumine
CMC	Critical micellar concentration
CMT	Critical micellar temperature
CPM	Counts per molecule
CRP	Controlled radical polymerization
Cu/ZnSOD	Copper-zinc superoxide dismutase
DLS	Dynamic light scattering
DMSO	Dimethyl sulphoxide
DNPH	2,4-Dinitrophenylhydrazine
EEv	Encapsulation efficiency based on vesicles
EGFP	Enhanced green fluorescent protein
FACS	Fluorescence-activated cell sorting
FCS	Fluorescence correlation spectroscopy
FhuA	Ferrichrome outer membrane transporter

ABBERVATIONS

FITC	Fluorescein IsoThioCynanate
G	Autocorrelation amplitude
gA	Gramicidin
GFP	Green fluorescent protein
GSH	Glutathione
GUV	Giant unilammelar vesicle
h	Hour
HCl	Hydrochloric Acid
He-Ne	Helium-Neon
HRP	Horseradish peroxidase
IPTG	β-D-thiogalactopyranoside
kDa	kilo Dalton
kHz	kilo Hertz
LamB	Maltoporin membrane protein
LB	Lysogen Broth
LBL	Layer by layer
LSM	Laser scanning microscopy
min	Minute
ms	Millisecond
MTS	(3-(4,5-dimethylthiazol-2-yl)-5-(3-carboxymethoxyphenyl)-2-(4-sulfophenyl)-2H-tetrazolium)
Mw	Molecular weighted polymer molecular eight
mW	Milliwat
MWCO	Molecular weight cutoff
NHS	N-hydroxysuccinimide

ABBERVATIONS

nm	Nanometre
nM	Nanomolar
NMP	Nitroxide-mediated radical polymerization
NMR	Nuclear magnetic resonance
NP	Nanoparticle
ºC	Degree Celsius
OG	n-Octyl-β-D-Glucoside
OmpF	Outer Membrane protein F
PAA	Polyarylamide
PAGE	Polyacrylamide gel electrophoresis
PBS	Phosphate buffer saline
PCL	Polycaprolactone
PDI	Polydyspersity
PDMAEMA	poly((dimethylamino)ethyl methacrylate)
PEG	Poly (Ethylene Glycol)
PLA	Poly Lactic Acid
PMCL	Poly(4-methyl-ε-caprolactone
PMOXA-*b*-PDMS-*b*-PMOXA	poly(2-methyloxazoline)-*block*-poly(dimethylsiloxane)-*block*-poly(2-methyloxazoline)
RAFT	Reversible Addition–Fragmentation chain Transfer
RFP	Red fluorescent protein
RNS	Reactive nitrogen species
ROP	ring-opening polymerization
ROS	Reactive oxygen species
s	Second

ABBERVATIONS

SAMSA-CF	5-((2-(and-3)-S-(acetylmercapto) succinoyl) amino) Fluorescein
SANS	Small angle neutron scattering
SDS	Sodium dodecyl sulfate
SEM	Scanning electron microscopy
SLS	Static light scattering
SPT	Single particle tracking
TB	Terrific broth
TCA	Trichloroacetic acid
t_d	Diffusion time
TEM	Transmission electron microscopy
TEM	Transmission Electron Microscopy
TMB	3,3’,5,5’-Tetramethylbenzidine
t_{trip}	Triplet time
ZFE	Zebrafish Embryo
λem	Emission wavelength
λem	Emission wavelength
λex	Excitation wavelength
λex	Excitation wavelength
μL	Microliter
μM	Micromolar
μs	Microsecond

ABOUT THE AUTHOR AND CV

Tomaž Einfalt was born on April 25th 1990 in Celje, Slovenia. In 2013, he graduated at the Faculty of Pharmacy, University of Ljubljana, receiving his Msc in Pharamceutical Sciences and licence to practice as a Pharmacist. During his studies he participated in the European Erasmus exchange programme, which enabled him to do research at the Department of Pharmaceutical Technology and Biopharmacy at the University of Regensburg, DE and the Department of Pharmaceutical Technology, School of Life and Health sciences, University of Aston, UK. Since 2014 he has been a PhD student at the Swiss Nanoscience Institute.

During his PhD he worked as a teaching assistant and actively participated in the SNI public outreach programme, bringing science closer to the public.

In his private life, Tomaž Einfalt is a competitive triathlete, enjoying the challenges faced in sports just as much as those faced in science.

SUMMARY OF QUALIFICATIONS

- In depth knowledge in molecular and synthetic biology, solid and nanoscale pharmaceutical formulations for drug delivery.
- Excellent skills in designing, planning and conducting controlled experiments to improve understanding of active compound pharmacokinetics and pharmacodynamics.
- Excellent communication and presentation skills in the field of pharmaceutical sciences, good organizational and administrative skills. Strong IT skills, including data retrieval and analysis.

ABOUT THE AUTHOR AND CV

EDUCATION

2013-Present: Doctorate studies in Physical Chemistry - Nanosciences at the Swiss Nanoscience Institute, University of Basel, Switzerland. Doctorate thesis under the supervision of Prof. Dr. Cornelia Palivan and Prof. Dr. Jörg Huwyler.

2009-2013: Uniform master's study program of Pharmacy, Faculty of Pharmacy Ljubljana, University of Ljubljana, Slovenia

- Passed all exams in the normal curriculum with an average grade of 9.04. (On a 10-point scale.)
- Graduated with an average grade of 9.04 (On a 10 point scale.) and successfully defended master degree with the highest mark possible.

2011-2013: Erasmus programme - scientific research exchange at the University of Regensburg, Germany and Aston University, UK.

- Scientific research exchanges the department of Pharmaceutical Technology and Biopharmacy at the University of Regensburg and the department of Pharmaceutical Technology at Aston University.

2004-2008: High school education at the First Grammar School in Celje, Slovenia

- Graduated with 96/100 points. Ranked among the top 5% nationwide.

PROFESSIONAL EXPERIENCE

Fall 2012-Spring 2013: Assistant Pharmacist at the communal Pharmacy - Center Celje, Celjske Lekarne d.d, Slovenia

- Prepared pharmaceutical preparations for pediatric patients and aseptic pharmaceutical preparations.
- Specialized in clinically relevant drug interactions, clinical pharmacy, pharmacotherapy and patient counseling.

Summers 2009-2011: Internship at the community pharmacy Cizej s.p, Laško, Slovenia

- Helped out with magistral pharmaceutical preparations and drug dispensing.

- Organized repeat prescriptions (stock i.e. stock counts and date checking).
- carried out blood pressure, diabetes, cholesterol and BMI reading tests for the provision of personalized healthcare advice.

RESEARCH

2013-Present: *Researcher* at the Swiss Nanoscience institute, University of Basel, Department of Chemistry and Department of Pharmaceutical Technology

Topic: “Design of controlled enzymatic reactions by engineering of polymer and lipid based membranes intended for protein drug delivery”

- Biotechnological production, purification and characterization of soluble and membrane proteins for pharmaceutical formulations.
- Preparation of polymersome and liposome based nanoscale formulations for drug delivery.
- Characterization of size, charge and concentration of nanoscale formulations (TEM, advanced light scattering, fluorescence and absorbance based methods, high pressure liquid chromatography) to insure compound safety and stability.
- Aseptic work with cell cultures for testing cytotoxicity and biocompatibility of pharmaceutical formulations.
- Advanced confocal laser scanning microscopy, fluorescence assisted flow cytometry for determination of drug delivery efficiency.
- Administrative tasks: contacting collaborators, writing project proposals and reports, translating to German.
- Active participation in the Swiss Nanoscience Institute public outreach to communicate with general public.

Spring 2013: Assistant researcher at the department of Pharmaceutical Technology at Aston University, Birmingham, UK under the mentorship of Prof. Dr. Andrew Ingham.

Topic: “Development of a novel lyophilisation methods and in line powder flow characterization of lyophilisates”.

- Worked in a team of bio-engineers and pharmaceutical scientists to develop lyophilisation methods and devices for in-line testing of powder flow characteristics of pharmaceutical lyophilisates.
- Patent retrieval, research and analysis.

- Scientific database search.

2011-2012: Assistant researcher at the department of Pharmaceutical Technology and Biopharmacy at the University of Regensburg

Topic: *"Preparation of Drug Loaded DSPE-PEG-cRGD receptor Targeted Micelles."*

- Preparation of PEG based nanoscale formulations by lyophilisation.
- Characterization of nanoscale formulations by light scattering experiments, UV-VIS, mass spectrometry, Fluorescence spectroscopy and high-pressure liquid chromatography.
- Statistical data analysis and scientific database research

2009-2013: Assistant researcher at the department of Pharmaceutical Technology at the Faculty of Pharmacy in Ljubljana, University of Ljubljana under the mentorship of Prof. Dr. Odon Planinšek

Topic *"Preparation and evaluation of Different crystalline and amorphous forms of Clarithromycin and Hydrochlorothiazide"*

- Development of different solid state preparation methods (lyophilisation, melt quenching, spray drying and cryo-milling).
- Characterization of solid state preparations (X-ray diffraction spectroscopy, raman spectroscopy, solid state NMR, differential scanning calorimetry measurements, dissolution testing),
- Extensive scientific database research and patent database research.

2010-2012: Assistant researcher, research Krka d.d at the department of Biopharmacy and Pharmacokinetics at the Faculty of Pharmacy, University of Ljubljana under the mentorship of doc. Dr. Simon Žakelj

Topic: *"Investigation of Transport Mechanisms of N-desmethylimatinib Trough the Rat Small Intestine"*

- Preparation of live animal tissue (rat small intestines) for biopharmaceutical testing of drug metabolite transport on modified sweetana-grass diffusion chambers.
- Pharmaceutical metabolite evaluation using high-pressure liquid chromatography and statistical data analysis.
- Statistical data analysis and high performance liquid chromatography.

OTHER

- **Languages: English** (C2), **German** (C2), **Slovenian** (native). Able to converse in **Russian (A2)**, **Serbian and Croatian** (A2)
- Swiss Working / Resident Permit B (Expires 2018), EU – Citizenship
- **Advanced computer skills**: Mac OSX and Windows platforms, proficient in the use of Microsoft Office applications, SPSS Statistics, R, SAS, MATLAB, Ruby.
- Valid EU driving license.
- German golden lifeguard certificate
- Licensed Pharmacists in Slovenia and Switzerland.
- **Extracurricular activities:** Swiss Nanoscience Institute PhD delegate, active member at the Schwimmverein Beider Basel, competitive member at the Wildcats Swiss Triathlon Team.
- **Awards and achievement:** Zois national scholarship for talented young people, Swiss Nanoscience Institute Outreach award, Science Slam 2016 presenter.

PUBLICATIONS

- V. Postupalenko, T. Einfalt, M. Lomora, I. A. Dinu. C.G. Palivan, Bionanoreactors: From Confined Reaction Spaces to Artificial Organelles. In *Organic Nanoreactors*; Elsevier, **2016**; 341–371.
- E. Ekenlebie, T. Einfalt, A. Karytinos, A. Ingham, Pharmaceutical Patent Applications in Freeze-Drying., *Pharmaceutical Patent Analyst,* **2016**, *5*, 407–416.
- T. Einfalt, R. Goers, J. Gaitzsch, G. Gunkel Grabole, C. A. Schoenenberger, C. G.Palivan, Vesikel Aus Polymeren. *Nachrichten aus der Chemie,* **2016**, *64*, 965–967.
- D. Vasquez, T. Einfalt, W. Meier, C. G. Palivan, Asymmetric Triblock Copolymer Nanocarriers for Controlled Localization and pH-Sensitive Release of Proteins. *Langmuir,* **2016**.
- X. Zhang, M. Lomora, T. Einfalt, W. Meier, N. Klein, D. Schneider, C.G. Palivan, Active Surfaces Engineered by Immobilizing Protein-Polymer Nanoreactors for Selectively Detecting Sugar Alcohols. *Biomaterials,* **2016**, *89*, 79–88.
- M. Garni, T. Einfalt, M. Lomora, A. Car, W. Meier, C.G. Palivan, Artificial Organelles: Reactions Inside Protein-Polymer Supramolecular Assemblies. *CHIMIA,* **2016**, *70*, 424–427.
- T.Einfalt, R. Goers, I. A. Dinu, A. Najer, M. Spulber, O. Onaca-Fischer, C. G. Palivan, Stimuli-Triggered Activity of Nanoreactors by Biomimetic Engineering Polymer Membranes. *Nano Letters*. **2015**, *15*, 7596–7603.
- T. Einfalt, G. Gunkel, M. Spulber, A. Najer, C. G. Palivan, Supramolecular Architectures from Self-Assembled Copolymers. In *CRC Concise Encyclopedia of Nanotechnology,* Taylor and Francis, **2015**, pp 1055-1072
- T. Einfalt, O. Planinšek, K. Hrovat, Methods of Amorphization and Investigation of the Amorphous State. *Acta Pharmaceutica* **2013**, *63*, 305–334.
- *Publications in preparation upon request*

SCIENTIFIC OUTPUT

- T. Einfalt, R. Goers, I. A. Dinu, A. Najer, M Spulber, O. Onaca-Fischer, C.G. Palivan, *Biomimetic engineering of reductive responsive nanoreactors*, Nanoscience in the Snow, Zinal (Switzerland), **Poster**, January, **2016**
- T. Einfalt, R. Goers, I. A. Dinu, A. Najer, M Spulber, O. Onaca-Fischer, C.G. Palivan, *Biomimetic engineering of polymersome membranes for stimuli triggered activity of nanoreactors,* Peroxsisystem conference*,* Weizmann Insitute of Science (Israel), **Poster**, Ferbruary, **2016**
- T. Einfalt, R. Goers, I. A. Dinu, A. Najer, M Spulber, O. Onaca-Fischer, C.G. Palivan, *Biomimetic Engineering of Stimuli Responsive Artificial Cell Organelles,* Swiss Soft Days*,* Zürich (Switzerland), **Talk**, May, 2016
- T. Einfalt, R. Goers, I. A. Dinu, A. Najer, M Spulber, O. Onaca-Fischer, C.G. Palivan, *Biomimetic Engineering of Stimuli Responsive Artificial Cell Organelles,* Swiss Nanoconvention*,* Basel (Switzerland), **Poster**, June, **2016**
- T. Einfalt, C. Edlinger, R. Goers, A. Najer, M Spulber, C.G. Palivan, *Towards stimuli responsive artificial cell organelles by biomimetic engineering of complex membrane processes*, 80th PMM conference Self-assembly in the World of Polymers, Prague (Czech Republic), **Talk**, July, 2016.
- T. Einfalt, R. Goers, I. A. Dinu, A. Najer, M Spulber, O. Onaca-Fischer, C.G. Palivan, *Towards stimuli responsive artificial cell organelles by biomimetic engineering of complex membrane processes*, SNI Annual Meeting, Lenzerheide (Switzerland), **Talk**, September, **2016**
- T. Einfalt, C. Edlinger, A. Najer, R. Goers, M. Spulber, D. Witzigmann, J. Huwyler, C. G. Palivan, *Biomimetic engineering of stimuli responsive artificial cell organelle membranes*, N.I.C.E conference, Nice (France), **Talk**, October **2016**.
- T. Einfalt, A. Najer, R. Goers, M. Spulber, D. Witzigmann, J. Huwyler, C. G. Palivan, *Design of polymer nanoreactors with triggered activity for medicine and biosensing applications*, Nano DDS Symposium, Seattle (USA), **Poster**, October **2015**.
- T. Einfalt, A. Najer, R. Goers, M. Spulber, D. Witzigmann, J. Huwyler, C. G. Palivan, *Design of polymer nanoreactors with triggered activity for medicine and biosensing applications*, Swiss Soft Days, Freiburg (Switzerland), **Poster**, October **2015**.

- T. Einfalt, A. Najer, R. Goers, M. Spulber, D. Witzigmann, J. Huwyler, C. G. Palivan, *Design of polymer nanoreactors with triggered activity for medicine and biosensing applications*, Swiss Soft Days, Neuchatel (Switzerland), **Poster**, June **2015**.
- T. Einfalt, A. Najer, R. Goers, M. Spulber, D. Witzigmann, J. Huwyler, C. G. Palivan, *Design of polymer nanoreactors with triggered activity for medicine and biosensing applications,* Nanoscience in the Snow, Belalp (Switzerland), **Talk**, January, **2015**
- T. Einfalt, A. Najer, R. Goers, M. Spulber, D. Witzigmann, J. Huwyler, C. G. Palivan, *Design of polymer nanoreactors with triggered activity for medicine and biosensing applications,* N.I.C.E conference, Nice (France), **Talk**, January, **2014**